A Hybrid Nonlinear FDTD Method and Its Application to Nonlinear Optical and Millimeter-Wave Devices

by

Vien Van

A thesis
presented to the University of Waterloo
in fulfillment of the thesis requirement for
the degree of
Doctor of Philosophy
in
Electrical Engineering

Waterloo, Ontario, Canada, 1999

0-612-51235-5

Abstract

The search for new device concepts for applications in optical and millimeter-wave communications has recently led to the possibility of utilizing the nonlinear electronic properties of optical and high-temperature superconducting (HTS) materials. However, analysis of these devices is considerably complicated by the very fact that the material constitutive relations are nonlinear, and a rigorous solution of the problem in general requires a numerical approach. Toward this aim, we propose in this thesis an efficient hybrid Finite-Difference Time-Domain (FDTD) method for analyzing nonlinear wave propagation in two-dimensional optical and millimeter-wave devices. By employing different numerical schemes to solve for the electromagnetic fields separately in the regions of linear and nonlinear materials, the computation time of the overall method can be reduced without compromising the accuracy of the solution. In particular, for TE-polarized wave, the hybrid method combines the computational simplicity of the conventional explicit FDTD scheme with the superior stability property of a partially-implicit discretization to provide efficient and stable solutions to the scalar wave equation. For the case of TM polarization, a full-wave analysis using the leap-frog scheme with subgridding capability is integrated into the explicit scalar solution. In addition, in order to extend the FDTD method to nonlinear HTS media, a method of analysis based on the nonlinear London theory of superconductivity is proposed. The formulation directly incorporates the nonlinear Meissner effect into the analysis to give an approach that is expedient to FDTD solution and yields considerable saving in computation time over the traditional technique based on the Ginzburg-Landau theory. The result is an efficient and accurate algorithm for analyzing nonlinear propagation in HTS waveguides.

The hybrid FDTD method introduced provides a powerful tool for analyzing a large class of two-dimensional nonlinear devices. We demonstrate its application to a number proposed novel devices for optical and millimeter-wave signal processing. Examples include nonlinear periodic optical waveguides for wavelength and power discrimination, nonlinear HTS transmission lines for impulse generation via shock-wave formation, and nonlinear resonating structures for frequency mixing and harmonic generation with high conversion efficiencies. Numerical results obtained for these devices serve to demonstrate the potential applications of material nonlinearity in millimeter-wave and optical integrated circuits.

Acknowledgments

This page is by far the easiest to write in the whole thesis, and yet this work would not have been possible without the people or organizations mentioned herein.

First and foremost, I would like to express my gratitude and appreciation to my advisor, Prof. Sujeet K. Chaudhuri, for his continuous guidance and inspiration throughout the duration of my graduate study.

Several people have also provided valuable suggestions and assistance in the course of my work. I would like to thank Dr. Sai Tak Chu, Dr. Brent Little, Prof. Peter Forsyth, Prof. Wei-Ping Huang, Prof. Raafat R. Mansour and Prof. S. Safavi-Naeini. Much gratitude and appreciation also goes to my external examiner, Prof. Richard W. Ziolkowski of the University of Arizona at Tucson, for taking the time to review this work and for offering many valuable suggestions and comments.

And finally, I would like to acknowledge the vital financial support of the Natural Science and Engineering Research Council, the Institute for Computer Research and the Faculty of Engineering of the University of Waterloo.

Table of Contents

List of Figures

List of Tables

Chapter 1

Introduction

The ever-increasing demand for larger bandwidth for high-speed communication is constantly pushing the telecommunication technology to higher frequencies and higher bit rates. Already terabit optical networks are well under way to commercialization, and sub-millimeter-wave wireless systems aimed at meeting the increasing need for mobility have been proposed. The technology of tomorrow's information systems depends crucially on the development of electronic and optical components that can perform efficiently and reliably at tens-of-gigahertz frequencies and beyond. This engineering challenge is pushing research effort worldwide forward in two general directions: optimizing existing technology for more efficient and faster devices, and searching for new and novel technologies. In the latter case, it is often true that with the introduction of a new technology, new mathematical tools are also needed to facilitate the analysis of the device performances.

The continuous exploration of new device concepts for applications in optical and millimeter-wave communications and signal processing has recently led to the possibility of using the nonlinear electronic properties of materials. Some examples of nonlinear devices that have been suggested are switches, beam steerers and logic elements. In the optical frequency range, material nonlinearity is commonly manifested in the form of second-order Pockels effect and third-order Kerr effect. In the millimeter-wave regime, high-temperature superconducting (HTS) materials provide a strong nonlinearity that can be exploited to realize novel devices. The nonlinear characteristics of these materials afford one an additional degree of design flexibility in experimenting with new device structures. At the same time, however, the resulting complex and sometimes non-intuitive behaviour of nonlinear systems presents a barrier in the understanding of the device operation. In this respect, the ability to numerically simulate and analyze the device accurately and quickly would be an invaluable asset in the design process. In time-critical market production, such a simulation tool would also prove to be an essential aid in enabling the engineer to predict and optimize device characteristics before fabrication, thus resulting in a significant saving in both development time and cost.

Analysis methods of millimeter-wave and optical devices range from approximate analytical techniques, such as the Coupled-Mode Theory, to full-wave numerical solution of Maxwell's equations in the time domain. Within the class of numerical simulators there are several widely-used techniques such as the Beam Propagation method (BPM), the Finite-Difference Time-Domain method (FDTD), and the Finite Element method (FEM). Of these, however, the FDTD method proves to be the most versatile because it can readily incorporate almost any type of constitutive relation describing the medium in use, including nonlinear media. Recently, reports of its application to simulate nonlinear dispersive slab waveguides, optical grating structures, and HTS microstrips have demonstrated the power of FDTD in solving nonlinear problems [3–6,98]. However, many relevant numerical issues associated with the nonlinear method have not been addressed or are not fully understood.

To date, many reported applications of the FDTD method to nonlinear media commonly employ an explicit-time discretization scheme in which the field-dependent permittivity at the unknown time step $n+1$ is computed using the electric field at the current time step n. This scheme results in a simple explicit linear propagator which can be used to march the field efficiently through time without requiring an iterative solution. A major drawback of this approach, however, is the restrictive stability condition which places a severe constraint on the time step and mesh sizes [16,46]. It has been shown that in some cases the time step has to be reduced 20 to 30 times below the limit set by the CFL stability condition in order to achieve stability in the nonlinear regions [16]. In other cases, the stability of the numerical solution may not even be guaranteed. On a more fundamental level, the method introduces an artificial time lag equal to the discrete time step Δt, because the displacement vector at time $(n+1)\Delta t$ is computed using the permittivity at time $n\Delta t$ and electric field at $(n+1)\Delta t$, i.e., $D^{n+1} \approx \varepsilon\left(E^{n}\right)E^{n+1}$. A more accurate approach is to solve the nonlinear discrete equations exactly by using an iterative method of root finding. Furthermore, to enhance the overall stability of the method, an implicit-time discretization may be used, although the computation effort required can be prohibitively large if the scheme is applied to the entire computational domain. In this thesis we will introduce a hybrid implicit-explicit FDTD method for solving the TE scalar wave equation in two dimensions. The method applies a partially-implicit scheme selectively only to regions of nonlinear materials to eliminate the instability issue associated with nonlinearities, while retaining the computational simplicity of the explicit scheme in the linear material regions. The proposed hybrid method demonstrates superior stability properties over the existing explicit FDTD scheme, and is particularly suitable to structures comprising of small nonlinear regions in an otherwise linear medium.

Central to any numerical scheme are the questions of stability and accuracy. Both of these issues, as well as the phenomenon of numerical dispersion inherent in any hyperbolic system, will be dealt with. The validity of the numerical solutions will then be verified by applying the method to a variety of nonlinear optical devices such as slab waveguides, periodic waveguides, and microring resonators. The results obtained from the hybrid scheme will also be compared to those of the non-iterative explicit scheme to demonstrate the advantages of the proposed technique.

In the millimeter-wave frequency range, it was mentioned that nonlinearity can be derived from the magnetic field dependence of the penetration depth of high-temperature superconducting materials. However, as there is no explicit model for the nonlinear constitutive relation of HTS materials, a phenomenological model will be adopted based on the two-fluid London theory of superconductivity and the nonlinear Meissner effect. This constitutive relation along with Maxwell's equations forms the basis for a full-wave time-domain formulation of propagation in HTS media. An efficient FDTD algorithm is then proposed for solving the resulting equations for nonlinear wave propagation in HTS materials.

The nonlinear FDTD simulator provides a powerful tool which will enable us to explore and analyze a variety of novel nonlinear devices, both in the optical and millimeter-wave frequency ranges. In general, with some minor modifications, device concepts in optics can be transferred to millimeter-wave applications and vice versa. For example, the same principle of operation of an optical grating filter can be used to design a periodic millimeter-wave filter, and the idea of using ring waveguides as resonators in microwave can also be applied to make optical resonators. In this thesis, we extend the functions of these structures by introducing nonlinearity into the materials. One way of exploiting the nonlinear material properties is to construct devices whose responses depend on the applied power. A particularly important application is the distributed Bragg resonator with nonlinear corrugations. Such a filter can provide a response that is both wavelength and power selective. In another application, nonlinearity is used for the generation of new frequencies. We propose an optical nonlinear microring for three-wave mixing with high conversion efficiency. The same device can also be realized in the millimeter-wave regime using one-dimensional resonators. These proposed devices serve to demonstrate the potential applications of material nonlinearity in millimeter-wave and optical integrated circuits.

1.1 Thesis Organization

This thesis is organized into six chapters. This chapter presents the research problem and gives the motivations for the work. A general background of the problem is provided through an overview of nonlinear devices and a review of the current state of computational electromagnetics. Chapter 2 gives the mathematical formulation of the new hybrid FDTD scheme for simulating nonlinear wave propagation. Relevant numerical issues such as absorbing boundary conditions, stability, accuracy, and convergence are also discussed. Chapter 3 presents the application of the proposed FDTD scheme to nonlinear optical devices. The versatility of the method is demonstrated and comparison to the conventional non-iterative FDTD method is made. Chapter 4 addresses the issues specific to the numerical analysis of propagation in high-temperature superconducting materials. An approach for describing the nonlinear behaviour of superconductors that is expedient to numerical analysis is introduced. In Chapter 5, the proposed FDTD method is used to analyze nonlinear HTS millimeter-wave devices. Here the emphasis will be placed on the investigation of the phenomena associated with nonlinear propagation in HTS waveguides, and their potential applications in millimeter-wave signal processing. Finally, Chapter 6 summarizes the thesis, provides conclusions drawn from the research and outlines directions for future work.

1.2 Background

To set the stage and provide proper perspective for the thesis, an overview of nonlinear microwave and optical devices for communications and signal processing is given in this section, followed by a review of existing numerical techniques for electromagnetic analysis. The focus will be placed on the phenomenon of nonlinear wave propagation and the numerical techniques available for its analysis.

1.2.1 Nonlinear devices

Nonlinear devices are those whose response depends on the amplitude of the applied signal. This nonlinear characteristic can be utilized to perform functions that are not possible in linear devices, such as pulse shaping and frequency generation. In other cases, nonlinear effects may be used to improve the performance of a device or a network. For example, in long-haul optical communication networks solitons offer a potential solution to the problem of bandwidth degradation due to dispersion in the fibre.

Nonlinear microwave and optical devices can be classified as either active or passive elements. Although active devices exhibit stronger nonlinearity than passive elements, the former need external biasing sources which complicate the implementation of the device. Examples of active devices are semiconductor microwave *p-n* junctions and transistors, and *p-i-n* photodiodes and lasers for optical applications. In this work we concentrate only on passive devices in which the nonlinearity arises solely from the direct interaction of electromagnetic waves propagating through the material. In this case the nonlinear effect manifests itself in the dependence of the complex propagation constant of the wave on the amplitude of the propagating electromagnetic field. Common nonlinear effects which can be found in many optical crystals such as SiO_2, $LiNbO_3$, $LiTaO_3$, GaAs, are the linear electro-optic Pockels effect, the quadratic Kerr effect and Raman scattering [58,59]. The refractive index of these crystals is a function of the amplitude of the impinging electric field. In the microwave and millimeter-wave frequency range, high-temperature superconductors such as Ytrium-based and Thallium-based cuprate oxide compounds also exhibit nonlinear properties through the dependence of the penetration depth on the magnetic field, a behaviour often referred to as the nonlinear Meissner effect [91–94].

Nonlinearity in passive microwave and optical devices is used to perform two types of functions: phase modification due to self-phase modulation and frequency generation due to cross-phase modulation. In the first class of devices. the phase of a wave propagating in the medium is altered by its amplitude so that the device response can be controlled by varying the power of the input signal. Examples of this type of devices are pulse-sharpening circuits for the generation of sub-picosecond and femtosecond optical pulses, soliton formation for high-bandwidth optical transmission systems. and microwave and optical couplers used as switching elements. The second class of nonlinear devices concerns the generation of new frequencies by nonlinear mixing and harmonic generation. The phenomena of frequency doubling. sum and difference frequency mixing associated with second-order optical effect. and third-harmonic generation and four-wave mixing associated with third-order optical effect are all well-known in nonlinear optics. There is experimental evidence that some of these phenomena can also be observed in HTS microwave devices where the mixing is provided by the nonlinear Meissner effect in the superconductor [82].

1.2.2 Numerical techniques for electromagnetic analysis

With the increasing availability of powerful computers. numerical techniques are becoming more popular in electromagnetic analysis. especially for handling complicated structures or media with complex constitutive relations. The past several years have seen a dramatic increase in research effort in developing more efficient and accurate numerical algorithms. To date there are three prominent differential equation-based methods that have been applied to a wide range of electromagnetic propagation problems: the Beam Propagation method. the Finite Element method, and the Finite-Difference Time-Domain method. Each of these methods will be reviewed in the following. with an emphasis on how they can be extented to handle nonlinear media.

(a) Beam Propagation Method

The Beam Propagation method is used extensively in the simulation of wave propagation in inhomogenous wave-guiding structures where the energy flow is primarily along a single direction (e.g.. the z-direction). The method finds a wide range of applications in integrated optical devices such as gratings [17], couplers [18], and waveguide junctions [19,20]. The central assumption of the method is the decomposition of the transverse electric field into a slowly-varying envelope and a fast-oscillating carrier,

$$\mathbf{E}_t(x, y, z) = \hat{\mathbf{E}}_t(x, y, z)e^{-j\beta z} .$$

This assumption enables the vectorial Helmholtz wave equation to be reduced to the Fresnel wave equation describing the spatial evolution of the envelope. The latter equation is then solved numerically using the finite difference method [22].

The BPM method has a great advantage over the FDTD method in that a coarser mesh can be used since only the slowly-varying envelope is solved for. The drawback is that the phase across an index discontinuity is correct only to the first order of the Taylor series, so that phase-critical phenomena such as reflections and diffractions are usually not properly accounted for [22]. Within the slowly-varying envelope approximation, the BPM method can be extended to accomodate nonlinear media, where the index of refraction is now a function of the electric field. The formulation in general results in the nonlinear Schrödinger equation, which can be discretized and solved using an iterative procedure. The method has been used by Thylen *et. al.* to analyze nonlinear directional couplers [23]. However, due to the envelope approximation, not all nonlinear effects can be observed, especially for ultrafast pulses whose bandwidths are comparable to the carrier frequency.

(b) Finite Element Method

The Finite Element method is a powerful numerical technique which is widely used in structural analysis and hydrodynamic flow problems. The past ten years also saw an increasing interest in applying the method to solve electromagnetic problems. The mathematical principle of the method lies in expanding the solution field in terms of a set of basis functions, which ultimately reduce the vector wave equation to an algebraic system [24]. The versatility of the method arises from its use of unstructured grids, which greatly facilitate the modeling of complex geometries. In guided-wave technology, this capability allows waveguides of arbitrary shape and refractive index profile, including nonlinear index, to be analyzed [25]. Of particular importance is the method's ability to conform smoothly with curved geometries such as ring waveguides, thereby drastically reducing the staircase discretization errors which are always present in finite-difference techniques.

The drawback of the method lies in the greater complexity of the algorithm as compared to BPM and FDTD methods, and the challenge in generating unstructured meshes. As a result the FEM method has not enjoyed as much popularity as its two counterparts, especially in wave-guiding devices which have relatively simple geometries. Nevertheless, some applications of the method to analyze nonlinear structures have been reported: for example, rectangular channel waveguides with instantaneous nonlinearities [26], and strip-loaded optical waveguides with saturable nonlinearity [27]. As in the BPM method, the common approach in all these finite element analyses is to assume an $e^{j(\omega t-\beta z)}$ dependence of the field and solve for the slowly-varying modal field profile.

(c) Finite-Difference Time-Domain Method

The Finite-Difference Time-Domain method is arguably the most versatile and widely-used of the three numerical techniques. Since its first application by Yee in 1966 to solve electromagnetic scattering problems [1], the method has been refined and extended to handle a wide range of problems involving wave interactions in complex media, including frequency dispersive, nonlinear, and highly-conductive media [15,16]. By directly solving Maxwell's equations simultaneously with the medium constitutive relation in the time domain, the method fully accounts for the effects of reflection, diffraction and radiation. The versatility of the FDTD method enables virtually any constitutive relation to be incorporated into the solution of Maxwell's equations. Since the method makes no assumption regarding the nature of the solution field, it fully accounts for the complete time evolution of the field, and is therefore particularly suitable for nonlinear problems where subtle nonlinear effects cannot be predicted by approximate analytical or other numerical techniques. Furthermore, since nonlinearity causes frequency mixing and harmonic generation, frequency-domain techniques such as BPM are strictly not valid as the principle of linear superposition of frequency components cannot be invoked. Therefore, a rigorous solution of the nonlinear wave equation must be obtained in the time domain [98].

In recent years, as the power of the FDTD method is increasingly appreciated within the optics community, there has been growing interest in applying the method to nonlinear structures. Phenomena associated with pulse propagation in nonlinear waveguides, such as self-focusing effect and soliton formation, have been studied by Jamid and Al-Bader [7], Chu [8], Ackerly and Chaudhuri [9], and Schulz *et. al.* [10]. Goorjian, Taflove and coworkers used FDTD to model femtosecond optical solitons in nonlinear Lorentz-dispersive media by direct time integration of Maxwell's equations [5,6,11]. Their nonlinear model included such effects as the instantaneous Kerr and Raman interactions. Ziolkowski and Judkins studied the interaction of ultra-short pulses in Kerr media exhibiting finite response time by solving an additional phenomenological susceptibility equation simultaneously with Maxwell's equations [3]. The method was also used to analyze pulse propagation in nonlinear corrugated waveguides [4]. Ziolkowski later extended the scheme to incorporate a general microscopic, quantum mechanical material model to produce a semi-classical FDTD method for ultra-fast optical pulse simulation [12]. Finally, Megahed and El-Ghazaly recently applied a 3D FDTD scheme to model nonlinear high-temperature superconducting microstrip lines [98]. In their approach, the authors first solved the Ginzburg-Landau equations for the magnetic field and position dependence of the penetration depth of the superconducting strips, which was then used in the FDTD calculation of the electric and magnetic fields in the structure.

The most serious drawback of the FDTD method is the restrictive stability constraint imposed on the time step and mesh sizes, which often incurs extensive computational resource requirement in performing a simulation. With the aim of improving the computation speed and accuracy of the algorithm, the idea of using hybrid FDTD schemes has long been introduced to linear problems. For example, in an inhomogeneous domain, it is sometimes desirable to use finer meshes in small sub-regions to obtain more accurate solutions. Toward this aim, Chevalier *et. al.* recently introduced a local-grid method which allows dielectric and/or conducting material traverse to cross the boundaries between the main grid and local grids [39]. With a different motivation, Lu and Shen proposed a domain decomposition technique which partitions the computation domain into sub-regions, whereby parallel solution of the finite-difference equations can be more efficiently sought [41]. While these approaches are differently motivated from our research goals, they represent ideas that compliment our hybrid algorithm to produce a more computationally efficient nonlinear FDTD scheme.

Parallel to the work in refining the FDTD algorithm, much progress has also been made in the treatment of the computational boundaries as absorbing or impedance boundary conditions. One of the most widely-used absorbing boundary conditions (ABC's) is Mur's second-order one-way wave equation [29]. This ABC provides adequate results for most structures, although its performance deteriorates for incidence angles far from the normal incidence. An improved ABC is Liao's transmitting boundary, which uses Newton extrapolation to predict the fields on the computational boundaries from the fields at interior points [32]. More recently, Berenger proposed an artificial absorbing layer that is perfectly matched to the physical medium at all frequencies and incidence angles [30,31]. The perfectly matched layer has been shown to yield significant improvement in accuracy over Mur's ABC. So far, however, no attempt at extending these absorbing boundary conditions to handle nonlinear boundaries has been reported.

1.3 Summary

In summary, our research objective is to develop an efficient hybrid FDTD scheme for simulating nonlinear propagation in millimeter-wave and optical devices. We will limit the scope of our present work to instantaneous nonlinearities in optical and HTS materials, and leave nonlinear media with finite response time to future research effort. The proposed FDTD scheme will be used to investigate the possibility of constructing power-dependent devices and passive frequency generators for use in communications and signal processing. Unlike others who study nonlinearity in HTS devices as an undesirable parasitic effect, our objective here is to exploit and enhance this property for practical use. The aims of this research effort are to contribute to the field of electromagnetic computation, to enhance the understanding of wave interaction in nonlinear media, especially superconducting materials, and to demonstrate the potential practical applications of material nonlinearity.

Chapter 2

The Hybrid FDTD Technique

The basic principle behind the hybrid FDTD method is to apply different numerical schemes separately to regions of linear and nonlinear materials in the computation domain in order to maximize the efficiency and accuracy of the overall simulation. We introduce in this chapter a hybrid implicit-explicit FDTD method which combines the explicit and partially-implicit time-stepping schemes to produce a stable and efficient algorithm for solving the nonlinear TE wave equation. This method is particularly suited for optical structures which comprise of small nonlinear regions in an otherwise linear medium. For TM-polarized wave propagation, a combination of scalar and full-wave solvers with subgridding capability is introduced as an efficient and accurate way of simulating thin-film conducting waveguides at the microwave and millimeter-wave frequencies. This hybrid method, which we refer to as the single-field leap-frog scheme, will serve as the tool for analyzing nonlinear HTS devices in Chapters 4 and 5. In this chapter we present the formulation of the two hybrid FDTD schemes, followed by a detailed discussion on related numerical issues such as error, stability, dispersion, and convergence.

2.1 The Nonlinear Wave Equation

In a source-free, isotropic, non-magnetic medium, the propagation of electromagnetic waves is governed by the two Maxwell's curl equations:

$$\nabla \times \mathbf{E} = -\mu_0 \frac{\partial \mathbf{H}}{\partial t}, \tag{2.1}$$

$$\nabla \times \mathbf{H} = \frac{\partial}{\partial t}(\varepsilon \mathbf{E}) + \sigma \mathbf{E}, \tag{2.2}$$

where μ_0 is the vacuum permeability, ε is the permittivity, and σ is the conductivity. The permittivity ε, which describes the polarizability of the material in response to an applied electric field, is in general a function of the field,

$$\varepsilon = \varepsilon(\mathbf{E}), \tag{2.3}$$

with the specific functional dependence being a property of the material. Furthermore, for certain media such as plasma and superconducting materials, the conductivity may also depend on either the electric or magnetic field. Thus for generality we allow σ to be also field-dependent in the following analysis.

In the conventional full-wave FDTD method, Eqs.(2.1) and (2.2) are discretized using a leap-frog scheme where the electric and magnetic field components are offset in time and space with respect to each other by half a grid size and half a time step. The scheme thus requires storage of all six field components at each time step. In order to reduce the memory requirement and simplify the computation, we seek to reduce the two Maxwell's curl equations to one second-order partial differential equation in terms of either the electric or magnetic field. Toward this goal, we take the curl of both sides of Eq.(2.1) to obtain

$$\nabla \times \nabla \times \mathbf{E} = -\mu_0 \frac{\partial}{\partial t}(\nabla \times \mathbf{H}) = -\mu_0 \frac{\partial^2}{\partial t^2}(\varepsilon \mathbf{E}) - \mu_0 \frac{\partial}{\partial t}(\sigma \mathbf{E}),$$

or
$$\mu_0 \frac{\partial^2}{\partial t^2}(\varepsilon \mathbf{E}) + \mu_0 \frac{\partial}{\partial t}(\sigma \mathbf{E}) = \nabla^2 \mathbf{E} - \nabla(\nabla \cdot \mathbf{E}). \tag{2.4}$$

Using the fact that $\nabla \cdot (\varepsilon \mathbf{E}) = \varepsilon \nabla \cdot \mathbf{E} + \mathbf{E} \cdot \nabla \varepsilon = 0$, we obtain $\nabla \cdot \mathbf{E} = \nabla(1/\varepsilon) \cdot \varepsilon \mathbf{E}$, which, when substituted into Eq.(2.4), results in

$$\mu_0 \frac{\partial^2}{\partial t^2}(\varepsilon \mathbf{E}) + \mu_0 \frac{\partial}{\partial t}(\sigma \mathbf{E}) = \nabla^2 \mathbf{E} - \nabla\left(\nabla \frac{1}{\varepsilon} \cdot \varepsilon \mathbf{E}\right). \tag{2.5}$$

The above equation expresses the electromagnetic propagation in a general nonlinear and inhomogeneous medium in terms of the electric field. The term $\nabla[\nabla(1/\varepsilon)\cdot\varepsilon\mathbf{E}]$ on the right hand side represents the polarization coupling effect. To obtain an equation similar to Eq.(2.5) in terms of the magnetic field, we take the curl of both sides of Eq.(2.2) to get

$$\nabla\times\nabla\times\mathbf{H}=\nabla\times\left(\frac{\partial}{\partial t}\varepsilon+\sigma\right)\mathbf{E},$$

$$-\nabla^2\mathbf{H}=\left(\frac{\partial}{\partial t}\varepsilon+\sigma\right)\nabla\times\mathbf{E}+\left(\frac{\partial}{\partial t}\nabla\varepsilon+\nabla\sigma\right)\times\mathbf{E},$$

which, with the use of Eq.(2.1), becomes

$$\mu_0\left(\frac{\partial}{\partial t}\varepsilon+\sigma\right)\frac{\partial\mathbf{H}}{\partial t}=\nabla^2\mathbf{H}+\left(\frac{\partial}{\partial t}\nabla\varepsilon+\nabla\sigma\right)\times\mathbf{E},$$

or $$\mu_0\left(\frac{\partial}{\partial t}\varepsilon\frac{\partial\mathbf{H}}{\partial t}\right)+\mu_0\sigma\frac{\partial\mathbf{H}}{\partial t}=\nabla^2\mathbf{H}+\left(\frac{\partial}{\partial t}\nabla\varepsilon+\nabla\sigma\right)\times\mathbf{E}. \tag{2.6}$$

If the medium is linear and homogeneous, $\nabla\varepsilon=\nabla\sigma=0$, and the polarization coupling term vanishes to yield a wave equation in terms of only the magnetic field:

$$\mu_0\varepsilon\frac{\partial^2\mathbf{H}}{\partial t^2}+\mu_0\sigma\frac{\partial\mathbf{H}}{\partial t}=\nabla^2\mathbf{H}. \tag{2.7}$$

For nonlinear and inhomogeneous media, the duality between **E** and **H** collapses and Maxwell's curl equations cannot be reduced to a single wave equation containing only the magnetic field.

In two-dimensional (2D) wave-guiding structures where $\partial/\partial y=0$, Maxwell's equations can be separated into two independent sets of equations corresponding to the transverse electric (TE) case:

$$\frac{\partial}{\partial t}(\varepsilon E_y)=\frac{\partial H_x}{\partial z}-\frac{\partial H_z}{\partial x}-\sigma E_y \tag{2.8a}$$

$$\mu_0\frac{\partial H_x}{\partial t}=\frac{\partial E_y}{\partial z} \tag{2.8b}$$

$$\mu_0\frac{\partial H_z}{\partial t}=-\frac{\partial E_y}{\partial x}, \tag{2.8c}$$

and the transverse magnetic (TM) case:

$$\mu_0 \frac{\partial H_y}{\partial t} = \frac{\partial E_z}{\partial x} - \frac{\partial E_x}{\partial z} \tag{2.9a}$$

$$\frac{\partial}{\partial t}(\varepsilon E_x) = -\frac{\partial H_y}{\partial z} - \sigma E_x \tag{2.9b}$$

$$\frac{\partial}{\partial t}(\varepsilon E_z) = \frac{\partial H_y}{\partial x} - \sigma E_z . \tag{2.9c}$$

Note that the above decomposition of the solution of Maxwell's equations into two independent sets of TE and TM modes is completely general and valid even in nonlinear media. This important property applies only to 2D but not 3D structures. Since there is only one component of the electric field in the TE case, we can reduce Eqs.(2.8) to a single nonlinear scalar wave equation in E_y with the help of Eq.(2.5):

$$\mu_0 \frac{\partial}{\partial t}(\sigma E_y) + \frac{1}{c^2}\frac{\partial^2}{\partial t^2}(\varepsilon_r E_y) = \frac{\partial^2 E_y}{\partial x^2} + \frac{\partial^2 E_y}{\partial z^2} . \tag{2.10}$$

in which c is the velocity of light in vacuum and ε_r is the relative permittivity. The polarization coupling term $\nabla[\nabla(1/\varepsilon)\cdot \varepsilon \mathbf{E}]$ vanishes for the TE mode in 2D media because the gradient vector $\nabla(1/\varepsilon)$ does not have a component in the y-direction. Moreover, the above equation is general and exact; no assumption is made as to the nature of the electric permittivity or the conductivity. By contrast, the equations for the TM case cannot be reduced to a single nonlinear equation in H_y unless the medium is linear and homogeneous or the assumption of no polarization coupling is made. For accurate analysis, the coupling term must be included and all three equations (2.9a), (2.9b) and (2.9c) must be solved simultaneously for the fields.

In the terminology of partial differential equations, the scalar wave equation in (2.10) is of a mixed parabolic and hyperbolic type. However, assuming a principally sinusoidal field variation of frequency ω, if $\omega\varepsilon \gg \sigma$, the second-order time derivative term dominates over the first-order time derivative and the equation can be regarded as predominantly hyperbolic. This case is applicable to dielectric materials with small loss. On the other hand, if $\omega\varepsilon \ll \sigma$, which corresponds to highly conducting materials, the situation reverses and the equation is characterized as predominantly parabolic. A characteristic of a hyperbolic system is that the field evolves through time in a wave-like manner, whereas in a parabolic system the field is governed by a diffusion-like equation. Thus in a medium with low conductivity the electric field behaves as a wave, whereas in a highly conductive medium it propagates in a diffusive manner. As will be shown later, the stability condition of the general wave equation depends on the dominant type of behaviour.

In addition, the formal distinction between the two types of behaviour suggests the discretization scheme to be used for each case. A characteristic of parabolic equations is that the domain of dependence is infinite; i.e., the solution at a point (i, j) at time step $n+1$ depends on the field values at all the other points in the domain at the same time step. This property suggests that an implicit or partially-implicit discretization scheme is more suitable since at each time step all the node values are simultaneously solved for. On the other hand, hyperbolic equations have finite domain of dependence, which implies that an explicit scheme is sufficient provided the stability criterion is met. The choices of discretization schemes will be examined in more detail in light of stability and other numerical issues.

2.2 Nonlinear Medium Models

The interaction of electromagnetic wave with a medium is characterized by the material's constitutive relations. For the materials of interest in this thesis, the relevant constitutive relations are those that describe the macroscopic dependence of the displacement current **D** and the electric current **J** on the electric field:

$$\mathbf{D} = \varepsilon \mathbf{E} \tag{2.11}$$

and

$$\mathbf{J} = \sigma \mathbf{E}. \tag{2.12}$$

If the dielectric constant ε and the conductivity σ are field-dependent, the wave equations (2.5) and (2.6) become nonlinear. In this section we focus on dielectric materials whose constitutive relation (2.11) is nonlinear. The case where relation (2.12) is nonlinear applies to superconducting materials and will be treated in more detail in Chapter 4.

In dielectric materials nonlinear response arises from the anharmonic motion of bound electrons under the influence of an applied electric field. In an isotropic medium, the induced polarization **P**, defined as **D** – ε_0**E**, depends on the applied field according to the general relation [61]

$$\mathbf{P} = \varepsilon_0\left[\chi^{(1)} + \chi^{(2)}|\mathbf{E}| + \chi^{(3)}|\mathbf{E}|^2 + \ldots\right]\mathbf{E}, \tag{2.13}$$

where ε_0 is the vacuum permittivity and $\chi^{(j)}$ is the jth-order susceptibility. The linear susceptibility, $\chi^{(1)}$, is usually the dominant effect, with higher-order susceptibilities representing nonlinear contributions. The second-order susceptibility, $\chi^{(2)}$, is responsible for the Pockels effect and is present only in materials with asymmetric molecular structures. For most optical materials the dominant nonlinearity comes from the third-order susceptibility, $\chi^{(3)}$, which is responsible for the Kerr effect. The relative permittivity of Kerr-type materials is commonly expressed as

$$\varepsilon_r = \left(1 + \chi^{(1)}\right) + \chi^{(3)}|\mathbf{E}|^2 = n_0^2 + \alpha|\mathbf{E}|^2, \tag{2.14}$$

where n_0 represents the linear refractive index and α is the nonlinear constant describing the dependence of the permittivity on the electric field intensity.

Equation (2.14) describes the simplest instantaneous nonlinear medium model, which is often adequate for weak applied fields. In some cases, however, the model may be modified to include other effects. One common effect is the saturation of the polarization under intense electric field. In such saturable media, the simple Kerr law is replaced by either an exponential saturation model [62],

$$\varepsilon_r = n_0^2 + \Delta\varepsilon_{sat}\left[1 - \exp\left(-\alpha|\mathbf{E}|^2/\Delta\varepsilon_{sat}\right)\right] \tag{2.15}$$

or a two-level saturation model,

$$\varepsilon_r = n_0^2 + \frac{\alpha|\mathbf{E}|^2}{1 + \alpha|\mathbf{E}|^2/\Delta\varepsilon_{sat}}. \tag{2.16}$$

In either model, the permittivity is still a function of the electric field intensity and may be expressed generally as

$$\varepsilon_r = n_0^2 + f\left(|\mathbf{E}|^2\right). \tag{2.17}$$

where f is a function describing the particular model in use.

Another modification to the Kerr law is the finite response time of the material, which gives rise to retarded nonlinear effects. Strictly speaking, the electronic response of a material is not instantaneous but is characterized by a time delay. The nonlinear susceptibility is usually assumed to be governed by the phenomenological equation

$$\frac{\partial}{\partial t}\chi_{NL} + \frac{1}{\tau}\chi_{NL} = \frac{\alpha}{\tau}|\mathbf{E}|^2, \tag{2.18}$$

where τ is the material relaxation time, usually of the order of 1–10fs [3]. Approximating Eq.(2.18) as

$$\tau\frac{\Delta\chi_{NL}}{\Delta t} + \chi_{NL} = \alpha|\mathbf{E}|^2, \tag{2.19}$$

we see that if $\Delta t \gg \tau$, the phenomenological equation reduces to the instantaneous Kerr model,

$$\chi_{NL} = \alpha|\mathbf{E}|^2. \tag{2.20}$$

Thus, if our working time scale, e.g. the rise time of the incident light pulse, is much larger than the material response time, the instantaneous model will suffice. On the other hand, in sub-femtosecond systems where the pulse duration is comparable to or shorter than τ, the finite-response model in Eq.(2.18) must be used. In this thesis, we will be concerned with pulses of the order of tens of femtoseconds or longer so that the material response can be assumed to be instantaneous.

2.3 The Hybrid Implicit-Explicit FDTD Method

A new hybrid implicit-explicit FDTD method is introduced in this section to solve the scalar wave equation (2.10) for TE polarization in structures with mixed nonlinear and linear regions. The hybrid technique combines the computational simplicity of the explicit scheme in linear medium regions with the superior stability property of a partially-implicit scheme in regions of nonlinear materials. As a result, potential problems of instabililty associated with nonlinearity are eliminated and the restrictive stability condition imposed by the linear non-iterative scheme in nonlinear regions is also removed. The formulation of the finite-difference equations in each of the linear and nonlinear material regions, and the procedure for solving them, are discussed below.

2.3.1 Discretization

In the finite-difference method the computational domain is partitioned into a rectangular grid of sizes Δz and Δx. Figure 2.1 shows a mesh superposed onto a region of mixed linear and nonlinear media. Each node corresponds to an unknown electric field value E_y to be solved for. We designate a node as being explicit if it falls in a linear medium region, and implicit if it belongs to a nonlinear medium region. In the hybrid FDTD method we apply the explicit discretization scheme to the linear regions and a partially-implicit scheme to the nonlinear regions.

In the linear regions, an explicit discretized form of the scalar wave equation (2.10) is obtained using the forward-difference formula for the first-order time derivative and central-difference formulae for the second-order time and space derivatives. Thus for an explicit node i,

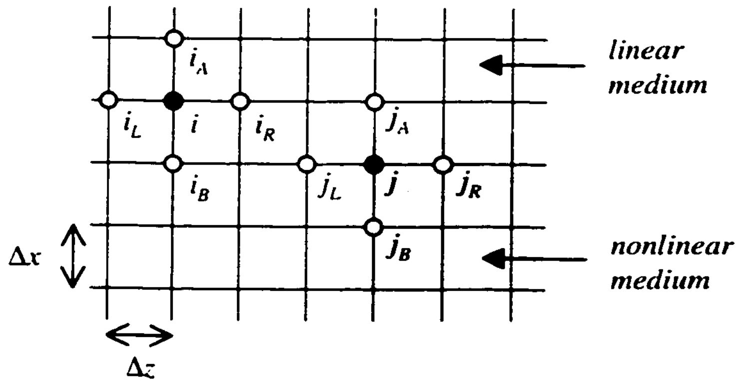

Figure 2.1. Rectangular mesh superposed onto both linear and nonlinear medium regions. Node i is an explicit node, while node j is an implicit node with both implicit and explicit neighbours.

using the notation E_i^n to denote the field value at node i and time step n, we discretize Eq.(2.10) as

$$\begin{aligned}\mu_0\sigma_i \frac{E_i^{n+1}-E_i^n}{\Delta t} &+ (\varepsilon_r)_i \frac{E_i^{n+1}-2E_i^n+E_i^{n-1}}{(c\Delta t)^2} \\ &= \frac{E_{i_L}^n-2E_i^n+E_{i_R}^n}{(\Delta z)^2} + \frac{E_{i_A}^n-2E_i^n+E_{i_B}^n}{(\Delta x)^2}.\end{aligned} \tag{2.21}$$

The subscripts i_L, i_R, i_A and i_B indicate the neighbour nodes left, right, above and below, respectively, of node i. In the nonlinear material regions, a weighted-average time-stepping scheme is employed in which the spatial derivatives are averaged over the three time steps $n-1$, n, and $n+1$. The general discrete equation for an implicit node j with possibly explicit neighbours is

$$\begin{aligned}\mu_0 \frac{(\sigma E)_j^{n+1}-(\sigma E)_j^n}{\Delta t} &+ \frac{(\varepsilon_r E)_j^{n+1}-2(\varepsilon_r E)_j^n+(\varepsilon_r E)_j^{n-1}}{(c\Delta t)^2} \\ &= a_1\left[\frac{E_{j_L}^l-2E_j^{n+1}+E_{j_R}^l}{(\Delta z)^2} + \frac{E_{j_A}^l-2E_j^{n+1}+E_{j_B}^l}{(\Delta x)^2}\right] \\ &+ a_2\left[\frac{E_{j_L}^n-2E_j^n+E_{j_R}^n}{(\Delta z)^2} + \frac{E_{j_A}^n-2E_j^n+E_{j_B}^n}{(\Delta x)^2}\right] \\ &+ a_3\left[\frac{E_{j_L}^m-2E_j^{n-1}+E_{j_R}^m}{(\Delta z)^2} + \frac{E_{j_A}^m-2E_j^{n-1}+E_{j_B}^m}{(\Delta x)^2}\right].\end{aligned} \tag{2.22}$$

In the above equation, a_1, a_2, and a_3 are weighting factors such that $a_1 + a_2 + a_3 = 1$. Setting $a_1 = a_3 = 0$ and $a_2 = 1$ reduces Eq.(2.22) to the nonlinear explicit form, which is often adequate for low-loss dielectrics. However, for highly-conducting media at frequencies for which $\sigma \gg \omega\varepsilon$, the wave equation (2.10) becomes predominantly parabolic, and a partially-implicit scheme with weightings $a_1 = a_3 = 1/4$ and $a_2 = 1/2$ yields better stability than the explicit form. It is also noted that the fully-implicit scheme with $a_1 = 1$ and $a_2 = a_3 = 0$ suffers from amplitude attenuation and thus results in erroneous solutions.

To handle the interfaces between the linear and nonlinear material regions, the time indexes l and m of the neighbour nodes in Eq.(2.22) are assigned as follows: if a neighbour node

$j_\eta \in \{j_L, j_R, j_A, j_B\}$ is also an implicit node, then $l(j_\eta) = n+1$ and $m(j_\eta) = n-1$; if j_η is an explicit node, then $l(j_\eta) = n$ and $m(j_\eta) = n$. This convention of assigning time indexes to the neighbour nodes is observed to minimize the numerical discontinuity, and hence reflection, at the interfaces between the explicit and implicit schemes. Furthermore, as will be apparent, it results in a symmetric Jacobian matrix for the nonlinear system.

2.3.2 Numerical solution

The discrete equations (2.21) and (2.22) are algebraically solved to obtain the unknown field at time step n+1 at each node. For the linear material regions, the unknown field E_i^{n+1} in Eq.(2.21) can be explicitly expressed in terms of the known field values at time steps n and n−1:

$$E_i^{n+1} = \frac{1}{a_i}\left[b_i E_i^{n-1} + c_i E_i^n + c_{LR,i}\left(E_{iL}^n + E_{iR}^n\right) + c_{AB,i}\left(E_{iA}^n + E_{iB}^n\right)\right], \tag{2.23}$$

where a_i, b_i, c_i, $c_{LR,i}$, and $c_{AB,i}$ are position-dependent constants given by

$$a_i = \frac{\mu_0 \sigma_i}{\Delta t} + \frac{\varepsilon_{r,i}}{(c\Delta t)^2},$$

$$b_i = -\frac{\varepsilon_{r,i}}{(c\Delta t)^2},$$

$$c_i = \frac{\mu_0 \sigma_i}{\Delta t} + \frac{2\varepsilon_{r,i}}{(c\Delta t)^2} - 2\left[\frac{1}{(\Delta z)^2} + \frac{1}{(\Delta x)^2}\right],$$

$$c_{LR,i} = \frac{1}{(\Delta z)^2},$$

$$c_{AB,i} = \frac{1}{(\Delta x)^2}.$$

On the other hand, Eq.(2.22) is nonlinear because ε_r and possibly σ depend on the field and thus has to be solved by an iterative algorithm such as Newton-Raphson's method. Observing that Eq.(2.22) can be re-arranged in the form

$$f_j^{n+1}\left(\varepsilon_j^{n+1}, E_j^{n+1}, E_{j_\eta}^{n+1}\right) = g_j^n\left(\varepsilon_j^n, \varepsilon_j^{n-1}, E_j^n, E_{j_\eta}^n, E_j^{n-1}, E_{j_\eta}^{n-1}\right). \qquad (2.24)$$

we define the residue of node j at the k^{th} Newton-Raphson iteration as

$$r_j^{(k)} = f_j^{(k)} - g_j^n.$$

Let $\mathbf{r}^{(k)} = \begin{bmatrix} r_1 \\ r_2 \\ \vdots \\ r_M \end{bmatrix}^{(k)}$ and $\mathbf{E}^{(k)} = \begin{bmatrix} E_1 \\ E_2 \\ \vdots \\ E_M \end{bmatrix}^{(k)}$,

where M is the number of implicit nodes, the $(k+1)^{\text{th}}$ estimate to the true solution of $\mathbf{E}^{n+1}$ is given by the matrix equation

$$\mathbf{J}^{(k)}\left(\mathbf{E}^{(k+1)} - \mathbf{E}^{(k)}\right) = -\mathbf{r}^{(k)} \qquad (2.25)$$

or

$$\mathbf{E}^{(k+1)} = \mathbf{E}^k - \left[\mathbf{J}^{(k)}\right]^{-1}\mathbf{r}^{(k)}. \qquad (2.26)$$

The Jacobian $\mathbf{J}^{(k)}$ is computed at each k^{th} iteration; its (j, l) element is obtained numerically from

$$\left[\mathbf{J}^{(k)}\right]_{j,l} = \left(\frac{\partial r_j}{\partial E_l}\right)^{(k)} = \frac{r_j\left(E_l^{(k)} + \Delta E\right) - r_j\left(E_l^{(k)}\right)}{\Delta E} \qquad (2.27)$$

where ΔE is a small differential (usually about 10^{-6}V/m). The Jacobian is a square, symmetric $M \times M$ matrix with five non-zero diagonals. Solution of the linear matrix equation (2.25) may be efficiently sought using an iterative matrix solving algorithm.

Because at each time step the weighted-average scheme requires solution of a linear matrix equation, the method may become unattractively slow if the computation overhead in solving the matrix equation is not minimized. Therefore it is essential that we use an efficient matrix solving algorithm by exploiting the properties of the Jacobian matrix. For most optical materials we observe that the conductivity σ can be assumed constant; furthermore, for the particular case of materials obeying the nonlinear intensity law (2.14), the Jacobian matrix has the important property that it is symmetric positive definite. To prove this, consider the weighted-average discrete equation with $a_1 = a_3 = 1/4$ and $a_2 = 1/2$. The function $f_j^{(k)}$ defined in Eq.(2.24) is

$$f_j^{(k)} = \left[\frac{(\varepsilon_r)_j^{(k)}}{(c\Delta t)^2} + \frac{\mu_0 \sigma}{\Delta t} + \frac{1}{2(\Delta z)^2} + \frac{1}{2(\Delta x)^2} \right] E_j^{(k)}$$
$$- \frac{1}{4(\Delta z)^2}\left(E_{jL}^{(k)} + E_{jR}^{(k)}\right) - \frac{1}{4(\Delta x)^2}\left(E_{jA}^{(k)} + E_{jB}^{(k)}\right)$$

from which the elements of the Jacobian matrix can be computed. For a general row j of the Jacobian, there are 5 non-zero elements:

$$\ldots 0 \ldots \quad -\frac{1}{4(\Delta x)^2} \quad \ldots 0 \ldots \quad -\frac{1}{4(\Delta z)^2} \quad D_j \quad -\frac{1}{4(\Delta z)^2} \quad \ldots 0 \ldots \quad -\frac{1}{4(\Delta x)^2} \quad \ldots 0 \ldots$$

where the diagonal element D_j is given by

$$D_j = \frac{\partial f_j^{(k)}}{E_j^{(k)}} = \left[\frac{(\varepsilon_r)_j^{(k)}}{(c\Delta t)^2} + \frac{\mu_0 \sigma}{\Delta t} + \frac{1}{2(\Delta z)^2} + \frac{1}{2(\Delta x)^2} \right] + \frac{2\alpha \left(E_j^{(k)}\right)^2}{(c\Delta t)^2}.$$

It is clear that for each row, the diagonal element is always positive and greater than the sum of the absolute values of the off-diagonal elements, implying that the matrix is positive definite. This property of the Jacobian enables the linear system in Eq.(2.25) to be solved very efficiently by the iterative method of Conjugate Gradient [56].

2.3.3 Absorbing boundary conditions

At the boundaries of the computational domain we need to apply outward radiating conditions to guide the waves without reflection out into the infinite space surrounding the structure. We review here two commonly-used absorbing boundary conditions, Mur's 2nd-order one-way wave equation and Liao's transmitting boundary condition. The former method is used for linear boundaries while the latter can absorb waves at the boundary of a nonlinear medium.

In Mur's 2nd-order ABC, a wave which arrives at a boundary node is approximated by a plane wave over a local region surrounding the node. This wave can then be guided out of the computational domain by the one-way wave equation. Consider a plane wave in two-dimensional space,

$$E_y = E_0 e^{j(\omega t \pm \beta_z z \pm \beta_x x)}, \tag{2.28}$$

crossing the boundary at $z = z_0$. In the above equation the minus signs indicate propagation in the positive x- and z-directions. Using the relationship

$$\beta_x^2 + \beta_z^2 = k^2,$$

where $k = \omega\sqrt{\mu_0 \varepsilon}$ is the wave number, we can estimate β_z in terms of β_x as

$$\beta_z = k\sqrt{1 - \frac{\beta_x^2}{k^2}} \approx k\left(1 - \frac{\beta_x^2}{2k^2}\right). \tag{2.29}$$

The above approximation is accurate to second order. Differentiating Eq.(2.28) with respect to z gives

$$\frac{\partial E_y}{\partial z} = \pm j\beta_z E_y,$$

and making use of the approximation in Eq.(2.29), we get

$$\left[\frac{\partial}{\partial z} \mp jk\left(1 - \frac{\beta_x^2}{2k^2}\right)\right] E_y = 0,$$

or $$\left[jk\frac{\partial}{\partial z} \mp (jk)^2 \pm \frac{1}{2}(j\beta_x)^2\right] E_y = 0.$$

By identifying $jk = \sqrt{\mu_0 \varepsilon}(\partial/\partial t)$ and $j\beta_x = \partial/\partial x$, we arrive at Mur's absorbing boundary condition for a wave crossing a boundary at $z = z_0$,

$$\left(\sqrt{\mu_o \varepsilon}\frac{\partial^2}{\partial t \partial z} \mp \mu_0 \varepsilon \frac{\partial^2}{\partial t^2} \pm \frac{1}{2}\frac{\partial^2}{\partial x^2}\right) E_y = 0. \tag{2.30}$$

The boundary condition for a wave crossing a boundary at $x = x_0$ can be similarly obtained:

$$\left(\sqrt{\mu_0 \varepsilon} \frac{\partial^2}{\partial t \partial x} \mp \mu_0 \varepsilon \frac{\partial^2}{\partial t^2} \pm \frac{1}{2} \frac{\partial^2}{\partial z^2} \right) E_y = 0. \tag{2.31}$$

Equations (2.30) and (2.31) are discretized using a finite-difference scheme and incorporated into the FDTD solution. Mur's 2nd-order ABC has been shown to yield good radiation condition with little reflection for waves crossing the boundaries at close to normal incidence [29].

The above absorbing boundary condition is applicable only to linear boundaries. In the case where the nodes on the boundary have nonlinear material property, a simple and straightforward ABC that can be used is Liao's transmitting boundary condition. The method predicts the field value at a boundary node by using Newton's extrapolation of interior nodes at the previous time steps [15,32]. Thus Liao's ABC does not depend on the material property of the boundary node and works for both linear and nonlinear boundaries.

The method is based on the assumption that a wave arriving at a boundary can be expressed as a summation of plane waves, each traveling in a different direction but at the same speed equal to αc along the axis perpendicular to the boundary. The parameter α is called the unified transmitting coefficient and is usually chosen between 0.5 and 2.0. Figure 2.2 shows a boundary node at x_0 in a nonlinear medium. Liao's transmitting formula for the boundary field $u_0^{n+1} = u((n+1)\Delta t, x_0)$ is

$$u_0^{n+1} = \sum_{j=1}^{N} (-1)^{j+1} C_j^N u((n-j+1)\Delta t, x_0 - j\alpha c \Delta t), \tag{2.32}$$

where

$$C_j^N = \frac{N!}{(N-j)!\, j!},$$

and N is the order of corrections (in this work we used $N = 3$). Since in general the values $u((n-j+1)\Delta t, x_0 - j\alpha c\Delta t)$ do not correspond to nodal locations in the FDTD grid, as illustrated in Figure 2.2, a quadratic interpolation scheme is used to express them in terms of those at the nodal points. We thus have

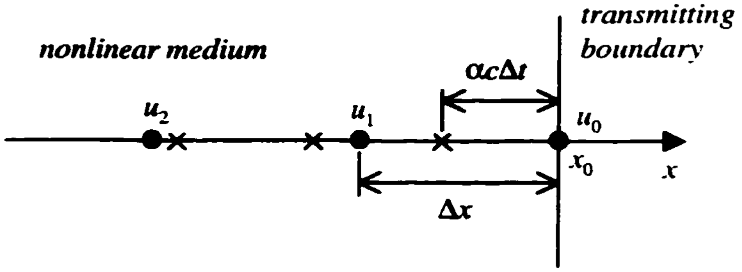

Figure 2.2. Location of nodes used in Liao's transmitting boundary condition: u_0, u_1, u_2 are nodes on the FDTD grid, whereas nodes marked by × are interpolated values that are actually used in Liao's transmitting formula.

$$u((n-j+1)\Delta t, x_0 - j\alpha c\Delta t) = \mathbf{T}_j\mathbf{u}_j$$

where

$$\mathbf{u}_j = \left[u_1^{n-j+1} \quad u_2^{n-j+1} \quad \cdots \quad u_{2j+1}^{n-j+1}\right]^T.$$

and

$$\mathbf{T}_j = \mathbf{T}_1 \begin{bmatrix} \mathbf{T}_{j-1} & 0 & 0 \\ 0 & \mathbf{T}_{j-1} & 0 \\ 0 & 0 & \mathbf{T}_{j-1} \end{bmatrix},$$

in which

$$\mathbf{T}_{j-1} = [T_{j-1,1} \quad T_{j-1,2} \quad \cdots \quad T_{j-1,2j-1}],$$
$$\mathbf{T}_1 = [T_{11} \quad T_{12} \quad T_{13}],$$
$$T_{11} = (2-s)(1-s)/2$$
$$T_{12} = s(2-s),$$
$$T_{13} = s(s-1)/2,$$
$$s = \alpha c\Delta t/\Delta x.$$

The resulting Liao's boundary condition is

$$u_0^{n+1} = \sum_{j=1}^{N} (-1)^{j+1} C_j^N \mathbf{T}_j \mathbf{u}_j. \tag{2.33}$$

The above absorbing boundary condition has been shown to yield excellent results in both scalar and vector electromagnetic problems [33], although it was observed that for certain values of α the transmitting formula causes instability.

2.3.4 Computation flow

Figure 2.3 illustrates the computation flow of the hybrid implicit-explicit FDTD algorithm. Starting with known field profiles at time steps $n-1$ and n, the field in the nonlinear material regions at the next time step $n+1$ is computed first using Newton-Raphson's iterative procedure, with the initial guess taken to be the field at the current time step n. Next, the field in the linear material regions is computed. Note that since we are not using any neighbour field values at time step $n+1$ in our linear explicit scheme (Eq.(2.21)), the explicit time-marching step can be performed before or after the Newton-Raphson iteration loop. On machines capable of parallel processing, the fields in both the linear and nonlinear material regions can be solved simultaneously, yielding a saving in computation time. Finally, absorbing boundary conditions are applied and time is advanced to the next step.

2.4 Subgridding for TM Polarization

It was shown that for TE polarization in two-dimensional structures, Maxwell's equations can be reduced to a single second-order wave equation in terms of E_y, given by Eq.(2.10). We refer to this scheme as the single-field formulation. By contrast, for TM-polarized waves in inhomogeneous or nonlinear media, it is not possible to reduce Maxwell's equations to an analogous second-order wave equation in H_y, even in two dimensions. Therefore all three field components E_x, E_z and H_y must be solved from the system of equations (2.9) using Yee's leap-frog scheme. These equations are conventionally discretized as

$$\mu_0 \frac{H_y\big|_{i,j}^{n+1} - H_y\big|_{i,j}^{n}}{\Delta t} = \frac{E_z\big|_{i+1/2,j}^{n+1/2} - E_z\big|_{i-1/2,j}^{n+1/2}}{\Delta x} - \frac{E_x\big|_{i,j+1/2}^{n+1/2} - E_x\big|_{i,j-1/2}^{n+1/2}}{\Delta z} \tag{2.34a}$$

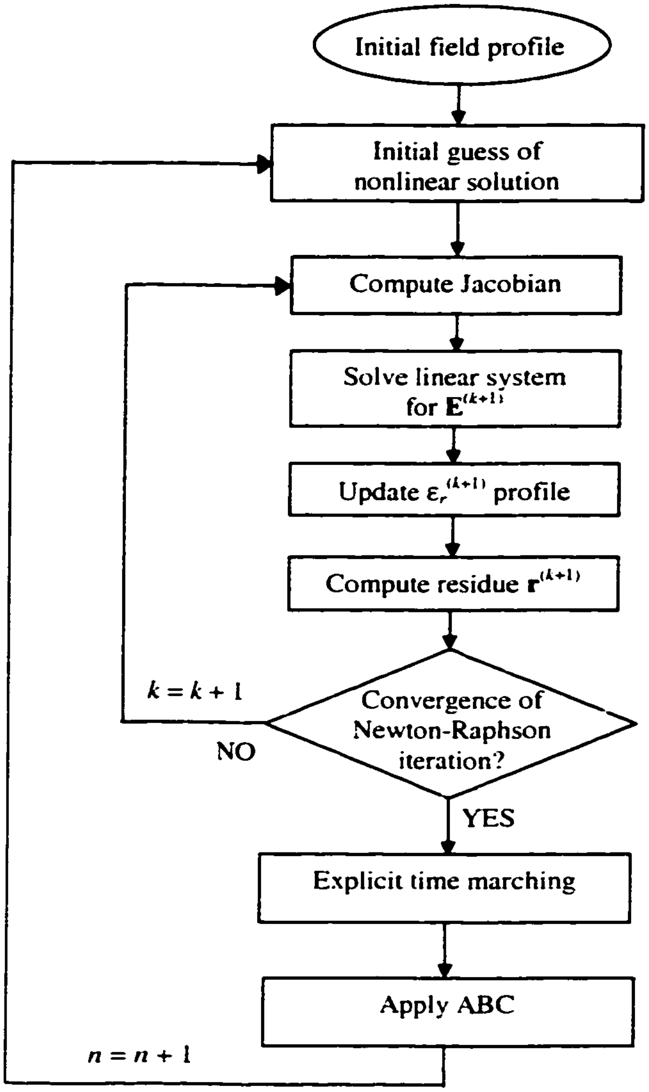

Figure 2.3. Computation flow for the hybrid implicit-explicit FDTD method.

$$\frac{\varepsilon E_x|^{n+1/2}_{i,j+1/2} - \varepsilon E_x|^{n-1/2}_{i,j+1/2}}{\Delta t} = -\frac{H_y|^{n}_{i+1,j} - H_y|^{n}_{i,j}}{\Delta z} - \sigma E_x|^{n+1/2}_{i,j+1/2} \tag{2.34b}$$

$$\frac{\varepsilon E_z|^{n+1/2}_{i+1/2,j} - \varepsilon E_z|^{n-1/2}_{i+1/2,j}}{\Delta t} = \frac{H_y|^{n}_{i,j+1} - H_y|^{n}_{i,j}}{\Delta x} - \sigma E_z|^{n+1/2}_{i+1/2,j} \tag{2.34c}$$

The leap-frog time-marching algorithm starts by assuming H_y at time step n and E_x and E_z at time step $n-1/2$ are known, and solves for the unknown fields E_x and E_z at $n+1/2$ from Eqs.(2.34b) and (2.34c). The new field H_y at $n+1$ is then obtained from Eq.(2.34a).

The above leap-frog scheme requires storage of the fields E_x, E_z at $n-1/2$ and H_y at n, so the memory requirement is $3N$, where N is the number of nodes in the mesh. By contrast, the memory requirement of the single-field scheme given by Eq.(2.21) is only $2N$. For large problems, the saving in memory from using the latter scheme can be considerable. Therefore, for structures containing small regions of inhomogeneous materials, we can use a combination of the leap-frog scheme and the single-field scheme to maximize memory efficiency. In the inhomogeneous region all three TM field components E_x, E_z and H_y are solved for using the leap-frog scheme, while in the homogeneous region only the field H_y is solved for using the single-field scheme. Besides the memory saving, such a hybrid scheme also allows for the possibility of having different grid sizes in the two regions. This capability is particularly important in the simulation of thin-film conducting waveguides, in which the thin conductors can have much finer discretization than the dielectric substrate, and consequently a more accurate solution can be obtained for the field inside the conducting strips.

Many subgridding algorithms have been proposed in the literature, starting with Kunz and Simpson's sequential technique in which a coarse FDTD calculation is refined by a second solution on a finer grid [35]. More recent approaches allow for the simultaneous computation of the fields in both the coarse and fine grids by special treatment of the fields at the boundaries between the two grids. Notable among these works are Kim and Hoefer's method of time and space interpolation to obtain the fields on the grid boundaries [36], and Zivanovic *et. al.*'s approach of using the wave equation to estimate the boundary fields [37]. The latter method was observed to have poor stability property, so in the following we adopt the interpolation approach because of its simple implementation and superior stability.

We begin by designating the homogeneous material region as the main domain and the inhomogeneous medium region as the local domain. Figure 2.4 shows the interface between the main domain and the local domain for the case where the local grid is three times finer than the main grid, so that the ratio of the main grid sizes (Δz, Δx) to the local grid sizes (δz, δx) is $r = 3$. In order to preserve the stability of the hybrid scheme, the ratio of the main time step Δt to the

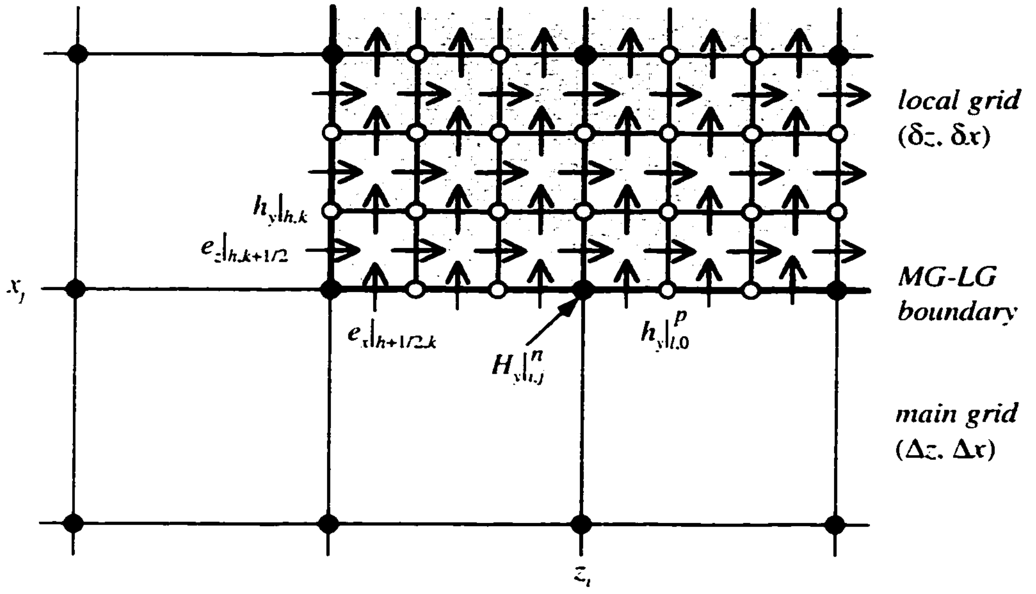

Figure 2.4. Interface between global and local domains in the hybrid single-field leap-frog FDTD method. The main-grid-local-grid ratio is $r = 3$. The black circles represent the main-grid magnetic field H_y; the white circles and arrows represent the local magnetic field h_y and local electric fields e_x, e_z, respectively.

local time step δt must also be equal to r. In the hybrid time-marching algorithm, the global field H_y in the main grid is first obtained using the single-field discrete equation

$$H_y\Big|_{i,j}^{n+1} = \frac{1}{a}\left[bH_y\Big|_{i,j}^{n-1} + c_1 H_y\Big|_{i,j}^{n} + c_2\left(H_y\Big|_{i-1,j}^{n} + H_y\Big|_{i+1,j}^{n}\right) + c_3\left(H_y\Big|_{i,j+1}^{n} + H_y\Big|_{i,j-1}^{n}\right)\right] \tag{2.35}$$

where $H_y\Big|_{i,j}^{n} = H_y(i\Delta z, j\Delta x, n\Delta t)$,

$$a = \frac{\mu_0\sigma}{\Delta t} + \frac{\varepsilon_r}{(c\Delta t)^2},$$

$$b = -\frac{\varepsilon_r}{(c\Delta t)^2},$$

$$c_1 = \frac{\mu_0\sigma}{\Delta t} + \frac{2\varepsilon_r}{(c\Delta t)^2} - 2\left[\frac{1}{(\Delta z)^2} + \frac{1}{(\Delta x)^2}\right],$$

$$c_2 = \frac{1}{(\Delta z)^2},$$

$$c_3 = \frac{1}{(\Delta x)^2}.$$

The fields in the local domain are then computed using the leap-frog equations (2.34):

$$e_z\Big|_{h,k+1/2}^{m+1/2} = \frac{\left(\varepsilon_{h,k+1/2}/\delta t\right)e_z\Big|_{h,k+1/2}^{m-1/2} + \left(1/\delta x\right)\left(h_y\Big|_{h,k+1}^{m} - h_y\Big|_{h,k}^{m}\right)}{\varepsilon_{h,k+1/2}/\delta t + \sigma_{h,k+1/2}}. \tag{2.36a}$$

$$e_x\Big|_{h+1/2,k}^{m+1/2} = \frac{\left(\varepsilon_{h+1/2,k}/\delta t\right)e_x\Big|_{h+1/2,k}^{m-1/2} - \left(1/\delta z\right)\left(h_y\Big|_{h+1,k}^{m} - h_y\Big|_{h,k}^{m}\right)}{\varepsilon_{h+1/2,k}/\delta t + \sigma_{h+1/2,k}}. \tag{2.36b}$$

$$h_y\Big|_{i,j}^{m+1} = h_y\Big|_{i,j}^{m} + \frac{\left(e_z\Big|_{h,k+1/2}^{m+1/2} - e_z\Big|_{h,k-1/2}^{m+1/2}\right)}{\mu_0\delta x/\delta t} - \frac{\left(e_x\Big|_{h+1/2,k}^{m+1/2} - e_x\Big|_{h-1/2,k}^{m+1/2}\right)}{\mu_0\delta z/\delta t}. \tag{2.36c}$$

where the subscripts h and k denote the nodes of the local grid, and the superscript m indicates the local time step. For each coarse time interval from n to $n+1$, the local time index m runs from 0 to r, with $m = 0$ coinciding to the coarse time n and $m = r$ coinciding to $n+1$. Thus for each global time step Δt, the local fields are marched r times, each at the fine time step δt.

In the fine grid FDTD calculations, Eq.(2.36c) can be used to march the magnetic field h_y at all local nodes except for the nodes on the boundaries between the main grid and the local grid (MG-LG boundaries). On the other hand, in the coarse grid calculations, Eq.(2.35) can be used to obtain the field H_y at the global nodes on the boundaries only at the global time steps $n-1$, n and $n+1$. Hence the values of h_y on the boundaries cannot be computed by either Eq.(2.35) or (2.36c) but must be obtained by interpolation of the global fields H_y. Since the wave equation is a second-order equation, it is natural to use a quadratic interpolation scheme to minimize the approximation errors. Moreover, it was observed that linear interpolation results in instability of the overall hybrid scheme. Higher-order interpolation schemes such as cubical splines and shape preserving splines have also been experimented by others [40]. These in general yield smoother transition at the boundaries between the main grid and the local grid but require more numerical effort.

Quadratic interpolation in time and space of the magnetic fields on the MG-LG boundaries is obtained by expressing the field around a main grid point in terms of the second-order Taylor series. Since along the MG-LG boundaries the field is a function of time t and only one spatial dimension, z or x, we have, as an example, the following expansion for the field around the main grid point (i, j, n) on the boundary parallel to the z-axis (refer to Figure 2.4):

$$\begin{aligned} h_y(z, x_j, t) = {} & h_y(i\Delta z, j\Delta x, n\Delta t) + \frac{\partial h_y}{\partial z}(z - i\Delta z) + \frac{\partial^2 h_y}{\partial z^2}\frac{(z - i\Delta z)^2}{2} \\ & + \frac{\partial h_y}{\partial t}(t - n\Delta t) + \frac{\partial^2 h_y}{\partial t^2}\frac{(t - n\Delta t)^2}{2} + \frac{\partial^2 h_y}{\partial z \partial t}(z - i\Delta z)(t - n\Delta t). \end{aligned} \tag{2.37}$$

The value of the field h_y at the local grid point $(i\Delta z + l\delta z, j\Delta x, n\Delta t + p\delta t)$ is thus

$$h_y\Big|_{l,0}^{p} = H_y\Big|_{i,j}^{n} + D_z(l\delta z) + \frac{D_{zz}}{2}(l\delta z)^2 + D_t(p\delta t) + \frac{D_{tt}}{2}(p\delta t)^2 + D_{zt}(l\delta z)(p\delta t), \tag{2.38}$$

in which the discrete derivatives D are computed as follows:

$$D_z = \frac{1}{2\Delta z}\left(H_y\Big|_{i+1,j}^{n} - H_y\Big|_{i-1,j}^{n} \right),$$

$$D_{zz} = \frac{1}{(\Delta z)^2}\left(H_y\Big|_{i+1,j}^{n} - 2H_y\Big|_{i,j}^{n} + H_y\Big|_{i-1,j}^{n} \right),$$

$$D_t = \frac{1}{2\Delta t}\left(H_y\Big|_{i,j}^{n+1} - H_y\Big|_{i,j}^{n-1} \right),$$

$$D_{tt} = \frac{1}{(\Delta t)^2}\left(H_y\Big|_{i,j}^{n+1} - 2H_y\Big|_{i,j}^{n} + H_y\Big|_{i,j}^{n-1} \right),$$

$$D_{zt} = \frac{1}{(\Delta z)(\Delta t)}\left(H_y\Big|_{i+1,j}^{n+1} - H_y\Big|_{i-1,j}^{n+1} - H_y\Big|_{i+1,j}^{n-1} + H_y\Big|_{i-1,j}^{n-1} \right).$$

Equation (2.38) allows the magnetic field h_y at all local grid points on the MG-LG boundaries at all local time steps m, $m = 0, 1, 2, \ldots, r$, to be estimated from the field values at the adjacent main grid points. In Figure 2.5, we summarize the computation flow of the hybrid single-field leap-frog FDTD method.

Recall that the main reason for implementing the leap-frog scheme in the local domain is to support TM propagation in inhomogeneous media. Material inhomogeneity in the local domain is accomodated by aligning the material boundaries to the locations of the tangential electric fields e_z or e_x. In calculating these tangential electric fields at the material boundaries using Eqs.(2.36a) and (2.36b), the material properties ε and σ are taken to be the arithmetic averages of the properties of the two interfacing media. Thus, for example, we have

$$\varepsilon_{h,k+1/2} = \frac{1}{2}\left(\varepsilon_{h,k} + \varepsilon_{h,k+1}\right),$$

and
$$\sigma_{h,k+1/2} = \frac{1}{2}\left(\sigma_{h,k} + \sigma_{h,k+1}\right).$$

Note that material inhomogeneity must be located at least one main grid cell deep from the MG-LG boundaries, and that no material traverse is allowed along the MG-LG boundaries. However, an important case which is relevant to our study of TM propagation in conducting waveguides

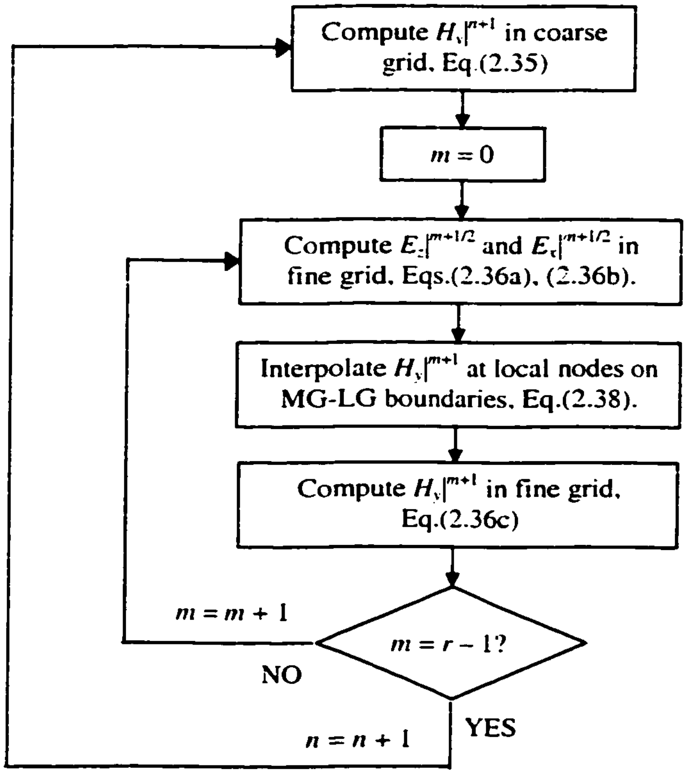

Figure 2.5. Computation flow of the hybrid single-field leap-frog FDTD method.

concerns the crossing of the MG-LG boundaries by a perfect electric conductor (PEC). This situation is depicted in Figure 2.6 and is considered next.

For all points on the MG-LG boundary that are inside the PEC (points 2b, 3, 3a), the magnetic field is identically zero for all time steps and hence they do not need further consideration. The field H_y at the global nodes 2 and 4 can be obtained from the boundary condition that $E_z = 0$ on the PEC surface. However, the field h_y at the local nodes 2a and 3b cannot be obtained by quadratic interpolation using H_y at the adjacent main grid nodes in the manner of Eq.(2.38), because the tangential magnetic field H_y is discontinuous across the PEC surfaces. Nonetheless, interpolation is still possible if we make use of the boundary condition that $\partial H_y / \partial x = 0$ on the PEC surfaces. Toward this end, we construct a parabola through the points $(x_1, H_y|_1)$ and $(x_2, H_y|_2)$ such that

$$\left.\frac{\partial H_y}{\partial x}\right|_{x=x_b} = 0.$$

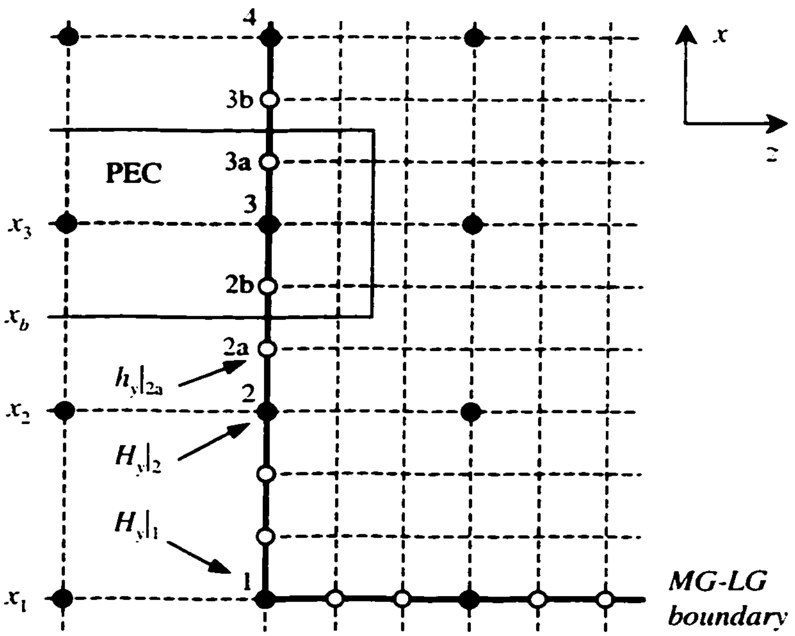

Figure 2.6. A PEC plate traversing the MG-LG boundary, for the case where the MG-LG ratio $r = 3$. The black circles represent the main-grid magnetic fields H_y; the white circles are the local-grid magnetic fields h_y.

Writing the equation for the approximating parabola as

$$P(x) = a(x - x_b)^2 + b, \tag{2.39}$$

it is straightforward to show that the fitting coefficients a and b are given by

$$a = \frac{4}{3}\frac{H_y\big|_1 - H_y\big|_2}{(\Delta x)^2},$$

$$b = \frac{1}{3}\left(4H_y\big|_2 - H_y\big|_1\right).$$

From Eq.(2.39) for the parabola, we can compute the derivatives D_x, D_{xx} and D_{xt} at node 2:

$$D_x = 2a(x_2 - x_b),$$

$$D_{xx} = 2a,$$

$$D_{xt} = \left(D_x^{n+1} - D_x^{n-1}\right)\big/2\Delta t.$$

where D_x^{n+1} and D_x^{n-1} are obtained from the parabolas passing through $H_y\big|_1^{n+1}$ and $H_y\big|_2^{n+1}$ and through $H_y\big|_1^{n-1}$ and $H_y\big|_2^{n-1}$, respectively. The derivatives D_x, D_{xx} and D_{xt} can then be used in the interpolation formula (2.38) to estimate the local-grid field value $h_y\big|_{2a}^{m}$.

2.5 Numerical Issues

Because the FDTD method approximates the partial differential wave equation with finite-difference operators over a finite grid, the numerical solution necessarily suffers from discretization and dispersion errors. In this section the approximation error, the stability of the numerical scheme, and the dispersive effects of the finite grid are analyzed in detail.

Most of the numerical analyses in this section were carried out for the single-field second-order discrete wave equation. However, the results apply equally to the leap-frog equations because the two schemes are numerically equivalent. To demonstrate this, consider the conventional leap-frog equations for TE-polarized wave in a general lossy dielectric medium:

$$\frac{(\varepsilon E_y)_{i,j}^{n+1} - (\varepsilon E_y)_{i,j}^{n}}{\Delta t} + (\sigma E_y)_{i,j}^{n+1} = \frac{H_x\big|_{i+1/2,j}^{n+1/2} - H_x\big|_{i-1/2,j}^{n+1/2}}{\Delta z} - \frac{H_z\big|_{i,j+1/2}^{n+1/2} - H_z\big|_{i,j-1/2}^{n+1/2}}{\Delta x} \tag{2.40a}$$

$$\frac{\mu_0}{\Delta t}\left(H_x\big|_{i+1/2,j}^{n+1/2} - H_x\big|_{i+1/2,j}^{n-1/2} \right) = \frac{1}{\Delta z}\left(E_y\big|_{i+1,j}^{n} - E_y\big|_{i,j}^{n} \right) \tag{2.40b}$$

$$\frac{\mu_0}{\Delta t}\left(H_z\big|_{i,j+1/2}^{n+1/2} - H_z\big|_{i,j+1/2}^{n-1/2} \right) = -\frac{1}{\Delta x}\left(E_y\big|_{i,j+1}^{n} - E_y\big|_{i,j}^{n} \right). \tag{2.40c}$$

We shall now show that the above equations are reducible to a single second-order wave equation. Applying Eq.(2.40b) to node $(i-1/2, j)$ and Eq.(2.40c) to node $(i, j-1/2)$, we get

$$\frac{\mu_0}{\Delta t}\left(H_x\big|_{i-1/2,j}^{n+1/2} - H_x\big|_{i-1/2,j}^{n-1/2} \right) = \frac{1}{\Delta z}\left(E_y\big|_{i,j}^{n} - E_y\big|_{i-1,j}^{n} \right), \tag{2.41a}$$

$$\frac{\mu_0}{\Delta t}\left(H_z\big|_{i,j-1/2}^{n+1/2} - H_z\big|_{i,j-1/2}^{n-1/2} \right) = -\frac{1}{\Delta x}\left(E_y\big|_{i,j}^{n} - E_y\big|_{i,j-1}^{n} \right). \tag{2.41b}$$

Next subtracting Eq.(2.41a) from Eq.(2.40b) and dividing by Δz, and likewise subtracting Eq.(2.41b) from Eq.(2.40c) and dividing by Δx, we obtain

$$\frac{H_x\big|_{i+1/2,j}^{n+1/2} - H_x\big|_{i-1/2,j}^{n+1/2}}{\Delta z} = \frac{H_x\big|_{i+1/2,j}^{n-1/2} - H_x\big|_{i-1/2,j}^{n-1/2}}{\Delta z} + \frac{\Delta t}{\mu_0}\,\frac{E_y\big|_{i+1,j}^{n} - 2E_y\big|_{i,j}^{n} + E_y\big|_{i-1,j}^{n}}{(\Delta z)^2}. \tag{2.42a}$$

$$\frac{H_z\big|_{i,j+1/2}^{n+1/2} - H_z\big|_{i,j+1/2}^{n+1/2}}{\Delta x} = \frac{H_z\big|_{i,j-1/2}^{n-1/2} - H_z\big|_{i,j-1/2}^{n-1/2}}{\Delta x} - \frac{\Delta t}{\mu_0}\,\frac{E_y\big|_{i,j+1}^{n} - 2E_y\big|_{i,j}^{n} + E_y\big|_{i,j-1}^{n}}{(\Delta x)^2}. \tag{2.42b}$$

Substitution of Eqs.(2.42a) and (2.42b) into Eq.(2.40a) gives

$$\frac{(\varepsilon E_y)_{i,j}^{n+1} - (\varepsilon E_y)_{i,j}^{n}}{\Delta t} + (\sigma E_y)_{i,j}^{n+1} - \frac{\Delta t}{\mu_0}\left[\frac{E_y\big|_{i+1,j}^{n} - 2E_y\big|_{i+1,j}^{n} + E_y\big|_{i-1,j}^{n}}{(\Delta z)^2} + \frac{E_y\big|_{i,j-1}^{n} - 2E_y\big|_{i+1,j}^{n} + E_y\big|_{i,j-1}^{n}}{(\Delta x)^2} \right]$$
$$= \frac{H_x\big|_{i+1/2,j}^{n-1/2} - H_x\big|_{i-1/2,j}^{n-1/2}}{\Delta z} - \frac{H_z\big|_{i,j+1/2}^{n-1/2} - H_z\big|_{i,j-1/2}^{n-1/2}}{\Delta x}.$$

Eliminating H_x and H_z on the right hand side of the above equation using Eq.(2.40a), we arrive at

$$\frac{(\varepsilon E_y)^{n+1}_{i,j}-(\varepsilon E_y)^{n}_{i,j}}{\Delta t}+(\sigma E_y)^{n+1}_{i,j}-\frac{\Delta t}{\mu_0}\left[\frac{E_y\big|^n_{i+1,j}-2E_y\big|^n_{i+1,j}+E_y\big|^n_{i-1,j}}{(\Delta z)^2}+\frac{E_y\big|^n_{i,j-1}-2E_y\big|^n_{i+1,j}+E_y\big|^n_{i,j-1}}{(\Delta x)^2}\right]$$
$$=\frac{(\varepsilon E_y)^{n}_{i,j}-(\varepsilon E_y)^{n-1}_{i,j}}{\Delta t}+(\sigma E_y)^{n}_{i,j}$$

which can be simplified to

$$\mu_0\frac{(\varepsilon E_y)^{n+1}_{i,j}-2(\varepsilon E_y)^{n}_{i,j}+(\varepsilon E_y)^{n-1}_{i,j}}{(\Delta t)^2}+\mu_0\frac{(\sigma E_y)^{n+1}_{i,j}-(\sigma E_y)^{n}_{i,j}}{\Delta t}=$$
$$\frac{E_y\big|^n_{i+1,j}-2E_y\big|^n_{i+1,j}+E_y\big|^n_{i-1,j}}{(\Delta z)^2}+\frac{E_y\big|^n_{i,j-1}-2E_y\big|^n_{i+1,j}+E_y\big|^n_{i,j-1}}{(\Delta x)^2} \tag{2.43}$$

We recognize Eq.(2.43) as being identical to the single-field discrete equation of the second-order wave equation. The leap-frog scheme therefore is expected to have the same numerical behaviour as the single-field scheme.

2.5.1 Discretization errors

The wave equation (2.21) is discretized using the forward finite-difference formula for the first-order time derivative $\partial/\partial t$ which is accurate only to order $O(\Delta t)$. Therefore the error due to truncation of the Taylor series is proportional to the first order of the time step, i.e., $\Delta E_i \propto \Delta t$. A second-order accuracy can be obtained if a central difference scheme is used for the derivative $\partial/\partial t$, but such a scheme is not practical since it is always unstable in the parabolic limit. There are also contributions of second order from the grid sizes Δz and Δx, so that the total local discretization error for each node i is

$$\Delta E_i \propto O\{(\Delta t),(\Delta z)^2,(\Delta x)^2\}. \tag{2.44}$$

For optical materials having small losses, $\sigma \ll \omega\varepsilon$, the first-order time derivative is much smaller than the other terms in Eq.(2.21). In this case the discretization approaches second-order accuracy in both time and space:

$$\Delta E_i \propto O\{(\Delta t)^2, (\Delta z)^2, (\Delta x)^2\}. \tag{2.45}$$

Other errors, such as those due to convergence of the Newton-Raphson iterations, numerical dispersion and attenuation, may also exist and add to degrade the accuracy of the schemes below the order of accuracy formally defined in Eqs.(2.44) or (2.45). These errors are discussed next.

2.5.2 Stability

The issue of stability is intimately related to accuracy because an unstable scheme will necessarily result in inaccurate and non-physical solutions. More fundamentally, according to the Lax Equivalence Theorem, stability is a necessary condition for convergence of the finite-difference solution to the exact solution in the limit as Δt, Δx, and Δz approach zero [48]. Since stability is a local effect, we can study it separately in each of the linear and nonlinear medium regions.

In the linear material regions the stability of the explicit scheme has been extensively studied. We consider two cases of the wave equation:

- Hyperbolic limit ($\omega\varepsilon \gg \sigma$):

For the hyperbolic case, stability is given by the well-known Courant-Friedrichs-Lewy (CFL) condition [15,16]

$$\frac{(c\Delta t)^2}{\varepsilon_r}\left[\frac{1}{(\Delta z)^2}+\frac{1}{(\Delta x)^2}\right] \le 1. \tag{2.46}$$

The above condition implies that smaller time step is required for materials with smaller permittivity. Since $\varepsilon_r \ge 1$, free space imposes the most stringent stability requirement.

- Parabolic limit ($\omega\varepsilon \ll \sigma$):

For the parabolic case, the scheme is stable if Δt, Δz, and Δx satisfy the condition (e.g., [48])

$$\frac{\Delta t}{\mu_0 \sigma}\left[\frac{1}{(\Delta z)^2}+\frac{1}{(\Delta x)^2}\right] \le \frac{1}{2}. \tag{2.47}$$

In the mixed case where both ε and σ are present, stability is determined by the more stringent of the two conditions (2.46) and (2.47), which is usually the CFL condition for problems of our interest.

In the nonlinear material regions, stability analysis becomes considerably more complicated by the dependence of ε_r and σ on the field. We consider here the important case of the explicitly discretized wave equation ($a_1 = a_3 = 0$, $a_2 = 1$):

$$\frac{(\varepsilon_r E)_i^{n+1} - 2(\varepsilon_r E)_i^n + (\varepsilon_r E)_i^{n-1}}{(c\Delta t)^2} = \frac{E_{i_L}^n - 2E_i^n + E_{i_R}^n}{(\Delta z)^2} + \frac{E_{i_A}^n - 2E_i^n + E_{i_B}^n}{(\Delta x)^2}. \tag{2.48}$$

where $\sigma = 0$ and nonlinearity appears only in the field dependency of the relative permittivity, $\varepsilon_r(E)$. The analysis presented in Appendix A results in the stability condition

$$(c\Delta t)^2 \left(\frac{\partial g_i^n}{\partial E_i^n}\right)^{-1} \left[\frac{1}{(\Delta z)^2}+\frac{1}{(\Delta x)^2}\right] \le 1. \tag{2.49}$$

where $g_i^n = (\varepsilon_r E)_i^n$. This condition is similar to the CFL stability condition for the linear scheme except that in place of the constant relative permittivity ε_r, we have the term

$$\frac{\partial g_i^n}{\partial E_i^n} = \frac{\partial}{\partial E_i^n}(\varepsilon_r E)_i^n = \varepsilon_r\left(E_i^n\right) + \left(\frac{\partial \varepsilon_r}{\partial E}\right)_i^n E_i^n. \tag{2.50}$$

We consider below the two most common types of optical nonlinearities, the third-order Kerr effect and the second-order Pockels effect.

- Third-order optical nonlinearity:

For third-order nonlinearity the permittivity depends on the electric field intensity and can be expressed in the general form

$$\varepsilon_r = n_0^2 + f\left(|E|^2\right). \tag{2.51}$$

where n_0 is the linear refractive index and f is a positive, monotonically increasing function describing the nonlinear model (e.g., exponential saturation, two-level saturation). We thus have

$$\frac{\partial g_i^n}{\partial E_i^n} = n_0^2 + f\left(\left|E_i^n\right|^2\right) + 2\left(\frac{df}{dE}\right)_i^n \left|E_i^n\right|^2 \geq n_0^2. \tag{2.52}$$

Substituting the above into Eq.(2.49) gives

$$\frac{(c\Delta t)^2}{n_0^2}\left[\frac{1}{(\Delta z)^2} + \frac{1}{(\Delta x)^2}\right] \leq 1. \tag{2.53}$$

which shows that the stability condition for the nonlinear scheme is the same as the CFL condition for a linear medium with refractive index n_0.

- Second-order optical nonlinearity:

For second-order nonlinearity, the relative permittivity is given by

$$\varepsilon_r = n_0^2 + \chi^{(2)} E. \tag{2.54}$$

where $\chi^{(2)}$ is the second-order susceptibility. In this case we have

$$\frac{\partial g_i^n}{\partial E_i^n} = n_0^2 + 2\chi^{(2)} E_i^n \geq n_0^2 - 2\chi^{(2)} E_{\max}. \tag{2.55}$$

where $E_{\max}$ is the maximum field occurring during the simulation. The stability condition of the FDTD scheme for second-order nonlinearity is thus

$$\frac{(c\Delta t)^2}{n_0^2 - 2\chi^{(2)}E_{\max}}\left[\frac{1}{(\Delta z)^2}+\frac{1}{(\Delta x)^2}\right]\leq 1, \qquad (2.56)$$

which is equivalent to the CFL condition for a linear medium with relative permittivity equal to $n_0^2 - 2\chi^{(2)}E_{\max}$.

The above nonlinear stability conditions apply only to the explicitly-discretized wave equation. For the weighted-average scheme, a closed-form expression for the monotonicity condition cannot be derived, but simulations running with third-order nonlinearity have been experimentally observed to be stable if the CFL condition is satisfied. The fully-implicit scheme was not considered because it suffers from numerical attenuation.

The stability conditions derived in this section give the maximum time step that can be used in the FDTD simulation without causing unbounded growth in the numerical solution. The overall stability of the hybrid implicit-explicit FDTD scheme is determined by the most stringent stability condition imposed by each of the linear and nonlinear medium regions in the computational domain. For the important case of third-order optical nonlinearity, the stability of the hybrid method is determined only by the linear part of the refractive indexes present in the structure. Consequently, the strength of the nonlinearity does not affect the stability, and hence the grid sizes and time step used. This is in contrast with the conventional non-iterative scheme where in general, stronger nonlinearity requires the grid sizes and time step be further reduced below the CFL limit in order to ensure stability [16].

We conclude this section by noting that since the hybrid single-field leap-frog FDTD method is a linear scheme, the stability condition is formally defined by either Eq.(2.46) or (2.47). In practice, however, stability is degraded because interpolation at the MG-LG boundaries introduces additional approximation errors. Furthermore, the interfaces between the coarse and fine grids cause numerical reflections, and the energies from these reflections can build up inside the local domain, which acts as a numerical resonant cavity, and eventually causes the solution to blow up.(a) In general it was observed that for larger MG-LG ratio r, the time step must be further reduced below the maximum stability value given by Eq.(2.46) or (2.47) in order to ensure

---

(a) Acknowledgment goes to Prof. Raj Mitra of Penn State University for this illuminating observation.

stability. Also, introduction of a small artificial or physical loss into the local domain helps dampen the energy build-up in the numerical cavity and enhances the stability of the solution.

2.5.3 Numerical dispersion and dissipation

Due to the use of finite grid sizes and time step, the numerical solution of a hyperbolic system suffers from frequency dispersion and amplitude attenuation. For linear problems, Fourier mode analysis is often used to estimate the amounts of dispersion and dissipation, which depend on the discretization scheme used. The same analysis, however, cannot be applied to nonlinear problems because of the resulting frequency mixing effect. Moreover, in problems of wave propagation through a nonlinear medium, the dispersive effect inherent in the physical medium is also present, which may be further enhanced or reduced by the type of nonlinearity in the material. Therefore it is difficult to separate the numerical dispersive effect from the physical effect. Nonetheless, results obtained from linear analysis give an indication of the relative amount of dispersion and attenuation introduced by different discretization schemes. In the following, we compare the explicit scheme, the weighted-average scheme and the fully-implicit scheme based on their dispersion and dissipation in a lossless linear medium.

In Fourier mode analysis, we apply to the discrete equation a test solution of the form

$$E_{h,k}^{n} = \lambda^{n} e^{j\beta_z h\Delta z} e^{j\beta_x k\Delta x}, \tag{2.57}$$

where $j = \sqrt{-1}$, $\lambda = |\lambda| e^{j\phi}$ is in general a complex number, and β_z and β_x are the propagation constants in the z- and x-direction, respectively. Over one period, the change in the amplitude $|\lambda|$ gives the attenuation or amplification factor, and the phase ϕ gives the amount of dispersion due to both the material and the numerical scheme. The results obtained from the analyses presented in Appendix B are as follows:

- <u>Explicit scheme</u>: $(a_1 = 1, a_2 = a_3 = 0)$

$$|\lambda| = 1,$$

and $$\phi \approx kv\Delta t\left\{1-\frac{1}{24}\left[\left(\frac{\beta_z^2\Delta z}{k}\right)^2+\left(\frac{\beta_x^2\Delta x}{k}\right)^2\right]+\frac{1}{24}(kv\Delta t)^2\right\}. \tag{2.58}$$

where $v = c/\sqrt{\varepsilon_r}$ is the velocity of light in the medium, and $k^2 = \beta_z^2 + \beta_x^2 = (\omega/v)^2$ is the wave number. The first term in Eq.(2.58), $kv\Delta t$, accounts for the material dispersion and the other terms are due to numerical dispersion. It is seen that the explicit scheme has no amplitude attenuation but suffers from a negative phase error, i.e., phase lag. Note that the phase lag is zero only for the special case where $\beta_z = \beta_x$ and the time step and grid sizes satisfy the condition

$$(\Delta x)^2 + (\Delta z)^2 = (2v\Delta t)^2.$$

- Weighted-average scheme: ($a_1 = a_3 = 1/4$, $a_2 = 1/2$)

$$|\lambda| = 1,$$

$$\phi \approx kv\Delta t\left\{1-\frac{1}{24}\left[\left(\frac{\beta_z^2\Delta z}{k}\right)^2+\left(\frac{\beta_x^2\Delta x}{k}\right)^2\right]-\frac{1}{12}(kv\Delta t)^2\right\}. \tag{2.59}$$

Thus the weighted-average scheme has no amplitude error, but suffers from a phase lag slightly greater than that of the explicit case.

- Fully-implicit scheme: ($a_1 = a_3 = 0$, $a_2 = 1$)

$$|\lambda| \approx 1-\tfrac{1}{2}(kv\Delta t)^2 < 1. \tag{2.60}$$

Thus the fully-implicit scheme, while unconditionally stable, suffers from amplitude attenuation. This attenuation is multiplied at each time step, so that after several hundred time steps the amplitude of the wave becomes greatly attenuated from the correct solution.

The foregoing discussion concerns only with dispersion in a lossless linear medium. For lossy conducting media the numerical dispersive effect becomes more pronounced and is the dominant source of numerical error. To quantify the dispersion error, we again apply the test solution (2.57) to the discrete wave equation and derive the dispersion relation. The result for the explicit discretization scheme is

$$\frac{\sin^2(\beta_z \Delta z/2)}{(\Delta z)^2}+\frac{\sin^2(\beta_x \Delta x/2)}{(\Delta x)^2}=\left(\mu_0\varepsilon+\tfrac{1}{2}\mu_0\sigma\Delta t\right)\frac{\sin^2(\omega\Delta t/2)}{(\Delta t)^2}-j\tfrac{1}{4}\mu_0\sigma\frac{\sin(\omega\Delta t)}{\Delta t}. \tag{2.61}$$

Assuming, for simplicity, a z-propagating wave so that $\beta_x = 0$ and the wave number $k = \beta_z$, we can then calculate the effective index of refraction $\tilde{n}(\omega) = ck(\omega)/\omega$ from the above equation. Given that the exact analytical refractive index of the medium is

$$n(\omega)=\sqrt{\varepsilon_r - j\sigma/\omega\varepsilon_0}\,, \tag{2.62}$$

we can compute the relative dispersion error, $\mathrm{Re}\{\tilde{n}(\omega)-n(\omega)\}/\mathrm{Re}\{n(\omega)\}$, and the relative dissipation error, $\mathrm{Im}\{\tilde{n}(\omega)-n(\omega)\}/\mathrm{Im}\{n(\omega)\}$. Figures 2.7(a) and 2.7(b) show the relative errors as a function of the frequency. The effects of the conductivity parameter σ and the grid size Δz are illustrated by calculating the errors for two different values of σ, 10^6S/m and 10^7S/m, and two different values of Δz, 1μm and 10μm. In all the calculations $\varepsilon_r = 1$ and the time step Δt is set at the maximum CFL limit. The plots in Figure 2.7 show that both the dispersion and dissipation errors increase with the frequency, the grid size, and the conductivity. In the millimeter-wave regime (~100GHz) the dispersion error for a 1μm grid size can be as high as 30% for a good conductor such as copper ($\sigma = 6\times10^7$S/m). This error poses a serious limitation to the ability of the FDTD method to simulate millimeter-wave devices. However, since in this work we are concerned only with thin-film waveguides in which the conducting material occupies very thin layers, the dispersion error is tolerably small and can be further minimized by the use of subgridding to reduce the grid size in the conducting regions.

2.5.4 Convergence

In the hybrid implicit-explicit method, beside the convergence of the discrete solution to the exact solution, which has been discussed in conjunction with stability, there is also the issue of convergence of the Newton-Raphson iterative procedure for solving the nonlinear system in Eq.(2.22). If the system has a single root, then for a sufficiently close initial guess, Newton-Raphson iteration will converge to the true solution at an almost quadratic rate. Because our

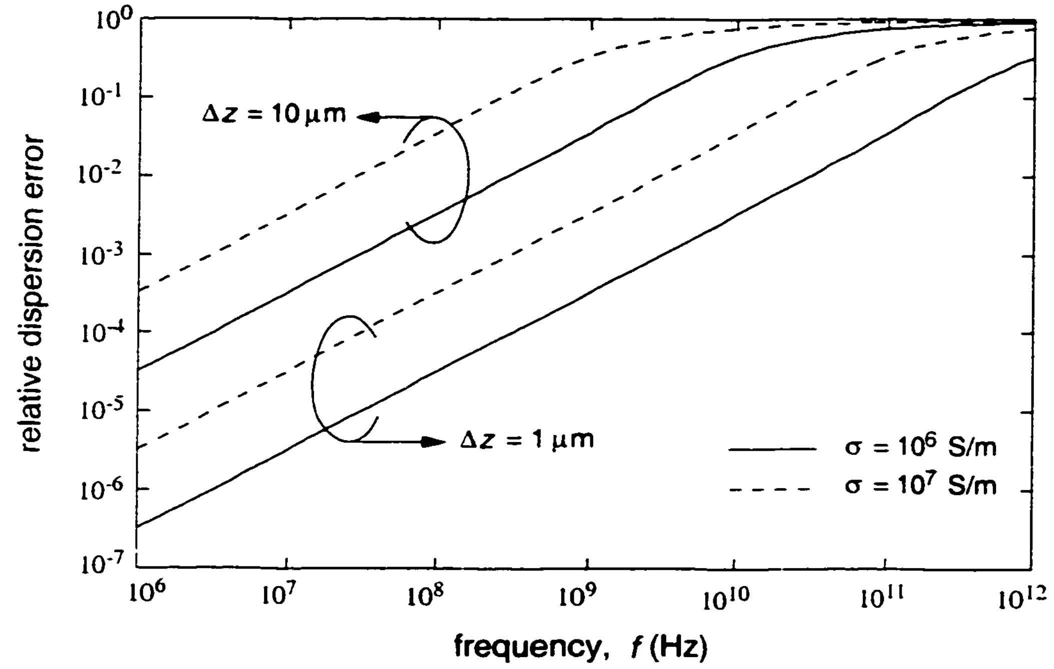

(a)

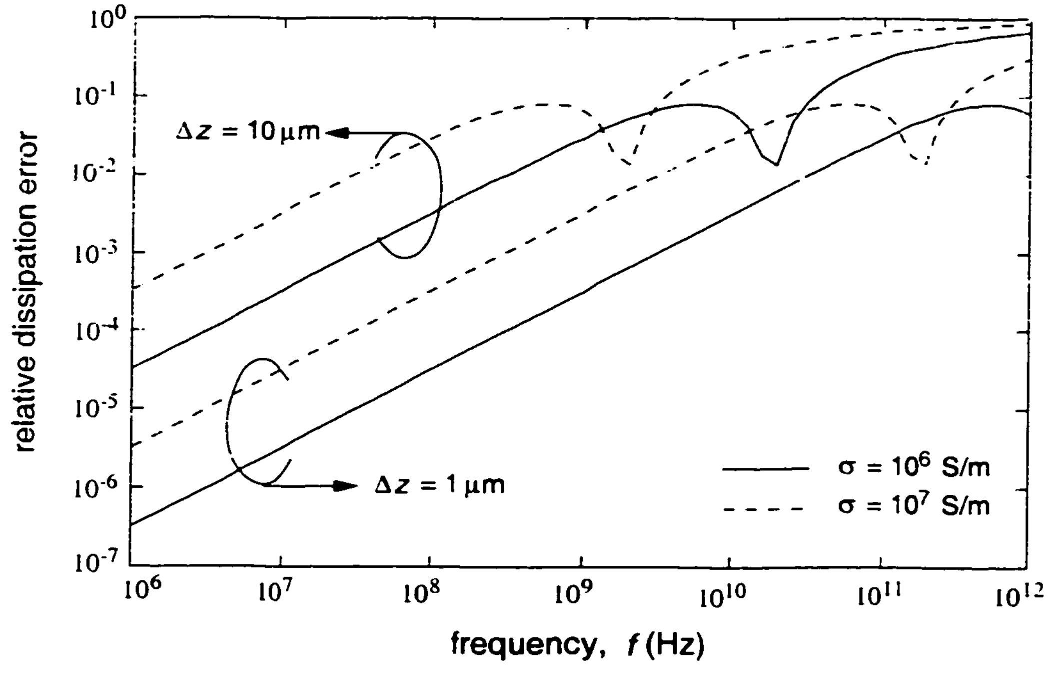

(b)

Figure 2.7. (a) Relative dispersion error and (b) relative dissipation error for the explicit FDTD scheme in lossy conducting media.

initial guess of the field values at time step $n+1$ is taken to be the field at time step n, for sufficiently small time steps, the iterate will already be very close to the true solution, and near quadratic convergence of the Newton-Raphson method can be achieved. As shall be demonstrated in Chapter 3, convergence is usually obtained after 4 or 5 iterations.

2.6 Summary

We introduced in this chapter two hybrid FDTD techniques: a hybrid implicit-explicit scheme for solving the scalar TE wave equation in mixed linear and nonlinear media, and a hybrid single-field leap-frog scheme with subgridding for simulating TM propagation in inhomogeneous media. For the implicit-explicit method we presented three alternative discretization schemes – explicit, weighted-average, and implicit – for the nonlinear medium regions and investigated the stability and numerical dispersion of each. The conclusion is that the explicit scheme is the best choice for nonlinear dielectric media, whereas the weighted-average scheme provides better stability condition for solutions in highly lossy materials. The implicit scheme is not practical because it suffers from severe numerical attenuation. In the next chapter the hybrid implicit-explicit FDTD method will be applied to analyze nonlinear optical structures.

In the second hybrid FDTD scheme, which combines the single-field and leap-frog formulations of the wave equation, a subgridding algorithm based on time and space interpolation of the fields on the grid boundaries was presented. This method will be used for simulating propagation in microwave and millimeter-wave devices, and will be extended to include nonlinear HTS materials in Chapter 4.

Chapter 3

Optical Device Applications

In this chapter application of the hybrid implicit-explicit FDTD scheme developed in the previous chapter for analyzing wave propagation in nonlinear optical devices will be presented. We shall first demonstrate the stability and accuracy of the two nonlinear schemes – the nonlinear explicit and the weighted-average schemes, by applying them to the simple cases of an open nonlinear dielectric medium and a nonlinear slab waveguide. The versatility and applicability of the hybrid FDTD method will then be illustrated by exploring more complicated nonlinear wave-guiding structures. Two specific devices will be focused on: the nonlinear periodic waveguide and the nonlinear microring resonator, with an emphasized view on how they may be used as elements in optical communication systems.

3.1 Stability of the Nonlinear FDTD Method

We investigate numerically the stability of the two nonlinear FDTD schemes introduced in Chapter 2, the nonlinear explicit scheme and the weighted-average scheme. Two numerical experiments are presented, the open nonlinear dielectric medium for validation of the analytical stability condition (2.49) for the nonlinear explicit FDTD method, and the nonlinear slab waveguide for comparison and physical verification of the nonlinear explicit and weighted-average schemes.

3.1.1 Stability of the nonlinear explicit method

It was shown that for the nonlinear explicit FDTD scheme the stability condition can be expressed analytically by condition (2.49). Moreover, for the specific case of third-order optical nonlinearity the stability condition is given by Eq.(2.53), which depends only on the linear part of the refractive index of the medium; while for second-order optical nonlinearity the stability condition requires an estimation of the maximum electric field $E_{\max}$ occurring during the simulation, as stated in Eq.(2.56). To verify these conditions, we performed numerical experiments by applying the hybrid FDTD method on the test structure shown in Figure 3.1. A linear dielectric waveguide with index contrast 3:1 is used to launch a TE_0 mode at the source plane, which radiates into an open nonlinear dielectric region having the linear part of the refractive index, n_0, equal to 1.0. The structure is surrounded by vacuum so that the minimum refractive index, which determines the linear stability limit, is also 1.0. With the grid size choice of $\Delta z = \Delta x = 0.025\mu m$, the maximum CFL time step allowed, assuming all materials are linear, is $(\Delta t)_{CFL} = 0.058966fs$. At this Δt value the CFL coefficient defined by

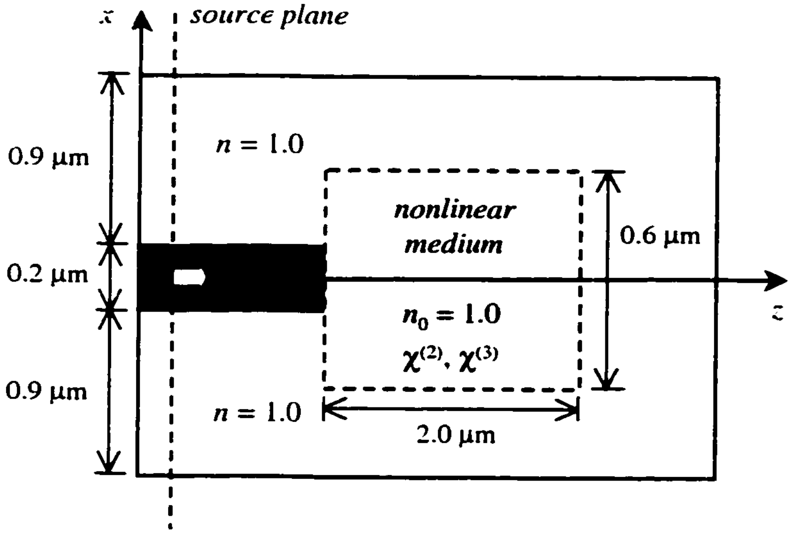

Figure 3.1. Open nonlinear dielectric structure for testing the stability condition of the nonlinear explicit FDTD scheme. The nonlinear medium has susceptibility $\chi^{(2)} = 10^{-6}m/V$ or $\chi^{(3)} = 10^{-10}m^2/V^2$ depending on the type of nonlinearity under investigation.

$$\mathrm{CFL} = \frac{c\Delta t}{n_0}\sqrt{1/(\Delta z)^2 + 1/(\Delta x)^2} \tag{3.1}$$

is equal to 0.99999. A continuous-wave signal at wavelength $\lambda = 1\mu\mathrm{m}$ with peak electric field $E_0 = 0.04\mathrm{V}/\mu\mathrm{m}$ was launched into the dielectric waveguide. We performed FDTD simulations of wave propagation through the dielectric block for two types of nonlinearity: third-order nonlinearity with susceptibility coefficient $\chi^{(3)} = 10^{-10}\mathrm{m}^2/\mathrm{V}^2$, and second-order nonlinearity with $\chi^{(2)} = 10^{-6}\mathrm{m/V}$.

Since third-order nonlinearity imposes no additional constraint on the stability of the FDTD method, the maximum stable time step in this case can be taken to be $\Delta t = (\Delta t)_{\mathrm{CFL}} = 0.058966\mathrm{fs}$. The simulation was run for 10,000 time steps and the electric field profile was recorded. Figures 3.2(a) and 3.2(b) show in solid lines, respectively, the longitudinal field profile along the z-axis and the transverse field profile at the centre of the nonlinear dielectric region. For comparison, the field profiles obtained from simulating the same structure without nonlinearity are also shown in the plots by the dashed lines. From both plots it is seen that the nonlinear simulation remained stable up to 10,000 time steps at CFL = 1, as predicted by the stability condition (2.53).

For second-order nonlinearity the stability limit is slightly more difficult to determine because it requires knowledge of the maximum electric field, $E_{\max}$, occurring during the simulation. This maximum field value can be estimated by performing a linear simulation over a few time periods, and recording the maximum field that occurs in the region where the nonlinearity would be present. The value of $E_{\max}$ determined in this way was $0.05\mathrm{V}/\mu\mathrm{m}$, which gives a minimum equivalent permittivity, $n_0^2 - 2\chi^{(2)}E_{\max}$, of 0.9 in the nonlinear region. The maximum stable time step, for $\Delta z = \Delta x = 0.025\mu\mathrm{m}$, given by condition (2.56) is 0.055940fs, which corresponds to a CFL coefficient of 0.94868. The simulation was then performed at this value of Δt up to 100,000 time steps, and the longitudinal and transverse field profiles through the centre of the dielectric were recorded and shown by the solid lines in Figures 3.3(a) and 3.3(b), respectively. No signs of instability are observed in both plots, indicating that the numerical solution was stable. By contrast, when the simulation was run at the maximum CFL time step $(\Delta t)_{\mathrm{CFL}}$, which corresponds to CFL = 1.0, the solution became unstable after only 460

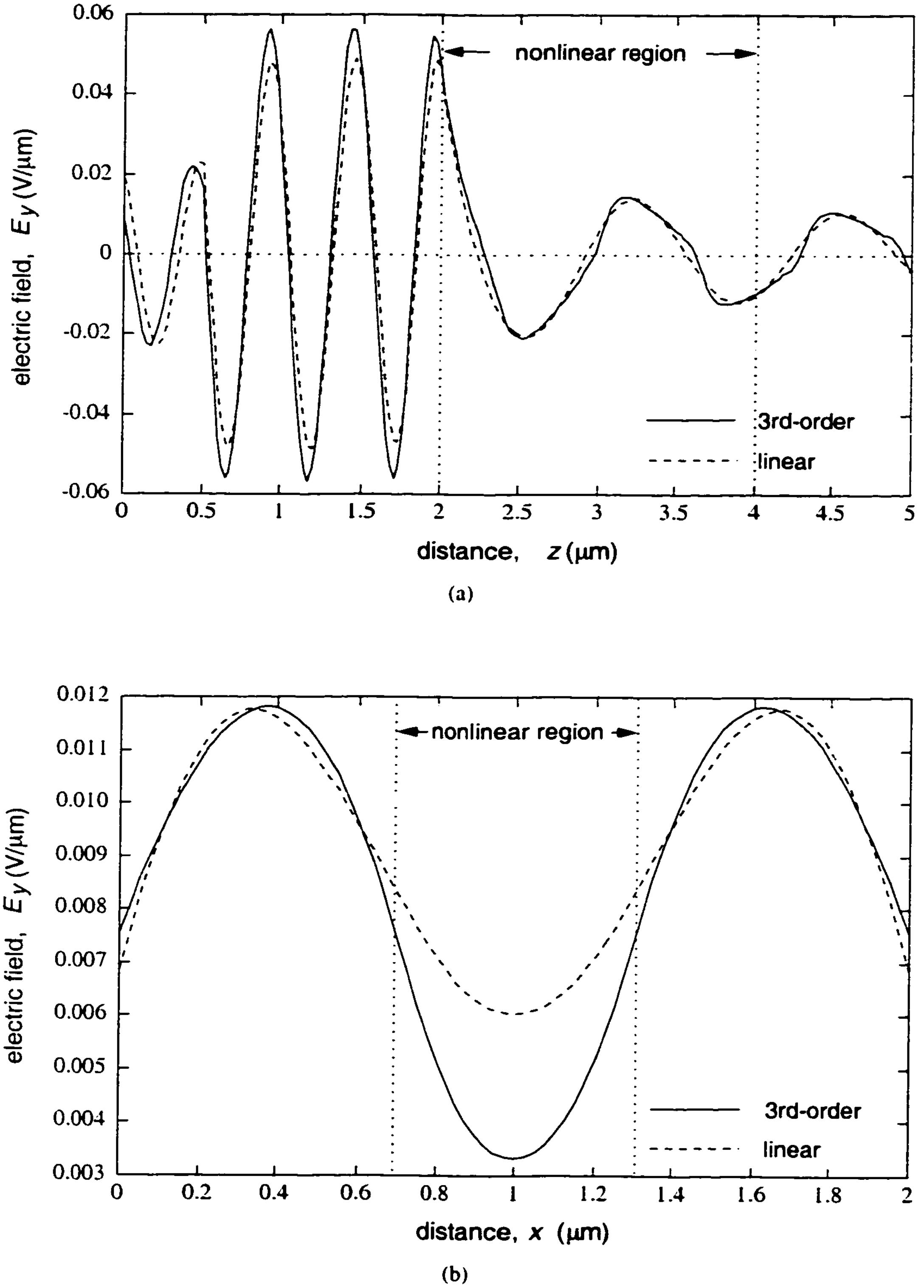

Figure 3.2. Simulation results with third-order nonlinearity after 10,000 time steps: (a) longitudinal electric field profile along z-axis; (b) transverse electric field profile through the centre of the nonlinear dielectric.

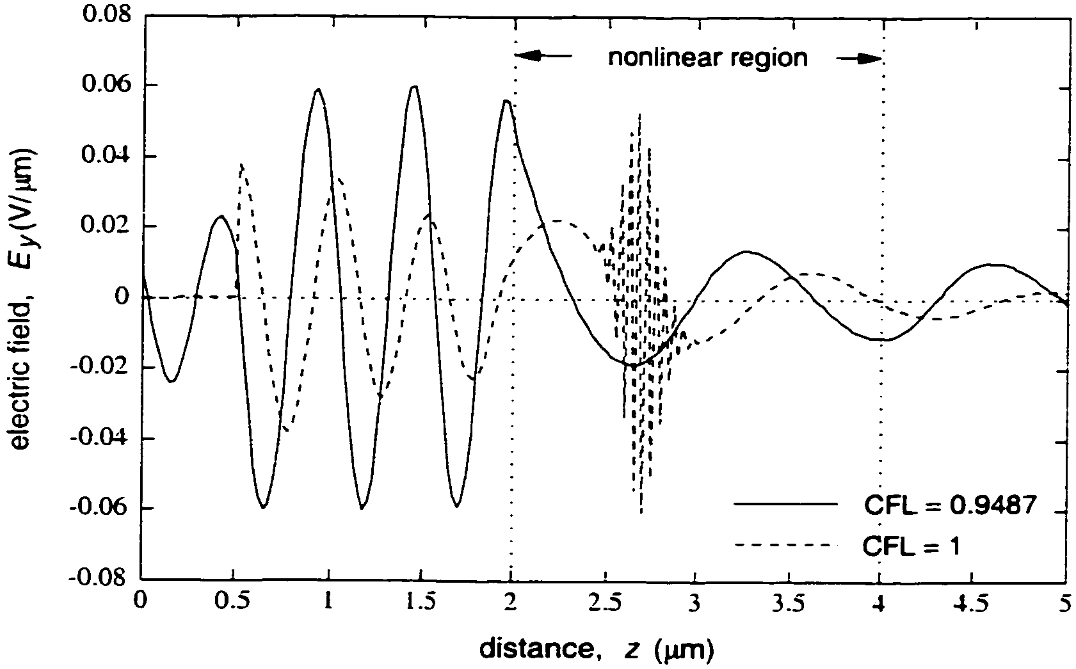

(a)

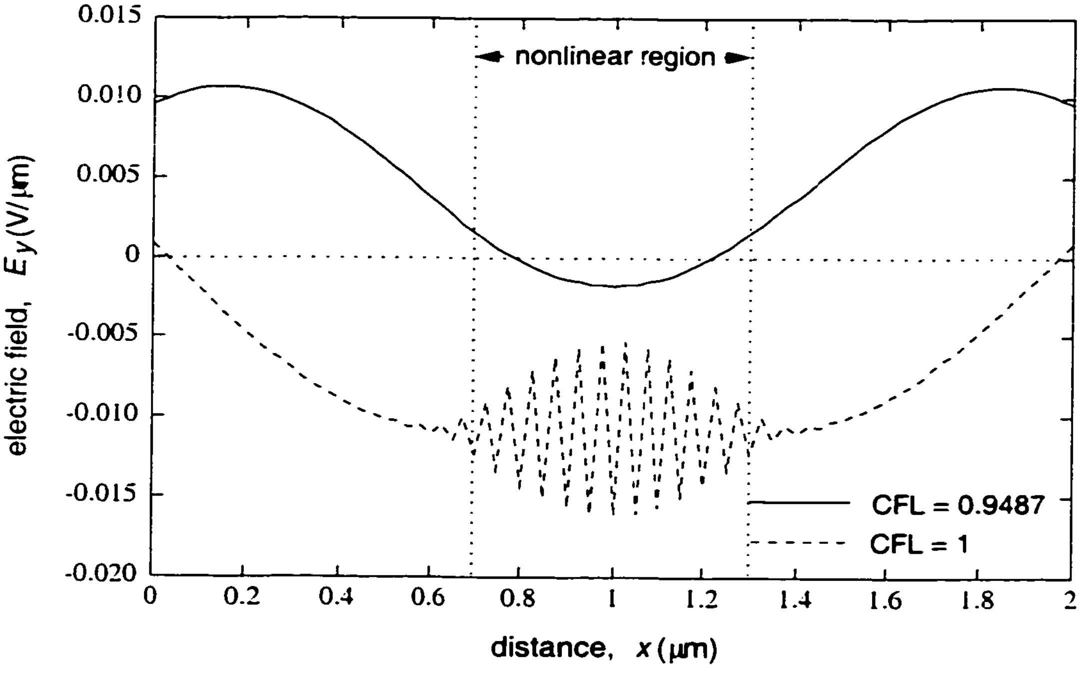

(b)

Figure 3.3. Simulation results with second-order nonlinearity after 100,000 time steps: (a) longitudinal electric field profile along z-axis; (b) transverse electric field profile through the centre of the nonlinear dielectric. When CFL = 1, instability (dashed lines) resulted after 460 time steps.

time steps, as indicated by the dashed lines in the same figures. Note that the instability originates inside the nonlinear region in the form of oscillations whose amplitudes grow unboundedly with time. The appearance of these oscillations signifies that the monotonicity condition required for stability in the analysis in Appendix A is no longer satisfied, thus leading to the observed instability.

The onset of the instability was further investigated by numerically determining the time step at which the nonlinear FDTD method became unstable. In Figure 3.4 the number of time steps until the first signs of instability were observed is plotted as a function of the CFL coefficient. At CFL = 1, the simulation became unstable after only a few hundred time steps. As the CFL coefficient was reduced, it took increasingly longer before instability set in until at CFL = 0.982, an abrupt change occurred in the plot indicating that the method became stable. Note that our stability condition (2.56) predicts a slightly more conservative CFL figure of 0.95 as the point at which the simulation becomes stable.

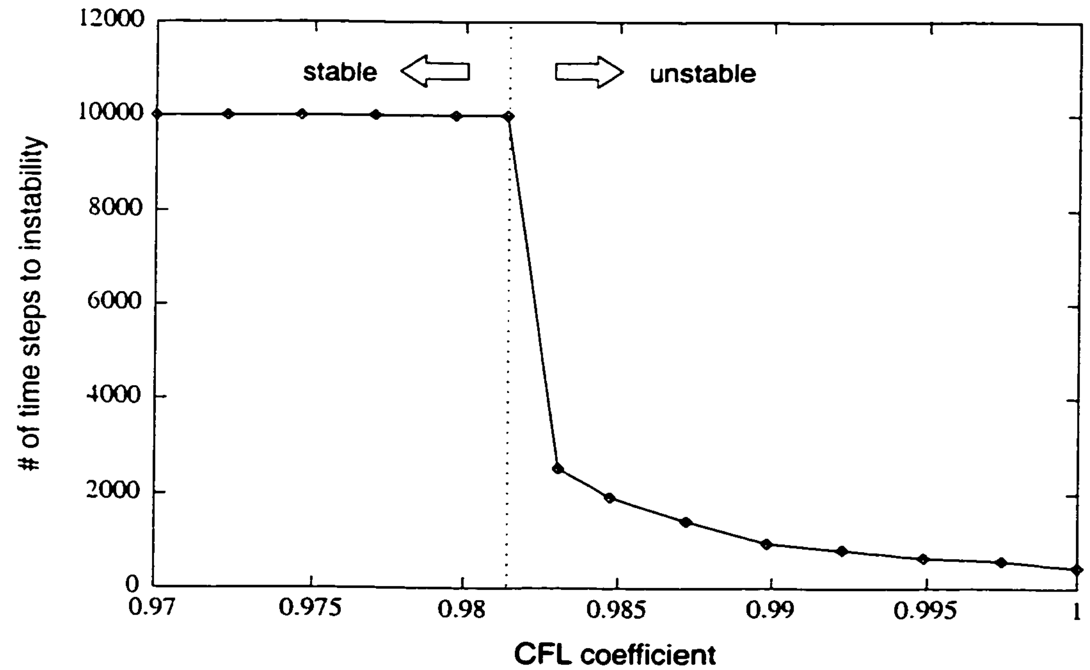

Figure 3.4. Number of time steps to instability as a function of the CFL coefficient for the nonlinear explicit FDTD method with second-order nonlinearity.

The numerical results presented in this section provide experimental validation to the analytical formula (2.49) for the stability condition of the nonlinear explicit FDTD method. This stability condition gives the maximum time step Δt that can be used in the simulation without causing unbounded growth in the numerical solution. This result represents a valuable contribution to the nonlinear FDTD technique since up to date, stability could only be verified by actually running the simulation at various reduced time steps until the numerical solution is observed to remain bounded up to the simulation time of interest.

As mentioned in Chapter 2 it is not possible to derive a closed-form expression for the stability condition of the weighted-average scheme. However, simulations running with Kerr-type nonlinearity were observed to be stable up to tens of thousands of time steps if the linear CFL condition is satisfied. In the next section we compare the numerical solutions of the weighted-average scheme and the nonlinear explicit scheme by studying propagation in a nonlinear dielectric slab waveguide. The slab waveguide also serves to provide physical validation to the hybrid FDTD method since approximate analytical solution is known for this simple structure.

3.1.2 The nonlinear dielectric slab waveguide

The nonlinear dielectric slab waveguide is the simplest nonlinear optical device with which we can study the effects of material nonlinearity on wave propagation. Figure 3.5 shows the structure of a two-dimensional slab waveguide with a core section having instantaneous Kerr-type nonlinearity. The linear waveguide adjacent to the left boundary with index contrast of 1.5:1.0 serves as the launcher in which the TE_0 mode is excited at the source plane. The linear part of the refractive index of the nonlinear waveguide, n_2, is also 1.5 and the strength of the nonlinearity is determined by the susceptibility $\chi^{(3)}$. The entire structure is discretized using grid sizes Δz = 0.01μm and Δx = 0.02μm. The maximum stable time step is Δt = 0.02983fs, corresponding to a CFL coefficient of 0.9998. The solution of the field in the nonlinear waveguide was obtained using three FDTD schemes: the nonlinear explicit scheme, the weighted-average scheme, and the non-iterative scheme. The last scheme uses the same explicit discretization in Eq.(2.48) but computes the permittivity values at time step $n+1$ using the field

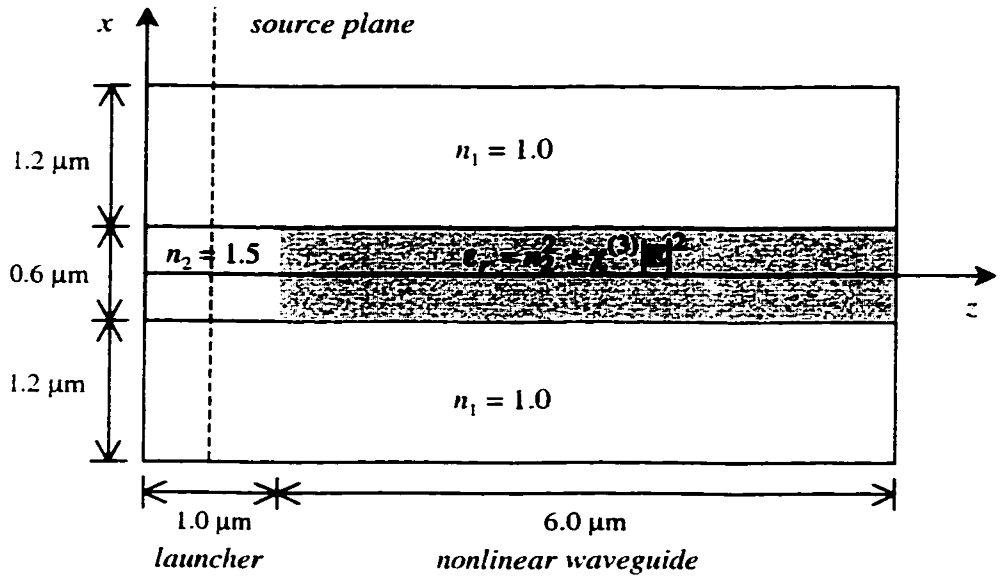

Figure 3.5. Two-dimensional nonlinear dielectric slab waveguide. The third-order susceptibility $\chi^{(3)}$ is $10^{-11}\text{m}^2/\text{V}^2$ for weak nonlinearity, and $10^{-10}\text{m}^2/\text{V}^2$ for moderate nonlinearity.

values at time step n, i.e., $\varepsilon_r\big|_i^{n+1} = \varepsilon_r\left(E_i^n\right)$. This approximation leads to a discrete equation that can be explicitly solved for the unknown field E^{n+1} without requiring any nonlinear iteration. We investigated propagation in the nonlinear waveguide under two modes of excitation: continuous wave and Gaussian pulse.

(a) Continuous-wave excitation

The input electric field for continuous-wave excitation is given by

$$E_{inc}(x, z_0, t) = E_0(x)\sin(\omega t - \beta z_0), \tag{3.2}$$

where $z = z_0$ is the location of the source plane, $E_0(x)$ is the modal field profile of the TE_0 mode, and β is the propagation constant. In the simulation the wavelength of the input signal was 1.0μm and the input power was 1W/m, corresponding to a wave amplitude E_0 of 0.0311V/μm. The waveguide was simulated for the cases of weak and moderate nonlinearities. For the weakly nonlinear waveguide, the third-order susceptibility $\chi^{(3)}$ was set to 10^{-11}m^2/V^2, which results in a maximum change of 0.12% in the refractive index of the core due to the applied electric field. Figure 3.6 shows the field profiles along the core center (z-axis) at the time instant T = 59.96fs, as obtained by the nonlinear explicit scheme, the weighted-average scheme and the non-iterative scheme. It is seen that the three results are stable and almost identical, although closer examination reveals that the weighted-average scheme yielded a slightly larger numerical phase dispersion (phase lag) than the explicit schemes, as was theoretically predicted in Section 2.5.3. For the case of moderate nonlinearity, $\chi^{(3)}$ was set to 10^{-10}m^2/V^2, corresponding to a maximum change of 1.2% in the refractive index of the core. The field profiles along the core centre at T = 59.96fs obtained by the three schemes are again compared and shown in Figure 3.7. The non-iterative scheme is seen to produce unstable solution which grew unboundedly with time, whereas the nonlinear explicit and weighted-average solutions remained bounded and were almost identical, with the wave amplitude slightly modulated due to the nonlinear effect of self-

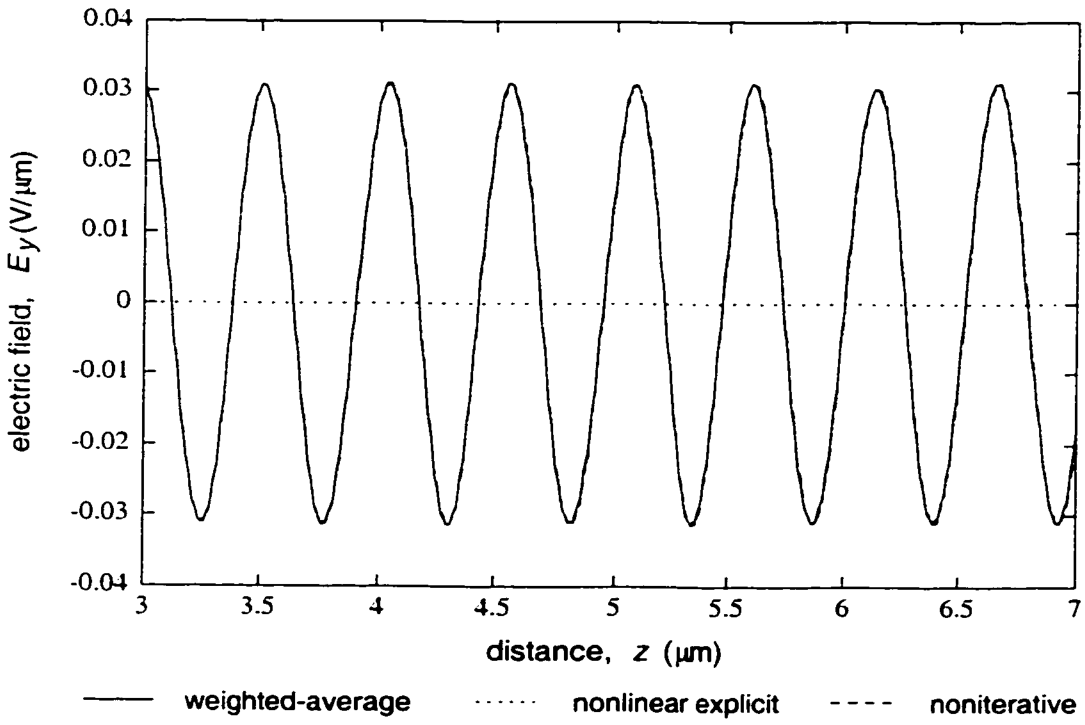

Figure 3.6. Electric field profile along the core centre (z-axis) of the weakly nonlinear slab waveguide under continuous-wave excitation (at T = 59.96fs). Results were obtained using the hybrid FDTD method with the nonlinear explicit scheme, the weighted-average scheme, and the non-iterative scheme.

phase modulation. It is thus concluded that the non-iterative method, while much faster than the other two schemes, is not suitable for simulating propagation in materials with moderate to strong nonlinearities.

The stability of both the nonlinear explicit and weighted-average schemes demonstrated above is achieved at the expense of greater computation effort. Since these nonlinear methods require a Newton-Raphson iteration loop at each time step to solve a nonlinear matrix equation, the overall computation speed is slower than that of the non-iterative method. Therefore the convergence rate of the nonlinear matrix solver has a major impact on the overall computation speed of the hybrid FDTD scheme. To give an indication of the extra computation requirement due to the nonlinear solver, we show in Table 3.1 the l_2-norm of the residue vector at several typical iteration steps for the weighted-average method. It is seen that for the nonlinear slab waveguide, with a convergence tolerance of 10^{-10} on the residue norm, convergence was obtained

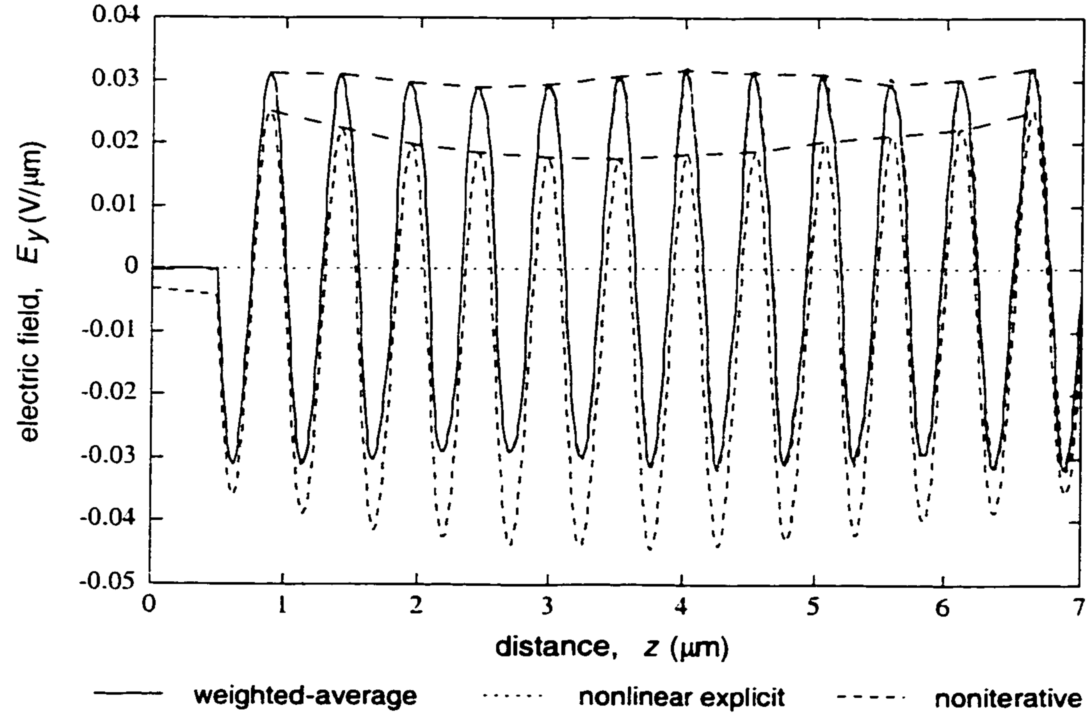

Figure 3.7. Electric field profile along the core centre of the moderately nonlinear slab waveguide under continuous-wave excitation (at T = 59.96fs). Results were obtained using the hybrid FDTD method with the nonlinear explicit scheme, the weighted-average scheme, and the non-iterative scheme.

Time T (fs)	NR iteration 0 Initial residue	NR iteration 1	NR iteration 2	NR iteration 3	NR iteration 4 Final residue
59.7	1.915×10^4	8.646×10^1	3.627×10^{-3}	9.350×10^{-9}	1.119×10^{-11}
59.8	1.918×10^4	8.554×10^1	3.619×10^{-3}	9.287×10^{-9}	1.110×10^{-11}
59.9	1.919×10^4	8.537×10^1	3.607×10^{-3}	9.211×10^{-9}	1.117×10^{-11}
60.0	1.926×10^4	8.605×10^1	3.589×10^{-3}	9.132×10^{-9}	1.106×10^{-11}

Table 3.1. The l_2-norm of the residue vector in the Newton-Raphson (NR) iteration of the weighted-average FDTD method. The convergence tolerance was set at 10^{-10}.

just after about four iterations. In practice, the tolerance is usually set at 10^{-6}, which results in even faster convergence. Thus the extra computation requirement for the Newton-Raphson iteration loop is tolerably small. As an example, the 3μm × 7μm slab waveguide structure in Figure 3.5 required about 44 minutes of CPU time on the Sun Ultra 10 Workstation when simulated using the weighted-average scheme, and 11 minutes when the nonlinear explicit scheme was used. The nonlinear explicit scheme is superior to the weighted-average scheme in terms of computation speed because the nonlinear matrix resulted at each time step has a simple diagonal structure which can be solved with minimum effort.

(b) Gaussian pulse excitation

The self-phase modulation (SPM) effect mentioned in the previous section can be more clearly observed with Gaussian pulse-modulated excitation. The input field in this case is described by the equation

$$E_{inc}(x, z_0, t) = E_0(x)\exp\left[-\left(\frac{t-T_0}{W}\right)^2\right]\sin(\omega t - \beta z_0). \tag{3.3}$$

where T_0 defines the pulse center and $2W$ is the pulse width at $1/e$ amplitude. In the simulation the temporal pulse width was set to about $4T_{opt}$, where T_{opt} is the optical period of the carrier signal. Figure 3.8 shows the field profile along the waveguide center at T = 74.6fs for the moderately nonlinear waveguide ($\chi^{(3)} = 2\times10^{-10}\text{m}^2/\text{V}^2$) as obtained by the weighted-average scheme. The self-phase modulation effect is evident, manifesting itself in the rarefaction of the carrier signal at the front of the pulse and compression at the end, a phenomenon known as frequency chirping. In addition, the back (left) side of the pulse becomes steepened as it propagates along the waveguide. This nonlinear phenomenon can be understood in the context of the dependence of the phase velocity on the field intensity, which causes the peak of the pulse to see a larger refractive index and thus travel more slowly than the front and rear ends. The result is that the spatial pulse shape becomes increasingly skewed to the left as it propagates along the waveguide, as seen in the figure. The frequency spectra of the pulse recorded at z = 1μm and z = 8μm are shown in Figure 3.9, where the effect of spectrum broadening accompanying self-phase modulation can be seen.

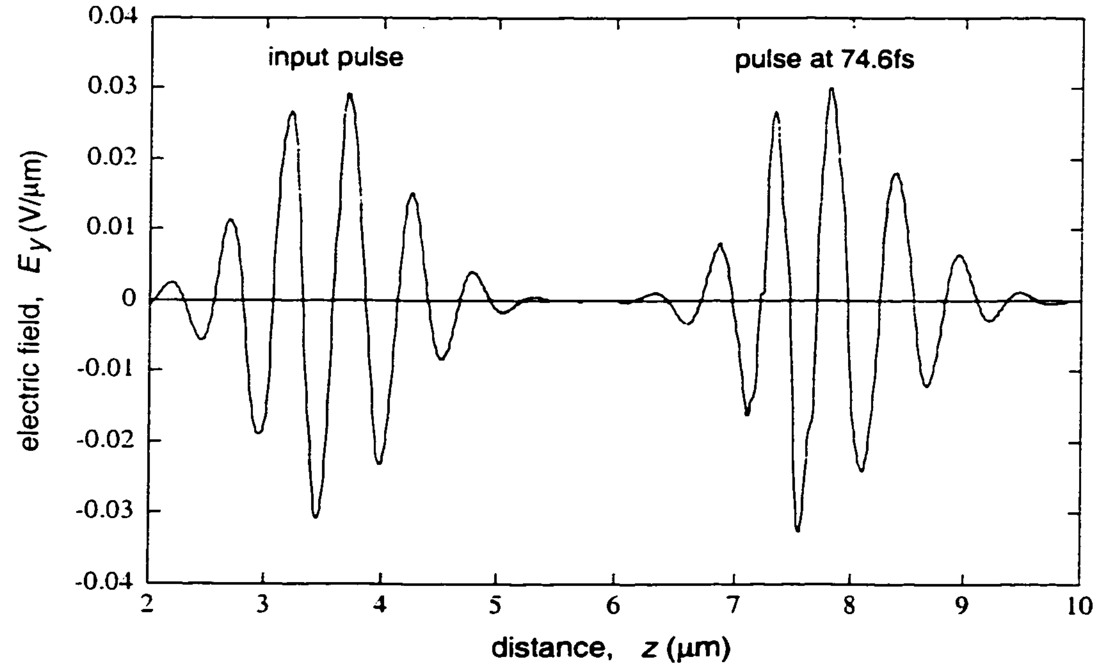

Figure 3.8. Electric field profile along the core centre (z-axis) of the moderately nonlinear slab waveguide under Gaussian pulse-modulated excitation (at T = 74.6fs). The result was obtained using the hybrid FDTD method with weighted-average nonlinear scheme.

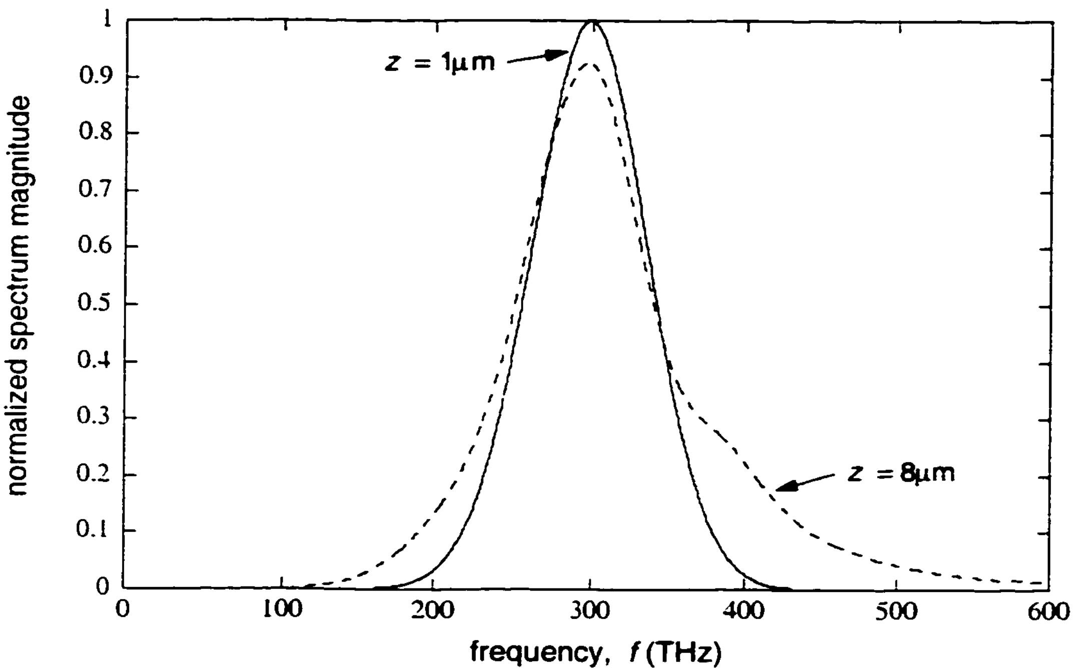

Figure 3.9. Frequency spectra of the Gaussian pulse at z = 1.0μm and z = 8.0μm of the moderately nonlinear slab waveguide. Spectral broadening due to self-phase modulation is observed after the pulse has travelled a distance of 7.0μm.

For pulses whose temporal width W is greater than 10fs, approximate analytical solution of the nonlinear wave equation can be obtained if second- and higher-order effects of waveguide dispersion are neglected [61]. Since the period of the optical carrier frequency, T_{opt}, is in the order of 1fs, the assumption $W >$ 10fs allows us to make use of the slow envelope approximation and express the electric field as

$$E_y(x,z,t) = \mathrm{Re}\left\{E_0 F(x) U(z,t) e^{j(\omega t - \beta_0 z)}\right\}. \qquad (3.4)$$

where $F(x)$ is the transverse modal profile, $U(z,t)$ is the normalized pulse envelope, and β_0 is the propagation constant of the linear waveguide. In the absence of second- and higher-order waveguide dispersion effects (i.e., $\beta_2 = \beta_3 = 0$), it can be shown that the evolution of $U(z,t)$ in a Kerr medium is governed by the equation [61]

$$\frac{\partial U}{\partial Z} + s\frac{\partial}{\partial \tau}\left(|U|^2 U\right) = -j|U|^2 U \, . \qquad (3.5)$$

in which s is a parameter defined as

$$s = \frac{T_{opt}}{\pi W/\sqrt{2}} = \frac{2\sqrt{2}}{\omega W}, \tag{3.6}$$

and τ and Z are normalized time and length scales given by

$$\tau = \frac{t - z/v_g}{W/\sqrt{2}}, \tag{3.7}$$

$$v_g = 1/\beta_1 = \left(\frac{d\beta}{d\omega}\right)^{-1}, \tag{3.8}$$

$$Z = \frac{z}{L_{NL}} = \frac{\omega \chi^{(3)} E_0^2}{2 n_0 c A_{eff}} z, \tag{3.9}$$

$$A_{eff} = \frac{\int_{-\infty}^{\infty} |F(x)|^2 dx}{\int_{-\infty}^{\infty} |F(x)|^4 dx}. \tag{3.10}$$

In the above, v_g is known as the group velocity and A_{eff} is the effective core area of the waveguide. The term involving s in Eq.(3.5) is responsible for self-steepening effects, while the term on the right hand side accounts for self-phase modulation. Equation (3.5) can be solved analytically if we let

$$U(z,\tau) = \sqrt{I(z,\tau)}\, e^{j\phi(z,\tau)}, \tag{3.11}$$

where $I(z,\tau)$ is the normalized intensity profile. For the specific case of a Gaussian pulse input, $I(0,\tau) = e^{-\tau^2}$, the solution for $I = U^2$ can be implicitly expressed as

$$I(Z,\tau) = e^{-(\tau - 3sIZ)^2}. \tag{3.12}$$

Given a propagated distance Z, the value of I at each time τ can be obtained from Eq.(3.12) by an iterative method. In Figure 3.10 we show the analytical result for a pulse envelope with initial width W = 29fs and amplitude E_0 = 0.0311V/μm, after having travelled a distance of 7μm in the

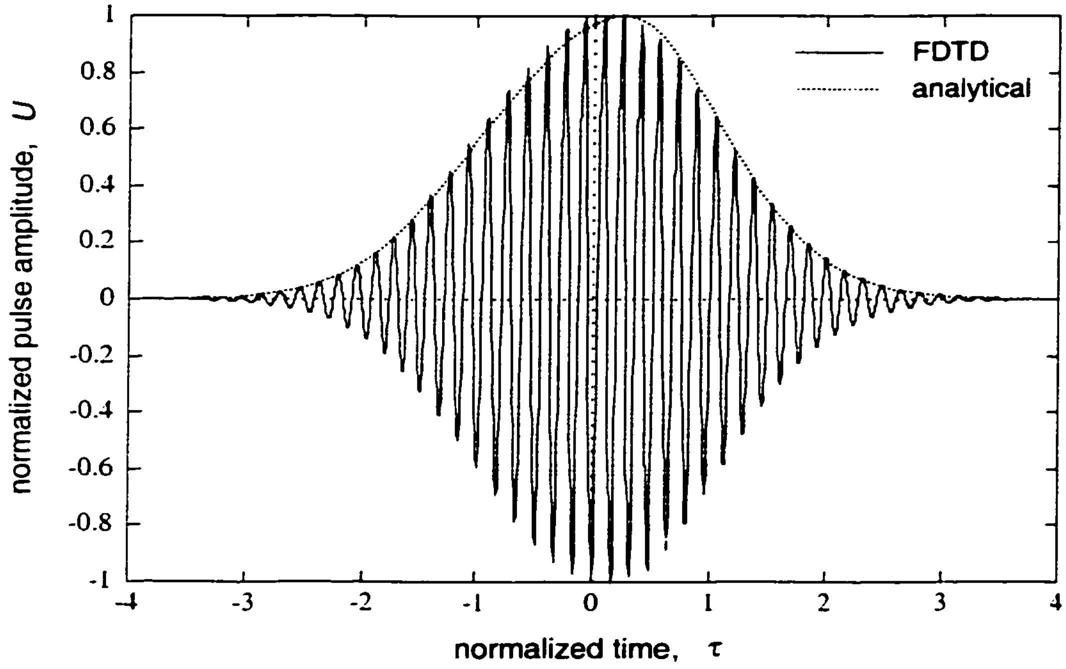

Figure 3.10. Normalized amplitude $U(\tau)$ of a Gaussian pulse after having travelled 7μm in a moderately nonlinear dielectric waveguide, as obtained by analytical solution and FDTD simulation. The pulse has initial width $W = 29$fs and amplitude $E_0 = 0.0311$V/μm.

moderately nonlinear waveguide. The steepening of the pulse's falling edge due to nonlinearity can be seen. Also shown in the plot is the instantaneous field of a carrier signal modulated by the same pulse as obtained by the hybrid FDTD method. It is seen that the envelope profile of the numerical result agrees well with the analytical solution. This agreement, however, was observed to deteriorate as the pulse width was decreased, due to the fact that second- and higher-order dispersive effects became important and could no longer be neglected in the analytical solution.

We have in this section provided numerical verifications to the hybrid implicit-explicit FDTD method for simulating propagation in nonlinear optical media. The results showed that for most nonlinear optical materials, the hybrid FDTD method with the nonlinear explicit scheme produces accurate and stable solutions, and is considerably faster than the weighted-average scheme. However, it was observed that the nonlinear explicit solution tends to suffer from oscillations in cases where the nonlinearity is strong or the applied power is high [67]. In these cases the weighted-average FDTD scheme provides more accurate solutions at the expense of greater computational effort.

The remainder of this chapter will be devoted to studying propagation characteristics in more complicated nonlinear structures that have potential applications in optical communication systems. As mentioned previously, the two structures we are interested in are the nonlinear periodic waveguide and the nonlinear microring resonator. We will assume that the materials are moderately nonlinear so that the simulations can be performed using the nonlinear explicit FDTD method.

3.2 Nonlinear Periodic Waveguides

Periodicity provides a wavelength selection mechanism in optical devices. In periodic waveguides, the structural or index grating serves to assist the coupling between the forward and backward modes whose propagation constant β satisfies the phase-matching condition,

$$2\beta - \frac{2m\pi}{\Lambda} = 0, \qquad (m = 1, 2, 3, \ldots). \tag{3.13}$$

where Λ is the grating period. The result is that reflection is enhanced at wavelengths that approximately satisfy the condition

$$\Lambda = m\lambda_0/2 \tag{3.14}$$

and suppressed at all other wavelengths, thus producing a bandstop filter response. In Eq.(3.14) the integer m is referred to as the grating order. An important feature of gratings of order 2 and higher is that they induce radiation loss, making them more useful as beam-steering elements. For our study of grating filters, we are interested only in first-order gratings which do not suffer from radiative loss. By introducing nonlinearity into the index gratings, we can produce filters whose frequency responses depend on the power of the input signal. We consider two types of periodic waveguides: distributed feedback resonators and distributed Bragg resonators.

3.2.1 Distributed feedback resonators

The simplest periodic waveguide structure is the distributed feedback resonator (DFR), shown in Figure 3.11. The structure consists of a volume index grating which produces a periodic longitudinal index profile. For first-order grating, the period Λ is chosen to be equal to $\lambda_g/2$. The index discontinuities in each period cause reflections that reinforce each other to produce a high reflection coefficient for input wavelengths near λ_g.

Distributed feedback structures with linear index gratings have been extensively studied using the Coupled-Mode Theory (e.g., [64,65]) as well as numerical methods [2]. The reflection spectrum has the shape of the sinc function centered around λ_0, which resembles the response of a bandstop filter. By introducing nonlinearity into the gratings, we can produce a reflection characteristic that is dependent on the power of the input pulse. Specifically, since self-focusing nonlinearities such as Kerr effect cause the guided wavelength in the medium to decrease with increasing power, the phase-matching condition (3.14) will be satisfied for frequencies corresponding to longer free-space wavelengths. Consequently, the reflection spectrum will be shifted toward longer wavelengths as the input power is increased.

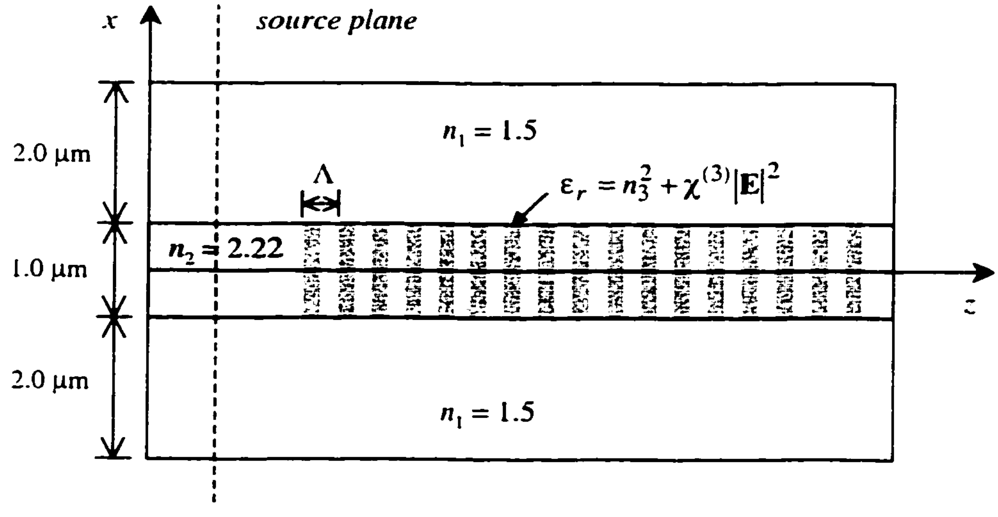

Figure 3.11. Nonlinear distributed feedback resonator with volume index grating. For first-order grating, $\Lambda = \lambda_g/2$. The linear part of the refractive index of the nonlinear regions is $n_3 = 2.30$, and $\chi^{(3)} = 10^{-10}\,\mathrm{m}^2/\mathrm{V}^2$.

To demonstrate this nonlinear shift in the resonance spectrum, we simulated a DFR structure with instantaneous Kerr-type nonlinear grating. As shown in Figure 3.11, the grating consists of alternating linear regions of index n_2 = 2.22 and nonlinear regions having relative permittivity given by $\varepsilon_r = n_3^2 + \chi^{(3)}|\mathbf{E}|^2$, with n_3 = 2.30 and $\chi^{(3)} = 10^{-10}\,\mathrm{m^2/V^2}$. At the free-space wavelength λ_0 = 1.3µm, the non-corrugated waveguide with index contrast 2.22:1.50 supports a TE$_0$ mode with propagation constant β = 10.457rad/µm, which corresponds to a guided wavelength λ_g of 0.60µm. We thus chose the grating period Λ to be $\lambda_g/2$ = 0.30µm, and assumed N = 25 for the number of periods in the grating. The structure was then excited by a Gaussian pulse-modulated signal with centre wavelength λ_0 = 1.3µm.

Figure 3.12 shows the incident pulse carrying 1W/m of power and the reflected pulse in the time domain, as obtained by the hybrid FDTD method with the nonlinear explicit scheme. Similar to the linear case, the amplitude of the reflected pulse was observed to increase with increasing index discontinuities in the grating, and the reflected pulse duration was longer for

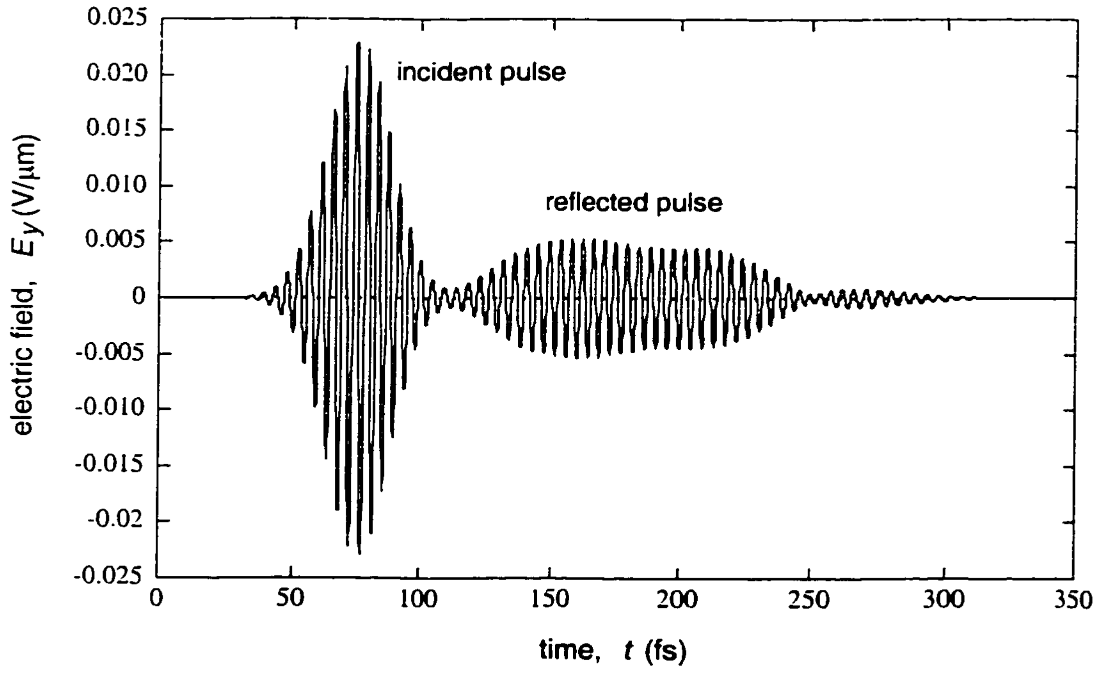

Figure 3.12. Incident and reflected pulses recorded at the core centre of the nonlinear DFR. The power of the input Gaussian pulse is 1W/m and the corresponding pulse amplitude E_0 is 0.023V/µm.

larger *N*. The reflection spectra for three different incident powers, 1W/m, 10W/m and 20W/m, are plotted in Figure 3.13, where it can be seen that the resonance spectrum experiences a larger shift toward longer wavelengths as the input power is increased. For instance, at 20W/m the shift is almost 20nm. Also, the reflectivity is higher for spectra at higher incident powers because the nonlinear Kerr law causes the index discontinuities in the grating to increase with power.

The reflection spectrum of a DFR can be improved for practical use as a notch filter by increasing the number of periods per grating. However, bandstop filters are not as useful as bandpass filters in wavelength division multiplexing (WDM) systems. In the next section we look at another periodic wave-guiding structure which can be used as a channel filter: the distributed Bragg resonator.

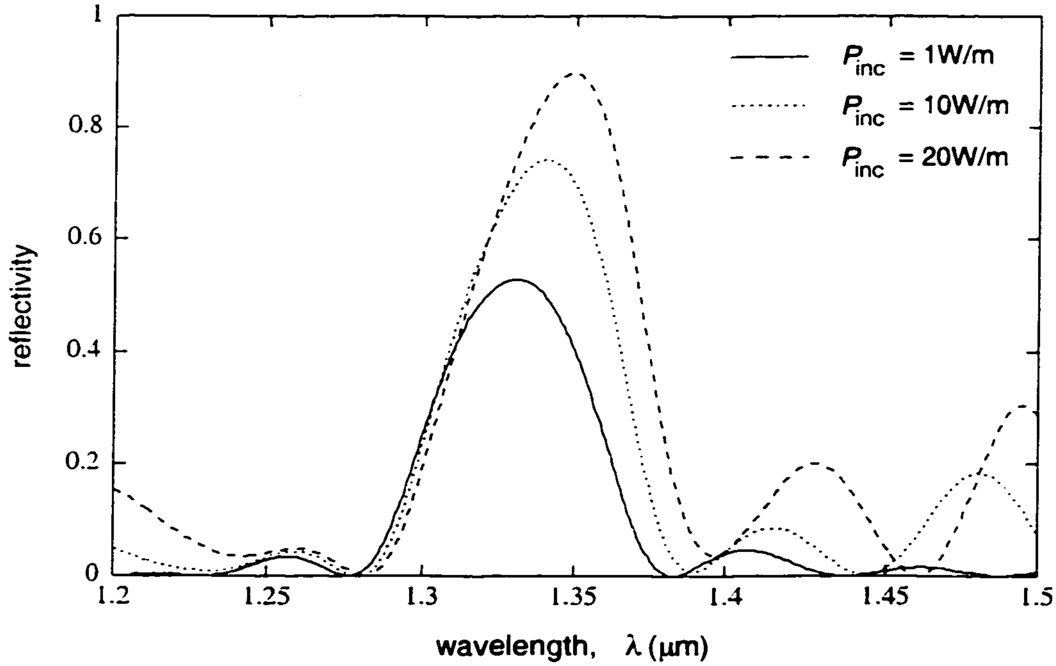

Figure 3.13. Reflection spectra of the nonlinear DFR at 1W/m, 10W/m and 20W/m incident powers. Each spectrum is normalized with respect to the spectrum of the input Gaussian pulse.

3.2.2 Distributed Bragg resonators

Distributed Bragg resonators (DBR) consist of two distributed feedback structures separated by a phase-shift region, as shown in Figure 3.14. The length l of the phase-shift region is chosen to satisfy Bragg's condition,

$$l = \frac{(2n+1)\lambda_g}{4}, \qquad (n = 0, 1, 2, \ldots), \tag{3.15}$$

so that the phase-shift region can be viewed as providing impedance matching at the guided wavelength λ_g. As a result, wavelengths that satisfy Bragg's condition are transmitted with little reflection. The reflection spectrum of a DBR thus has a null at the centre wavelength λ_g and large reflection lobes on both sides, making the device suitable for use as a bandpass filter in optical communication systems. By introducing nonlinearity into the gratings, the transmission characteristic of the DBR filter can be made to depend on the power of the input signal in the same way as with the nonlinear DFR structure. We will first investigate the frequency response of a simple quarter-wave-shifted Bragg resonator, then modify the structure to obtain more practical filter response shapes.

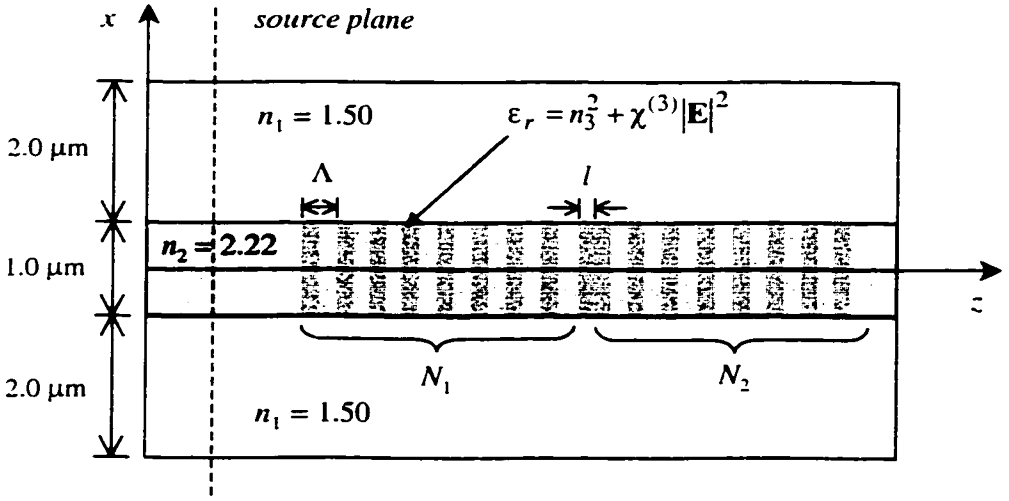

Figure 3.14. Nonlinear distributed Bragg resonator as a bandpass filter. For first-order grating, $\Lambda = \lambda_g/2$. The linear part of the refractive index of the nonlinear regions is $n_3 = 2.30$, and $\chi^{(3)} = 10^{-10}\mathrm{m}^2/\mathrm{V}^2$.

(a) ***Quarter-wave-shifted Bragg resonator***

In a quarter-wave-shifted DBR, the length l of the phase-shift region satisfies Bragg's condition (3.15) with $n = 0$, so that $l = \lambda_g/4$. At the free-space wavelength $\lambda_0 = 1.3\mu m$, the guided wavelength of the TE_0 mode is $0.60\mu m$, so for first-order gratings ($m = 1$), we have $\Lambda = \lambda_g/2 = 0.30\mu m$ and $l = 0.15\mu m$. The number of periods per grating was set to $N_1 = N_2 = 25$. Both the grating and phase-shift region were given Kerr-type nonlinearity with $\chi^{(3)} = 10^{-10} m^2/V^2$. A 1W/m Gaussian pulse was applied to the structure and the reflected pulse was recorded. The time-domain signal is shown in Figure 3.15, in which it is seen that the reflected signal actually consists of two large consecutive pulses produced by reflections from the two gratings. Figure 3.16 shows the reflected spectra normalized by the incident spectrum at three different input power levels, 1W/m, 10W/m and 20W/m. Two effects due to the nonlinear grating are observed. Firstly, as the incident power is increased, Kerr nonlinearity causes the periodic steps in the refractive index to become effectively higher, resulting in stronger reflections for wavelengths in the stopbands. At 10W/m and 20W/m incident powers, the reflectivities of the two side lobes are actually greater than unity because spectrum broadening associated with SPM causes the signal components at these wavelengths to gain in magnitude over the incident spectrum. The second observed effect is that Kerr-type nonlinearity causes the reflection spectra to shift towards longer wavelengths, in a similar manner to that observed in the nonlinear DFR structure. Figure 3.16 shows that the spectrum at 20W/m incident power is shifted by nearly 10nm toward longer wavelengths compared to the spectrum at 1W/m.

Next we investigated the effect of the phase-shift region on the reflection spectrum. It is expected that a phase-shift region composed of nonlinear material will further enhance the shift in the reflection spectrum because the impedance of the quarter-wave section will also depend on the power level. Moreover, the length l of the phase-shift region will also modify the reflection spectrum via self-phase modulation. Figure 3.17 compares the reflection spectrum of a DBR filter having a nonlinear $5\lambda_g/4$-shift region with one in which the phase-shift region is linear. The gratings in both structures were of the same nonlinear material. The power of the incident signal was 10W/m. As expected, the DBR filter with nonlinear phase-shift region shows a slightly larger spectral shift than the filter with linear phase-shift region. In Figure 3.18, the reflection spectra of three DBR filters with different nonlinear phase-shift lengths, $l = \lambda_g/4$,

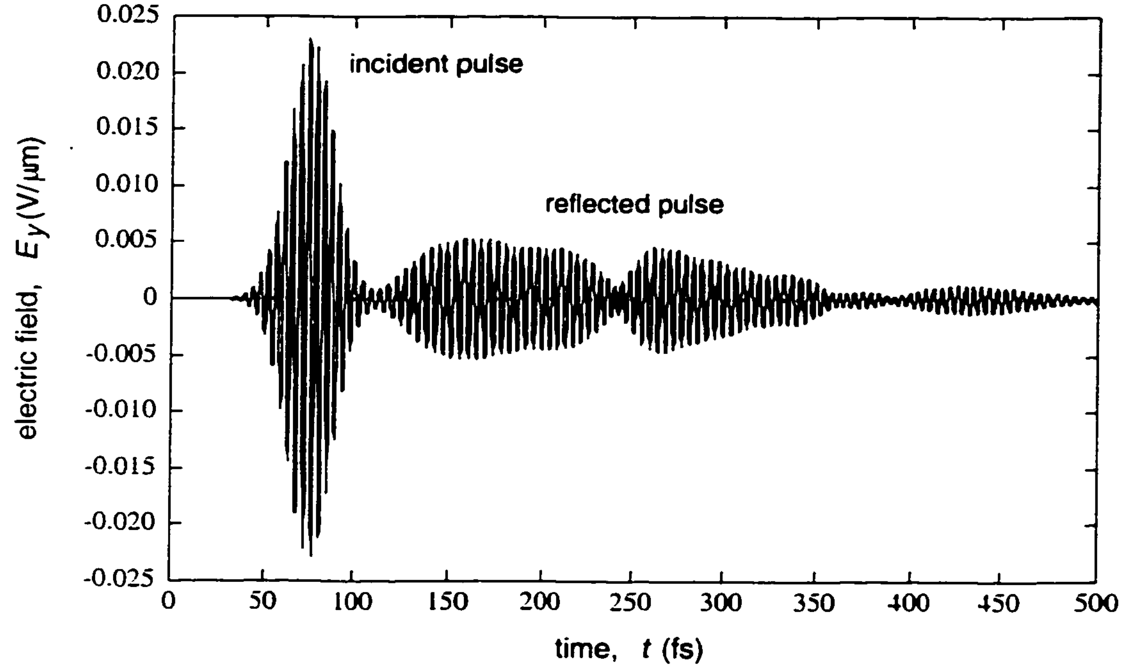

Figure 3.15. Incident and reflected pulses recorded at the core centre of the nonlinear DBR. The power of the input Gaussian pulse is 1W/m.

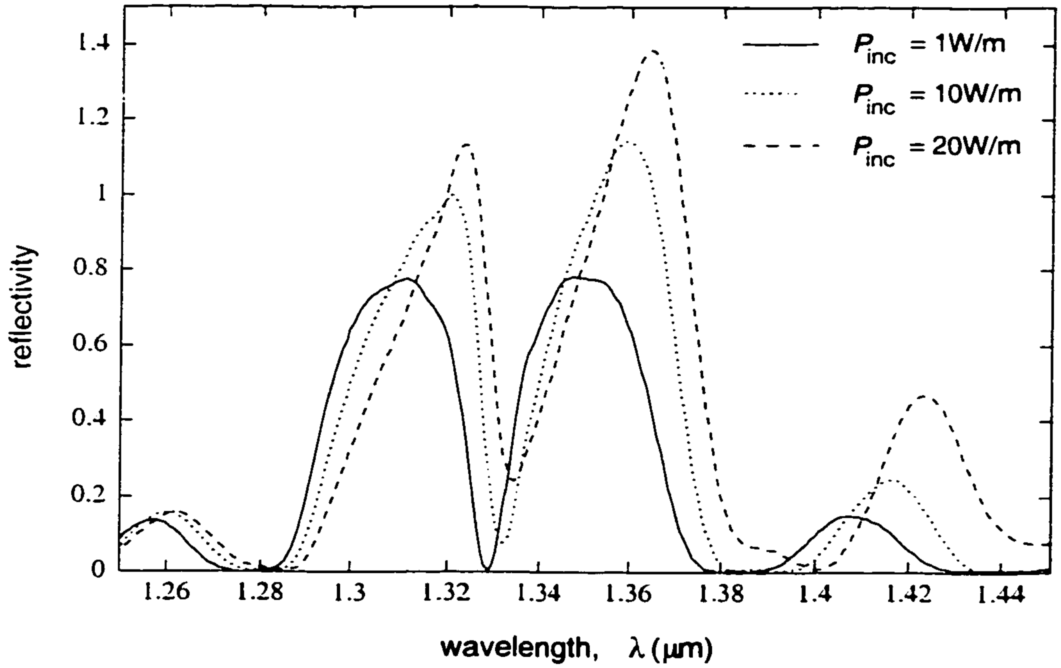

Figure 3.16. Reflection spectra of the nonlinear DBR at 1W/m, 10W/m and 20W/m incident powers. Each spectrum is normalized with respect to the spectrum of the input Gaussian pulse.

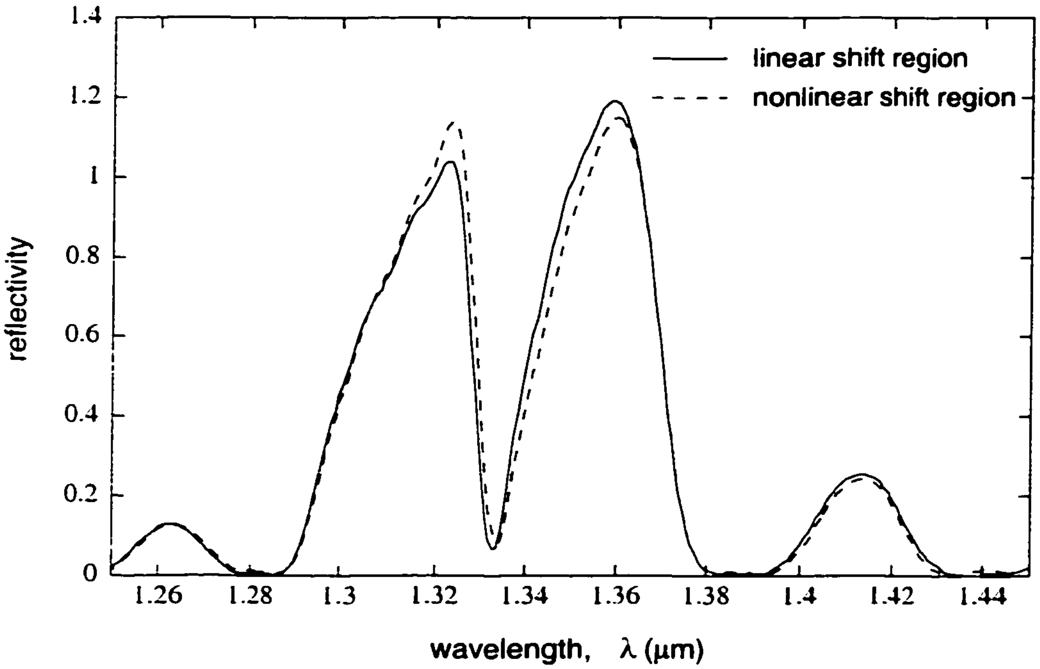

Figure 3.17. Reflection spectra of DBR filters with linear and nonlinear $5\lambda_g/4$-shift regions. The gratings are nonlinear, having 25 periods to each grating. The power of the input Gaussian pulse is 10W/m. Each spectrum is normalized with respect to the incident spectrum.

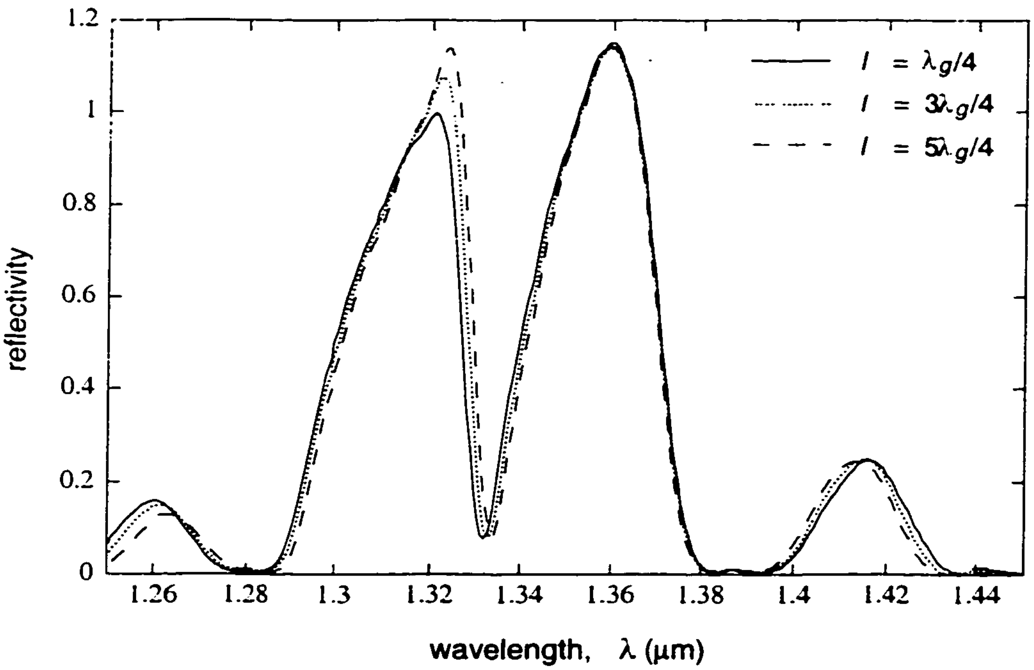

Figure 3.18. Reflection spectra of nonlinear DBR filters with nonlinear phase-shift lengths $l = \lambda_g/4$, $3\lambda_g/4$, and $5\lambda_g/4$. The gratings are nonlinear, having 25 periods to each grating. The power of the input Gaussian pulse is 10W/m. Each spectrum is normalized with respect to the incident spectrum.

$3\lambda_g/4$, and $5\lambda_g/4$, are shown. The spectrum corresponding to $l = 5\lambda_g/4$ is observed to experience the largest shift. However, these spectral shifts are negligibly small, indicating that the variation in the phase-shift length l has little effect on the reflection characteristic. The reason for this observation is that the phase-shift lengths are too short to cause an appreciable change in the spectrum of the pulse as it traverses the phase-shift region. From the results for the nonlinear slab waveguide in Section 3.1.2, we saw that even for moderately strong nonlinearities, distances over 10 wavelengths were required to produce any visible nonlinear effect.

(b) Compound phase-shifted Bragg resonator

The responses of the quarter-wave-shifted DBR filter in Figure 3.16 are not suitable for practical use because of the shallow filter slopes and poor out-of-band rejection. By using multiple gratings and phase-shift regions, Zengerle and Leminger demonstrated that the DBR filter can be synthesized to have better transmission characteristics [66]. Figure 3.19 shows an example of such a compound phase-shifted Bragg resonator with four gratings and three quarter-wave-shifted regions, all having Kerr-type nonlinearity. The grating parameters are $\Lambda = 0.30\mu$m,

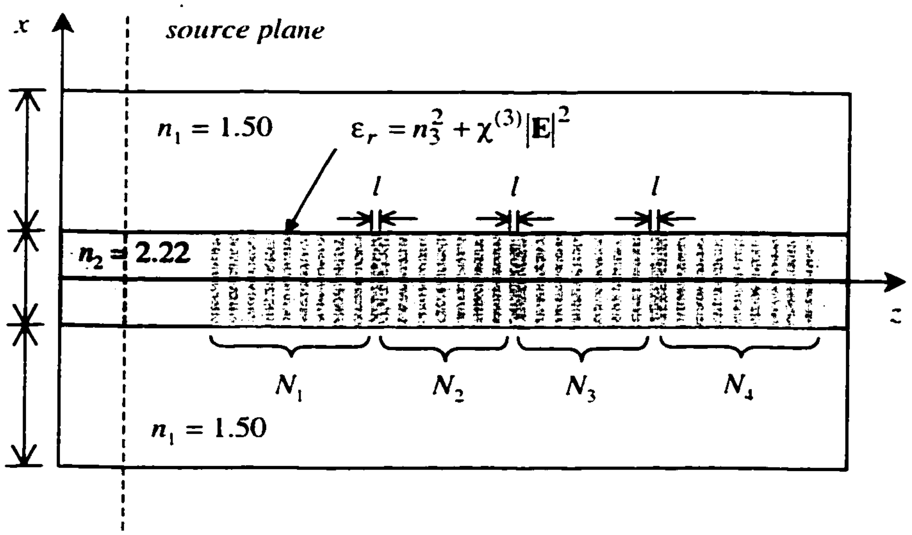

Figure 3.19. Nonlinear compound phase-shifted Bragg resonator with 4 gratings and 3 quarter-wave-shifted regions. The number of periods per grating are $N_1 = N_4 = 15$, $N_2 = N_3 = 35$. The linear part of the refractive index of the nonlinear regions is $n_3 = 2.30$, and $\chi^{(3)} = 10^{-10}\,\mathrm{m}^2/\mathrm{V}^2$.

$l = 0.15\mu m$, $N_1 = N_4 = 15$, $N_2 = N_3 = 35$, $n_3 = 2.30$ and $\chi^{(3)} = 10^{-10}m^2/V^2$. In Figure 3.20 we show the time-domain incident and reflected signals at 1W/m input power. The reflected signal is seen to consist of a train of pulses due to reflections from the four gratings. Figure 3.21 compares the transmission spectrum of the compound phase-shifted DBR filter to that of a simple DBR. The compound DBR is seen to have a more box-like filter response, steeper slopes, better out-of-band rejection, and wider stopbands than the simple DBR. For our design, the 3dB-bandwidth of the filter is 17nm, with 20nm stopbands on both sides. Compound DBRs afford greater design flexibility than simple DBR structures because their transmission characteristics can be controlled by varying the number of phase-shift regions and the number of periods per grating. In general, the more phase-shift regions used, the more box-like the shape of the filter response becomes. The transmission loss and out-of-band rejection can be improved by increasing the number of periods per grating. And finally, the relative widths of the passband and stopband can be controlled by varying the ratio of the number of periods in the inner gratings to the number of periods in the outer gratings (e.g., N_2/N_1 and N_3/N_4).

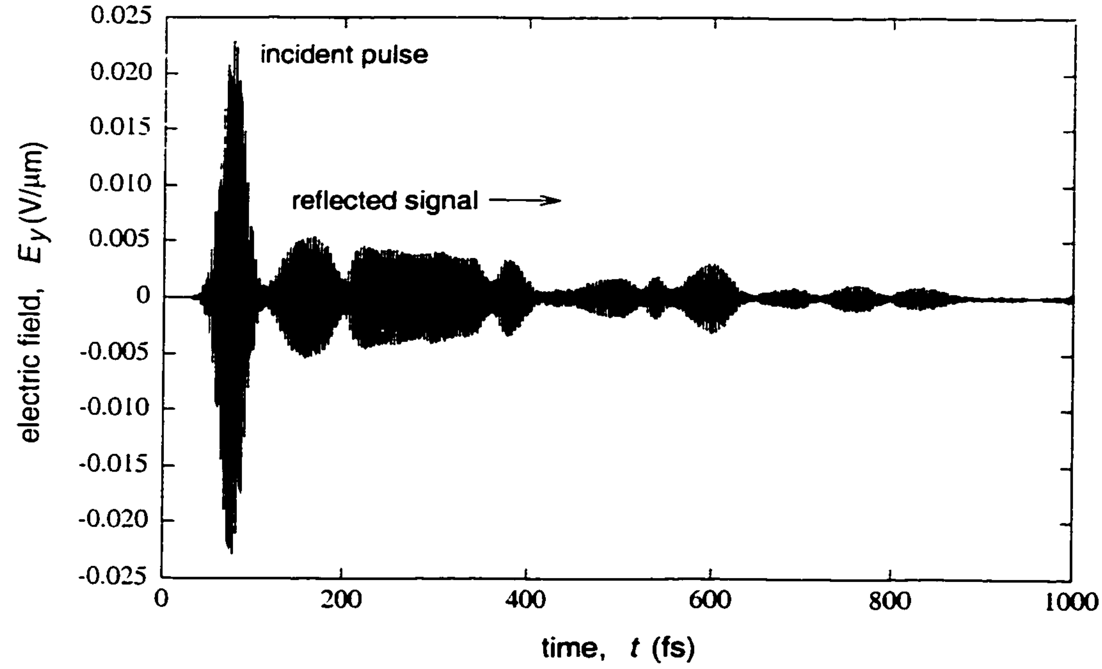

Figure 3.20. Incident and reflected pulses recorded at the core centre of the nonlinear compound phase-shifted DBR filter. The power of the input Gaussian pulse is 1W/m.

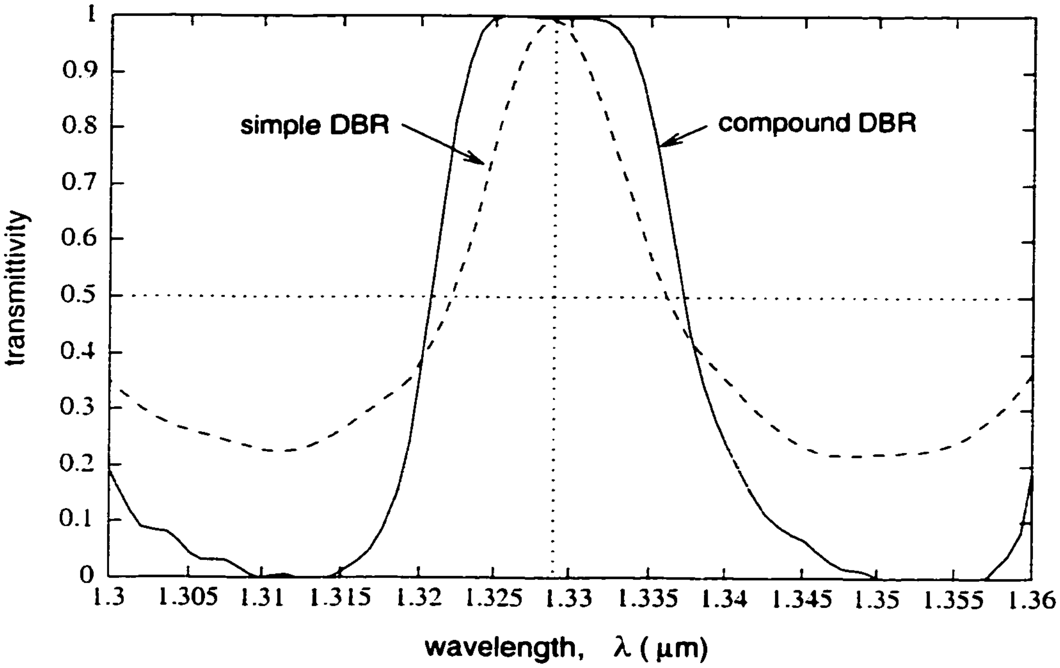

Figure 3.21. Filter responses of the compound phase-shifted DBR and the simple DBR filter.

The reflection spectra of the nonlinear compound DBR filter at two input powers, 1W/m and 10W/m, are shown in Figure 3.22. Nonlinearity causes the passband of the filter with 10W/m input power to be shifted by about 8nm with respect to the passband at 1W/m. This means that a 1W/m signal at the centre wavelength 1.327μm will pass through the filter with little loss, but a 10W/m signal at the same wavelength will experience very strong reflection. The ability to discriminate both the wavelength and power of nonlinear DBR filters make them potentially useful as wavelength switching elements in WDM systems or as optical limiters.

The practicality of the nonlinear DBR filter as a switching element is determined by its sensitivity with respect to the applied power. In Figure 3.23 we plotted the percentage change in the resonance wavelength of a nonlinear grating with 25 periods as a function of the input power. The plot shows that the resonance wavelength increases linearly with respect to the power. The rate of change is 0.072% per W/m, which translates to 0.95nm per W/m of the input signal power. Considering that each channel in current commercial WDM systems occupies about

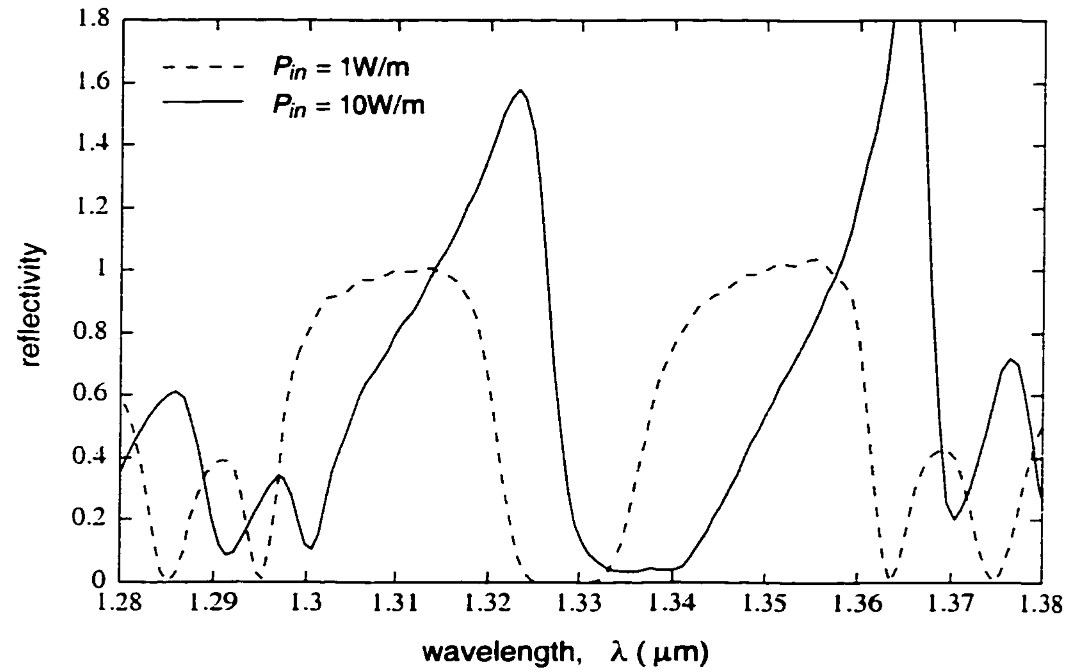

Figure 3.22. Reflection spectra of the nonlinear compound phase-shifted DBR filter at 1W/m and 10W/m incident powers. The passband at 10W/m input power is shifted by about 8nm with respect to the passband at 1W/m.

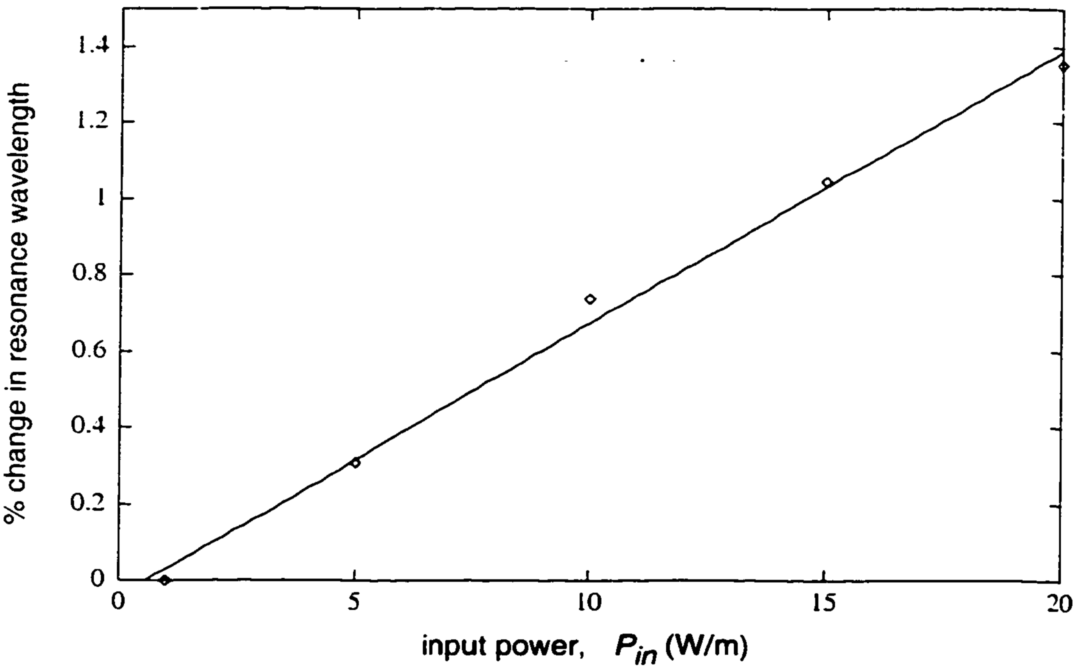

Figure 3.23. Percentage change of the resonance wavelength of a nonlinear DFR filter as a function of the input power. The number of periods per grating is 25. The solid line represents the best fit. The power sensitivity of the resonance wavelength is 0.072% per W/m, or 0.95nm per W/m.

1nm, the power required to switch a channel is thus less than 2W/m. Note from Figure 3.22, however, that the filter shape becomes distorted at high powers so that there is a practical limit on the maximum power level that can be applied to the nonlinear DBR.

3.3 Nonlinear Microring Resonators

Optical ring resonators are commonly used for wavelength filtering, switching, multiplexing and demultiplexing [69–71]. Recent fabrication advances have made it possible to realize high index contrast microrings with strong mode confinement and negligible bending loss, leading to resonators having theoretical quality factors Q in the order of 10^4 [70]. Since the ratio of the input field amplitude to the field amplitude inside the ring is inversely proportional to the coupling coefficient between the input/output (I/O) waveguides and the ring, the field stored in the ring of a high-Q resonator can be one to two orders of magnitude higher than the input field. It is obvious that with such an intense field circulating in the ring, a slight nonlinearity in the material can induce large nonlinear effects, making the resonator ideal for nonlinear mixing processes. In particular, we are interested in the degenerate case of four-wave mixing in which a material having third-order optical nonlinearity illuminated with two waves at frequencies ω_1 and ω_2 radiates a third wave at frequency $2\omega_1 - \omega_2$. In this section, we present the design and FDTD analysis of a nonlinear microring resonator for use as a frequency mixing device.

Consider the standard single-ring resonator evanescently coupled to two straight waveguides serving as input and output buses, as shown in Figure 3.24. The core index of the straight waveguides is n_1, which is assumed to be linear, while the ring waveguide has third-order nonlinearity characterized by susceptibility coefficient $\chi^{(3)}$, so that its relative permittivity is given by the usual expression $\varepsilon_r = n_1^2 + \chi^{(3)}|\mathbf{E}|^2$. A pump beam at frequency ω_1 and an input signal at frequency ω_2 are coupled into the ring via port P_1 of the input waveguide. In order for the energies of the pump beam and input signal to be amplified and sustained in the ring, ω_1 and ω_2 must be resonant frequencies of the ring:

$$\omega_1 = m_1 \frac{c}{n_{eff} R}$$

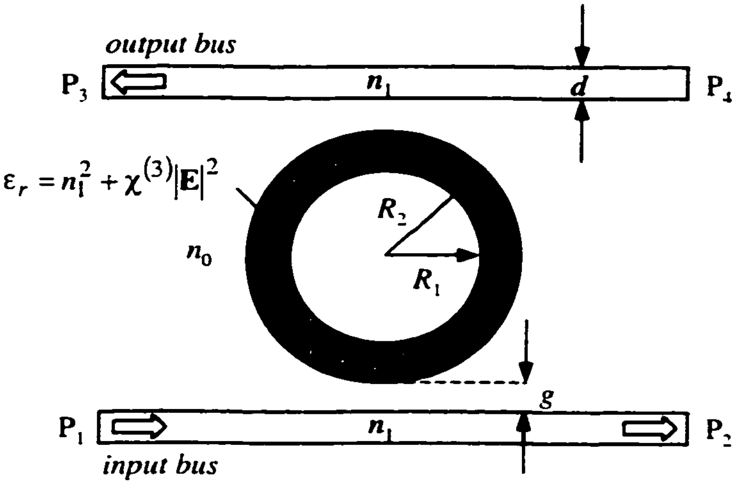

Figure 3.24. Nonlinear microring resonator. The input and output straight waveguides are linear, while the ring waveguide is made of a material with third-order nonlinearity.

and $\omega_2 = m_2 \dfrac{c}{n_{eff} R}$,

where m_1 and m_2 are integer resonance mode numbers, and n_{eff} and R are the effective core index and radius, respectively, of the ring waveguide. Third-order mixing generates a new wave at $\omega_3 = 2\omega_1 - \omega_2$, which is also at resonance since

$$\omega_3 = 2\omega_1 - \omega_2 \approx (2m_1 - m_2)\frac{c}{n_{eff} R}. \tag{3.16}$$

In the above we have assumed that the frequencies ω_1, ω_2 and ω_3 are sufficiently close to each other so that the effect of waveguide dispersion is small.

The resonant frequencies and the spacing between them (usually referred to as the free-spectral range) are controlled by choosing a suitable radius, width, and index contrast for the ring. However, since the index contrast is usually fixed by the process technology, and the ring width d should be chosen small in order to obtain a high confinement factor in the ring, the only flexible parameter is the ring radius. In our design, with $n_0 = 1.00$, $n_1 = 3.00$, and $d = 0.2\mu m$, we set $R_1 = 0.9\mu m$ and $R_2 = 1.1\mu m$, which results in the resonance spectrum shown in Figure 3.25. In using the resonator as a mixer, the pump beam was fixed at resonance mode $m_1 = 12$ ($\lambda_1 = 1.36\mu m$), and the input signal was set at another resonance, for example, at mode $m_2 = 14$ ($\lambda_2 = 1.20\mu m$). The result of third-order mixing will then occur at $\lambda_3 = 1.58\mu m$, which corresponds to the resonance mode $m_3 = 10$.

In order to achieve high conversion efficiency in the mixer, we require the microring resonator to have a high quality factor, since the conversion efficiency is proportional to the pump power in the active region [58], which in our case is the ring. It can be shown that the quality factor Q of a ring resonator depends on the effective radius R and the coupling coefficient κ between the ring and the I/O waveguides via [70]

$$Q \approx \frac{2\pi^2 R n_{eff}}{\lambda_0 \kappa^2}. \tag{3.17}$$

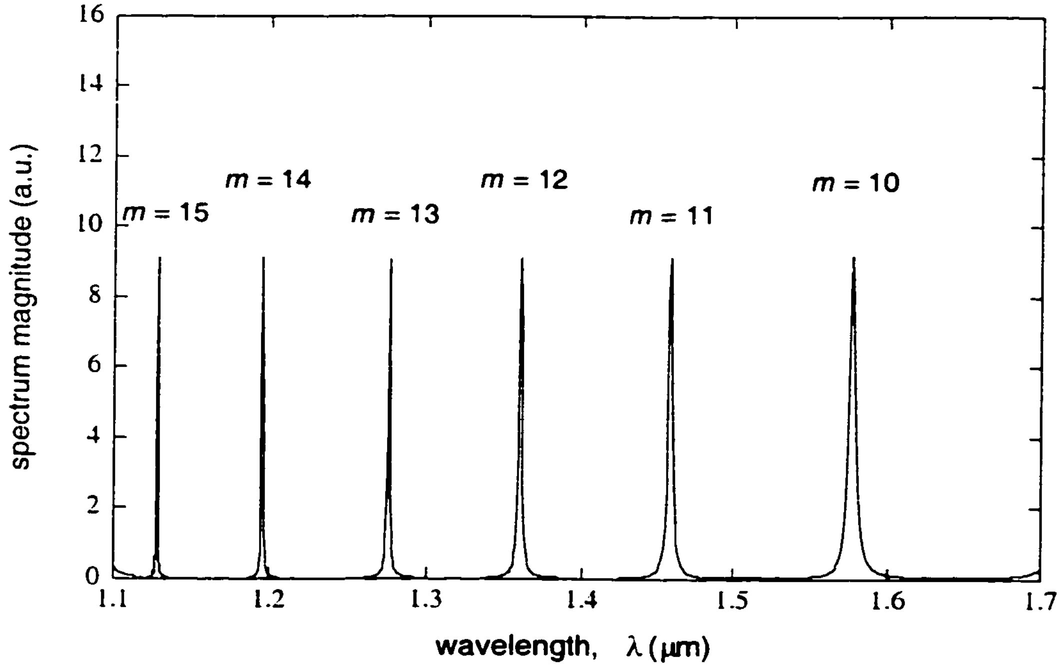

Figure 3.25. Resonance spectrum of the linear microring with radii $R_1 = 0.9\mu m$, $R_2 = 1.1\mu m$. Other parameters are $n_0 = 1.00$, $n_1 = 3.00$, and $d = g = 0.2\mu m$.

Thus with R fixed by the choice of the resonant frequencies, we can maximize Q by minimizing κ. The coupling coefficient, which depends on the gap g and the frequency, is usually set to around 5% for high quality-factor rings. Figure 3.26 shows the variation of κ with wavelength for a fixed coupling gap g = 0.2μm. The plot was obtained by simulating the coupling of a Gaussian pulse between a straight waveguide and a semi-circular waveguide, as depicted in the

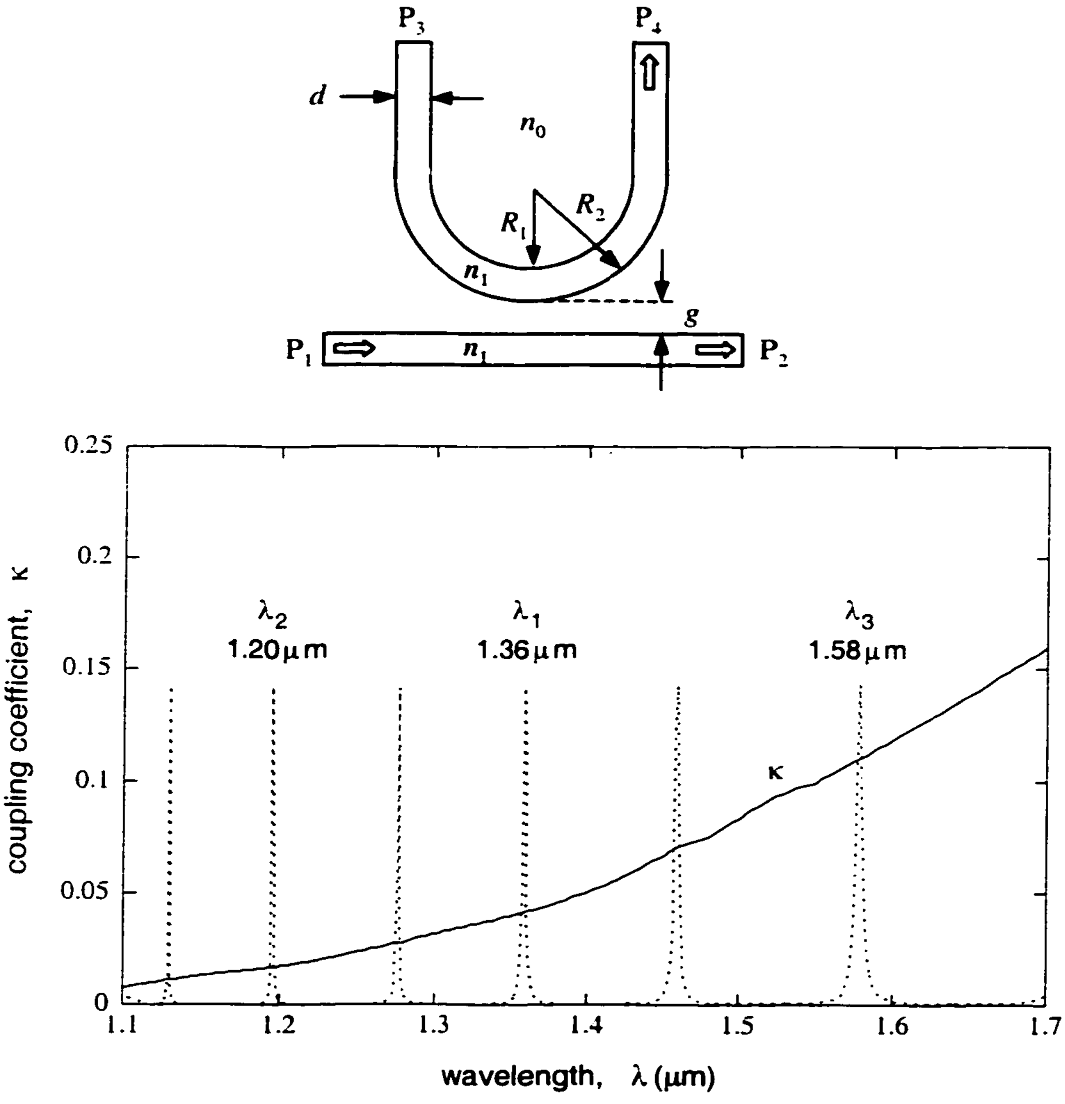

Figure 3.26. Coupling coefficient between a straight waveguide and a semi-circular waveguide, as shown in the diagram. The parameters of the structure are: n_0 = 1.00, n_1 = 3.00, d = g = 0.2μm, R_1 = 0.9μm and R_2 = 1.1μm.

figure. Since the energy coupled into the curved waveguide exits directly at port P_4, the coupling coefficient is simply the square of the ratio of the output signal amplitude at P_4 to the input signal amplitude at P_1. The plot in Figure 3.26 shows that the coupling coefficient is around 1.7% at the 1.20μm resonance and 4.2% at the 1.36μm resonance. Both of these values are suitably low for achieving high quality factors at these wavelengths. Simulations indicated that the loaded Q of the resonator was on the order of 1000.

Third-order nonlinearity causes the effective index n_{eff} of a nonlinear waveguide to increase with increasing input power. In fact, using first-order perturbation analysis, it can be shown that n_{eff} varies approximately as the square of the signal amplitude, E_0 [61]:

$$n_{eff} = n_{e,0} + \frac{2\chi^{(3)}}{n_0 A_{eff}} E_0^2. \tag{3.18}$$

where $n_{e,0}$ is the effective index of the linear waveguide, and A_{eff} is the effective core area given by Eq.(3.10). Consequently, the resonance wavelengths λ_m of a nonlinear ring will also increase as E_0^2 since they are directly proportional to n_{eff}:

$$\lambda_m = \frac{2\pi n_{eff} R}{m}. \tag{3.19}$$

This power dependence of λ_m is simply another manifestation of the self-phase modulation effect and is numerically illustrated in Figure 3.27. The plot shows the resonance spectra of a nonlinear microring at two different applied powers, 1W/m and 50W/m. The physical parameters of the resonator are $n_0 = 1.0$, $n_1 = 3.0$, $\chi^{(3)} = 10^{-10}\mathrm{m}^2/\mathrm{V}^2$, $d = 0.2\mu\mathrm{m}$, $g = 0.2\mu\mathrm{m}$, $R_1 = 0.9\mu\mathrm{m}$ and $R_2 = 1.1\mu\mathrm{m}$. It is seen that the resonance peaks at the higher applied power are indeed slightly shifted towards longer wavelengths. The spectral shift observed in the nonlinear ring is completely analogous to the shift observed in the frequency response of the nonlinear DFR and DBR filters in Section 3.2. The effect, however, is especially amplified in a microring mixer, where the pump beam, whose amplitude is usually much larger than the signal beams, provides a constant bias intensity level in the ring which can cause the effective indexes seen by the signals to be very high. Figure 3.28 shows the shifts in the resonance wavelengths of the modes $m = 14$ and $m = 15$ as a function of the power of the pump beam, which was fixed at resonance mode $m = 12$ (λ

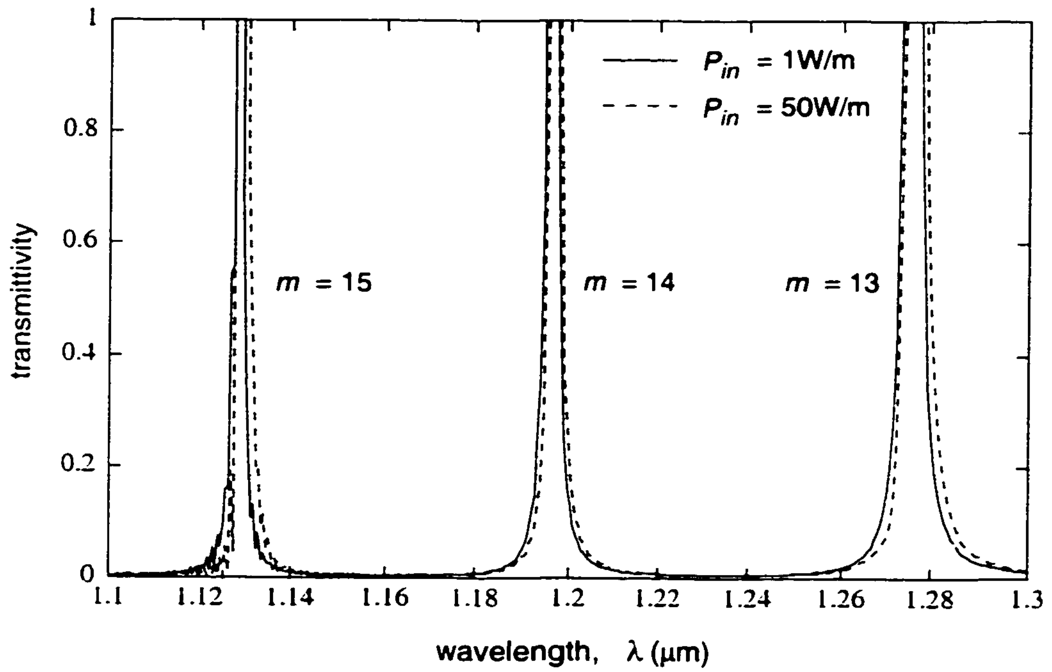

Figure 3.27. Resonance spectra of the nonlinear microring for input pulses with two different peak powers, 1W/m and 50W/m. The nonlinear coefficient $\chi^{(3)}$ is $10^{-10}\mathrm{m}^2/\mathrm{V}^2$. The spectra are normalized with respect to the incident spectra.

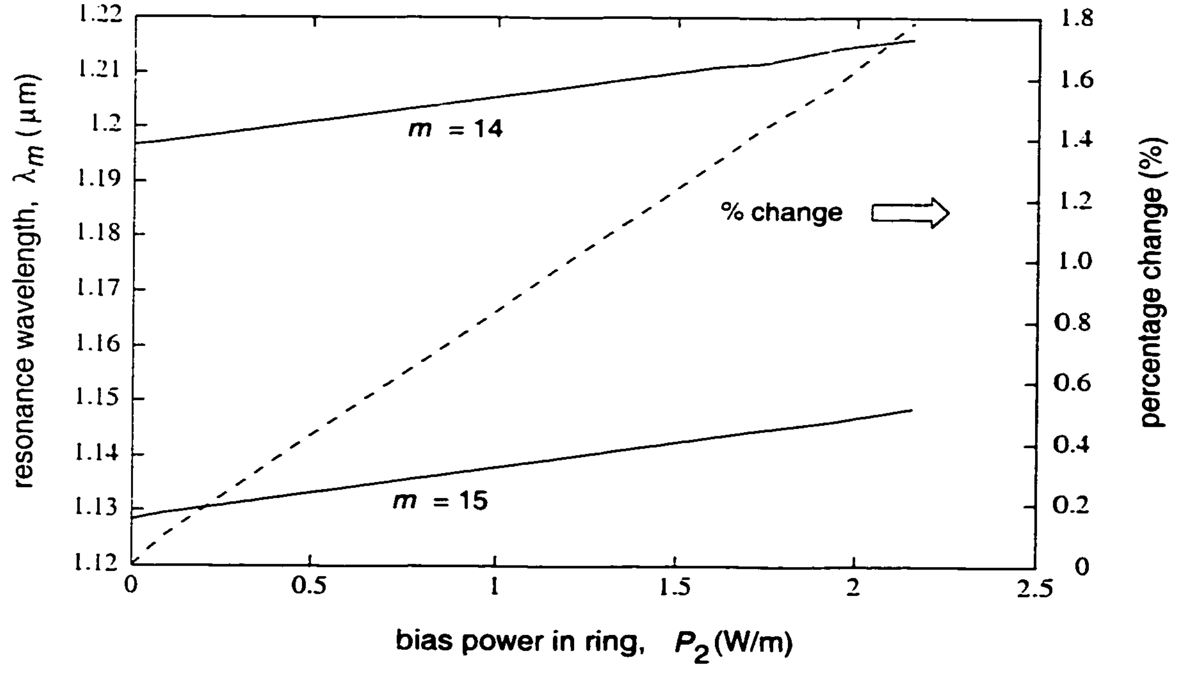

Figure 3.28. Variation of the resonance wavelength with respect to the pump beam power for resonance modes $m = 14$ and $m = 15$. The pump beam is fixed at resonance mode $m = 12$.

= 1.368μm). It is seen that for both modes, the resonance wavelength increases linearly with the pump power, i.e., quadratically with the field amplitude as expected, and that the percentage change is almost identical for the two different resonance modes.

In designing the nonlinear microring mixer, the detuning in the resonance due to self-phase modulation must be taken into account to ensure that the pump beam and signal beam are sustained in the ring by resonance. Following the result in Figure 3.28, we fixed the pump beam at wavelength λ_1 = 1.368μm and field amplitude E_0 = 0.04V/μm (P_1 = 1W/m). The input signal was chosen at λ_2 = 1.210μm, with amplitude equal to one-tenth that of the pump beam, or 0.004V/μm. Figure 3.29 shows the input amplitude spectrum (at port P_1), consisting of two tones at λ_1 and λ_2, normalized with respect to the pump amplitude. Simulation of the resonator was then performed until steady state was reached. Figure 3.30 shows the power spectrum of the signal recorded at point X inside the ring (refer to Figure 3.24), normalized by the input pump power. Note that the pump power inside the nonlinear ring is greater than the input pump power

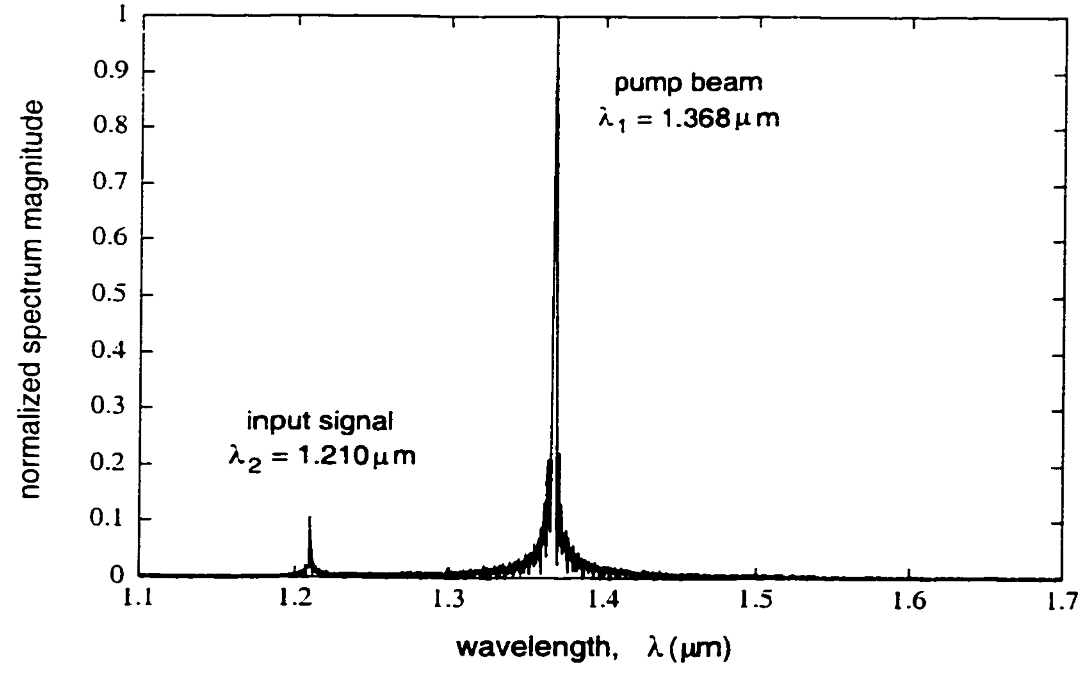

Figure 3.29. Amplitude spectrum at the input port, P_1, of the microring mixer, consisting of the pump beam λ_1 and the input wave λ_2. The spectrum is normalized with respect to the amplitude of the pump beam.

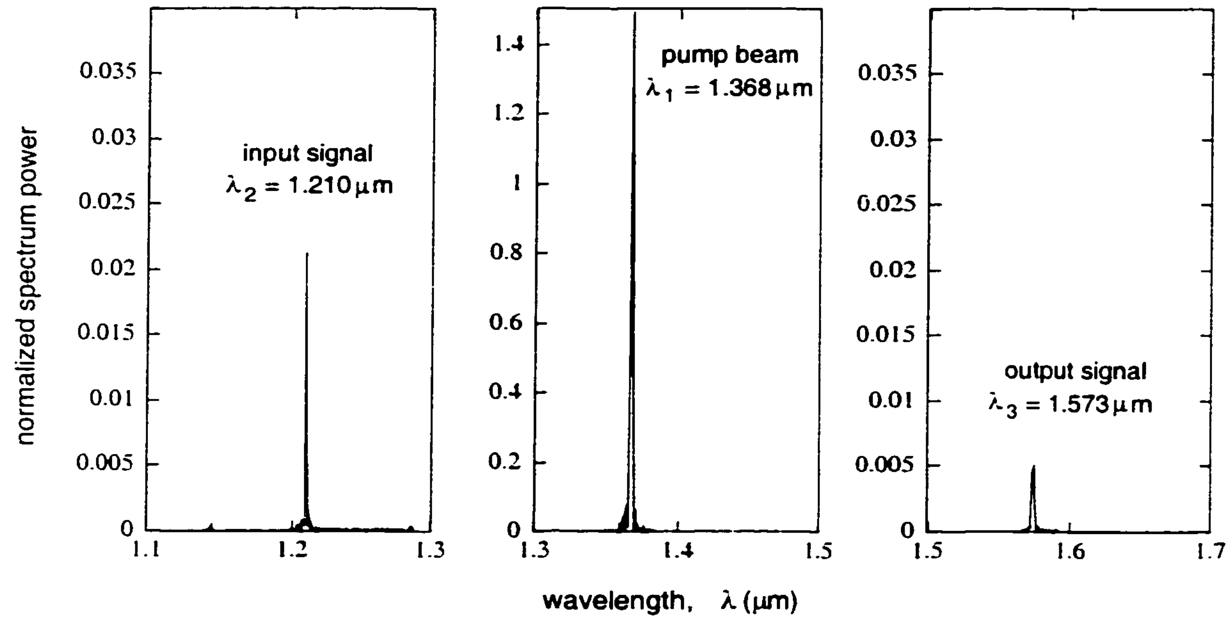

Figure 3.30. Power spectrum recorded at point X inside the nonlinear ring, consisting of the pump beam λ_1, the input wave λ_2, and the output (idler) wave at λ_3. The spectrum is normalized with respect to the power of the input pump beam.

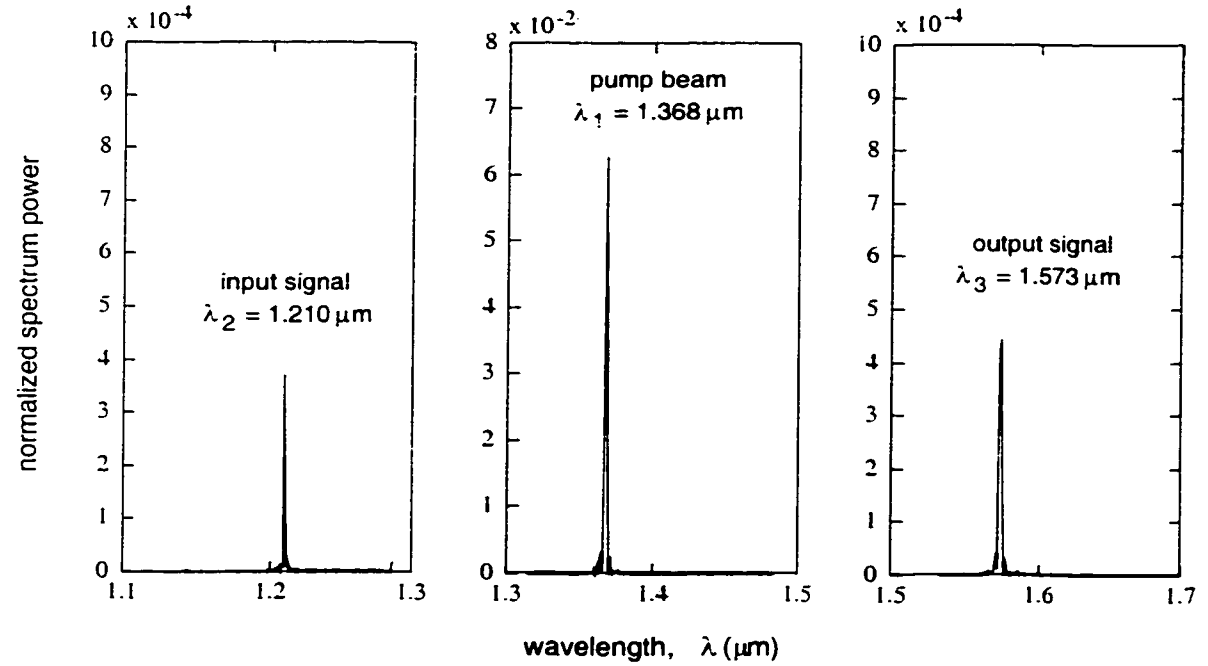

Figure 3.31. Power spectrum at output port, P_3, of the microring mixer, consisting of all three tones λ_1, λ_2 and λ_3. The spectrum is normalized with respect to the power of the input pump beam.

because resonance causes the energy to be built up in the ring. Also observed in the plot is the appearance of the idler wave at λ_3 = 1.573μm which is generated by the third-order mixing process. Figure 3.31 gives the power spectrum of the signal at the output port P_3, also normalized by the input pump power. All three tones at λ_1, λ_2 and λ_3 are observed at the output. Note that the signal λ_3 generated in the ring is actually coupled partly out into the output bus and partly back into the input waveguide to exit at port P_2. The conversion efficiency of the unloaded mixer, which is the ratio of the power inside the ring at λ_3 to the input power at λ_1, was calculated to be 40%. Compared to an efficiency of less than 10% obtained for a mixer using a nonlinear straight waveguide having the same length as the circumference of the microring, the superior performance of the ring topology is evident.

The biggest disadvantage of the nonlinear microring mixer is the detuning effect due to self-phase modulation. Since the most difficult aspect of fabricating a microring is the precise control of the gaps between the ring and the input and output waveguides, we studied the effect of the gap parameter g on the theoretical conversion efficiency η of the mixer. In Figure 3.32 the conversion efficiency is plotted for several values of g. The plot shows that η peaks at g = 0.2μm, which is the value for which the microring mixer was originally designed and optimized. As g is increased beyond 0.2μm, the conversion efficiency exhibits a drastic drop well below that of the straight-waveguide mixer The reason is that as g is increased, the stored power in the ring also increases, which causes both the pump beam and input signal to be detuned out of resonance. Consequently the efficiency of the mixer is severely degraded. The high sensitivity of the device performance on the gap size as illustrated in Figure 3.32 is likely to present a great challenge in the current fabrication technology in realizing microring mixers with high conversion efficiency.

3.4 Summary

In this chapter we demonstrated the validity and versatility of the hybrid implicit-explicit FDTD scheme by presenting simulation results for several nonlinear structures of practical interest. The stability of the nonlinear FDTD schemes was confirmed by numerical experiments

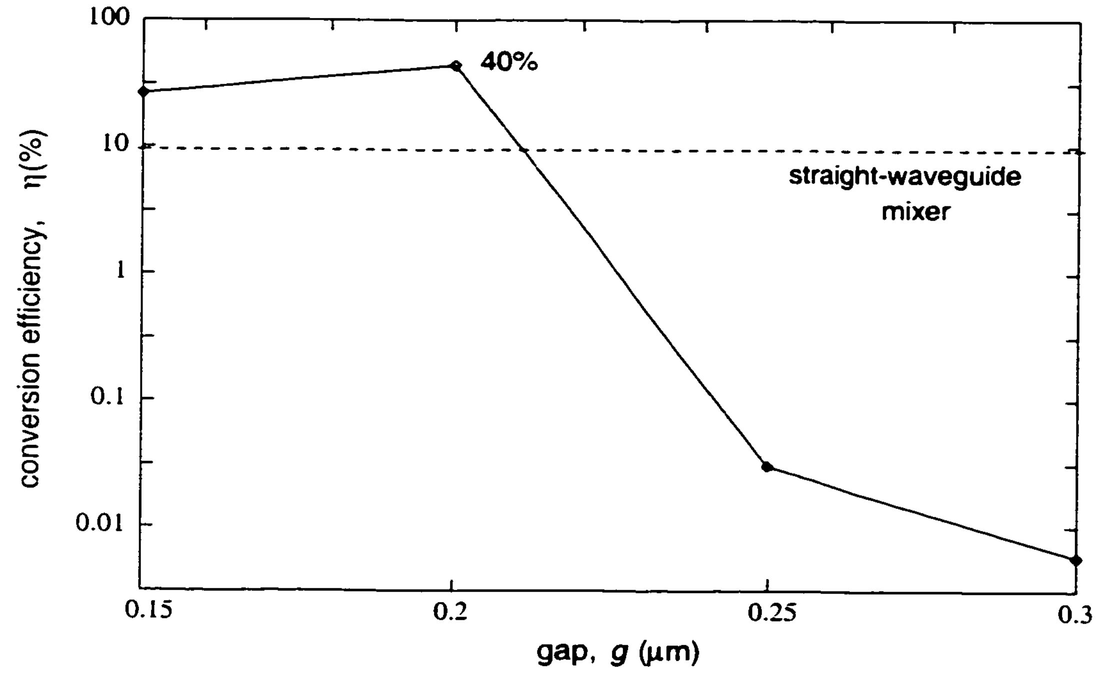

Figure 3.32. Effect of the gap size g on the unloaded conversion efficiency of the nonlinear microring mixer. Also shown for comparison is the conversion efficiency (9.4%) achievable for a mixer using a nonlinear straight waveguide having the same length as the circumference of the microring.

with open nonlinear dielectric test structure and nonlinear dielectric waveguide. The results also showed that the explicit non-iterative FDTD scheme is not suitable for simulating devices with strong nonlinearity because of instability problems.

Many important phenomena associated with nonlinear propagation were illustrated in a number of practical applications. In particular, the well-known self-phase modulation and self-steepening effects associated with optical Kerr nonlinearity were demonstrated in nonlinear slab waveguides. In nonlinear periodic dielectric waveguides, the SPM effect results in the power dependence of the phase-matching condition. Numerical analyses of nonlinear DFR and DBR structures showed that the transmission bands of the filters are shifted toward longer wavelengths as the input power is increased, so that these devices may be used to discriminate both signal wavelengths and powers.

Finally the design and FDTD analysis of a nonlinear microring resonator for third-order frequency mixing was presented. Along with the design concerns for high quality factor and wide free-spectral range of a linear ring resonator, the nonlinear spectral shifts in the resonance peaks also need to be taken into account. The nonlinear microring mixer has the advantage that due to resonance, a high-intensity pump beam can be achieved in the ring without requiring a strong input beam. In addition, very narrow output wavelength channels can be realized by increasing the quality factor of the ring resonator.

Our work on nonlinear optical device applications of the hybrid implicit-explicit FDTD scheme concludes with this chapter. In the remainder of the thesis, we explore a different type of material nonlinearity in the microwave and millimeter-wave regimes, the type that is found in high-temperature superconductors.

Chapter 4

FDTD Analysis of HTS Media

Since the discovery of high-temperature superconductors (HTS) in 1986, there has been increasing interest in using these novel materials in microwave and millimeter-wave applications. The advantages of HTS materials over normal conductors are manifold. Superconducting striplines have surface resistance several orders below that of copper, and can carry large current densities with very little heat dissipation. The frequency dispersion in HTS is also negligibly small compared to that of normal metals. Moreover, the drastic reduction in thermal noise at the superconducting temperatures makes the materials also ideal for low-noise applications. With these superior electrical properties, HTS materials are finding themselves in a growing number of applications, especially in the microwave and millimeter-wave areas.

Parallel to the search for novel HTS devices is a growing need to develop accurate numerical methods for analyzing electromagnetic propagation in HTS media. The analysis of wave propagation in superconductors is complicated by the now established fact that these materials are inherently nonlinear. Nonlinearity in HTS materials has been measured, studied and modeled over a wide range of frequencies, from DC to millimeter-wave, by many researchers [81–87,90–93]. In order to accurately simulate propagation in an HTS medium, a rigorous numerical method must take into account the nonlinear electrodynamic effects of the material. With the proven versatility of the FDTD method in the treatment of optical nonlinearities, it is the aim of this chapter to extend the time-domain method to provide a full-wave analysis of propagation in HTS materials that will fully account for the nonlinear effects.

Several numerical techniques have been proposed for modeling nonlinearities in superconductors, most assuming a power series dependence of the surface impedance on the field [83,86,87]. More rigorous techniques involve solution of the Ginzburg-Landau (GL) equations for the nonlinear response of the material to an applied magnetic field [95,98]. Most notably among these is Megahed and El-Ghazaly's approach of incorporating the GL equations into the FDTD solution of Maxwell's equations [98]. While the GL theory provides a rigorous treatment of the nonlinearity in superconductors, due to the complexity of the equations involved, the approach has the disadvantage of requiring substantial computational effort, especially when incorporated into an FDTD analysis. To overcome this limitation, we propose a new FDTD formulation which is based on the simpler London equations and the nonlinear Meissner effect. The approach directly employs the measured field dependency of the penetration depth of the HTS, and yields considerable saving in computation time over the traditional GL approach. In the course of developing the method, the relationship between the GL and London equations of superconductivity will also be discussed. In order to provide the proper theoretical background to the work, we begin below by first giving an overview of the origin and existing theories of the nonlinearity in HTS materials.

4.1 Nonlinearity in High-Temperature Superconductors

High-temperature superconducting materials are composed of conglomerates of oxides such as $YBa_2Cu_3O_y$ (YBCO), $Bi_2Sr_2CaCu_2O_y$ (BSCCO), and $Tl_2Ba_2CaCu_2O_y$ (TBCCO). In 1956 Cooper showed that, assisted by a certain mediating action of the lattice vibrations in a solid, two electrons can become bound to each other to form a pair, now known as a Cooper pair [78]. This remarkable finding later formed the foundation of the Bardeen-Cooper-Shrieffer (BCS) microscopic theory of superconductivity, which states that superconductivity results from the correlated electron-phonon interactions of Cooper pairs. These electron pairs exist in the superconducting state, which forms when the temperature, the magnetic field, and the current density in the material fall below their respective critical values of T_c, H_c, and J_c. At a constant temperature, the presence of a strong current or equivalently, a strong magnetic field, causes these pairs to dissociate, giving rise to a dependence of the superconducting electron population density on the applied current density. This current dependency is the origin of the so-called intrinsic nonlinearity in all superconductors. Other sources of nonlinearity may also be present. For example, because HTS materials do not have regular lattice structures but are composed of clusters of oxide grains, the boundaries between the grains act as weak superconductor-insulator-superconductor (SIS) junctions, also known as Josephson junctions. The nonlinear characteristics of these junctions collectively contribute to the macroscopic nonlinear phenomenon observed in the superconductor. In addition, in Type-II HTS materials such as cuprate oxides, a mixed state can form in which magnetic flux can penetrate the material one flux quantum at a time, forming flux tubes called vortices. The dynamics of these vortices, which are governed by the Lorentz forces exerted by the self magnetic field, also contribute to the nonlinear response of the HTS material.

Macroscopically, nonlinearity in HTS materials has been experimentally observed in the dependence of the surface impedance of a superconducting stripline on the magnetic field, or equivalently, on the surface current density. Figure 4.1 shows the experimental data of the surface resistance R_s of a YBCO stripline at 1.5GHz and 77K as a function of the peak RF magnetic field, H_{rf}, as reported by Oates *et. al.* [83]. The graph may be divided into three regions of nonlinearity. In the low-field limit, $H_{rf} < H_{c1}$, the field dependence of R_s is of first order, with the nonlinearity predominantly due to the weak Josephson links in the HTS thin films. In the intermediate-field region, $H_{c1} < H_{rf} < H_{c2}$, the nonlinearity is thought to arise from the dissociation of the Cooper pairs. The surface resistance in this region may be modeled by the quadratic relation

$$R_s(\omega, T, H_{rf}) = R_0(\omega, T) + A(\omega, T) \cdot H_{rf}^2, \qquad (4.1)$$

where R_0 is the zero-field surface resistance, and $A(\omega, T)$ is a fitting parameter depending on the frequency and temperature. In the high-field region, $H_{rf} > H_{c2}$, the surface resistance varies as H_{rf}^{α}, with $\alpha > 2$. The nonlinearity in this region is thought to be determined by the vortex dynamics in the HTS material.

Nonlinearity in superconductors can be expressed more intrinsically as the magnetic

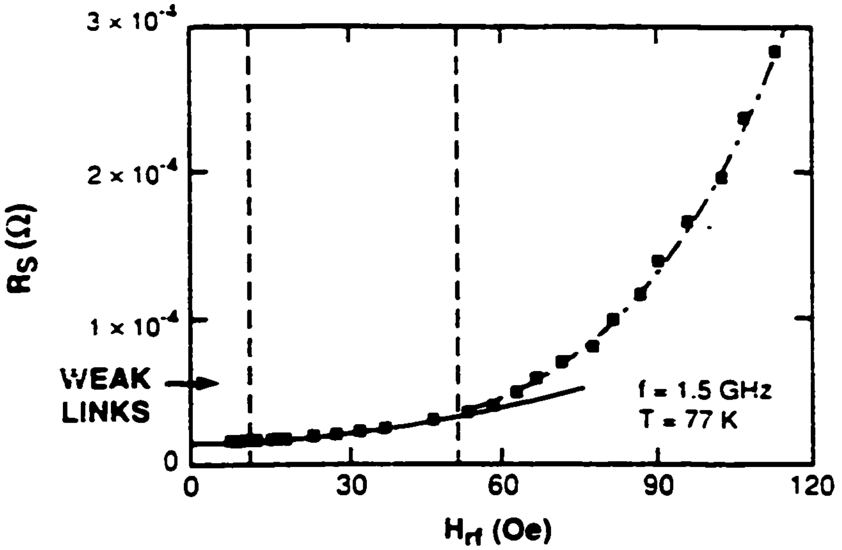

Figure 4.1. Empirical dependence of the surface resistance R_s on the peak RF magnetic field, H_{rf}, in a YBCO stripline at 1.5GHz and 77K [83].

field dependence of the penetration depth, a phenomenon known as the nonlinear Meissner effect. Analogous to the skin depth in normal metals, the penetration depth λ measures the degree of penetration of an applied magnetic field into the superconductor. Measurements of λ versus the magnetic field strength H have been reported for many high-temperature superconducting cuprates such as YBCO, TBCCO and BSCCO [91,92,93]. One of the latest results, shown in Figure 4.2, indicates a linear variation of λ with respect to H in the DC case [93]. Another group reported a quadratic dependence of λ on H as the field is decreased below a certain crossover value H' [91]. From a physics point of view, the behaviour of the penetration depth with respect to the magnetic field is important because it provides insight into the structure of the Cooper pairing state of the superconductor. For some time there has been much debate in the physics community as to whether HTS cuprates possess *s*-wave or *d*-wave symmetries, referring to the form of the energy function in the momentum space. In light of new experimental evidence, Xu, Yip and Saul recently proposed a theory based on the nonlinear current-velocity response of the superconducting pairs, which proves that *s*-wave and *d*-wave

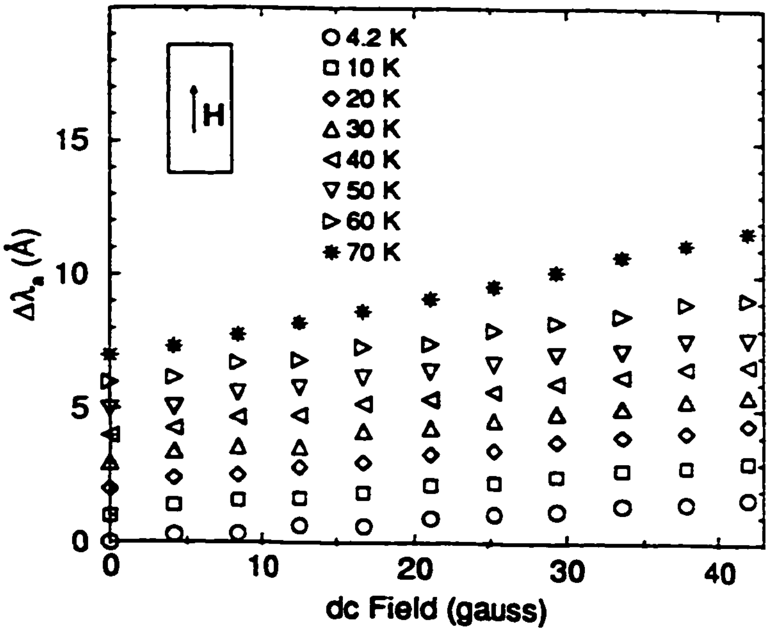

Figure 4.2. Experimentally measured linear dependence of the penetration depth λ on the applied DC magnetic field for $YBa_2C_3O_{6.95}$ [93].

superconductors can be distinguished from each other by measuring the functional dependence of the penetration depth on the magnetic field [94]. According to the theory, superconductors with the conventional *s*-wave symmetry predicted by the BCS theory exhibit a quadratic magnetic field dependence of λ,

$$\frac{\lambda(T,H)}{\lambda_0(T)}=\frac{1}{1-\zeta(T)[H/H_0(T)]^2}\approx 1+\zeta(T)\left[\frac{H}{H_0(T)}\right]^2, \tag{4.2}$$

in which λ_0 is the zero-field penetration depth, H_0 is a characteristic field of the order of the thermodynamic critical field H_c, and $\zeta(T)$ is a temperature-dependent coefficient. For unconventional *d*-wave superconductors, the dependence is characteristically linear, given by

$$\frac{\lambda(T,H)}{\lambda_0(T)}=\frac{1}{1-\gamma[H/H_0(T)]}\approx 1+\gamma\frac{H}{H_0(T)}, \tag{4.3}$$

where γ is a temperature-independent anisotropy parameter which has the value of 1 or $1/\sqrt{2}$ depending on the orientation of the field. However, below a crossover field $H' \approx (T/T_c)H_0$, thermal smearing effect causes λ to vary quadratically with H, even for *d*-wave superconductors. Both the linear dependency at high fields and quadratic variation at low fields of the penetration depth have been experimentally observed for YBCO, BSCCO and TBCCO, pointing to the suggestion that HTS cuprates possess *d*-wave symmetry [91,92,93].

To incorporate the nonlinear behaviour of the penetration depth discussed above into a numerical electromagnetic analysis of HTS devices, we require a theory of superconductivity which is accurate but mathematically tractable. Moreover, the theory should ideally be macroscopic so that it can be easily incorporated into Maxwell's equations. Among the many macroscopic theories that have been proposed, the most comprehensive is Ginzburg and Landau's theory [78]. The GL theory approaches the superconducting phenomenon from a thermodynamical point of view, treating the normal and superconducting states as two distinct thermodynamic phases. It postulates the existence of a complex-valued order parameter ψ which depends on the position $\mathbf{r}$, such that its squared absolute value gives the superconducting electron density:

$$|\psi(\mathbf{r})|^2 = n_s(\mathbf{r}).$$

Using quantum mechanical analogy, the order parameter can thus be thought of as a wave function of the superconducting electrons, except that ψ depends only on position, whereas wave functions are in general functions of both position and time. Ginzburg and Landau further assumed that near the critical temperature T_c and in the absence of a magnetic field, the Gibbs free energy density of a system consisting of normal and superconducting phases can be approximated by a power series in n_s:

$$g(T,n_s) = g_n(T) + \alpha(T)n_s + \tfrac{1}{2}\beta(T)n_s^2, \qquad (4.4)$$

where g_n is the zero-field Gibbs free energy density at temperature T of the normal state, and α and β are coefficients which depend only on the temperature. The parameters α and β can be shown to be related to the critical magnetic field H_c via

$$\alpha = -\frac{\mu_0 H_c^2}{n^*}, \tag{4.5}$$

and
$$\beta = \frac{\mu_0 H_c^2}{(n^*)^2}, \tag{4.6}$$

in which n^* is the equilibrium density of the superconducting electrons. In the presence of an applied magnetic field, the Gibbs free energy of the superconducting system also depends on the field. The equilibrium condition of the normal and superconducting states, which is achieved by minimizing the total Gibbs free energy of the system, is described by the two Ginzburg-Landau equations,

$$\alpha\psi + \beta|\psi|^2\psi + \frac{1}{2m_s}(j\hbar\nabla + q_s\mathbf{A})^2\psi = 0, \tag{4.7}$$

$$-\mathbf{J}_s = \frac{j\hbar q_s}{2m_s}(\psi^*\nabla\psi - \psi\nabla\psi^*) + \frac{q_s^2}{m_s}|\psi|^2\mathbf{A}. \tag{4.8}$$

In the above equations, m_s and q_s are the mass and charge, respectively, of the superconducting electrons. $\mathbf{J}_s$ is the supercurrent density, and $\mathbf{A}$ is the magnetic vector potential. It can be seen that Eq.(4.7) is nonlinear by virtue of the power relation (4.4). In the presence of a non-zero magnetic field, the above two equations also become coupled so that they have to be solved simultaneously for ψ and $\mathbf{A}$. Although derived only for temperatures near the critical temperature, the GL equations give a remarkably accurate description of many properties of superconductors. Furthermore, the theory can also be shown to be a direct consequence of the BCS microscopic theory [78].

Another macroscopic theory which is simpler but as widely-used is Londons' electrodynamic theory of superconductivity. Although originally derived only for linear superconductors, Londons' equations can be easily extended to include nonlinear effects. The theory is predicated on the two-fluid model, which assumes the existence of two kinds of electrons in the superconductor: the normal conducting electrons with population density n_n, and the superconducting electrons with population density n_s. The total current density $\mathbf{J}$ in a superconductor is thus $\mathbf{J}_n + \mathbf{J}_s$. The normal current component is assumed to obey the usual Ohm's Law,

$$\mathbf{J}_n = \sigma_n \mathbf{E}, \tag{4.9}$$

where the normal conductivity σ_n can be derived from the electron drift model for normal conductors:

$$\sigma_n = \frac{n_n e^2 \tau}{m_n}. \tag{4.10}$$

In the above equation e is the electronic charge. τ is the relaxation time. and m_n is the mass of the normal conducting electrons. On the other hand. the superconducting current is thought to experience zero resistance; therefore the motion of the superconducting electrons under the influence of an electric field obeys the simple acceleration equation.

$$\frac{d\mathbf{v}}{dt} = \frac{q_s}{m_s}\mathbf{E}, \tag{4.11}$$

where $\mathbf{v}$ is the electron velocity. and q_s and m_s denote. respectively. the effective charge and mass of the superconducting electrons. In light of the BCS theory. the superconducting electrons are found to be in fact pairs of electrons. or Cooper pairs as previously mentioned; hence q_s and m_s can be replaced by $2e$ and $2m_n$. Since the supercurrent density $\mathbf{J}_s$ is given by

$$\mathbf{J}_s = n_s q_s \mathbf{v}, \tag{4.12}$$

we can write Eq.(4.11) as

$$\frac{d}{dt}\left(\frac{m_s}{n_s q_s^2}\mathbf{J}_s\right) = \mathbf{E},$$

or

$$\frac{d}{dt}\left(\mu_0 \lambda^2 \mathbf{J}_s\right) = \mathbf{E}, \tag{4.13}$$

where λ is the London penetration depth. related to the superconducting electron density n_s by

$$\lambda = \sqrt{\frac{m_s}{\mu_0 n_s q_s^2}}. \tag{4.14}$$

Equation (4.13) is known as the first London equation. The second London equation.

$$\nabla\times\left(\lambda^2\mathbf{J}_s\right)=-\mathbf{H}\,. \tag{4.15}$$

is phenomenologically deduced from the Meissner effect, which describes the tendency of the superconductor to expel magnetic field from its interior. It should be noted that in the London theory, the penetration depth is assumed to be independent of the applied field, implying that Eqs.(4.13) and (4.15) are applicable only to linear superconductors.

For time-harmonic fields with $e^{j\omega t}$ variation, Eq.(4.13) becomes

$$\mathbf{J}_s=\frac{-j}{\omega\mu_0\lambda^2}\mathbf{E}\,, \tag{4.16}$$

from which we can define the complex-valued superconductivity $\tilde{\sigma}_s$ as

$$\tilde{\sigma}_s(\omega)=\frac{-j}{\omega\mu_0\lambda^2}=-j\sigma_s\,. \tag{4.17}$$

The total conductivity of the superconductor is thus

$$\sigma=\sigma_n-j\sigma_s=\frac{n_n e^2\tau}{m_n}-j\frac{1}{\omega\mu_0\lambda^2}\,. \tag{4.18}$$

Using the above expression for the conductivity, we can derive the surface impedance of an HTS parallel-plate transmission line having infinite thickness ($t \gg \lambda$) as [77]

$$Z_s=R_s+jX_s=\tfrac{1}{2}\omega^2\mu_0^2\lambda^3\sigma_n+j\omega\mu_0\lambda \tag{4.19}$$

Note that the above expression states that the surface resistance R_s of an HTS stripline varies as ω^2, a fact which has been confirmed experimentally.

To account for the dependence of the surface resistance on the magnetic field as observed in Figure 4.1, the assumption of a constant penetration depth must be relaxed and λ, or equivalently, n_s, allowed to vary with the current or the magnetic field. A theoretical dependence of n_s on the current density has been obtained by Xia *et. al.*, who employed an assumed Gaussian distribution function for the velocity $n(v)$ of the electrons at a constant temperature [90]. By assuming that those electrons with energies below the transition energy E_c are in the superconducting state, the superconducting electron density can be obtained from

$$n_s(J)=\int_{-v_c(T)}^{v_c(T)} n(v)dv, \tag{4.20}$$

where v_c is the maximum velocity for which the kinetic energy of the superconducting electron is equal to the transition energy at a given temperature T. Experimentally, n_s and λ can be obtained from measurements of the surface reactance X_s of an HTS stripline. By performing measurements on a YBCO stripline at 1.5GHz and 77K, Oates *et. al.* showed that the dependence of λ on the peak RF magnetic field, H_{rf}, at the HTS thin-film surface may be modeled by the power relation [83]

$$\lambda(T,H_{rf})=\lambda_0(T)+C(T)\cdot H_{rf}^{\alpha}, \tag{4.21}$$

where λ_0 is the zero-field penetration depth and $C(T)$ is a fitting parameter. Putting Eqs.(4.1), (4.19) and (4.21) together, we can derive a general empirical model for the surface impedance Z_s of an HTS stripline:

$$Z_s(\omega,H_{rf})=\omega^2\left(R_0+B\cdot H_{rf}^2\right)+j\omega\mu_0\left(\lambda_0+C\cdot H_{rf}^{\alpha}\right), \tag{4.22}$$

where B, C, and α are fitting parameters depending only on the temperature. Note that the above equation explicitly includes the ω^2 variation of the surface resistance R_s.

In applying the FDTD method to conducting waveguides, electrically thin conductors are usually treated as surface impedance boundary conditions so as to eliminate the need for fine meshes in the conducting regions. Superconducting microwave and millimeter-wave structures also consist of HTS films whose thicknesses are usually small compared to the entire device geometry; therefore it appears that the superconductors may also be conveniently treated as impedance boundaries. We will briefly explore this approach now to show that, contrary to the above argument, the technique is considerably complicated by the fact that the HTS materials are nonlinear. In the frequency domain, the electric field E_s on a superconducting surface is related to the magnetic field H_s by the surface impedance Z_s,

$$E_s(\omega)=Z_s(\omega)H_s(\omega). \tag{4.23}$$

Given the nonlinear empirical model for the surface impedance described by Eq.(4.22), the above equation becomes

$$E_s(\omega)=\omega^2\left[R_0+BH_s^2(\omega)\right]H_s(\omega)+j\omega\mu_0\left[\lambda_0+CH_s^{\alpha}(\omega)\right]H_s(\omega). \tag{4.24}$$

Assuming $\alpha \approx 2$, Eq.(4.24) translates into a sum involving double convolutions in the time domain for the case of monochromatic excitation,

$$\begin{aligned} E_s(t)=&-R_0\frac{\partial^2 H_s}{\partial t^2}-B\int_0^t\frac{\partial^2 H_s}{\partial \tau^2}\int_0^{t-\tau}H_s(\xi)H_s(t-\tau-\xi)d\xi d\tau \\ &+\mu_0\lambda_0\frac{\partial H_s}{\partial t}+\mu_0 C\int_0^t\frac{\partial H_s}{\partial \tau}\int_0^{t-\tau}H_s(\xi)H_s(t-\tau-\xi)d\xi d\tau. \end{aligned} \tag{4.25}$$

Numerical evaluation of the double convolution integrals in general requires saving H_s values at all time steps starting from $t = 0$. In the case of linear impedance boundary, which involves only a single convolution term, the discrete convolution can be approximated by a recursive expression which results in a significant saving in computational resources. For the nonlinear case given by Eq.(4.25), however, to date a computationally feasible scheme has not been found, so the nonlinear impedance boundary condition is currently not a practical approach.

It seems then that a rigorous analysis of wave propagation in HTS media requires a full solution of Maxwell's equations along with the appropriate nonlinear model for the constitutive relation of the superconductor. As mentioned previously, this approach was adopted by Megahed and El-Ghazaly, who incorporated the GL equations into Maxwell's solution [98]. Their method first solves the GL equations numerically for the superconducting electron density $n_s = |\psi|^2$, from which the penetration depth λ can be computed using Eq.(4.14).

$$\lambda(\mathbf{r},\mathbf{H})=\frac{\sqrt{m_s/\mu_0}}{q_s|\psi(\mathbf{r},\mathbf{H})|}. \tag{4.26}$$

The result is that λ depends on both the position $\mathbf{r}$ and the magnetic field $\mathbf{H}$ via $\psi(\mathbf{r},\mathbf{H})$. The value of the penetration depth is then used in the first London equation (4.13) to solve for the supercurrent density $\mathbf{J}_s$, from which the electric and magnetic fields can be updated in the usual

FDTD solution of Maxwell's equations. It is apparent that at each FDTD time step, the method requires solution of the two nonlinear GL equations, which amounts to substantial overall computational requirement for the algorithm.

In the next section we show that the GL equations can be replaced by the much simpler London equations and an appropriate model for the nonlinear Meissner effect. In particular, it will be shown that with the appropriate function for $\lambda(\mathbf{H})$, the nonlinear London equations give excellent approximation to the GL solutions. This result allows us to formulate an efficient FDTD algorithm for simulating propagation in HTS media based on the nonlinear London equations.

4.2 The Nonlinear London Equations

In the previous section it was stated that Londons' theory is strictly applicable only to linear superconductors since the penetration depth λ is assumed constant. Under weak field conditions where HTS materials can be assumed linear, the London theory provides a good approximation to the GL solution and can thus be used to model the electromagnetic response of the superconductors [96]. In the presence of strong magnetic fields, however, Eqs.(4.13) and (4.15) are no long accurate because they fail to account for the position dependence of the superelectron density $n_s = |\psi|^2$, as predicted by the GL theory [95]. We show in this section that the London equations can be used to describe the response of superconductors at high fields if the nonlinear Meissner effect is also included, i.e., if the penetration depth is allowed to vary with the magnetic field.

The rationale for our approach hinges on the link between the GL equations and the nonlinear London equations. By assuming that the field-dependent penetration depth is still related to the order parameter ψ by the relation,

$$\lambda(\mathbf{H}) = \frac{\sqrt{m_s/\mu_0}}{q_s|\psi(\mathbf{H})|}. \tag{4.27}$$

we can show that the second nonlinear London equation can be directly derived from the GL theory. Letting $\psi = |\psi| e^{j\theta}$ in the second GL equation (4.8), we obtain

$$-\mathbf{J}_s = -\frac{\hbar q_s}{m_s}|\psi|^2 \nabla\theta + \frac{q_s^2}{m_s}|\psi|^2 \mathbf{A} . \tag{4.28}$$

Making use of relation (4.27), we rewrite the above equation as

$$\mu_0 \lambda^2 \mathbf{J}_s = \frac{\hbar}{q_s}\nabla\theta - \mathbf{A} . \tag{4.29}$$

Taking the curl of both sides of Eq.(4.29) gives

$$\mu_0 \nabla\times\left(\lambda^2 \mathbf{J}_s\right) = \frac{\hbar}{q_s}\nabla\times\nabla\theta - \nabla\times\mathbf{A} .$$

and using the fact that $\nabla\times\nabla\theta = 0$ and $\nabla\times\mathbf{A} = \mu_0 \mathbf{H}$, we arrive at

$$\nabla\times\left(\lambda^2 \mathbf{J}_s\right) = -\mathbf{H} , \tag{4.30}$$

which is the second London equation (4.15). Note that Eq.(4.30) is in general nonlinear because we have allowed λ to depend on **H**. The foregoing result shows that the second GL equation and the second nonlinear London equation are identical to each other, both describing the flux-expelling tendency of superconductors. We conclude, then, that the first GL equation (4.7) is responsible for two effects: the nonlinear dependence of ψ on **H** and the anisotropy of the material. The nonlinear London theory accounts for these effects by the explicit inclusion of the nonlinear Meissner dependence of λ on **H**.

To verify that the second London equation along with the appropriate nonlinear Meissner model produces the same electromagnetic response as the GL equations, we considered the simple example of a one-dimensional HTS slab subject to an applied magnetic field H_a, as shown in Figure 4.3. The slab has thickness $5\lambda_0$, where λ_0 is the low-field London penetration depth. The GL solution for the slab has been obtained numerically by other researchers [95,98], so we will only briefly outline the approach. By introducing the normalized quantities,

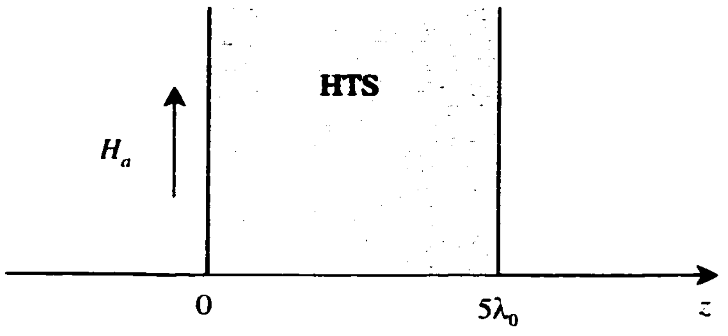

Figure 4.3. One-dimensional HTS slab subject to an external DC magnetic field H_a. The thickness of the slab is $5\lambda_0$, where λ_0 is the low-field penetration depth.

$$\psi' = \psi/\psi_0 ,$$

$$\mathbf{r}' = \mathbf{r}/\lambda_0 ,$$

$$|\psi_0|^2 = \frac{m_s}{\mu_0 q_s^2 \lambda_0^2} = n_s(\mathbf{H} = 0),$$

$$\xi = \frac{\hbar|\psi_0|}{\sqrt{2\mu_0 m_s} H_c},$$

$$\kappa = \lambda_0/\xi ,$$

$$\mathbf{A}' = \frac{q_s|\psi_0|}{\sqrt{\mu_0 m_s} H_c}\mathbf{A} ,$$

the two GL equations can be simplified to

$$\frac{1}{\kappa^2}\nabla'^2\psi' = \frac{j}{\sqrt{2}\kappa}\mathbf{A}'\cdot\nabla'\psi' + \psi'\left(|\psi'|^2 - 1 + \frac{1}{2}|\mathbf{A}'|^2\right), \tag{4.31}$$

$$\nabla'^2\cdot\mathbf{A}' = \frac{\sqrt{2}}{\kappa}\mathrm{Im}(\psi'\nabla'\psi'^*) + |\psi'|^2\mathbf{A}' . \tag{4.32}$$

For the one-dimensional case, letting $\mathbf{r}' = z'$, $\psi' = ue^{j\theta}$ and $\mathbf{A}' = a\hat{\mathbf{x}}$, we can further reduce the above system to

$$\frac{1}{\kappa^2}\frac{d^2u}{dz'^2}=\left(\frac{a^2}{2}-1\right)u+u^3. \tag{4.33}$$

$$\frac{d^2a}{dz'^2}=u^2a. \tag{4.34}$$

We then solved the above system of second-order differential equations using the finite-difference method, with boundary conditions

$$\left.\frac{da}{dz'}\right|_{z'=0}=-\mu_0 H_a'=-\frac{H_a}{H_c}$$

and $$\left.\frac{du}{dz'}\right|_{z'=0}=0.$$

The solutions for the normalized superconducting electron density $|\psi'|^2$, and the corresponding normalized penetration depth, $\lambda'=\lambda/\lambda_0=1/|\psi'|$, are shown in Figures 4.4 and 4.5, respectively, as functions of the normalized magnetic field, $H'=H/H_c$, inside the slab. The depletion of the superconducting electron density as the field approaches H_c, signifying the loss of superconductivity, can be observed in Figure 4.4. Note that the field dependencies of both ψ' and λ' are irrespective of the position z', implying that the penetration depth at an arbitrary point inside the superconductor is uniquely determined by the magnetic field at that point alone. This observation is important because it allows us to model the variation of the penetration depth as a function of only the magnetic field.

Recalling our hypothesis that the first GL equation can be replaced by an explicit model of the nonlinear Meisser effect, we next sought a functional description of the λ' versus H' curve in Figure 4.5 by performing curve fitting to the data. The best fit function was found to be

$$\frac{\lambda(H)}{\lambda_0}=\frac{1}{\left[1-(H/H_c)^2\right]^{1/4}}. \tag{4.35}$$

The above equation explicitly describes the nonlinear Meissner effect as predicted by the GL theory. Using this model for $\lambda(H)$, we then numerically solved the second nonlinear London equation for $H'(z')$ in the one-dimensional slab:

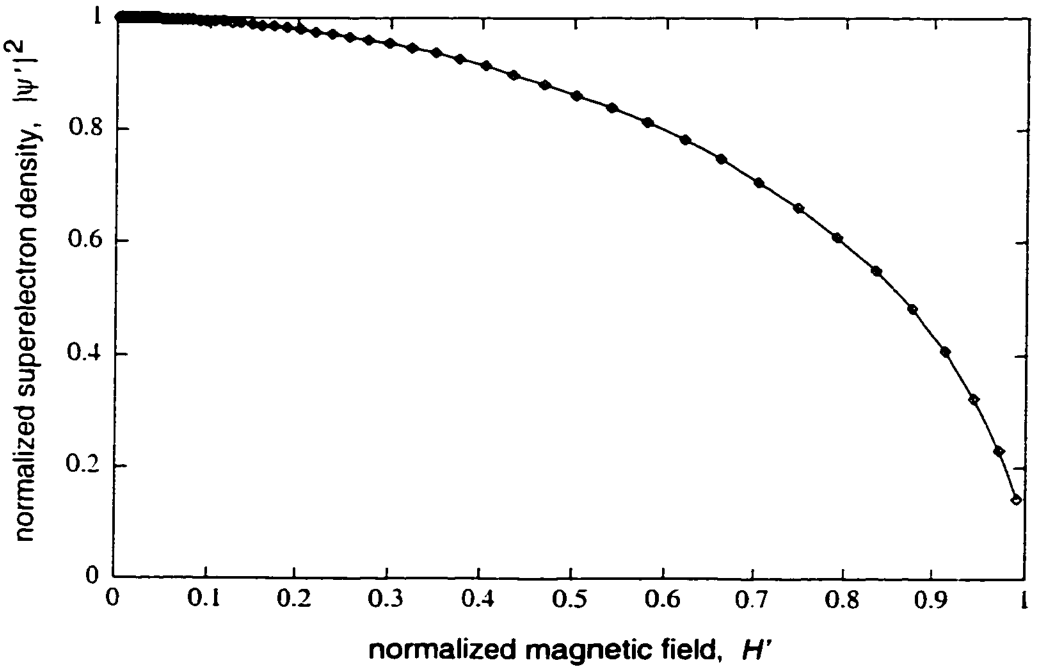

Figure 4.4. GL solution of the normalized superelectron density, $|\psi'|^2 = |\psi/\psi_0|^2$, as a function of the normalized magnetic field, $H' = H/H_c$. The gradual loss of superconductivity as H approaches H_c can be observed.

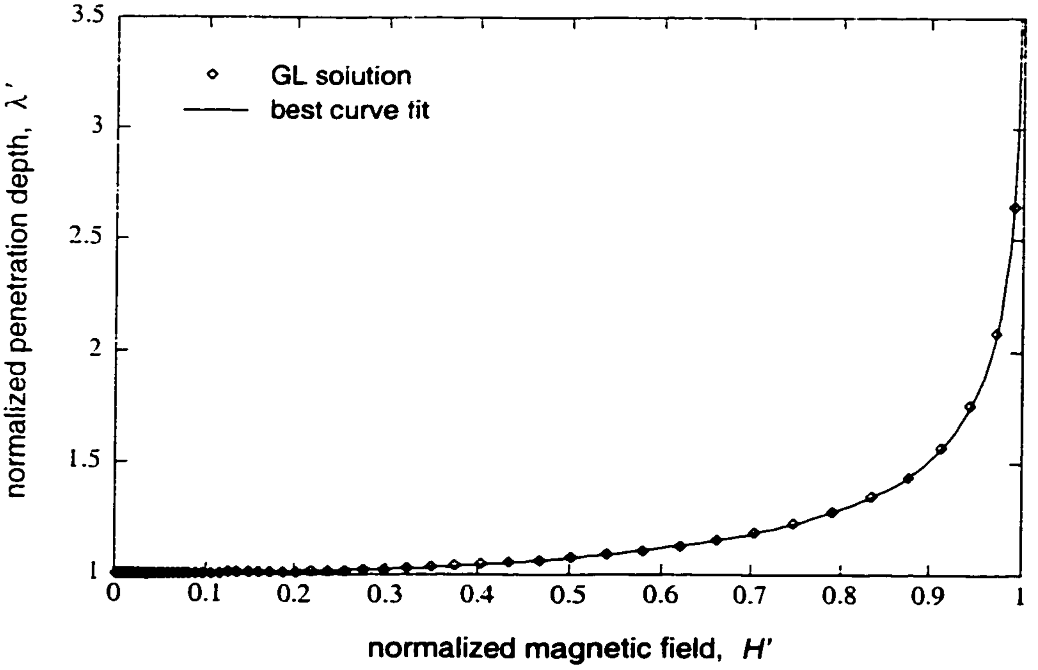

Figure 4.5. GL solution of the normalized penetration depth, $\lambda' = \lambda/\lambda_0$, as a function of the normalized magnetic field, $H' = H/H_c$.

$$\frac{d}{dz'}\left(\lambda'^2(H')\frac{dH'}{dz'}\right) = H'. \tag{4.36}$$

and compared the results with those obtained from the GL equations. The solutions for the normalized superconducting electron density, $n_s'(z') = |\psi'(z')|^2$, and the normalized supercurrent density, $J_s'(z') = \lambda_0 J_s / H_c$, are shown in Figures 4.6 and 4.7, respectively, along with the corresponding GL results. It is seen that both the London solutions and the GL solutions are in excellent agreement with each other. In particular, Figure 4.6 shows that the nonlinear London equation correctly modelled the position dependence of the superconducting electron density, predicting increased partial loss of superconductivity at the edge of the slab as the applied magnetic field was increased. In Figure 4.7, the London solutions also yielded the correct GL depairing critical current density, J'_{pair}, which occurs at the peaks of the $J_s'(z')$ plots for applied fields near the critical value (e.g., $H_a = 0.9H_c$) [95]. The depairing current density is the maximum current density that a Cooper pair can withstand without breaking up; it thus gives a measure of the critical current density J_c of the superconductor. The GL theory predicts a value $2\sqrt{2}/3\sqrt{3} \approx 0.54$ for J'_{pair} [78], which agrees with our numerical result shown in the figure.

The above exercise validates our claim that the GL equations can be approximated by the nonlinear London equations, which can be more readily incorporated into an FDTD solution of Maxwell's equations to simulate propagation in a general superconducting medium. It also shows that instead of solving the GL equations at every FDTD time step for λ at each point in the grid as proprosed in [98], the penetration depth can be directly obtained from the explicit GL model for $\lambda(H)$ given by Eq.(4.35) with negligible computational effort.

The analysis in this section also shows that a numerical model for the nonlinear Meissner effect can be extracted from the GL theory, which predicts an H^2-dependence for λ at low fields since for $H/H_c \ll 1$, Eq.(4.35) can be approximated by a quadratic function. As mentioned in Section 4.1, recent measurements on HTS cuprates indicated that the measured λ tends to vary as H^2 at low fields and as H at high fields. The deviation of the GL model from experimental data at high fields may be due to the fact that the theory was developed only for type-I superconductors, which do not exhibit a mixed state of gradual penetration of the magnetic field

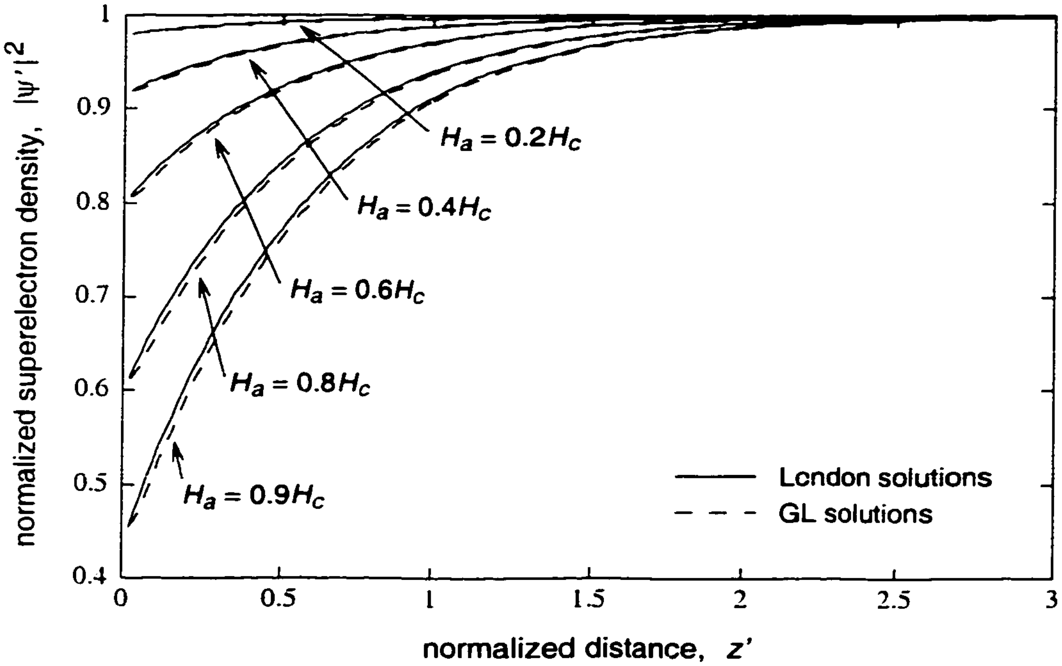

Figure 4.6. GL and London solutions for the normalized superelectron density inside the HTS slab. Both the GL and London results predict increased loss of superconductivity at the edge of the slab ($z' = 0$) as the applied magnetic field is increased.

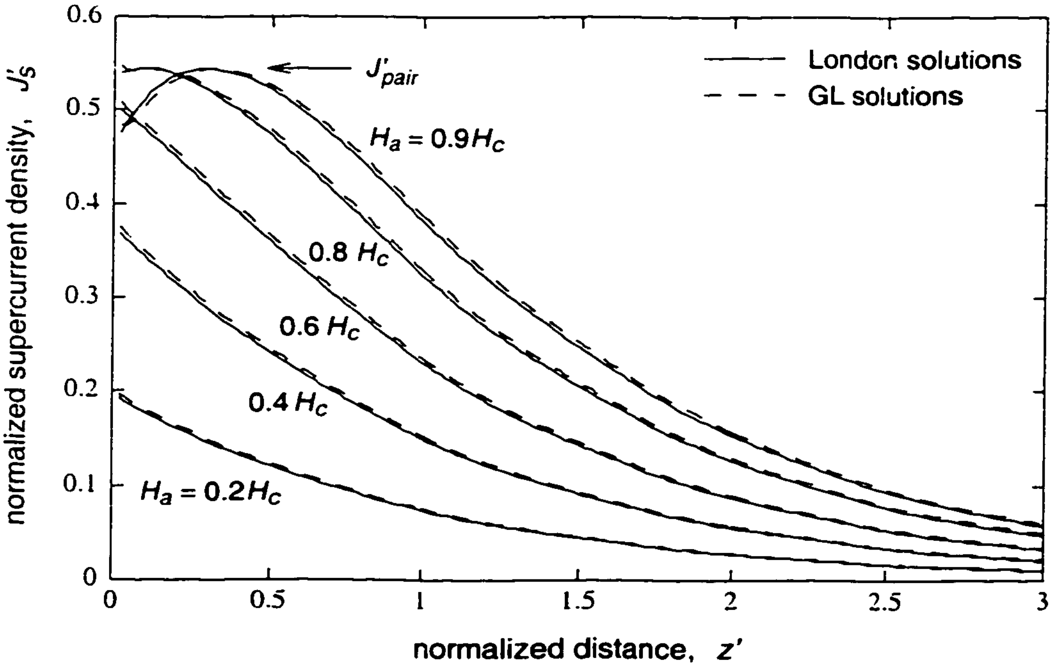

Figure 4.7. GL and London solutions for the normalized supercurrent density, $J_s' = \lambda_0 J_s / H_c$, inside the HTS slab. Both the GL and London results predict a peak supercurrent density of 0.54 near the edge of the slab.

in the form of vortices. For more realistic results, therefore, the empirical models of $\lambda(H)$ such as those reported in [91] and [93] can be directly used in the analysis of propagation in the HTS materials. This approach is much similar to that in nonlinear optics where the refractive index depends on the electric field and the material model is described by experimentally-determined nonlinear susceptibility coefficients.

4.3 FDTD Simulation of HTS Devices

The second nonlinear London equation and the GL equations provide accurate electromagnetic description of magnetoquasistatic superconducting systems such as the one-dimensional HTS slab example. For general electrodynamic systems it is more appropriate to use the time-varying first London equation in the analysis. Thus, to simulate propagation in an HTS medium, we require that the following system of equations based on the two-fluid model be satisfied everywhere in the material:

$$\nabla \times \mathbf{E} = -\mu_0 \frac{\partial \mathbf{H}}{\partial t}, \tag{4.37}$$

$$\nabla \times \mathbf{H} = \varepsilon \frac{\partial \mathbf{E}}{\partial t} + \sigma_n \mathbf{E} + \mathbf{J}_s, \tag{4.38}$$

$$\mu_0 \frac{\partial}{\partial t}\left(\lambda^2 \mathbf{J}_s\right) = \mathbf{E}. \tag{4.39}$$

Here the London equation can be regarded as the constitutive relation between the supercurrent density and the electric field. The parameters that characterize propagation in a superconducting medium are ε, σ_n, and λ; however, since $\omega\varepsilon \ll \sigma_n$ and $\varepsilon \ll 1/\lambda^2$, the permittivity can usually be neglected.

In Section 4.1 we defined the superconductivity σ_s of a superconducting medium in relation to the penetration depth λ via Eq.(4.17). Since λ is a function of the temperature T and magnetic field H, both the superconductivity σ_s and the normal conductivity σ_n will also depend on T and H [98]. The requirement of the conservation of the total electron density, $n = n_s + n_n$, establishes a relationship between the penetration depth, which depends on n_s via (4.14), and the normal conductivity, which is related to n_n via (4.10). Suppose $f(H/H_c)$ describes the field dependency of λ/λ_0; the penetration depth can be expressed as

$$\lambda(T,H)=\frac{\lambda_0}{\sqrt{1-(T/T_c)^4}}f(H/H_c). \tag{4.40}$$

where the Gorter-Casimir model for the temperature dependency has been used [79]. Solving for n_s from Eq.(4.14), we obtain

$$n_s(T,H)=\frac{m_s}{\mu_0 q_s^2[\lambda(T,H)]^2}=\frac{m_s}{\mu_0 q_s^2\lambda_0^2}\frac{1-(T/T_c)^4}{[f(H/H_c)]^2}=n_{s0}\frac{1-(T/T_c)^4}{[f(H/H_c)]^2}. \tag{4.41}$$

in which n_{s0} is the superconducting electron density at zero temperature and zero field. Since the total electron density is conserved and equal to n, we have

$$n_n(T,H)=n-n_s(T,H)=n-n_{s0}\frac{1-(T/T_c)^4}{[f(H/H_c)]^2}. \tag{4.42}$$

Recognizing that $n_{s0}=n$ since there are no normal electrons at 0K and zero field, we arrive at the following expression for the temperature and field dependency of the normal electron density:

$$n_n(T,H)=n\left\{1-\frac{1-(T/T_c)^4}{[f(H/H_c)]^2}\right\}. \tag{4.43}$$

The normal conductivity can be determined from n_n using Eq.(4.10):

$$\sigma_n(T,H)=\frac{ne^2\tau}{m_n}\left\{1-\frac{1-(T/T_c)^4}{[f(H/H_c)]^2}\right\}. \tag{4.44}$$

Moreover, since

$$\sigma_n(T_c,0)=\frac{ne^2\tau}{m_n}$$

and $\sigma_n(T,0)=\sigma_n(T_c,0)(T/T_c)^4$.

we can express Eq.(4.44) in the form

$$\sigma_n(T,H)=\sigma_n(T_c,0)-\frac{\sigma_n(T_c,0)-\sigma_n(T,0)}{[f(H/H_c)]^2}. \tag{4.45}$$

The above equation gives the complete temperature and field dependency of the normal conductivity and can be used in Eq.(4.38) in the analysis of propagation in HTS media.

Unlike common optical materials, we see that nonlinearity in HTS materials appears in the complex conductivity, $\sigma_n - j\sigma_s$, instead of the permittivity. The normal conductivity σ_n constitutes the real part of the complex conductivity of the HTS medium and is thus responsible for diffusive effects on wave propagation. On the other hand, the superconductivity σ_s makes up the imaginary part and is responsible for dispersive effects. Hence, nonlinearity in HTS materials acts on both the diffusive and dispersive mechanisms of wave propagation in the media.

Several techniques exist for analyzing nonlinear microwave circuits, most prominent among them being harmonic balance analysis and Volterra series analysis [119]. However, these methods are frequency-domain based which assume the input signal to consist of a finite number of discrete tones, and thus they are more applicable to steady-state problems such as harmonic generation and frequency mixing. A more rigorous solution of the system of equations (4.37) – (4.39) that fully accounts for all the nonlinear effects, steady-state and transient, must be sought in the time domain. We thus propose FDTD as the method of solution. Since the system cannot be reduced to a single differential equation in either **E** or **H** field, it must be solved in a leap-frog fashion for all components of **E**, **H** and $\mathbf{J}_s$. However, in two-dimensional structures, the system can still be decomposed into two independent sets of solutions, corresponding to the familiar TE and TM polarizations. Furthermore, in conducting waveguides, the magnetic field is maximum at the surfaces of the conductors for TM polarization and minimum for TE polarization; and since nonlinearity in HTS materials is manifested in the **H**-field dependence of λ and σ_n, the nonlinear effects will be more pronounced for TM case than for TE case. For this reason we will consider only TM polarization in our work.

In two-dimensional HTS structures with $\partial/\partial y = 0$, the equations for the propagation of the TM fields with components H_y, E_z, J_{sz}, E_x and J_{sx} are

$$\frac{\partial E_x}{\partial z} - \frac{\partial E_z}{\partial x} = -\mu_0 \frac{\partial H_y}{\partial t} \tag{4.46}$$

$$\frac{\partial H_y}{\partial x} = \varepsilon \frac{\partial E_z}{\partial t} + \sigma_n E_z + J_{sz} \tag{4.47}$$

$$-\frac{\partial H_y}{\partial z} = \varepsilon \frac{\partial E_x}{\partial t} + \sigma_n E_x + J_{sx} \tag{4.48}$$

$$\mu_0 \frac{\partial}{\partial t}\left(\lambda^2 J_{sz}\right) = E_z \tag{4.49}$$

$$\mu_0 \frac{\partial}{\partial t}\left(\lambda^2 J_{sx}\right) = E_x \tag{4.50}$$

We discretize the above equations using the leap-frog scheme, with the following space and time assignments for the field components: H_y at $(n\Delta t, i\Delta z, j\Delta x)$, E_z and J_{sz} at $((n+1/2)\Delta t, i\Delta z, (j+1/2)\Delta x)$, and E_x and J_{sx} at $((n+1/2)\Delta t, (i+1/2)\Delta z, j\Delta x)$. The locations of the field components are illustrated in Figure 4.8. With the above field assignments, Eqs.(4.46) – (4.50) are discretized as follows, which is based on a direct integration scheme proposed by Cummer for cold plasmas [50]:

$$\frac{E_x\big|_{i+1/2,j}^{n+1/2} - E_x\big|_{i-1/2,j}^{n+1/2}}{\Delta z} - \frac{E_z\big|_{i,j+1/2}^{n+1/2} - E_z\big|_{i,j-1/2}^{n+1/2}}{\Delta x} = -\mu_0 \frac{H_y\big|_{i,j}^{n+1} - H_y\big|_{i,j}^{n}}{\Delta t}. \tag{4.51}$$

$$\begin{aligned}\frac{H_y\big|_{i,j+1}^{n} - H_y\big|_{i,j}^{n}}{\Delta x} &= \frac{\varepsilon E_z\big|_{i,j+1/2}^{n+1/2} - \varepsilon E_z\big|_{i,j+1/2}^{n-1/2}}{\Delta t} \\ &\quad + \frac{\sigma_n}{2}\left(E_z\big|_{i,j+1/2}^{n+1/2} + E_z\big|_{i,j+1/2}^{n-1/2}\right) + \frac{1}{2}\left(J_{sz}\big|_{i,j+1/2}^{n+1/2} + J_{sz}\big|_{i,j+1/2}^{n-1/2}\right)\end{aligned} \tag{4.52}$$

$$\begin{aligned}-\frac{H_y\big|_{i+1,j}^{n} - H_y\big|_{i,j}^{n}}{\Delta z} &= \frac{\varepsilon E_x\big|_{i+1/2,j}^{n+1/2} - \varepsilon E_x\big|_{i+1/2,j}^{n-1/2}}{\Delta t} \\ &\quad + \frac{\sigma_n}{2}\left(E_x\big|_{i+1/2,j}^{n+1/2} + E_x\big|_{i+1/2,j}^{n-1/2}\right) + \frac{1}{2}\left(J_{sx}\big|_{i+1/2,j}^{n+1/2} + J_{sx}\big|_{i+1/2,j}^{n-1/2}\right)\end{aligned} \tag{4.53}$$

$$\mu_0 \frac{\lambda^2 J_{sz}\big|_{i,j+1/2}^{n+1} - \lambda^2 J_{sz}\big|_{i,j+1/2}^{n}}{\Delta t} = \frac{1}{2}\left(E_z\big|_{i,j+1/2}^{n+1/2} + E_z\big|_{i,j+1/2}^{n-1/2}\right) \tag{4.54}$$

$$\mu_0 \frac{\lambda^2 J_{sx}\big|_{i+1/2,j}^{n+1} - \lambda^2 J_{sx}\big|_{i+1/2,j}^{n}}{\Delta t} = \frac{1}{2}\left(E_x\big|_{i+1/2,j}^{n+1/2} + E_x\big|_{i+1/2,j}^{n-1/2}\right). \tag{4.55}$$

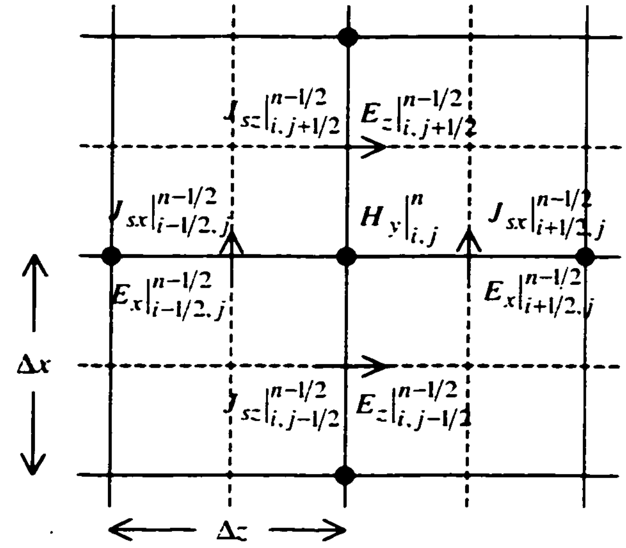

Figure 4.8. Space and time assignments of the field components for the HTS FDTD method. J_{sz} and J_{sx} are co-located with E_z and E_x, respectively, in time and space.

Note that in order to obtain a second-order accurate discretization, semi-implicit time indexing is used for the terms $\sigma_n E_z$ and $\sigma_n E_x$ in Eqs.(4.52) and (4.53) instead of the implicit scheme that was employed in Eqs.(2.34b) and (2.34c). This discretization is stable as long as either $\varepsilon \neq 0$ or $\lambda \neq \infty$.

In the FDTD procedure, we assume that at time step n the values of $H_y\big|^{n}$, $E_z\big|^{n-1/2}$, $E_x\big|^{n-1/2}$, $J_{sz}\big|^{n-1/2}$ and $J_{sx}\big|^{n-1/2}$ are known. The time-marching algorithm begins by first updating E_z and E_x using Eqs.(4.52) and (4.53). In order to express E_z and E_x in terms of known quantities, we first rewrite Eqs.(4.54) and (4.55) as

$$J_{sz}\Big|^{n+1/2}_{i,j+1/2} = J_{sz}\Big|^{n-1/2}_{i,j+1/2} + \frac{\Delta t}{2\mu_0\lambda^2\Big|^{n}_{i,j+1/2}}\left(E_z\Big|^{n+1/2}_{i,j+1/2} + E_z\Big|^{n-1/2}_{i,j+1/2}\right). \qquad (4.56)$$

$$J_{sx}\Big|_{i+1/2,j}^{n+1/2} = J_{sx}\Big|_{i+1/2,j}^{n-1/2} + \frac{\Delta t}{2\mu_0 \lambda^2\Big|_{i+1/2,j}^{n}}\left(E_x\Big|_{i+1/2,j}^{n+1/2} + E_x\Big|_{i+1/2,j}^{n-1/2} \right). \tag{4.57}$$

where the values of λ on cell boundaries are obtained using harmonic averages; for example,

$$\lambda\Big|_{i,j+1/2}^{n} = \left[\frac{1}{2}\left(\frac{1}{\lambda\Big|_{i,j}^{n}} + \frac{1}{\lambda\Big|_{i,j+1}^{n}}\right)\right]^{-1} = \frac{2\left(\lambda\Big|_{i,j}^{n}\right)\left(\lambda\Big|_{i,j+1}^{n}\right)}{\lambda\Big|_{i,j}^{n} + \lambda\Big|_{i,j+1}^{n}},$$

with $\lambda\Big|_{i,j}^{n} = \lambda\left(H_y\Big|_{i,j}^{n} \right).$

Note that since $\lambda \propto 1/\sigma_s$, harmonic averaging of the penetration depth is equivalent to taking the arithmetic average of the superconductivity. As will be shown later, the other material parameters, ε and σ_n, are also computed using arithmetic averaging, so for consistency λ must be averaged using the harmonic formula. Substituting Eqs.(4.56) and (4.57) into Eqs.(4.52) and (4.53), respectively, we obtain the marching formulas for E_x and E_z,

$$E_z\Big|_{i,j+1/2}^{n+1/2} = \frac{a_1}{a_2} E_z\Big|_{i,j+1/2}^{n-1/2} + \frac{1}{a_2 \Delta x}\left(H_y\Big|_{i,j+1}^{n} - H_y\Big|_{i,j}^{n} \right) - \frac{1}{a_2} J_{sz}\Big|_{i,j+1/2}^{n-1/2} \tag{4.58}$$

$$E_x\Big|_{i+1/2,j}^{n+1/2} = \frac{b_1}{b_2} E_z\Big|_{i+1/2,j}^{n-1/2} - \frac{1}{b_2 \Delta z}\left(H_y\Big|_{i+1,j}^{n} - H_y\Big|_{i,j}^{n} \right) - \frac{1}{b_2} J_{sx}\Big|_{i+1/2,j}^{n-1/2}, \tag{4.59}$$

in which

$$a_1 = \frac{\varepsilon_{i,j+1/2}}{\Delta t} - \frac{\sigma_n\Big|_{i,j+1/2}^{n}}{2} - \frac{\Delta t}{4\mu_0 \lambda^2\Big|_{i,j+1/2}^{n}},$$

$$a_2 = \frac{\varepsilon_{i,j+1/2}}{\Delta t} + \frac{\sigma_n\Big|_{i,j+1/2}^{n}}{2} + \frac{\Delta t}{4\mu_0 \lambda^2\Big|_{i,j+1/2}^{n}},$$

$$b_1 = \frac{\varepsilon_{i+1/2,j}}{\Delta t} - \frac{\sigma_n\Big|_{i+1/2,j}^{n}}{2} - \frac{\Delta t}{4\mu_0 \lambda^2\Big|_{i+1/2,j}^{n}},$$

$$b_2 = \frac{\varepsilon_{i+1/2,j}}{\Delta t} + \frac{\sigma_n\big|^n_{i+1/2,j}}{2} + \frac{\Delta t}{4\mu_0\lambda^2\big|^n_{i+1/2,j}}.$$

In the above, the values of the material properties, ε and σ_n, on cell boundaries are computed using arithmetic averaging; for example,

$$\varepsilon_{i,j+1/2} = \tfrac{1}{2}\left(\varepsilon_{i,j} + \varepsilon_{i,j+1}\right),$$

$$\sigma_n\big|^n_{i,j+1/2} = \frac{1}{2}\left[\sigma_n\left(H_y\big|^n_{i,j}\right) + \sigma_n\left(H_y\big|^n_{i,j+1}\right)\right].$$

Having obtained $E_z\big|^{n+1/2}$ and $E_x\big|^{n+1/2}$, the superconducting current components J_{sz} and J_{sx} can be updated using Eqs.(4.56) and (4.57). Finally the H_y field is marched using Eq.(4.51):

$$H_y\big|^{n+1}_{i,j} = H_y\big|^n_{i,j} + \frac{E_z\big|^{n+1/2}_{i,j+1/2} - E_z\big|^{n+1/2}_{i,j-1/2}}{\Delta t/\mu_0\Delta x} - \frac{E_x\big|^{n+1/2}_{i+1/2,j} - E_x\big|^{n+1/2}_{i-1/2,j}}{\Delta t/\mu_0\Delta z}. \tag{4.60}$$

In Figure 4.9 we summarize the computation flow of the FDTD algorithm for HTS media. Note that by virtue of our scheme of assigning time and space indexes to the field and current components, the above FDTD procedure does not require solution of nonlinear equations and can thus be executed in a speedy and efficient manner.

If the superconducting medium is assumed linear, the HTS FDTD algorithm can be shown to be stable if the CFL condition (2.46) is satisfied [50]. An analytical stability condition for the nonlinear case is unknown, but no problems of instability have been encountered for simulations running with CFL coefficient almost equal to 1. Also, the numerical dispersion relation for the HTS leap-frog scheme is similar to Eq.(2.61) derived for normal conducting media, except for an additional term involving λ:

$$\begin{aligned}&\frac{\sin^2(\beta\Delta z/2)}{(\Delta z)^2} + \frac{\sin^2(\beta\Delta x/2)}{(\Delta x)^2} = \\ &\quad -\frac{1}{(2\lambda)^2} + \left(\mu_0\varepsilon + \tfrac{1}{2}\mu_0\sigma_n\Delta t\right)\frac{\sin^2(\omega\Delta t/2)}{(\Delta t)^2} - j\tfrac{1}{4}\mu_0\sigma_n\frac{\sin(\omega\Delta t)}{\Delta t}\end{aligned} \tag{4.61}$$

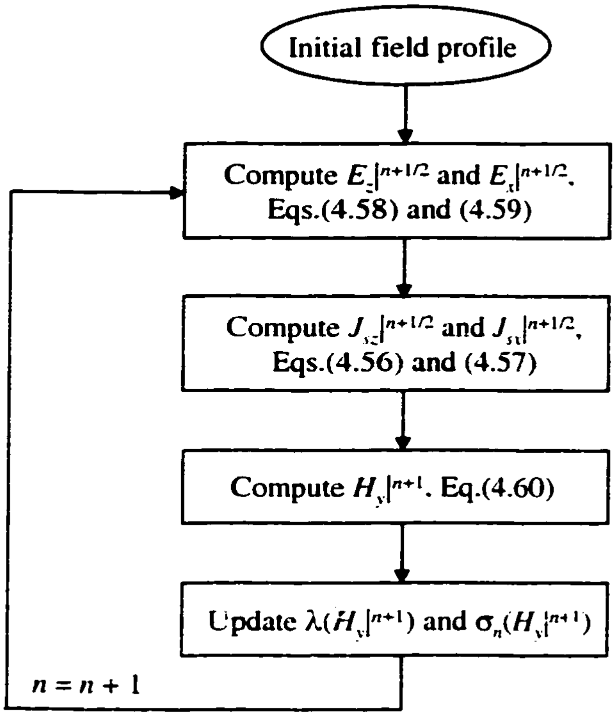

Figure 4.9. Computation flow for the HTS FDTD method.

As in the case of normal conductors, the errors due to numerical dispersion are dominated by finite grid-size effects at millimeter-wave frequencies, and can be reduced by using mesh refinement.

In this thesis, all HTS structures of interest can be canonically respresented by the 2D waveguide shown in Figure 4.10. The structure consists of a perfect electric-conducting (PEC) waveguide which serves as a launcher and in which various TM modes can be excited. These modes are then fed into the structure under simulation, which is an HTS waveguide whose superconducting walls may be patterned with normal conductors. The dielectric substrate is assumed to be linear. We use the hybrid single-field leap-frog FDTD method developed in Chapter 2 to simulate the structure, in which the HTS thin films are designated as local domains.

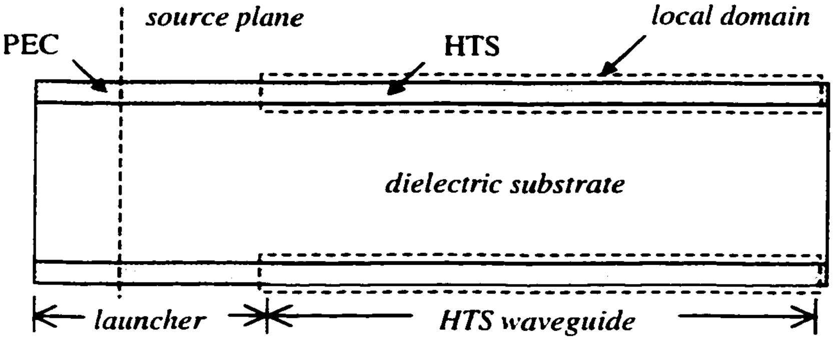

Figure 4.10. Canonical structure for simulating HTS waveguides. The PEC waveguide at the input serves as the mode launcher. Fields in the local domain are solved using the leap-frog HTS FDTD method, while fields in the main grid are marched using the explicit single-field FDTD scheme.

In the procedure, the fields in the HTS local domains are first computed using the full-wave HTS FDTD method developed in this section. The fields in the dielectric substrate and in the regions surrounding the waveguide are next obtained using the single-field scheme. Finally PEC boundary conditions are applied on the walls of the launcher. Note that the case of a PEC plate traversing a main-grid-local-grid boundary has been considered in our development of the hybrid single-field leap-frog FDTD scheme in Chapter 2. Also, since our hybrid scheme allows subgridding in the local domain, the mesh in the HTS regions can be made finer than the global grid in order to more accurately resolve the fields in the HTS thin films, where the nonlinear effects occur.

4.4 Summary

In this chapter a comprehensive discussion of nonlinearity in HTS materials was presented. We showed that by incorporating the nonlinear Meissner effect into the London theory of superconductivity, the resulting nonlinear London equations can be used to provide accurate analysis of the electromagnetic responses of HTS materials. We established a relationship between the London and GL theories by showing that the second nonlinear London equation is identical to the second GL equation, and along with the appropriate model for the field dependence of the penetration depth, provides excellent approximation to the GL solutions. For simulating wave propagation in HTS microwave and millimeter-wave devices, we developed an efficient FDTD method which incorporates the first nonlinear London equation into the solution of Maxwell's equations. The new technique has both the computational simplicity of the explicit FDTD method and the accuracy of the GL-based approach.

Chapter 5

HTS Device Applications

In this chapter we demonstrate the application of the FDTD method developed in the previous chapter to simulate practical HTS microwave and millimeter-wave devices. Using the linear HTS parallel-plate waveguide as a benchmark, we first validate the numerical method by comparing simulation results to analytical solutions. This is followed by investigation of more complicated HTS structures. In particular, nonlinear wave propagation in resonating and periodic waveguides are discussed in detail, and the practical applications of these devices to microwave and millimeter-wave signal processing will be explored.

5.1 HTS Parallel-Plate Waveguides

Like the two-dimensional dielectric slab waveguide, the HTS parallel-plate waveguide is the simplest structure with which we can study propagation of guided waves in HTS media. We will first consider the low-field case where the superconductors can be considered linear. The known analytical solution of the linear HTS transmission line allows us to verify the simulation results, thereby validating both the HTS FDTD method and the hybrid single-field leap-frog scheme proposed in Chapter 2. Nonlinearity is then introduced into the HTS thin films to study its effect on wave propagation in the waveguide. The various nonlinear Meissner models for the magnetic field dependency of λ are also investigated. An understanding of the propagation characteristics in the nonlinear HTS parallel-plate waveguide will help give insights into more complicated HTS devices to be investigated later in the chapter.

We consider the two-dimensional HTS parallel-plate waveguide shown in Figure 5.1. Both upper and lower plates of the waveguide are assumed to be made of YBCO deposited on $LaAlO_3$ substrate, which is chosen because of the relatively low loss tangent of the dielectric (less than 10^{-5}). Like most HTS materials, YBCO is highly anisotropic, exhibiting vastly different material properties depending on the direction of the current flow with respect to the Cu-O planes, commonly known as the *ab* planes, in the superconductor [77]. For example, the penetration depth of YBCO is 0.15μm for current flow parallel to the *ab* plane but can be as high as 0.77μm for current flow perpendicular to the plane. Because the direction parallel to the *ab* plane experiences the least resistance, it is the preferred direction for current flow, and hence HTS materials are usually deposited with the *ab* plane parallel to the substrate. Assuming this is the case for our waveguide, the value of the zero-field penetration depth at 0K, λ_0, for YBCO is then 0.15μm. Other parameters of the HTS are $\varepsilon = \varepsilon_0$, $\sigma_n(T_c) = 4.0$S/μm and $T_c = 92$K. The thickness of the superconducting plates is t. The $LaAlO_3$ substrate has a nominal dielectric constant of 24.0 and thickness h. The waveguide is excited by the TEM mode at the source plane located in the perfect electric-conducting waveguide launcher.

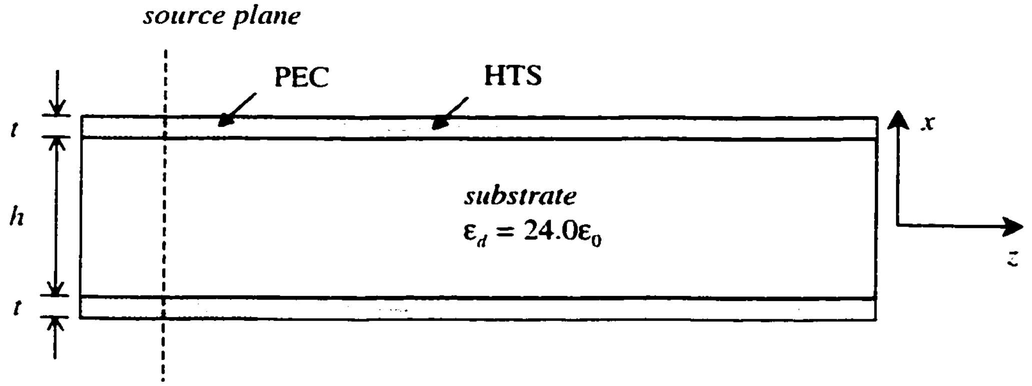

Figure 5.1. Two-dimensional HTS parallel-plate waveguide. The superconducting plates are assumed to be YBCO and the substrate is $LaAlO_3$.

(a) Linear response

It was stated that the response of an HTS material can be considered linear in the low field limit, $H \ll H_c$. Under this condition the superconductor can be assigned a complex but linear conductivity,

$$\tilde{\sigma} = \sigma_n + j(\omega\varepsilon_0 - \sigma_s) = \sigma_n + j\left(\omega\varepsilon_0 - 1/\omega\mu_0\lambda^2\right). \tag{5.1}$$

in which σ_n and λ are functions of temperature but independent of frequency. If the HTS plates are assumed to have infinite thickness ($t \gg \lambda$), we can derive the exact analytical expression for the complex propagation constant [102]:

$$\gamma = \alpha + j\beta = jk_d\sqrt{1 - j\frac{2Z_s}{\omega\mu_0 h}} \tag{5.2}$$

where $k_d = \omega\sqrt{\mu_0\varepsilon_d}$, and Z_s is the surface impedance of the HTS plates:

$$Z_s = \sqrt{\frac{j\omega\mu_0}{\sigma_n + j(\omega\varepsilon_0 - \sigma_s)}}. \tag{5.3}$$

Note that for the infinitely thick plates, Z_s is also equal to the intrinsic impedance of the HTS medium. In the superconducting state, $\sigma_s \gg \omega\varepsilon_0$ and $\sigma_s \gg \sigma_n$; in this case the surface impedance can be approximated from Eq.(5.3) as follows:

$$Z_s \approx \sqrt{\frac{j\omega\mu_0}{\sigma_n - j\sigma_s}} = \frac{j\sqrt{\omega\mu_0/\sigma_s}}{\sqrt{1 + j\sigma_n/\sigma_s}} \approx j\omega\mu_0\lambda\left(1 - j\frac{\sigma_n}{2\sigma_s}\right).$$

and hence

$$Z_s = R_s + jX_s \approx \tfrac{1}{2}\omega^2\mu_0^2\lambda^3\sigma_n + j\omega\mu_0\lambda. \tag{5.4}$$

The above equation is identical to Eq.(4.19). If we further assume that $2Z_s/\omega\mu_0 h \ll 1$ in Eq.(5.2), which is valid for thick plates with negligible loss, the complex propagation constant can be approximated to first order as

$$\gamma \approx jk_d\left(1 - j\frac{Z_s}{\omega\mu_0 h}\right). \tag{5.5}$$

Substituting Eq.(5.4) for Z_s into the above equation, we obtain

$$\beta \approx k_d(1 + \lambda/h). \tag{5.6}$$

and
$$\alpha \approx \frac{k_d R_s}{\omega\mu_0 h} = \frac{\omega^2\mu_0\sqrt{\mu_0\varepsilon_d}\lambda^3\sigma_n}{2h}, \tag{5.7}$$

which show that the propagation constant β varies linearly with frequency whereas the attenuation constant α varies as ω^2.

We simulated the HTS waveguide in Figure 5.1 under the assumption of linear response to study the temperature and frequency dependencies of the complex propagation constant γ. The thickness t of the HTS plates was set at 1.5μm and the substrate thickness h at 6.75μm. To investigate the effect of the temperature, we fixed the frequency of the input TEM-mode continuous-wave signal at 40GHz, and varied the normalized temperature, $T_n = T/T_c$, from 0 to 1. The temperature variations of the penetration depth and the superconductivity were assumed to follow the Gorter-Casimir relations [79]

$$\lambda = \frac{\lambda_0}{\sqrt{1 - T_n^4}}. \tag{5.8}$$

$$\sigma_n = \sigma_n(T_c)T_n^4. \tag{5.9}$$

The structure was discretized with grid sizes Δx = 0.25μm and Δz = 5.0μm, and the simulations were run at time step Δt = 4.0fs (CFL = 0.98). The ratio of the main grid to local grid was set to 1. Liao's absorbing boundary condition was used to absorb waves at the computational boundaries.

For each temperature value, the FDTD simulation was run for several time periods and the signals at two points separated by a distance dz in the waveguide were recorded. From the information on the phase and amplitude differences between these two signals, the propagation and attenuation constants can be computed. This method of extracting γ is referred to as the two-probe method; it gives a fast and relatively reliable way of calculating the complex propagation constant of the TEM mode. In Figures 5.2(a) and (b) we plotted the extracted propagation and attenuation constants as functions of the normalized temperature. The analytical values computed using Eq.(5.2) are also shown for comparison. The plots show that the FDTD results are in good agreement with theory. The error in β was determined to be less than 1%, while the error in α was less than 5% for $T_n > 0.4$ but could be as high as 20% for $T_n < 0.4$. A major source of these errors could be traced back to the extraction procedure of the complex propagation constant from the time signals recorded during the FDTD simulations. As the temperature approaches 0K, the corresponding decrease in the attenuation constant causes the amplitude difference at successive positions in the waveguide to be more difficult to be resolved accurately, leading to a degradation in the accuracy of the extracted α. In addition, numerical reflections due to imperfect absorption at the computational boundaries also contributed to the errors in the amplitudes. It was observed that these numerical reflections had a more adverse effect on the signal amplitude than on the phase, which explains the fact that the accuracy of β was generally better than that of α.

An important observation which can be made from the plots in Figure 5.2 is that α generally exhibits a stronger dependence on temperature than β. Over the entire normalized temperature range, α changes by almost six orders of magnitude, while β varies by only 5%. The reason for the large variation in α is partly due to assumed T_n^4 dependency of the normal conductivity. The logarithmic plot in Figure 5.2(b) has a slope close to 4 at low temperatures, indicating that the attenuation constant also varies as T_n^4. This relationship can be checked using Eq.(5.7), which states that

$$\alpha \propto \lambda^3(T_n)\sigma_n(T_n).$$

Substituting Eqs.(5.8) and (5.9) for the temperature dependencies of λ and σ_n into the above relation, we obtain

$$\alpha \propto \lambda_0^3\sigma_n(T_c)\frac{T_n^4}{\left(1-T_n^4\right)^{3/2}} \propto T_n^4, \qquad \text{for } T_n \ll 1,$$

which confirms that to first order, the attenuation constant of the waveguide increases as the fourth power of the temperature.

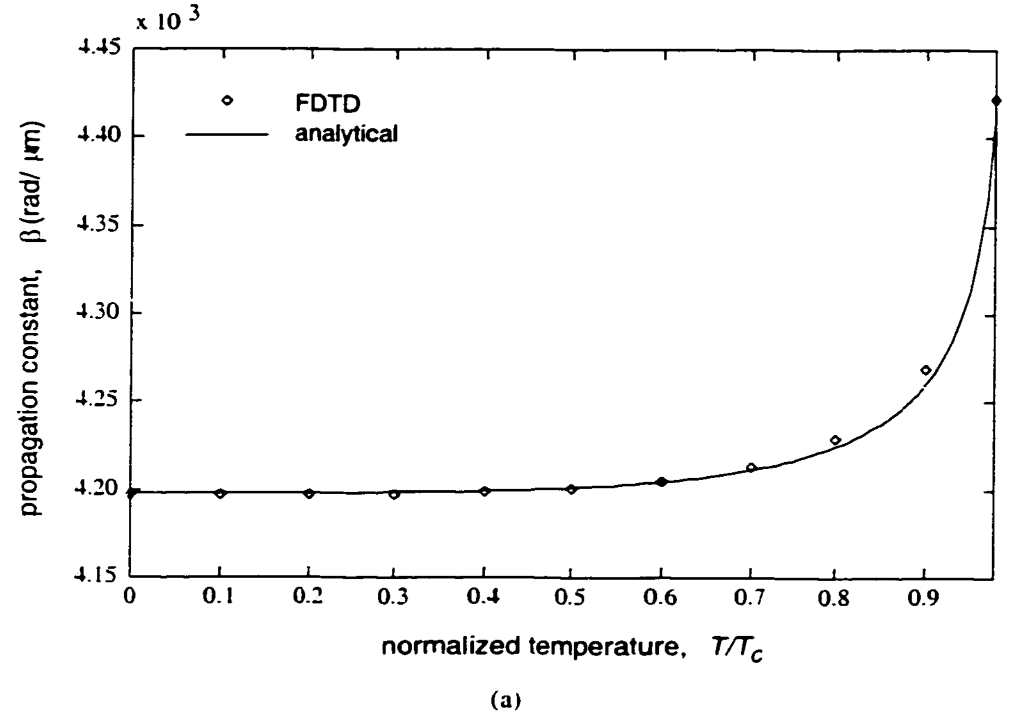

(a)

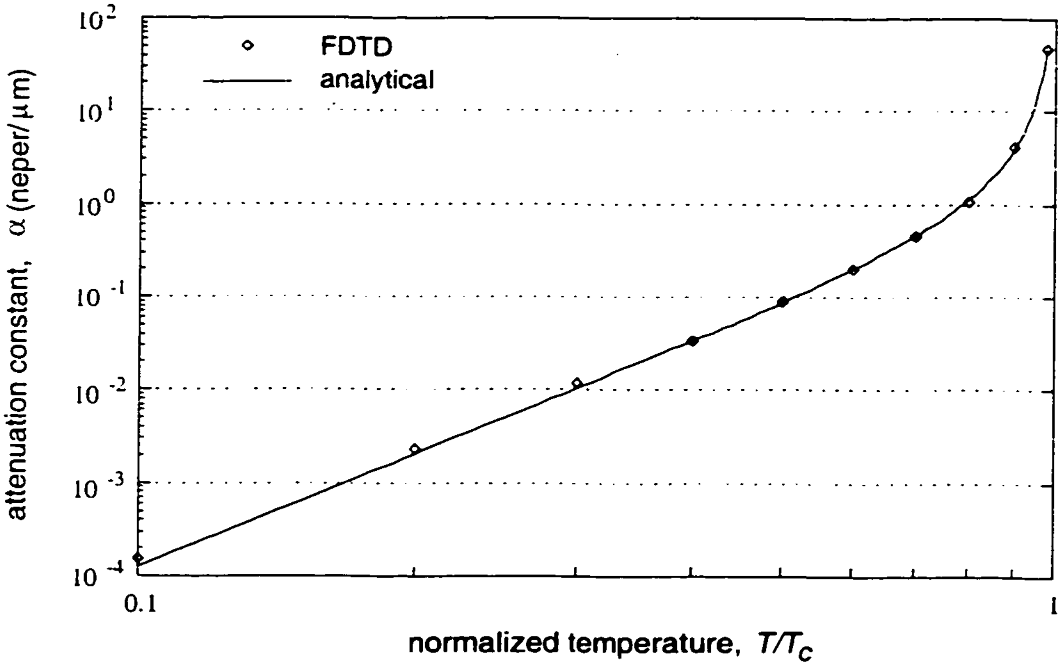

(b)

Figure 5.2. Analytical and simulated temperature variations of (a) the propagation constant β and (b) the attenuation constant α of the YBCO parallel-plate waveguide at f = 40GHz.

We next investigated the frequency variation of the complex propagation constant at a fixed temperature T = 77K. At this ambient temperature the values of the penetration depth λ and superconductivity σ_n were 0.210μm and 1.96S/μm, respectively. Simulations were performed over the frequency range 10 – 120GHz. The complex propagation constant was extracted from the simulation results using the two-probe method, and plotted against the frequency in Figures 5.3(a) and (b). Also shown in the plots by the solid lines are the analytical values of β and α computed using Eq.(5.2). The numerical and theoretical results are again seen to be in excellent agreement with each other, both showing the expected linear f dependency for β and f^2 dependency for α of the HTS waveguide. To compare these results with those of a normal conducting waveguide we also included in the plots, with dashed lines, the propagation and attenuation constants of a copper waveguide with identical dimensions to those of the HTS waveguide. The copper was also assumed to be at 77K; at this cryogenic temperature its conductivity is 255S/μm, nearly ten times higher than the value at room temperature. The plots show that the superconducting waveguide and the metal waveguide have almost the same propagation constant β, but the latter is one to two orders of magnitude more lossy. However, the attenuation constant of the metal waveguide varies only as $f^{1/2}$, whereas in the HTS waveguide, it increases as f^2. Thus there exists a cross-over frequency beyond which the superconducting waveguide becomes more lossy than the copper waveguide. For YBCO at 77K, this cross-over point occurs in the 200 – 300GHz range.

(b) Nonlinear response

As stated in Chapter 4, the nonlinear Meissner effect causes the field to penetrate more deeply into a superconductor as the external field is increased. This phenomenon was demonstrated in that chapter for the case of a static magnetic field applied to a one-dimensional HTS slab. We now show that the same field behaviour is also observed for the electrodynamic case of wave propagation in an HTS waveguide. Consider the same parallel-plate transmission line shown in Figure 5.1, except that the HTS was now assumed to exhibit nonlinear Meissner effect described by the XYS model. The expression for the dependence of λ on H is given by Eq.(4.3) with the anisotropy parameter γ = 1. The waveguide was assigned substrate thickness h = 5.70μm and superconducting film thickness t = 0.90μm. The ambient temperature T was set to 77K, which gives $\lambda(T)$ = 0.210μm and $\sigma_n(T)$ = 1.96S/μm. The structure was excited with a

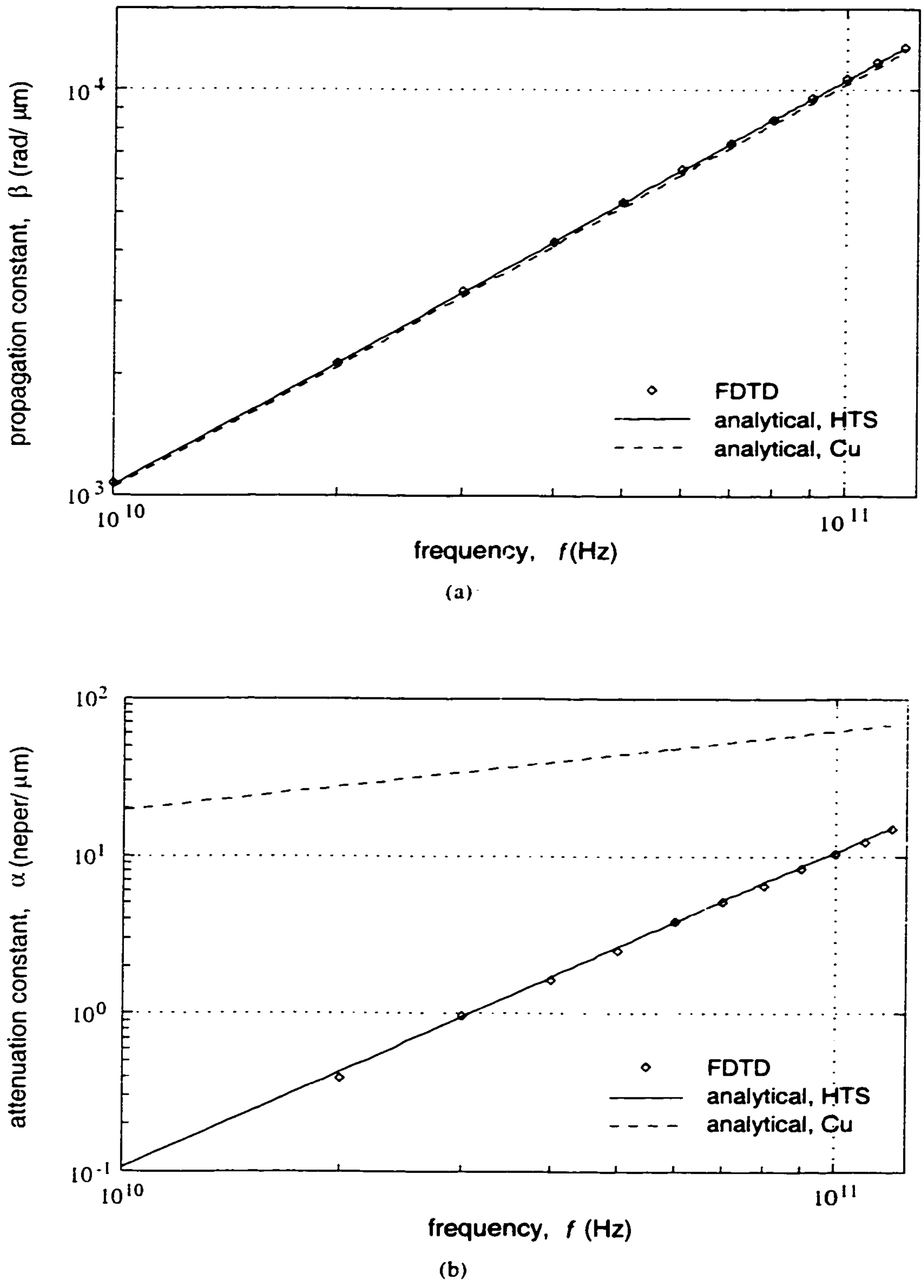

Figure 5.3. Analytical and simulated frequency variations of (a) the propagation constant β and (b) the attenuation constant α of YBCO and Cu parallel-plate waveguides at $T = 77$K.

TEM-mode continuous-wave signal at 40GHz. In order to better resolve the field profile inside the HTS thin films, we simulated the structure using the hybrid single-field leap-frog FDTD scheme with local-to-global mesh ratio $r = 3$. The main grid sizes were $\Delta x = 0.3\mu m$ and $\Delta z = 6.0\mu m$, with global time step $\Delta t = 4.8fs$ (CFL = 0.98). The simulation was observed to be stable for several thousand time steps, after which instability began to develop at the interfaces between the main grid and local grid. As discussed in Chapter 2, this instability resulted from interpolation errors at the main-grid-local-grid boundaries and from numerical resonance inside the local domain. To avoid erroneous solutions, all simulations were terminated well before they became unstable. It should be noted that for mesh ratio $r = 1$, instability was not observed because no interpolation was required.

In Figure 5.4 we show the transverse magnetic field profile inside the lower HTS plate for different input signal amplitudes. All the fields were normalized with respect to the maximum field value, H_{max}, which occurred at the inner HTS surface of the waveguide. For

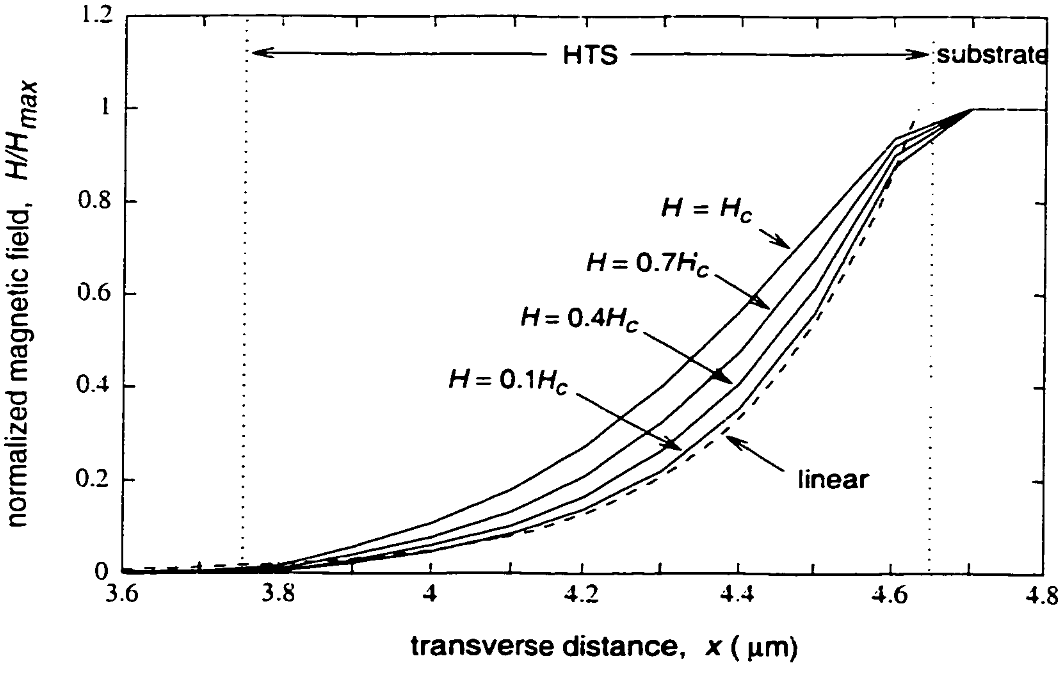

Figure 5.4. Transverse magnetic field profile inside the lower HTS plate with XYS nonlinearity. The field is normalized with respect to the maximum value at the surface of the superconducting plate. Also shown is the field profile in a linear HTS plate (dashed line).

comparison, the analytic $e^{-x/\lambda(T)}$ decay exhibited by the field inside a linear superconductor is also shown in the plot by the dashed line. It is evident from the figure that nonlinearity causes field penetration into the HTS plate to become more pronounced as the input power is increased. This effect implies that high-amplitude waves travel more slowly in the waveguide and suffer from higher loss than waves with low amplitudes.

To further investigate the effect of nonlinearity on wave propagation, we next looked at the variation of the complex propagation constant with respect to the input field amplitude. Four nonlinear models for $\lambda(H)$ were considered: the GL model, the first-order model, the second-order model and the XYS model, all of which are summarized in Table 5.1 along with the corresponding field dependencies of the normal conductivity. FDTD simulations for each case were performed and the complex propagation constant γ extracted using the two-probe method described previously. Figures 5.5(a) and 5.5(b) show the percentage changes of β and α with respect to the linear (low-field) values as functions of the input magnetic field amplitude. It is evident that the effect of nonlinearity is to decrease the phase velocity and increase the skin loss. We also observe that the variation of β with respect to H tends to follow the functional dependence of $\lambda(H)$; for example, β varies linearly with H when the HTS is assumed to have first-order nonlinearity. This is expected because, as indicated by Eq.(5.6), the propagation constant is proportional to $\lambda(H)$ at low fields where first-order approximations can be made. A

GL model	$\lambda' = (1 - H'^2)^{-1/4}$	$\sigma_n = \sigma_{nc} - (\sigma_{nc} - \sigma_{n0})(1 - H'^2)^{1/2}$
first-order model	$\lambda' = 1 + \lvert H' \rvert$	$\sigma_n = \sigma_{nc} - (\sigma_{nc} - \sigma_{n0})/(1 + \lvert H' \rvert)^2$
second-order model	$\lambda' = 1 + H'^2$	$\sigma_n = \sigma_{nc} - (\sigma_{nc} - \sigma_{n0})/(1 + H'^2)^2$
XYS model	$\lambda' = (1 - H')^{-1}$	$\sigma_n = \sigma_{nc} - (\sigma_{nc} - \sigma_{n0})(1 - H')^2$

$\lambda' = \lambda/\lambda_0$; $\sigma_{nc} = \sigma_n(T_c,0)$;

$H' = H/H_c$; $\sigma_{n0} = \sigma_n(T,0)$;

Table 5.1. Nonlinear Meissner models for $\lambda(H)$ and the corresponding field dependences of the normal conductivity.

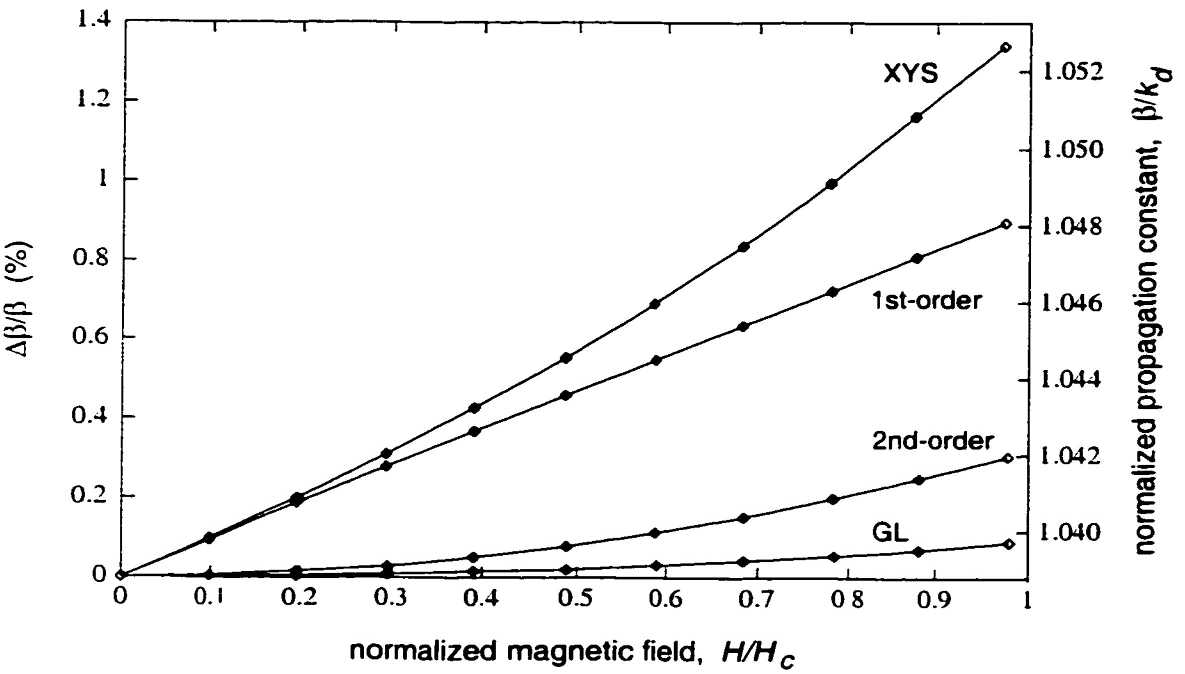

(a)

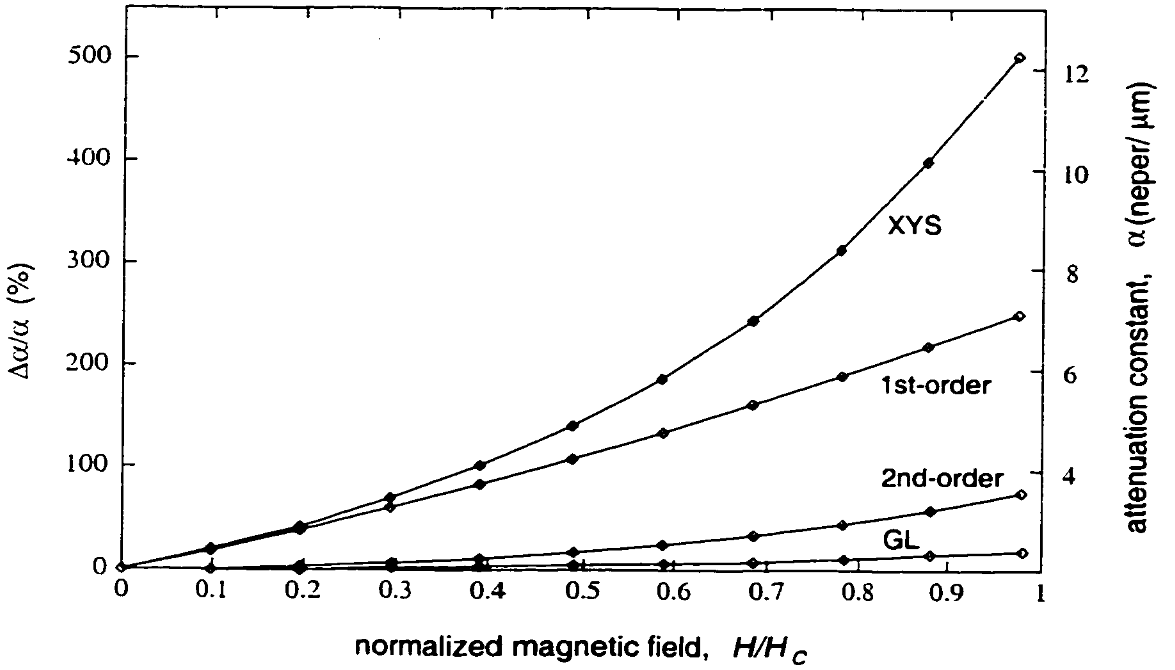

(b)

Figure 5.5. Percentage changes of (a) the propagation constant β and (b) the attenuation constant α with respect to linear (low-field) values as functions of the input field amplitude. The HTS waveguide is at 77K and the input frequency is 40GHz.

direct consequence of this observation is that the field dependence of β can provide a signature for the underlying field dependence of λ. Thus by measuring the variation of the propagation constant of an HTS transmission line with respect to the input signal amplitude, the nonlinear Meissner model for $\lambda(H)$ of the superconductor can be deduced.

From the formulas in Table 5.1 it is seen that both the XYS and GL nonlinear models predict that the penetration depth becomes infinitely large as the field approaches the critical value H_c. The normal conductivity σ_n, however, remains finite and approaches the value of the normal state, $\sigma_n(T_c,0)$. This implies that the normal skin depth δ constantly decreases as H approaches the transition point, and reaches the value corresponding to the normal state at H_c. We thus expect that there exists a cross-over field where the penetration depth λ exceeds the skin depth; at this point the normal conduction mechanism begins to dominate over the superconductive effect in the HTS. In the limit $\delta \ll \lambda$, which occurs near the critical field H_c, the propagation and attenuation constants in Eqs.(5.6) and (5.7) are simply replaced by the expressions for a normal conducting waveguide:

$$\beta = k_d(1 + \delta/2h) \tag{5.10}$$

$$\alpha = k_d\delta/2h. \tag{5.11}$$

Thus as H approaches H_c, we expect that the propagation and attenuation constants in Figures 5.5(a) and (b) approach the values of the waveguide in the normal conducting state. Note that in order for σ_n to approach $\sigma_n(T_c,0)$ at $H = H_c$, the function $f(H/H_c)$ in Eq.(4.45) must become infinite at H_c. This property is satisfied in the XYS and GL models but not in the first-order and second-order models, implying that the latter two models are not physically valid near the critical field. However, this observation does not completely invalidate these empirical models because they are simply fitting functions for measurements of λ at low fields, and are thus expected to be valid only in the low-field limit.

The dependence of the propagation constant on the field, as observed in Figure 5.5(a), implies that harmonic frequencies are generated during the nonlinear propagation through the HTS transmission line. Consider a wave traveling in the positive z direction; its propagation can be described to first order by the equation

$$\frac{\partial H}{\partial z} = -\gamma H \, . \tag{5.12}$$

where $\gamma = \alpha + j\beta$ is the complex propagation constant. Assuming the superconducting films have XYS nonlinearity, from the results in Eqs.(5.6) and (5.7), it is seen that both α and β are functions of $|H|$, which implies that γ is an even function of H. Supposing now that the transmission line is excited by an input wave of the form

$$H_{in}(t) = H_{dc} + H_{ac}\cos(2\pi f_0 t), \tag{5.13}$$

we consider two cases: (a) $H_{dc} = 0$ and (b) $H_{dc} \geq H_{ac} \neq 0$. In the first case, the applied signal oscillates about the origin with no DC offset, so in the small-signal limit, $\gamma(|H|)$ can be represented by a series expansion around 0 which contains only even-order terms:

$$\gamma(|H|) \approx a_2 H^2 + a_4 H^4 + \ldots \tag{5.14}$$

Substituting the above expression into Eq.(5.12), we obtain

$$\frac{\partial H}{\partial z} = -a_2 H^3 - a_4 H^5 - \ldots, \tag{5.15}$$

from which it is evident that only odd-order harmonics will be generated during the propagation. In the second case, the input sinusoidal signal is biased at a DC value, $H_{dc} \geq H_{ac}$, so the small-signal series expansion of $\gamma(|H|)$ around H_{dc} contains both odd- and even-order terms:

$$\gamma(|H|) \approx b_0 + b_1 H + b_2 H^2 + b_3 H^3 + b_4 H^4 + \ldots \tag{5.16}$$

Substituting this expression into Eq.(5.12) gives

$$\frac{\partial H}{\partial z} = -b_0 H - b_1 H^2 - b_2 H^3 - b_3 H^4 - b_4 H^5 - \ldots, \tag{5.17}$$

which shows that both even- and odd-order harmonics will be generated.

Experimentally, harmonic generation resulting from propagation through BSCCO and YBCO thin films has been observed and was reported, among others, by Golosovsky *et. al.* in [82]. That experiment, however, used low-frequency microwave transmission through HTS thin films instead of wave propagation in HTS waveguides. The authors also presented an analysis of the nonlinear process based on the dependence of the complex resistivity of the films on the applied magnetic field. In the following we will show by FDTD simulations that harmonic generation can also be observed for wave propagating in an HTS transmission line.

Assuming XYS nonlinearity for the YBCO, we simulated the HTS parallel-plate waveguide under two input conditions: for case (a), $H_{dc} = 0$ and $H_{ac} = 0.97H_c$; and for case (b), $H_{dc} = H_{ac} = 0.49H_c$. Note that in both cases the peak input magnetic field was less than the critical field H_c so that the HTS films were not driven into the normal conducting state. The frequency f_0 of the input sinusoid was 30GHz. The length l of the nonlinear transmission line, also acting as the active region, was 15mm. Figures 5.6 and 5.7 show the spectra of the output signals recorded under the two input conditions. The spectrum powers were normalized with respect to the power of the fundamental harmonic f_0. As expected, only odd-order harmonic frequencies are observed in the first case, whereas for the second case, the inclusion of the DC bias resulted in both even- and odd-order harmonics being generated. Note that the strength of the harmonics decreases with the harmonic order because of the corresponding increase in the energy required to generate them, and also because of the rapid increase in the superconductor loss at high frequencies. Also, the small spikes corresponding to even harmonics in Figure 5.6 are purely numerical artifacts, most likely due to imperfect numerical absorption at the computational boundaries.

The conversion efficiency, defined by the ratio of the harmonic power to the power of the fundamental frequency, was calculated to be 1.3% for the third-order harmonic under input condition (a). For case (b), the conversion efficiency was 2.3% for the second-order harmonic and 0.2% for the third-order harmonic. Note that these values correspond to a peak applied field almost equal to the critical magnetic field. In an analysis of nonlinear distributed *LC* transmission lines, Champlin and Singh showed that the conversion efficiency in general is proportional to the square of the input signal amplitude and the length of the active region [116]. The authors also showed that for low-loss transmission lines, the optimum length l for which the second-order harmonic power is maximized approaches infinity. In our HTS example, further increasing the applied field would only drive the HTS films into the normal state without improving the conversion efficiency. Therefore the only way to increase the efficiency is to increase the interaction length l of the nonlinear transmission line. Based on the analysis of

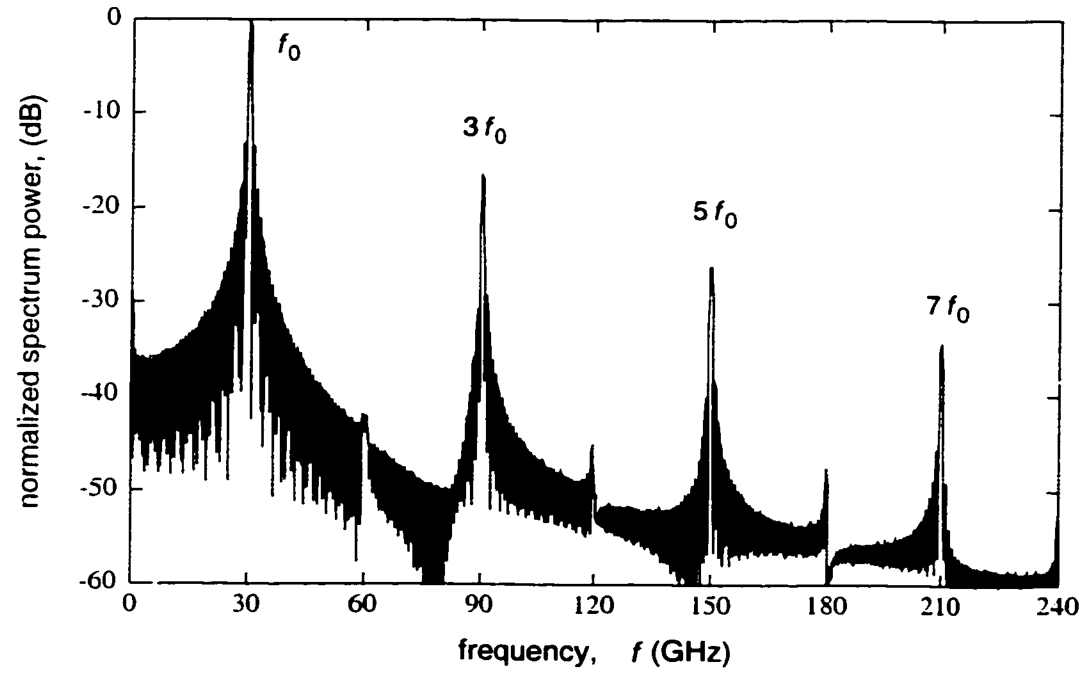

Figure 5.6. Generation of odd-order harmonics in an HTS transmission line with XYS nonlinearity. The input signal is a pure sinusoid, $H_{in}(t) = 0.97H_c\cos(2\pi f_0 t)$, where f_0 = 30GHz.

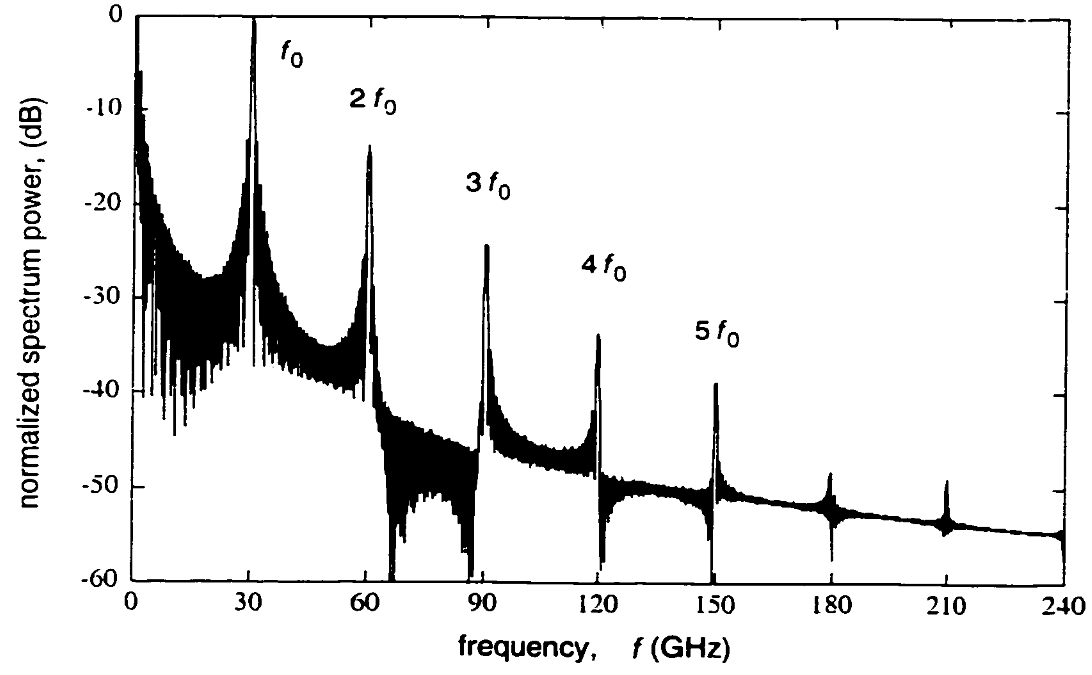

Figure 5.7. Generation of even- and odd-order harmonics in an HTS transmission line with XYS nonlinearity. The input signal is a sinusoid with DC offset, $H_{in}(t) = 0.47H_c(1 + \cos(2\pi f_0 t))$, where f_0 = 30GHz.

Champlin and Singh we also expect the optimum length l for second-order harmonic generation in the low-loss HTS transmission line to be also very large.

The numerical results presented above show that it is possible to generate harmonic frequencies using HTS transmission lines, although the conversion efficiencies are low compared to conventional technology using distributed active elements in normal transmission lines [112-115]. Also, although we considered only the case of XYS nonlinearity, all the other nonlinear models listed in Table 5.1 will result in harmonic generation since the mechanism for frequency generation is the same, namely, the dependence of λ and σ_n on the magnetic field. Note that since all the models describe field dependencies of λ which are even functions of H, it is expected that a pure AC input will result in the generation of only odd-order harmonics, whereas all harmonic orders will be generated if a DC bias is also applied. The difference among the models is the strength of the generated harmonics for a given applied field amplitude and a fixed length of the HTS transmission line. It is obvious that the stronger the nonlinearity, the higher the conversion efficiency that can be achieved.

(c) Applications

The most common application of HTS transmission lines is their use as delay elements. Delay lines are the basic elements of tapped delay line structures, which are used to perform a large number of analog signal processing functions [108]. Because of their extremely low insertion loss and compact size, HTS delay lines are superior to normal transmission lines. With the introduction of nonlinearity, the delay time of an HTS line also depends on the input signal power, presenting an additional parameter that can be exploited for signal processing. We saw in Figure 5.5(a) that the XYS nonlinear model resulted in a maximum increase of nearly 1.4% in the propagation constant, or an increase of 6×10^{-5}rad/μm at 40GHz. This translates to a delay time of 0.2fs/μm. As an example, a 1ns delay line using the parallel-plate transmission line in Figure 5.1 has a length of 60cm at 40GHz. For this delay line, nonlinearity would cause the delay time to vary by 13ps, corresponding to slightly over π radians in phase shift. With this sensitivity of the phase with respect to the input power, important functions could be achieved, such as power discrimination using HTS tapped delay lines, and signal switching using coupled HTS transmission lines.

The generation of higher frequency components in an HTS transmission line, as demonstrated in the previous section, implies that fast time-varying signals can be generated. This phenomenon leads to the potential application of nonlinear HTS transmission lines in the generation of picosecond impulses via shock-wave propagation. With only a small amount of dispersion in an HTS transmission line to counteract the nonlinearity, a current pulse traveling down the line will become increasingly sharpened and eventually form a shock wave. The mechanism for shock-wave formation arises from the amplitude-dependent velocity experienced by different parts of the pulse, which is given to first order by

$$v(H)=\frac{\omega}{\beta}\approx\frac{\omega/k_d}{1+\lambda(H)/h}\approx v_d[1-\lambda(H)/h], \tag{5.18}$$

where $v_d=1/\sqrt{\mu_0\varepsilon_d}$ is the wave velocity in an unbounded substrate medium with dielectric constant ε_d. Since λ increases with H, the peak of the pulse will travel more slowly than the front and the tail; consequently, the back side of the pulse will become increasing steepened as it propagates down the line. This phenomenon can be used to generate pulses with very fast fall-times.

To demonstrate this effect, we launched a Gaussian pulse into the nonlinear HTS waveguide described in the previous section. The nonlinearity of the superconductor was assumed to follow the XYS model. The initial width of the input pulse was 8ps (FWHM), which corresponds to a bandwidth of 65GHz. Figure 5.8 shows the evolution of the pulse shape after traveling 4mm and 9mm along the transmission line. The sharpening of the tail and broadening of the front of the pulse as it traverses the waveguide are evident from the plot. In addition, attenuation of the pulse amplitude with distance is also seen. By contrast, Figure 5.9 shows a pulse in a linear HTS waveguide in which only dispersive effect is present. Without nonlinearity in this case, frequency dispersion causes the pulse to constantly broaden as it propagates down the waveguide.

In Figures 5.10 and 5.11, we show the 90%–10% fall-time and the amplitude, respectively, of an 8ps pulse and a 4ps pulse as functions of the distance travelled. Also shown for comparison in the plots by the dashed lines are the fall-time and amplitude of a pulse traveling in a linear HTS waveguide. We make two important observations. Firstly, the fall-time

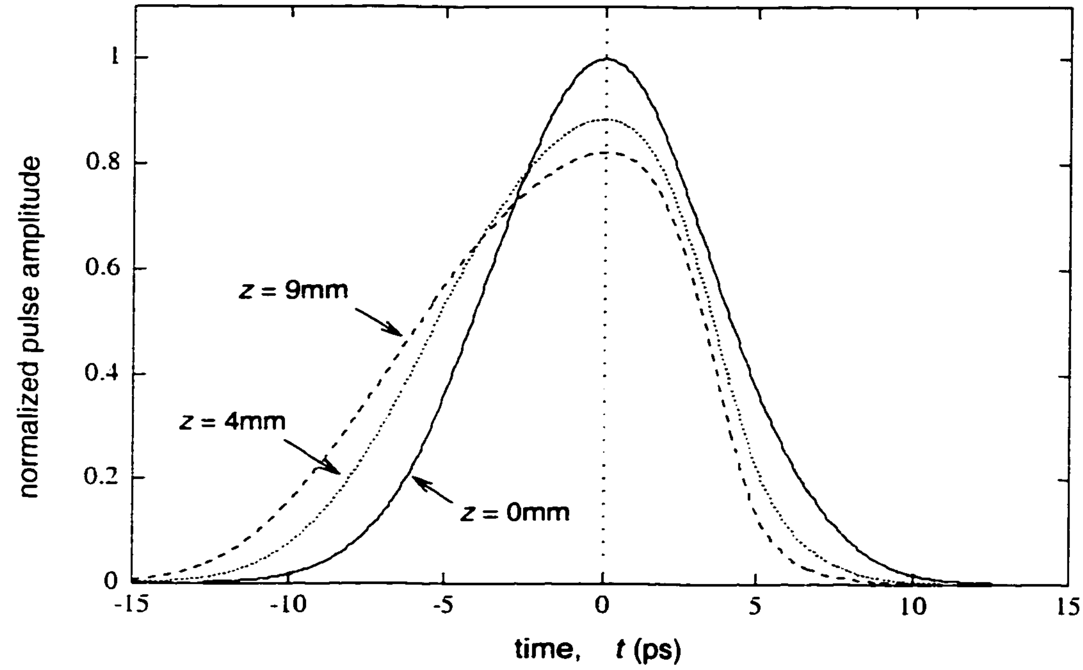

Figure 5.8. Initial pulse (z = 0mm) and pulse shapes after traveling 4mm and 9mm down an HTS transmission line with XYS nonlinearity Pulse amplitudes are normalized with respect to the amplitude of the input pulse.

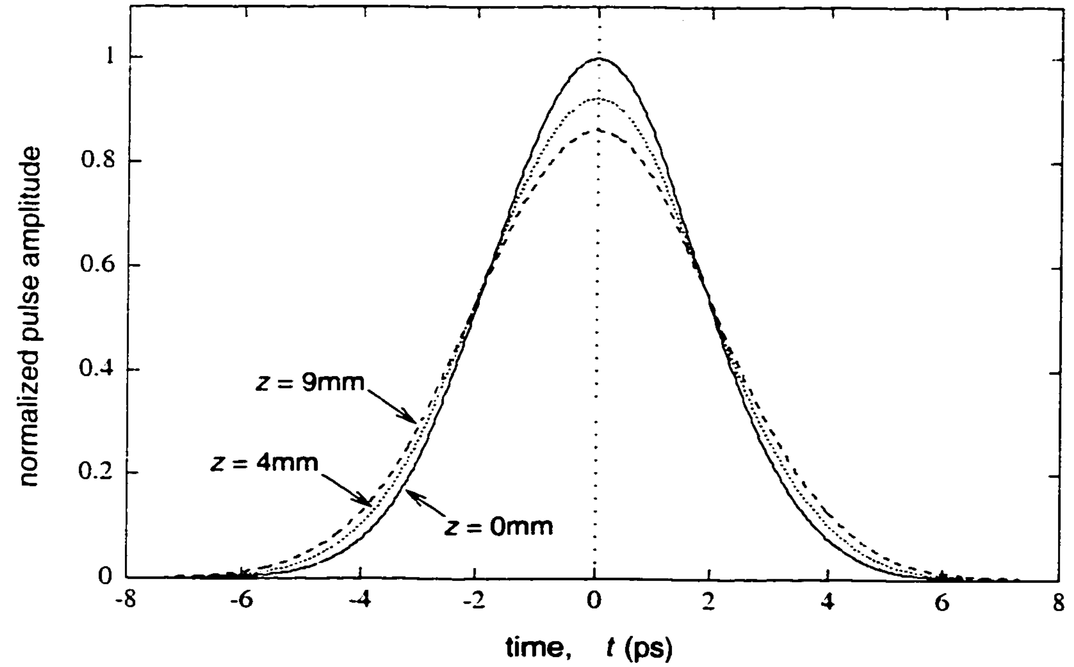

Figure 5.9. Initial pulse (z = 0mm) and pulse shapes after traveling 4mm and 9mm down a linear HTS transmission line. Pulse amplitudes are normalized with respect to the amplitude of the input pulse

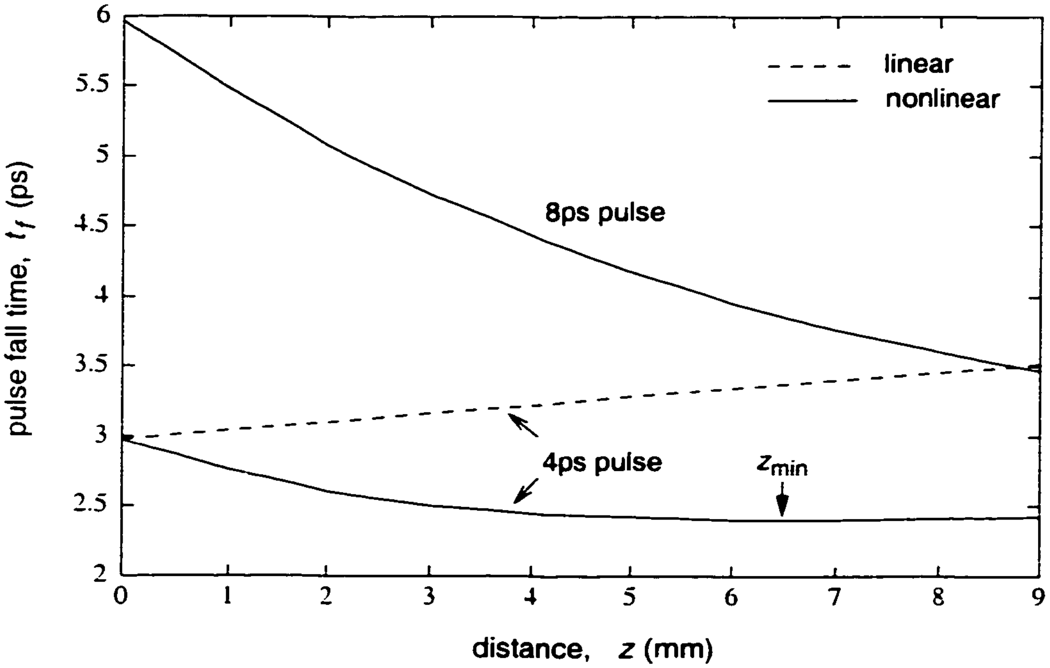

Figure 5.10. The 90%-10% pulse fall-time as a function of the distance travelled in linear and nonlinear HTS transmission lines.

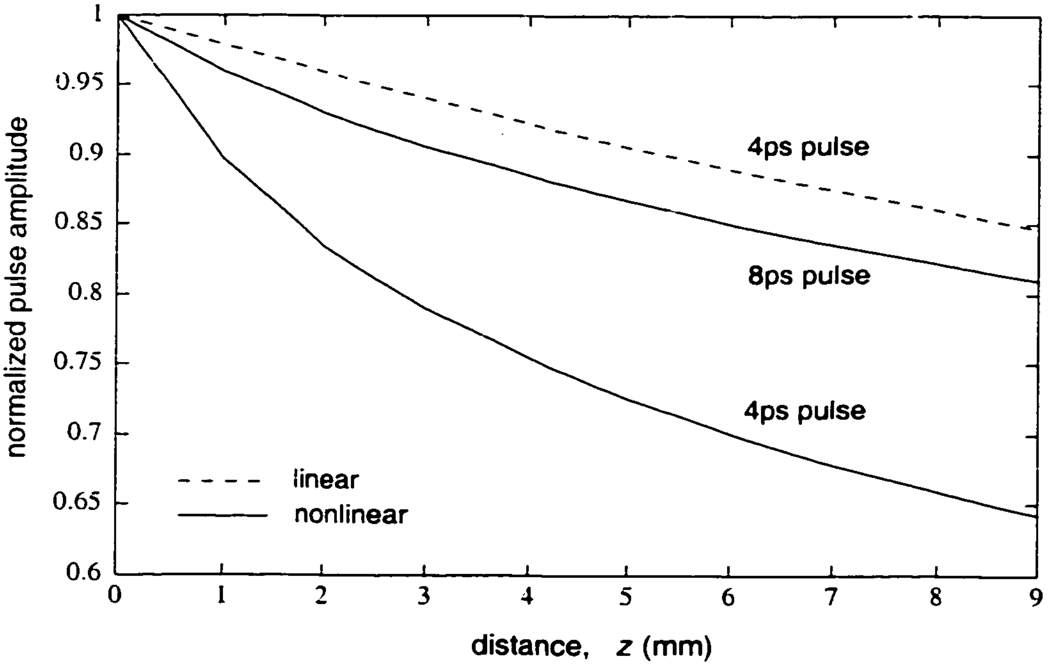

Figure 5.11. Pulse amplitude normalized with respect to the input amplitude, as a function of the distance travelled in linear and nonlinear HTS transmission lines.

of the 8ps pulse in the nonlinear HTS waveguide is seen to decrease constantly with distance, as expected. However, the initial rate of decrease is larger than the rate toward the end of the waveguide. The reason is that, as seen in Figure 5.11, as the pulse progresses down the waveguide, its amplitude is also attenuated, causing the velocity difference between the peak and the tail to lessen. Consequently, the pulse is steepening at a decreased rate. Secondly, the fall-time of the 4ps pulse is seen to decrease initially, then reaches a minimum point at z_{min} = 6.5mm, and begins to increase slightly again. Since the 4ps pulse has a wider spectral content than the 8ps pulse, it experiences larger frequency dispersion and greater attenuation, the latter effect is evident in Figure 5.11. At distances shorter than z_{min}, the pulse amplitude is still sufficiently large so that the nonlinear effect dominates over dispersion, and pulse sharpening occurs with the decreasing fall-time. After z_{min}, the pulse amplitude has attenuated so much that the induced nonlinear effect is weak and can be easily overcome by the dispersive effect; consequently the pulse begins to broaden again. At the minimum distance z_{min}, the two effects exactly balance out, creating a condition for soliton propagation. However, due to the large dissipation at high frequencies, the soliton may not be sustained indefinitely in the waveguide. It is expected that at lower frequencies and temperatures, where the superconductor loss is negligible, the HTS transmission line can potentially support soliton propagation. Also note in Figure 5.10 that for the linear HTS waveguide in which only dispersive effect is present, simulation showed that the fall-time constantly increases with the distance travelled.

Pulse sharpening by shock-wave generation has been previously reported for normal conducting transmission lines periodically loaded with nonlinear elements, and in several commercial microwave instruments, sampling circuits using shock-wave formation to generate 50GHz pulses have already been introduced [109,110]. In conventional technology the nonlinear elements in these periodic circuits are usually reverse-biased diode capacitances [109], and in superconducting technology Josephson junctions have been proposed as the source of nonlinearity [111]. Due to the discrete nature of these circuits, their bandwidths are limited by either the periodic Bragg frequency or the bandwidth of the nonlinear elements. By contrast the simple nonlinear HTS transmission line proposed here is a broadband device which can operate up to millimeter-wave frequencies. A disadvantage of our device, however, is the rapid f^2 increase in the skin loss of the superconducting films. One way to reduce this loss is to lower the operating temperature of the device.

5.2 HTS Resonators

One of the most important microwave applications of HTS materials is in the construction of high-Q resonators. Because of the extremely low surface resistance of the superconducting thin films, the quality factor of an HTS microwave resonator can be two to three orders of magnitude higher than that of its normal conducting counterpart [77]. At the same time, the high Q value also implies that intense fields can build up in the resonator, resulting in significant nonlinear effects such as resonance frequency shift and increased losses. In applications such as filters, the large currents concentrating at the edges of the HTS thin films can drive the superconductors into the normal conducting state, resulting in a degradation of the performance and power-handling capability of the resonator. In our work, however, we wish to exploit the amplified nonlinear effects in the HTS resonator without driving the device into the normal state, for the efficient generation of harmonic frequencies. The idea is analogous to the nonlinear optical microring resonator presented in Chapter 3, in which the intense optical field built up in the ring is used for frequency mixing with high conversion efficiency.

Consider the one-dimensional HTS resonator shown in Figure 5.12, which is coupled to the input and output waveguides via gaps of length g. The parameters of the waveguide were h = 4.5μm, t = 1.0μm, and $\varepsilon_d = 24.0\varepsilon_0$. The superconducting resonator was assumed to be made of YBCO, cooled to a fixed ambient temperature of 77K, with nonlinearity described by the XYS

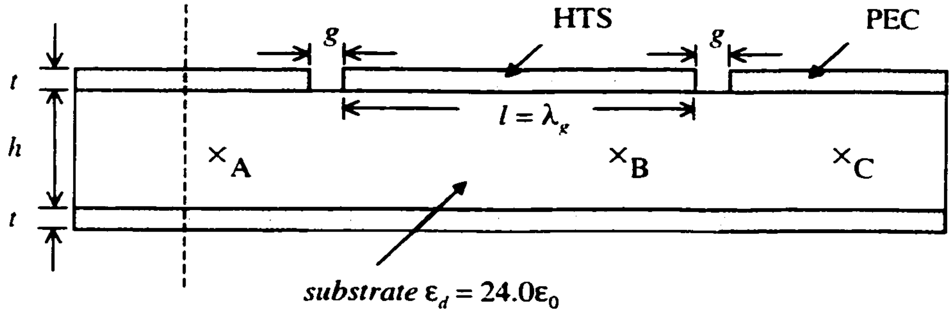

Figure 5.12. One-dimensional HTS resonator coupled to input and output PEC waveguides by gaps. The resonator has length $l = m\lambda_g/2$, with m = 2. The positions marked A, B and C are probe points.

model. The structure was designed to resonate at f_0 = 30GHz, which corresponds to a guided wavelength λ_g of 2.040mm. Assuming a resonance mode m = 2, the length of the resonating section was thus $l = m\lambda_g/2$ = 2040μm. The width g of the coupling gaps was set at 6.0μm.

A Gaussian pulse having a bandwidth of 10GHz and modulated on a 30GHz carrier was applied to the input waveguide of the device. Its amplitude was $4.3H_c$, which resulted in a maximum wave amplitude of $0.9H_c$ being coupled into the HTS resonator. Since this maximum value is less than the critical magnetic field, the HTS films remained in the superconducting state throughout the simulation. The signal at probe point B (indicated in Figure 5.12), which corresponds to the location of a maximum in the standing wave pattern in the resonator, was recorded and shown in Figure 5.13 along with the input pulse. The plot shows that the resonator was completely charged up and reached steady state after 0.4ns. It is also seen that the steady-state signal in the resonator is a sinusoidal wave oscillating at the fundamental frequency f_0. The Fourier transform of the signal power, shown in Figure 5.14 along with the input power spectrum, indicates that the resonance occurs at 28.10GHz. Note that the amplitude of the resonant peak is almost 12dB higher than the input power at the same frequency. The plot also indicates the appearance of the third- and fifth-order harmonics generated inside the resonator. In Figure 5.15 we show the power spectrum of the signal recorded in the output waveguide (at probe C). Again both the fundamental frequency and its odd harmonics can be seen.

The conversion efficiency, calculated from the ratio of the power of the harmonic frequency inside the resonator to that of the fundamental frequency at the input, was 7% for the third-order harmonic. This figure is more than five times higher than that achieved with the straight HTS transmission line presented in Section 5.1(b). The improvement in the conversion efficiency is due to two reasons. Firstly, as mentioned before, the resonance condition causes an intense field to be built up in the resonator, thereby amplifying the nonlinear process without requiring a high input field. Secondly, as stated in Section 5.1(b), the conversion efficiency of a nonlinear transmission line increases with the interaction length. By regarding the standing wave pattern inside the resonator as a sum of two waves traveling in opposite directions, it is clear that the effect of the two reflection ends of the resonator is to increase the interaction length infinite fold. However, due to coupling and radiation losses, the efficiency achieved is much smaller than that of an infinitely long nonlinear transmission line.

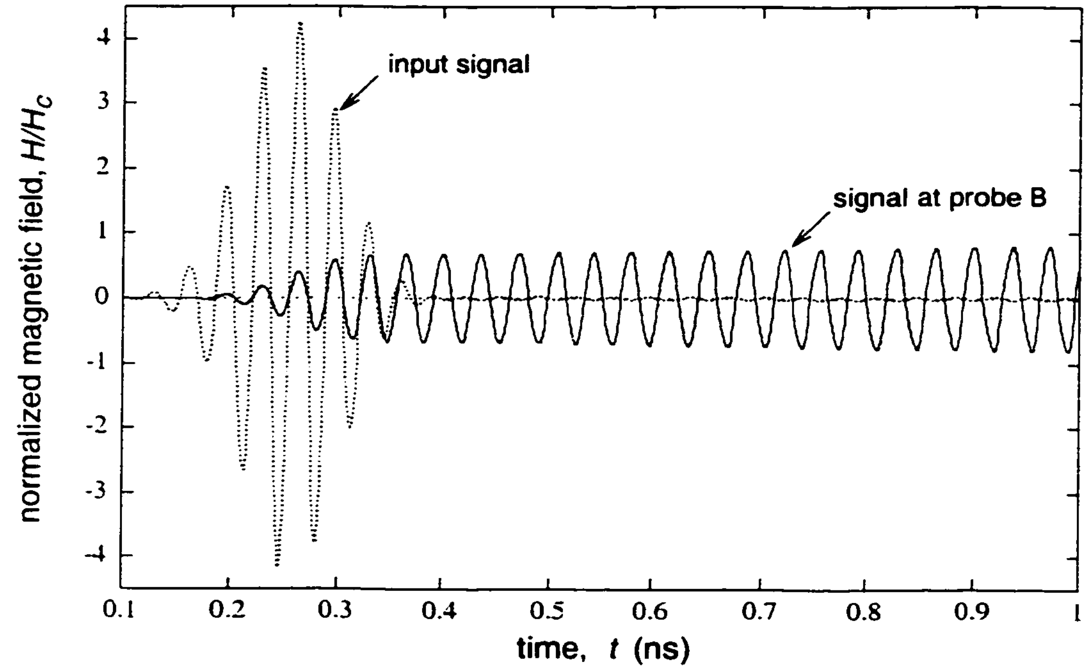

Figure 5.13. Input pulse and the signal recorded at probe B inside the resonator, where a field maximum of the standing-wave pattern occurs.

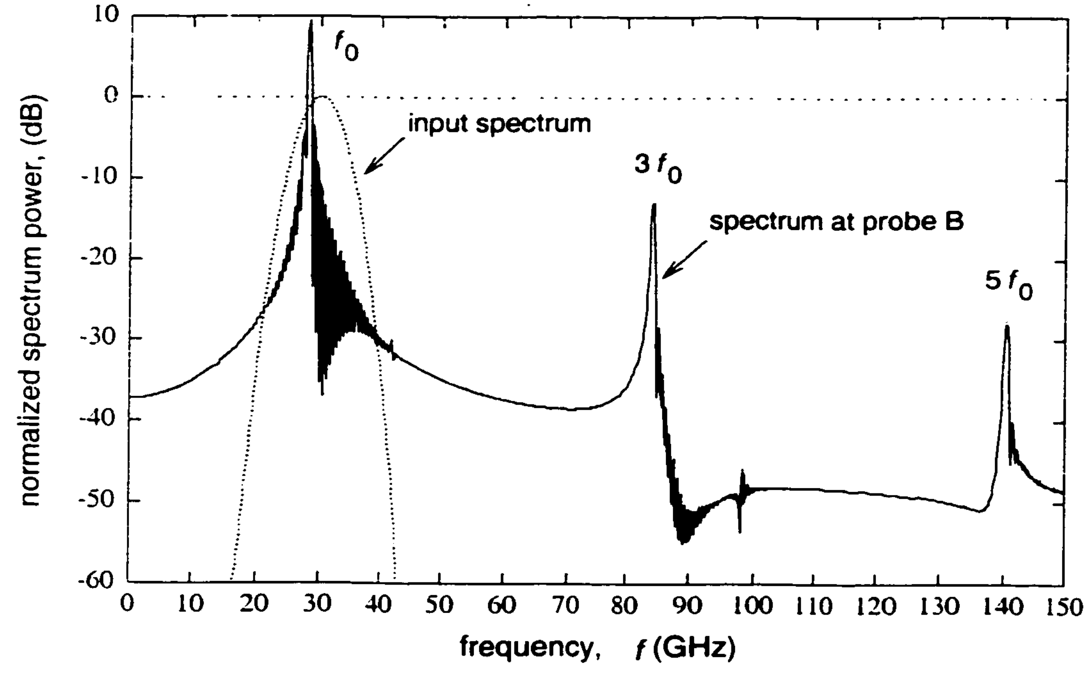

Figure 5.14. Power spectra of the input pulse and the signal recorded at probe B inside the resonator. The spectra are normalized with respect to the peak power of the incident spectrum.

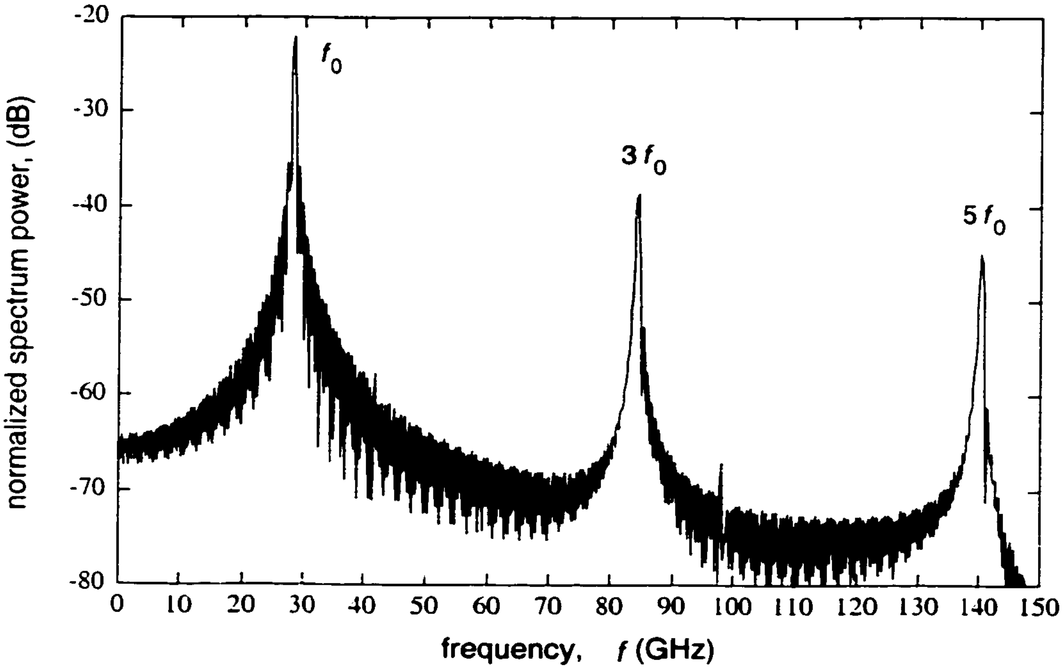

Figure 5.15. Power spectrum of the signal recorded at the output of the resonator (probe C). The spectrum is normalized with respect to the peak power of the incident spectrum.

5.3 HTS Periodic Waveguides

In this section we investigate nonlinear propagation in two-dimensional periodic waveguides in which the periodicity is produced by corrugations in the upper HTS thin film. Three different types of corrugations were considered, as depicted in Figure 5.16, to determine which provides the best frequency selection characteristics. In configuration (a), the corrugations are composed of YBCO sections alternating with normal conducting sections made of copper, both materials assumed to be at 77K. Numerical simulations of the structure showed that, because the difference in the characteristic impedances of the HTS and normal conducting sections was small, reflections in each period were not strong enough to produce good frequency selectivity. In configuration (b), the HTS sections are periodically separated by gaps. Numerical results for this case were opposite of those in case (a): the reflections in each period were too strong, leading to very weak transmitted signals. In configuration (c) the corrugations are realized in the form of rectangular teeth by periodically changing the substrate thickness. From the simulation results it was seen that this type of periodicity provided good frequency selection characteristics with well-defined stopbands. In microstrip or coplanar technology, analogous forms of corrugations may be realized by periodically varying the widths of the superconducting films.

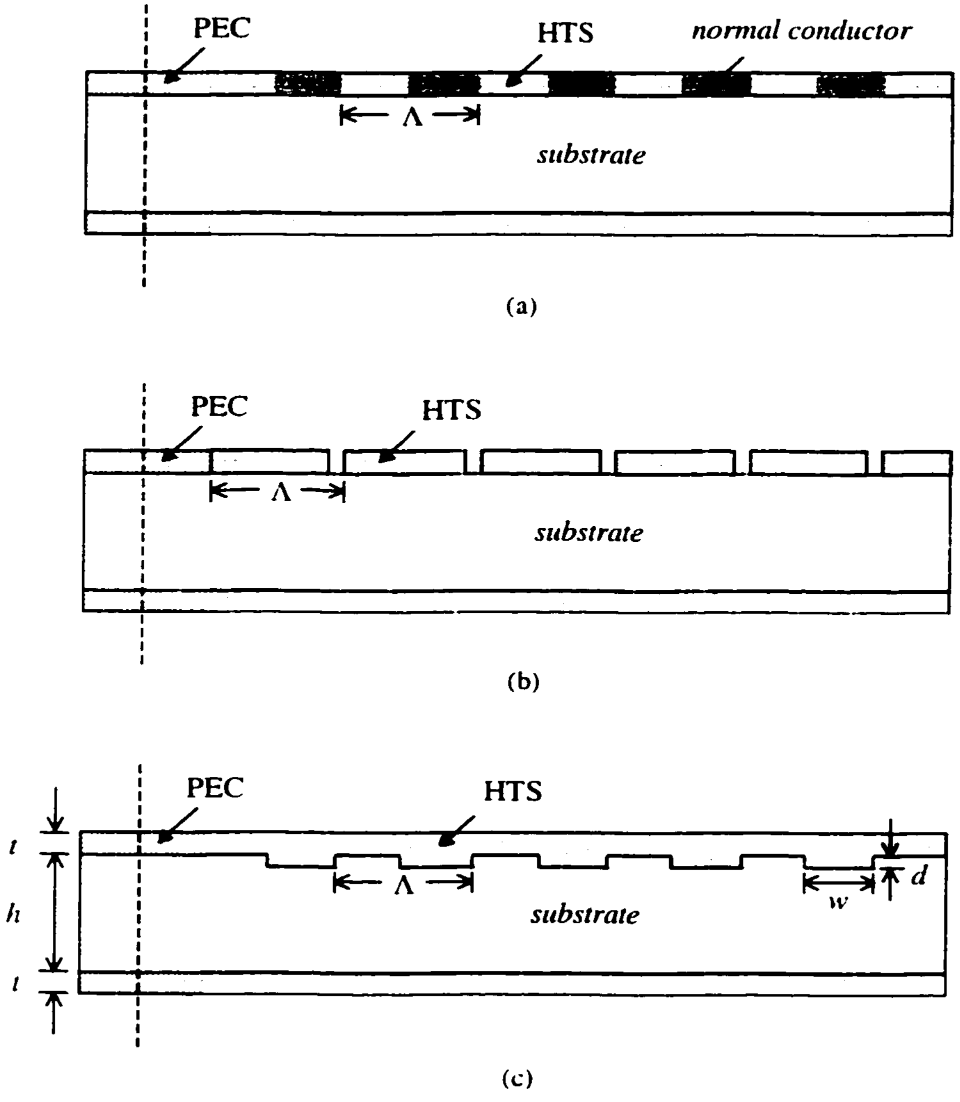

Figure 5.16. Different configurations of HTS periodic waveguides: (a) alternating HTS and normal conducting sections; (b) HTS sections periodically separated by gaps; (c) HTS waveguide with periodically varied substrate thickness.

We first studied the effect of nonlinearities in the HTS films on the reflection characteristics of the periodic waveguide used as a distributed feedback resonator. Both upper and lower conducting plates were assumed to be made of YBCO at 77K and exhibit XYS nonlinearity. The thickness t of the superconducting plates was 0.9μm. The substrate was assumed to be $LaAlO_3$ with permittivity $\varepsilon_d = 24.0\varepsilon_0$ and thickness h = 5.7μm. At 40GHz, the guided wavelength λ_g is 1.520mm, so for first-order grating we chose the period Λ to be $\lambda_g/2$ = 760μm. The height of the teeth was d = 0.6μm and the width was $w = \Lambda/2$ = 380μm. The number of periods was set to $N = 20$.

The waveguide was excited by a TEM-mode Gaussian pulse modulating on a 40GHz carrier. The signal recorded at the output is shown in Figure 5.17 for different input field

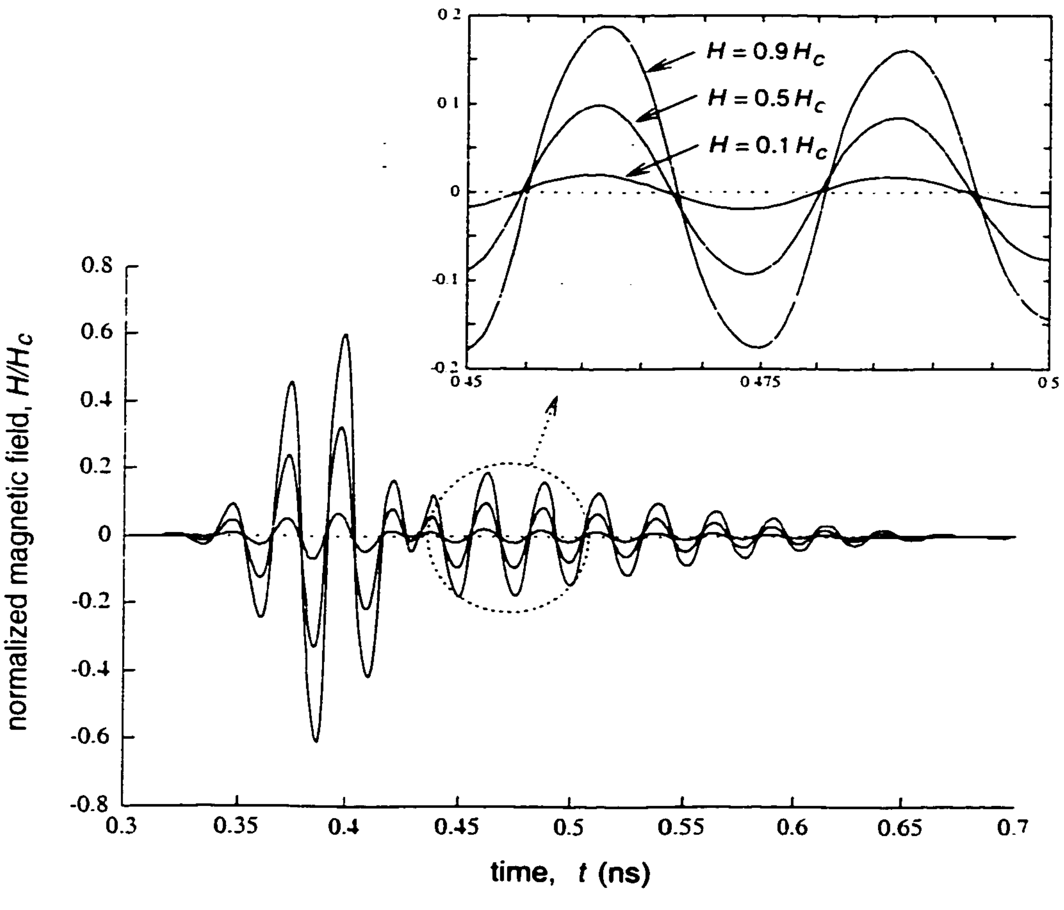

Figure 5.17. Transmitted signals recorded at the output of the HTS periodic waveguide for applied field amplitudes equal to $0.1H_c$, $0.5H_c$ and $0.9H_c$. The inset figure shows the zero-crossings of the signals.

amplitudes. From the inset of the figure we see that nonlinearity in the HTS films causes the transmitted signal to be increasingly delayed at higher input field amplitudes. Figure 5.18 shows the spectra of the reflected signals for input field amplitudes equal to $0.1H_c$ and $0.9H_c$. It is observed that the spectrum at the higher input field is slightly shifted towards lower frequencies with respect to the spectrum at the lower field. The reason is that the increase in the propagation constant β with input power causes the phase-matching condition of the grating to be satisfied at lower frequencies. Thus in the frequency domain, the effect of nonlinearity is to decrease the resonant frequency, similar to the effect caused by Kerr nonlinearity in optical DFR filters presented in Chapter 3. From the zero-crossings of the transmitted signals in Figure 5.17 we extracted the resonant frequencies and computed the percentage change with respect to the linear (low-field) value. The result is plotted against the input field amplitude in Figure 5.19. The decrease in the resonant frequency with respect to increased field amplitude is clearly seen. Associated with this nonlinear resonance shift is the signal attenuation due to increased superconductor loss at high input powers as a result of deeper field penetration into the HTS films. This effect is demonstrated in Figure 5.20, which shows the transmitted amplitudes,

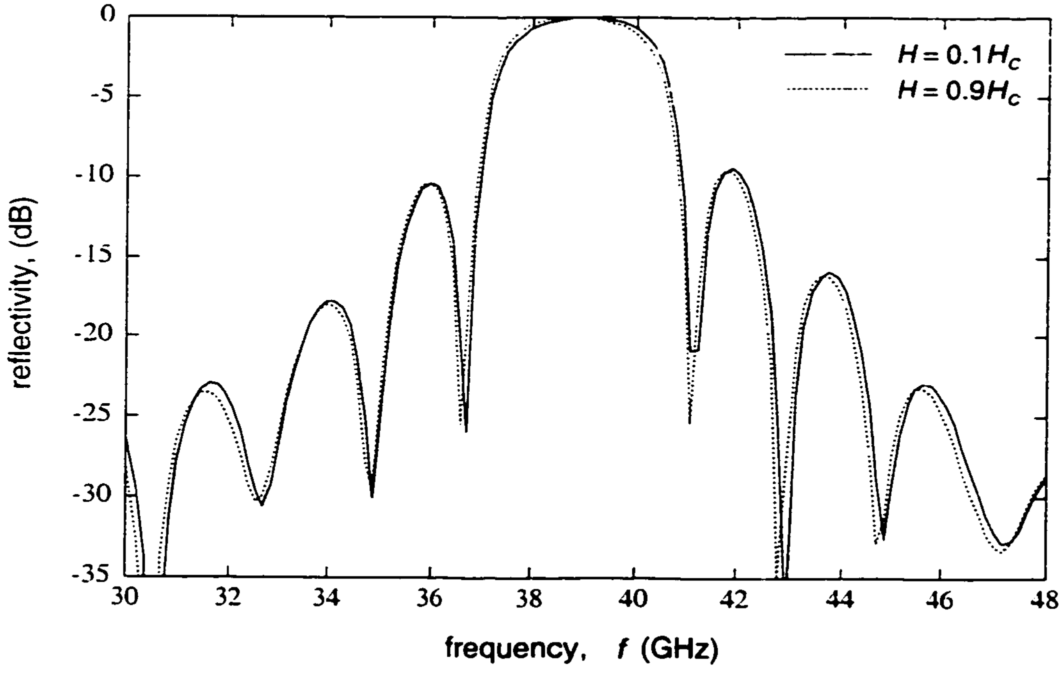

Figure 5.18. Magnitude spectra of the reflected signals of the HTS periodic waveguide at $0.1H_c$ and $0.9H_c$ input field amplitudes.

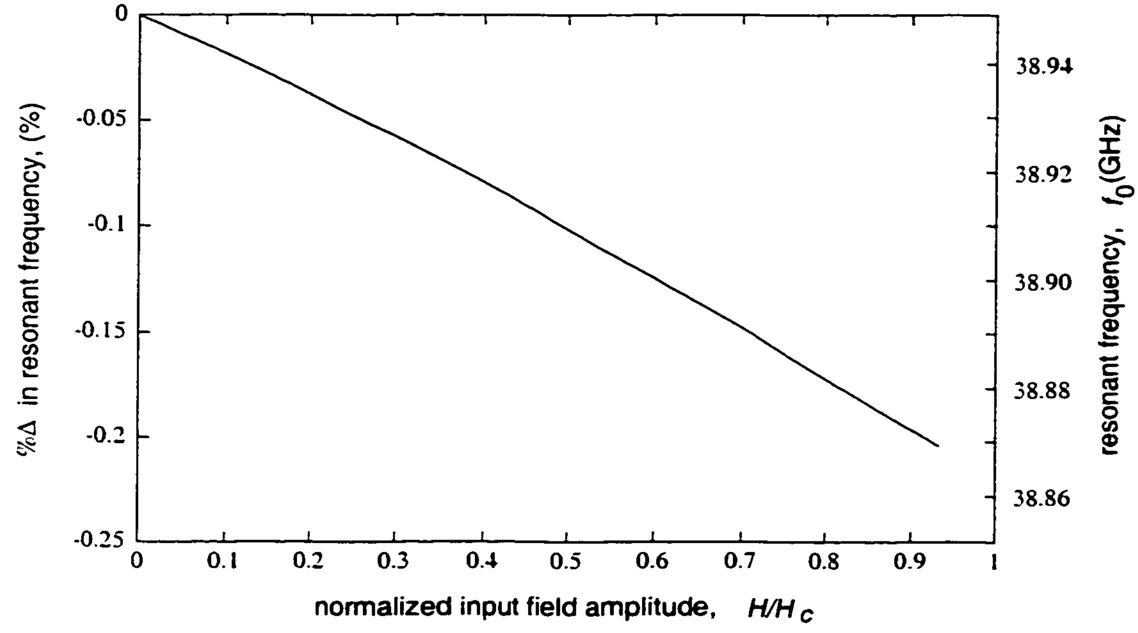

Figure 5.19. Percentage change of the resonant frequency of the HTS periodic waveguide with respect to the linear (low-field) value as a function of input field amplitude.

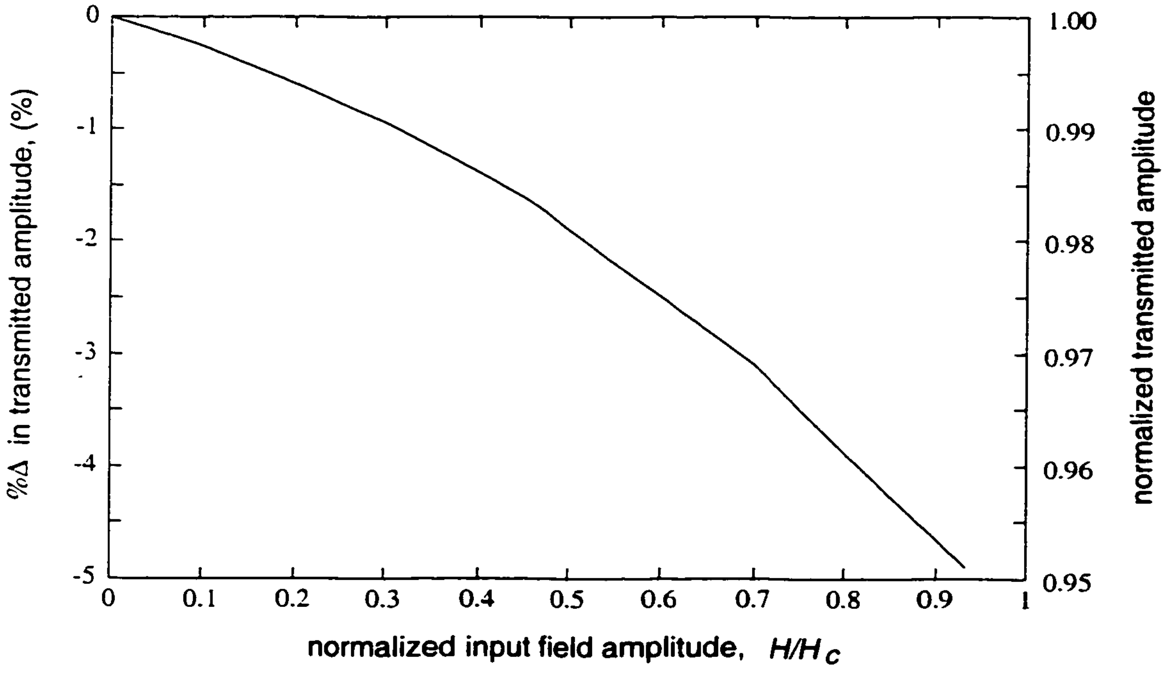

Figure 5.20. Percentage change of the transmitted amplitude at the resonant frequency of the HTS periodic waveguide with respect to the linear (low-field) value as a function of input field amplitude.

normalized with respect to the linear (low-field) value, as a function of the input field.

The reflection spectrum of the 20-period DFR shown in Figure 5.18 has a centre frequency of 38.9GHz and a 3dB bandwidth of 3.1GHz. Figure 5.19 also shows that the maximum change in the resonant frequency due to HTS nonlinearity was about 0.2%, or less than 0.1GHz. Therefore nonlinearity does not noticeably degrade the transmission characteristic of the DFR filter. Although it is expected that the frequency shift becomes more pronounced as the number of periods is increased, the shift is not likely to be large enough to provide power discrimination in this broadband filter, as was demonstrated for optical DBR filters in Chapter 3.

A potential application of the nonlinear HTS periodic waveguide is to provide harmonic generation simultaneously with frequency filtering. It was seen in Section 5.1(b) that propagation of a sinusoidal signal with a DC bias in an HTS transmission line generates second-order harmonic along with higher-order frequency components. If we are interested only in second-order harmonic generation, the higher-order frequencies represent unwanted components and should be suppressed. In particular, the third-order harmonic would be of greatest concern since it represents the parasitic component with the highest power. By designing a nonlinear DFR structure which suppresses the transmission of the third-order harmonic, a cleaner second-order harmonic signal can be obtained at the output of the device.

To demonstrate the operation of such a device, consider the DFR structure in Figure 5.16(c) used to generate the second-order harmonic of input frequency f_0 = 25.7GHz. For third-order harmonic suppression, we designed the periodic waveguide to have a stopband centered around $3f_0$ = 77.5GHz. The parameters of the waveguide were t = 0.9μm, h = 5.7μm, Λ = 380μm, w = 180μm ~ $\Lambda/2$, d = 0.6μm and N = 40. A signal consisting of a sinusoidal wave at the fundamental frequency, f_0, biased on a DC component with amplitude $H_{dc} = H_{ac} = 0.5H_c$, was applied to the input of the device. The power spectrum of the transmitted signal is shown in Figure 5.21. It is observed that both the second- and third-order harmonics are present, but the power of the third-order harmonic is much reduced. To determine how much suppression can be achieved by using corrugations, we compare in Figure 5.22 the power of the third-order harmonic obtained in the DFR waveguide with that obtained using an identical but non-periodic transmission line. The length of the nonlinear section, i.e. the interaction length, of the

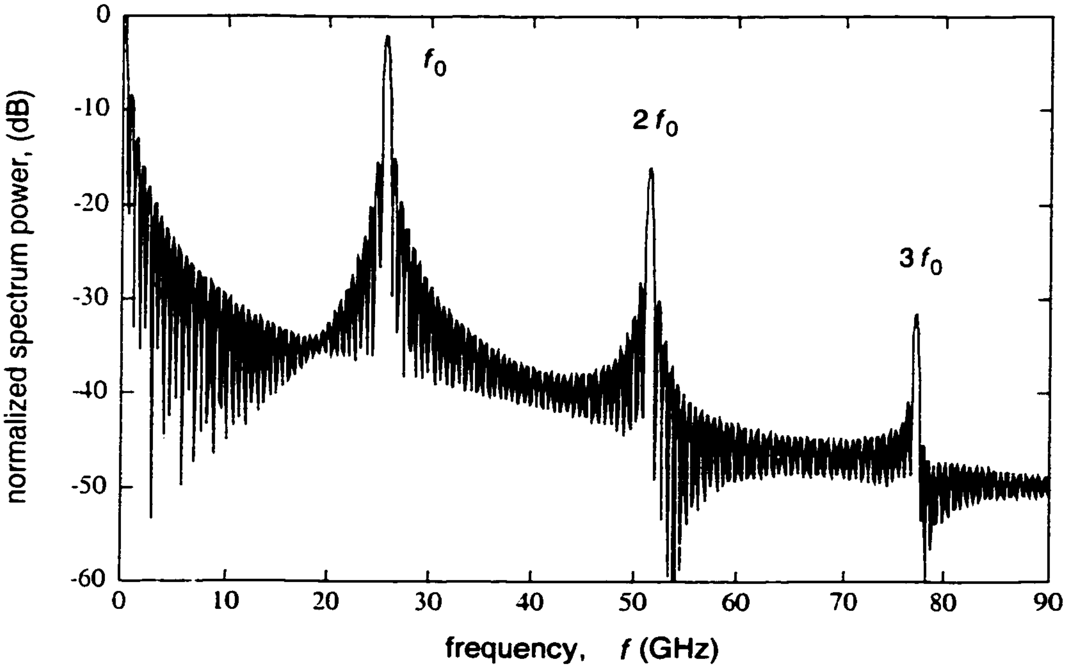

Figure 5.21. Power spectrum of the transmitted signal at the output of the HTS periodic waveguide for input signal $H_{in}(t) = 0.5H_c(1 + \cos(2\pi f_0 t))$, with $f_0 = 25.7$GHz. The spectrum is normalized with respect to the power of the input fundamental frequency.

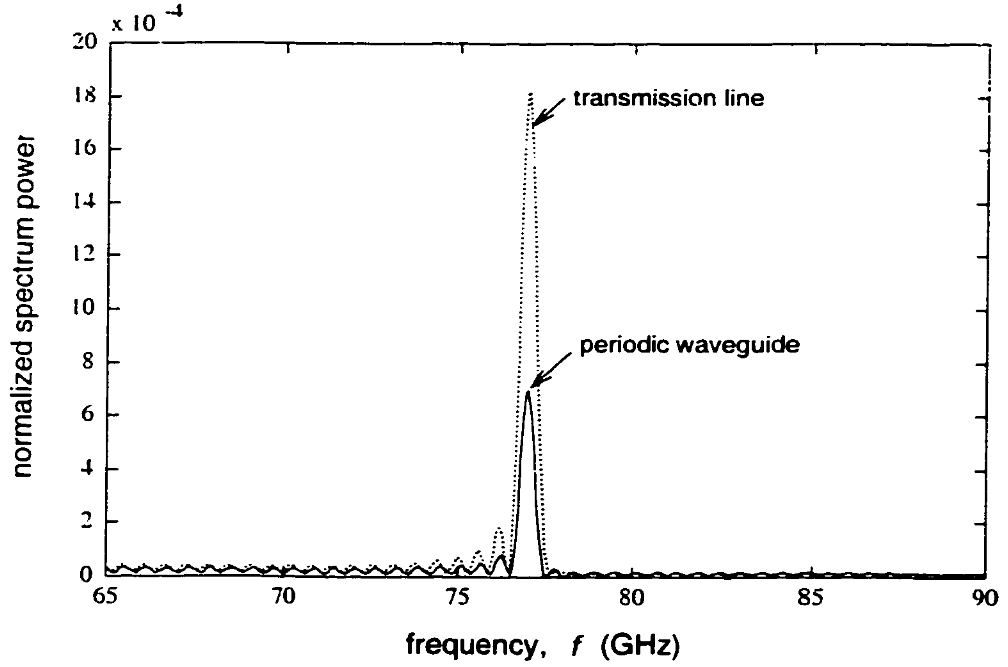

Figure 5.22. Power of the third-order harmonic frequency generated in the HTS periodic waveguide and in the non-periodic HTS transmission line. The spectrum is normalized with respect to the power of the input fundamental frequency.

transmission line was 15.2mm, which is equal to the length of the grating in the periodic waveguide. It is seen that the DFR structure indeed suppresses the transmission of the third-order harmonic by as much as 62%, or 4.2dB. The conversion efficiency for the second-order harmonic was calculated to be 2.5%, which is comparable to that of the nonlinear transmission line.

5.4 Summary

In this chapter we demonstrated the application of the nonlinear FDTD method for analyzing propagation in HTS media to several two-dimensional wave-guiding structures. The method was first validated against analytical solutions for the linear HTS parallel-plate waveguide. It was then applied to HTS transmission lines with XYS nonlinearity to demonstrate many important effects of nonlinear propagation. Specifically, it was shown that the effect of HTS nonlinearity is to slow down wave propagation and increase the skin loss as a consequence of deeper field penetration into the superconducting films. In addition, the dependence of the phase velocity on the wave amplitude results in the formation of shock waves and possibly solitons. It was suggested that the former phenomenon has the potential application for generating ultrafast impulses, possibly even in the sub-picosecond range. Finally, it was shown that the dependence of the propagation constant on $|H|$ also leads to the generation of harmonic frequencies. Both third-order and second-order harmonic generations were demonstrated as a result of nonlinear propagation in HTS resonating and periodic structures.

Chapter 6

Conclusions

A hybrid FDTD method for simulating electromagnetic propagation in nonlinear optical and HTS media has been presented. The method combines the conventional explicit FDTD scheme with a partially-implicit scheme for solving the TE scalar wave equation in nonlinear optical materials. For TM propagation in HTS materials, a hybrid single-field leap-frog scheme was introduced which also allows for mesh refinement via subgridding. By combining the computational simplicity of the explicit method with the accuracy and stability of the proposed nonlinear schemes, the hybrid FDTD technique provides an efficient algorithm for solving Maxwell's equations and the associated nonlinear material constitutive relation.

To assess the proposed nonlinear schemes, we presented a detailed discussion on the relevant numerical issues such as error, stability, dispersion and convergence. In particular, a stability condition for the nonlinear explicit FDTD method was derived. It was shown that for Kerr-type nonlinearities, the nonlinear schemes do not impose additional stability contraint on the algorithm, so that the overall stability of the hybrid FDTD technique is still given by the usual CFL condition.

We verified the hybrid FDTD method by comparing numerical simulations with analytical solutions of simple dielectric slab waveguides and HTS parallel-plate waveguides. The method was then applied to more complex structures such as periodic waveguides and resonators to study nonlinear wave propagation in these devices and to demonstrate potential applications of material nonlinearity to optical and millimeter-wave signal processing.

In the next section, we highlight the major contributions of this thesis, followed by an outline of suggested directions for future work in Section 6.2.

6.1 Summary of Contributions

The major contributions of this thesis can be categorized into four areas: nonlinear FDTD techniques, propagation characteristics in HTS media, nonlinear optical devices, and nonlinear HTS millimeter-wave devices. The contributions in each of these areas are discussed in more detail in the following.

6.1.1 Nonlinear FDTD techniques

- ***Implicit formulation of the FDTD method.*** We presented a general partially-implicit scheme for discretizing the scalar wave equation and provided an algorithm for solving the resulting discrete equation. The scheme reduces to the efficient nonlinear explicit FDTD method for lossless dielectric materials, while for nonlinear materials with high loss, a weighted-average scheme is suggested. Because an implicit scheme in general requires solution of a matrix equation at each FDTD time step, the extra burden in computational effort causes the method to be traditionally viewed as inefficient and not promising. However, for nonlinear problems and problems involving highly conductive materials, we showed that the superior stability property of the implicit scheme allows for accurate solutions to be obtained without the need to reduce the time step below the CFL limit.

  Furthermore, in low-loss linear media, the unconditional stability of the implicit scheme offers unique advantages that are worth pursuing. For example, one area that could benefit from the method is mesh refinement. In subgridding schemes, for every global time step the fields in the local domain have to be marched at the local reduced time step r times, where r is the local-to-global mesh ratio, to ensure that the CFL stability condition is satisfied. By applying implicit discretization to the local domain, the local time step can be made equal to the global time step, so that the local fields can be obtained in one single pass of the FDTD procedure. Another area that could benefit from using the implicit scheme is in the treatment of irregular boundaries that do not conform to the rectangular Yee mesh. Because the boundary elements are not rectangular, the CFL condition is not applicable, and the time step must usually be reduced below the CFL limit in order to ensure stability. This constraint on the time step can be removed by solving the fields in the boundary cells implicitly.

- ***Stability condition of the nonlinear explicit FDTD scheme.*** We presented a rigorous stability analysis for the nonlinear explicit FDTD method, and derived an analytical expression for the stability condition in general nonlinear optical media with instantaneous response. The specific cases of second-order and third-order optical nonlinearities were investigated and verified with numerical experiments. It was also shown that the nonlinear FDTD stability condition reduces to the CFL condition for linear media. The stability condition derived in this thesis represents a significant contribution to nonlinear FDTD techniques because until now, stability of the nonlinear explicit method has not been fully understood and has usually been determined by trial and error, i.e., by running the simulation at various reduced time steps and observing that the numerical solution remains bounded.

- ***Hybrid implicit-explicit FDTD technique.*** We introduced a method for integrating the explicit and partially-implicit discretization schemes into one hybrid FDTD algorithm. The technique provides a way of assigning time indexes to nodes on the interfaces between the explicit and implicit regions so that numerical reflections are minimized. One advantage of our proposed scheme is that the fields in both these regions can be independently computed, lending the algorithm naturally to parallel processing. Although the idea of incorporating different schemes in an FDTD simulation to maximize the computational efficiency is not new, our work represents the first attempt to integrate the implicit scheme into the conventional explicit FDTD method for analyzing structures with mixed linear and nonlinear materials.

- ***Hybrid single-field leap-frog FDTD technique with subgridding.*** A full-wave solution of Maxwell's equations using the leap-frog scheme was integrated with the TM solution of the second-order wave equation. In addition to the advantage of memory saving, the technique allows for the capability of mesh refinement in the local domains where the full-wave solutions are sought. An interpolation scheme in both space and time was used to compute the unknown local field values on the main-grid-local-grid (MG-LG) boundaries. The special case of a perfect electric-conducting (PEC) plate traversing the MG-LG boundary was also treated. This case is important because it allows a PEC mode-launching waveguide to be connected to the input of the device under simulation. When mesh refinement is used, the hybrid scheme is stable for finite-energy input signals such as pulses.

- ***FDTD method for nonlinear HTS media.*** An FDTD algorithm for solving Maxwell's equations simultaneously with the second nonlinear London equation as a constitutive relation for HTS materials was presented. Based on Cummer's Direct Integration scheme, the algorithm does not require solution of nonlinear equations at each time step, and thus can be executed with the numerical efficiency of the explicit FDTD scheme. As a result, the method is considerably faster than the traditional approach based on the Ginzburg-Landau equations. An expression for the numerical dispersion relation of the discrete equation was also derived. The method was verified for linear HTS parallel-plate waveguides for which approximate analytical solutions are known.

6.1.2 Propagation in HTS media

- ***Relationship between the London and Ginzburg-Landau theories of superconductivity.*** It was shown that, if the penetration depth is assumed to vary with the magnetic field, the second nonlinear London equation can be directly derived from the second GL equation. We then hypothesized and verified that the first GL equation is responsible for the nonlinear Meissner effect, and explicitly computed the functional dependence of the penetration depth on the magnetic field as predicted by the theory. The result allowed us to compare the GL theory with experimental measurements of λ and the more recently developed theory of Xu, Yip and Sauls. The conclusion is that the GL theory and experimental data agree in the low-field limit but deviate from each other as the field approaches the critical value.

- ***Electromagnetic analysis of HTS media using the London theory.*** The above relationship between the London and GL theories allows us to formulate an analysis of nonlinear propagation in superconductors using the second London equation as the material constitutive relation. Nonlinearity is accounted for via the nonlinear Meissner effect which describes the dependence of the penetration depth on the magnetic field. This method of analysis is universal in that it can accomodate both theoretical and empirical nonlinear material models, so that as more accurate and rigorous models of $\lambda(H)$ become available, they can be readily incorporated into the analysis.

- ***Nonlinear phenomena associated with propagation in HTS media.*** The effect of nonlinearity on wave propagation in a superconducting medium is to decrease the wave velocity and increase the dissipation, as a result of deeper field penetration into the material. Focusing our study on HTS materials with XYS nonlinearity, we went on to demonstrate that a superconducting transmission line can support shock waves and solitons. Specifically, depending on its amplitude and spectral content, an input pulse can evolve into a shock wave or a solitary wave as a result of the competition between waveguide dispersion and HTS nonlinearity. We also showed that under the condition of continuous-wave excitation, propagation in an HTS transmission line also leads to the generation of new harmonic frequencies.

6.1.3 Nonlinear optical devices

- ***Power-selective DBR filters.*** It was demonstrated by numerical simulations that Kerr-type optical nonlinearity causes the resonance spectrum of a dielectric waveguide with periodically varying index to shift toward longer wavelengths. Consequently, the passband of a nonlinear DBR filter can be made to vary depending on the power of the input signal. We suggested that this effect could potentially be used to realize optical filters that also discriminate the signal power.

- ***Nonlinear microring mixers.*** We proposed a nonlinear optical microring resonator for use as a three-wave mixing device. Due to the high intensity of the optical field circulating in the resonator, strong nonlinear mixing can be achieved which results in high conversion efficiency. In addition, very narrow output channel wavelengths can be obtained due to the high quality factor of the microring. Over a narrow bandwidth where waveguide dispersion is small, the microring mixer can be used to generate a spectrum of equally-spaced wavelength channels, each corresponding to a resonance mode, for use in wavelength division multiplexing optical communication systems.

6.1.4 Nonlinear HTS millimeter-wave devices

- ***Nonlinear HTS tapped-delay lines.*** It was stated that nonlinearity causes the phase velocity in an HTS transmission line to depend on the amplitude of the propagating signal. This phenomenon provides a way of controlling the phase delay of an HTS transmission line section by varying the signal amplitude. We showed that the sensitivity of the phase delay with respect to the signal amplitude is high enough to potentially allow for the use of HTS transmission lines as elements in a tapped-delay line. Such a structure may be used to perform novel analog signal processing functions based on the wave amplitude.

- ***Impulse generation using HTS transmission lines.*** The dependence of the phase velocity of a pulse on its amplitude causes the pulse falling edge to become increasingly sharpened with the propagating distance, eventually leading to the formation of shock waves. Using this phenomenon, we demonstrated picosecond pulse compression on a nonlinear HTS transmission line. At low operating temperatures where the skin loss of the waveguide is small, it is suggested that this technology has the potential of generating pulses in the sub-picosecond range.

- ***Harmonic frequency generation using HTS nonlinearity.*** The generation of second-order and third-order harmonic frequencies in a nonlinear HTS transmission line was demonstrated. We suggested that the conversion efficiency could be improved by taking advantage of the intense field stored in a resonating structure such as the one-dimensional HTS resonator. Also, suppression of high-order harmonics could be achieved by having the nonlinear process take place in a distributed feedback structure. Besides harmonic generation, HTS nonlinearity may also be used in similar devices for frequency mixing and parametric amplification.

6.2 Future Research Directions

The hybrid nonlinear FDTD method presented in this thesis solves the TE scalar wave equation and TM full-wave equations in two-dimensional structures, which do not exhibit cross-polarization effects. In order to account for this nonlinear phenomenon, the method needs to be extended to three dimensions. Many millimeter-wave devices, such as those based on coplanar waveguide and microstrip technologies, are inherently 3D structures. Furthermore, HTS materials and many optical crystals tend to be highly anisotropic, so a more accurate analysis would require the inclusion of anisotropy. Extension of the hybrid method to three dimensions with anisotropy is straightforward, requiring only minor reformulations of the scheme, although the computational complexity will increase considerably. In addition, numerical analyses of stability and convergence become significantly more unmanageable for the nonlinear wave equation in 3D.

Other types of material nonlinearities may also be incorporated into the FDTD solution of the wave equation. An immediate example is optical materials with finite response time. In this case, the medium constitutive relation is described by a differential equation, which must be solved simultaneously with the wave equation. The method of solution is not much different from our proposed FDTD scheme for HTS materials, whose constitutive relation is also governed by a differential equation. Other types of materials include nonlinear dispersive materials and nonlinear magnetic materials. In general, the more complex the constitutive relation, the more challenging it is to ensure stability and convergence of the numerical solution. In these cases, the implicit scheme could prove to be beneficial.

Several computational aspects of the FDTD method may also be improved to provide more accurate and efficient numerical solutions. For example, the perfectly-matched layer (PML) boundary condition may be implemented to reduce reflections from the boundaries. Also, the computation speed of the hybrid implicit-explicit scheme may be accelerated by employing parallel processing techniques.

A numerical method for electromagnetic analysis of HTS media was presented in this thesis. The next step is to experimentally verify the numerical results and the mathematical models used in the analysis. Specifically, the validity of the nonlinear London theory of superconductivity needs to be experimentally confirmed for different ranges of temperatures and frequencies, and for different types of superconductors such as low-T_c materials and type I and type II high-T_c materials. This is accomplished by performing microwave measurements on simple HTS structures such as microstrip transmission lines, and comparing the measured data against simulated results. The extent to which theory agrees with experiments will provide an assessment of the mathematical models used and their limitations.

Finally, a number of novel nonlinear device concepts were proposed, both in the optical and millimeter-wave regimes. Specifically, we demonstrated numerically the operations of nonlinear optical DBR filters, optical microrings for frequency mixing, HTS transmission lines for impulse generation, and HTS resonators for millimeter-wave frequency mixing. By fabricating these devices and experimentally evaluating their performances, practical issues such as power-handling capability and strength of material nonlinearities can be investigated to realistically assess the practicality and potential commercial applications of these devices.

Bibliography

[1] K. S. Yee, "Numerical solution of initial boundary value problems involving Maxwell's equations in isotropic media", *IEEE Trans. Antennas Propagat.*, vol. AP-14, pp. 302–307, May 1966.

[2] S. T. Chu and S. K. Chaudhuri, "Finite-difference time-domain method for optical waveguide analysis", *Progress in Electromagnetics Research*, PIER 11 (editor: W.P. Huang), pp. 225–300, 1995.

[3] R. W. Ziolkowski and J. B. Judkins, "Full-wave vector Maxwell equation modeling of the self-focusing of ultrashort optical pulses in a nonlinear Kerr medium exhibiting a finite response time", *J. Opt. Soc. Am. B*, vol. 10, no. 2, pp. 186–198, Feb. 1993.

[4] R. W. Ziolkowski and J. B. Judkins, "Nonlinear finite-difference time-domain modeling of linear and nonlinear corrugated waveguides", *J. Opt. Soc. Am. B*, vol. 11, no. 9, pp. 1565–1575, Sep. 1994.

[5] P. M. Goorjian, A. Taflove, R. M. Joseph and S. C. Hagness, "Computational modeling of femtosecond optical solitons from Maxwell's equations", *IEEE J. Quantum Electron.*, vol. 28, no. 10, pp. 2416–2422, Oct. 1992.

[6] P. M. Goorjian and A. Taflove, "Direct time integration of Maxwell's equations in nonlinear dispersive media for propagation and scattering of femtosecond electromagnetic solitons", *Opt. Lett.*, vol. 17, no. 3, pp. 180–182, Feb. 1992.

[7] H. A. Jamid and S. J. Al-Bader, "Finite-difference time-domain approach to nonlinear guided waves", *Electron. Lett.*, vol. 29, no. 1, pp. 83–84, 1993.

[8] S. T. Chu, "Analysis and design of guided-wave optical devices using finite-difference time-domain method", *Proc. 11th Ann. Rev. Progress Appl. Computat. Electromagn.*, Monterey, CA, vol. 2, pp. 929–935, Mar. 1995.

[9] N. Ackerly and S. K. Chaudhuri, "Finite-difference time-domain (FDTD) analysis of nonlinear optical waveguiding devices", *Proc. Integrated Photon. Res. Meet.*, OSA, Dana Point, CA, pp. 87–89, Mar. 1995.

[10] D. Schulz, M. Pohl, and E. Voges, "Time domain analysis of nonlinear optical waveguides", *Proc. Integrated Photon. Res. Meet.*, OSA, Dana Point, CA, pp. 90–92, Mar. 1995.

[11] R. M. Joseph, and A. Taflove, "FDTD Maxwell's equations models for nonlinear electrodynamics and optics", *IEEE Trans. Antennas Propagat.*, vol. 45, no. 3, pp. 364–374, Mar. 1997.

[12] R. W. Ziolkowski, "The incorporation of microscopic material models into the FDTD approach for ultrafast optical pulse simulations", *IEEE Trans. Antennas Propagat.*, vol. 45, no. 3, pp. 375–391, Mar. 1997.

[13] A. S. Nagra and R. A. York, "FDTD analysis of wave propagation in nonlinear absorbing and gain media", *IEEE Trans. Antennas Propagat.*, vol. 46, no. 3, pp. 334–340, Mar. 1998.

[14] D. M. Sullivan, "Nonlinear FDTD formulations using *Z* transforms", *IEEE Trans. Microwave Theory Tech.*, vol. 43, no. 3, pp. 676–682, Mar. 1995.

[15] A. Taflove, *Computational Electrodynamics, the Finite-Difference Time-Domain Method.* Norwood, MA: Artech House, 1995.

[16] K. S. Kunz and R. J. Luebbers, *The Finite Difference Time Domain Method for Electromagnetics.* Boca Raton, Fld.: CRC Press Inc., 1993.

[17] D. Yevick and L. Thylen, "Analysis of gratings by the beam-propagation method", *J. Opt. Soc. Am.*, vol. 72, no. 8, pp. 1084–1089, 1982.

[18] B. Lamouroux and B. Prade, "Three-dimensional beam-propagation method treatment of a monomode optical-fiber half-coupler", *J. Opt. Soc. Am. A*, vol. 4, no. 12, pp. 2228–2232, 1987.

[19] B. Hermansson, D. Yevick, and P. Danielsen, "Propagating beam analysis of multimode waveguide tapers", *IEEE J. Quantum Electron.*, vol. 19, no. 8, pp. 1246–1251, 1983.

[20] A. Neyer, W. Mevenkamp, L. Thylen and B. Lagerstrom, "A beam propagation method analysis of active and passive waveguide crossings", *IEEE/OSA J. Lightwave Tech.*, vol. 3, no. 3, pp. 635–642, 1985.

[21] C. L. Xu, "A finite-difference vector beam propagation method for guided-wave optics", Ph.D. dissertation, Dept. of Electrical and Computer Engineering, University of Waterloo, 1994.

[22] C. L. Xu and W. P. Huang, "Finite-difference beam propagation method for guided-wave optics", *Progress in Electromagnetics Research* (editor: W.P. Huang), PIER 11, pp. 1–49, 1995.

[23] L. Thylen, E. M. Wright, G. I. Stegeman, C. T. Seaton and J. V. Moloney, "Beam propagation method analysis of a nonlinear directional coupler", *Opt. Lett.*, vol. 11, no. 11, pp. 739–741, 1986.

[24] L. F. Lee, R. Lee and A. Cangellaris, "Time-domain finite-element methods", *IEEE Trans. Antennas Propagat.*, vol. 45, no. 3, pp. 430–442, Mar. 1997.

[25] B. M. A. Rahman, "Finite element analysis of optical waveguides", *Progress in Electromagnetics Research* (editor: W.P. Huang), PIER 10, pp. 187-216, 1995.

[26] K. Hayata and M. Koshiba, "Full vectorial analysis of nonlinear-optical waveguides", *J. Opt. Soc. Am. B*, vol. 5, no. 12, pp. 2494–2501, Dec. 1988.

[27] R. D. Ettinger, F. A. Fernandez, B. M. A. Rahman and J. B. Davies, "Vector finite element solution of saturable nonlinear strip-loaded optical waveguides", *IEEE Photonic Tech. Lett.*, vol. 3, no. 2, pp. 147–149, Feb. 1991.

[28] B. M. A. Rahman and J. B. Davies, "Finite-element solution of nonlinear bi-stable optical waveguides", *Int. J. Optoelectronics*, vol. 4, pp. 153–161, Mar. 1989.

[29] G. Mur, "Absorbing boundary conditions for the finite-difference approximation of the time-domain electromagnetic field equation", *IEEE Trans. Electromagn. Comput.*, vol. EMC-23, pp. 377–382, 1981.

[30] J. P. Berenger, "Perfectly matched layer for the absorption of electromagnetic waves", *J. Comput. Phys.*, vol 114, no. 2, pp. 185–200, Oct. 1994.

[31] J. P. Berenger, "Improved PML for the FDTD solution of wave-structure interaction problems", *IEEE Trans. Antennas Propagat.*, vol. 45, no. 3, pp. 466–473, Mar. 1997.

[32] Z. P. Liao, H. L. Wong, B. P. Yang and Y. F. Yuan, "A transmitting boundary for transient wave analysis", *Scientia Sinica*, vol. XXVII, no. 10, pp. 1063–1076, Oct. 1984.

[33] M. Moghaddam and W. C. Chew, "Stabilizing Liao's absorbing boundary conditions using single-precision arithmetic", *IEEE MTT-S Int. Microwave Symp. Dig.*, pp. 430–433, 1991.

[34] J. G. Maloney and G. S. Smith, "The user of surface impedance concepts in the finite-difference time-domain method", *IEEE Trans. Antennas Propagat.*, vol. 40, no. 1, pp. 38–48, Jan. 1992.

[35] K. S. Kunz and L. Simpson, "A technique for increasing the resolution of finite-difference solutions to the Maxwell equations", *IEEE Trans. Electromagn. Compat.*, vol. EMC-23, pp. 419–422, Nov. 1981.

[36] L. S. Kim and W. J. R. Hoefer, "A local mesh refinement algorithm for the time-domain finite-difference method using Maxwell's curl equations", *IEEE Trans. Microwave Theory Tech.*, vol. 38, no. 6, pp. 812–815, Jun. 1990.

[37] S. S. Zivanovic, K. S. Yee and K. K. Mei, "A subgridding method for the time-domain finite-difference method to solve Maxwell's equations", *IEEE Trans. Microwave Theory Tech.*, vol. 39, pp. 471–479, Mar. 1991.

[38] D. T. Prescott and N. V. Shuley, "A method for incorporating different sized cells into the finite-difference time-domain analysis technique", *IEEE Microwave Guided Wave Lett.*, vol. 2, pp. 434–436, Nov. 1992.

[39] M. W. Chevalier, R. J. Luebbers and V. P. Cable, "FDTD local grid with material traverse", *IEEE Trans. Antennas Propagat.*, vol. 45, no. 3, pp. 411–421, Mar. 1997.

[40] M. Okoniewski, E. Okoniewska and M. A. Stuchly, "Three-dimensional sub-gridding algorithm for FDTD", *IEEE Trans. Antennas Propagat.*, vol. 45, no. 3, pp. 422–429, Mar. 1997.

[41] Y. Lu and C. Y. Shen, "A domain decomposition finite-difference method for parallel numerical implementation of time-independent Maxwell's equations", *IEEE Trans. Antennas Propagat.*, vol. 45, no. 3, pp. 556–562, Mar. 1997.

[42] P. A. Forsyth and P. H. Sammon, "Practical considerations for adaptive implicit methods in reservoir simulation", *J. Comput. Phys.*, vol. 62, no. 2, pp. 265–281, Feb. 1986.

[43] P. A. Forsyth, "Adaptive implicit criteria for two-phase flow with gravity and capillary pressure", *SIAM J. Sci. Stat. Comput.*, vol. 10, no. 2, pp. 227–252, Mar. 1989.

[44] M. Celuch-Marcysiak and W. K. Gwarek, "Implicit incorporation of nonlinear elements for unconditionally stable FDTD analysis at coarse time-steps", *IEEE MTT-S Int. Microwave Symp. Dig.*, pp. 1381–1384, 1996.

[45] V. Van and S. K. Chaudhuri, "Recent progress in FDTD modelling of optical waveguiding devices", in *PIERS Proc. Progress in Electromag. Res. Symp.*, Cambridge, MA, pp. 220, 1997,.

[46] V. Van, S. K. Chaudhuri and S T. Chu, "A hybrid implicit-explicit FDTD scheme for solving the scalar wave equation in non-linear optical waveguides", *IEEE/AP-S Int. Symp. Dig.*, Montreal, PQ, pp. 372–375, 1997.

[47] V. Van and S. K. Chaudhuri, "A hybrid implicit-explicit FDTD scheme for nonlinear optical waveguide modeling", *IEEE Trans. Microwave Theory Tech.*, vol. 47, no. 5, pp. 540–545, May 1999.

[48] K. W. Morton and D. F. Mayers, *Numerical Solution of Partial Differential Equations*. Cambridge: Cambridge University Press, 1994.

[49] V. Van and S. K. Chaudhuri, "Stability condition of the nonlinear FDTD method for optical device simulation", in *IPR Proc. Integrated Photon. Res. Meeting*, Santa Barbara, CA, pp. 244–246, 1999.

[50] S. A. Cummer, "An analysis of new and existing FDTD methods for isotropic cold plasma and a method for improving their accuracy", *IEEE Trans. Antennas Propagat.*, vol. 45, no. 3, pp. 392–400, Mar. 1997.

[51] P. G. Petropoulos, "Stability and phase error analysis of FD-TD in dispersive dielectrics", *IEEE Trans. Antennas Propagat.*, vol. 42, no. 1, pp. 62–69, Jan. 1994.

[52] S. T. Chu and S. K. Chaudhuri, "Combining modal analysis and the finite-difference time-domain method in the study of dielectric waveguide problems", *IEEE Trans. Microwave Theory Tech.*, vol. 38, no. 11, pp. 1755–1760, Nov. 1990.

[53] X. Zhang, J. Fang, K. Mei and Y. Liu, "Calculations of the dispersive characteristics of microstrips by the time-domain finite difference method", *IEEE Trans. Microwave Theory Tech.*, vol. 36, no. 2, pp. 263–267, Feb. 1988.

[54] L. L. Liou, M. Mah and J. Cook, "An equivalent circuit approach for microstrip component analysis using the FDTD method", *IEEE Microwave and Guided Wave Letters*, vol. 8, no. 10, pp. 330–332, Oct. 1998.

[55] H. A. Van der Vorst, "Bi-CGSTAB: A fast and smoothly converging variant of Bi-CG for the solution of nonsymmetric linear systems", *SIAM J. Sci. Stat. Comput.*, vol. 13, no. 2, pp. 631–644, Mar. 1992.

[56] L. A. Hageman and D. M. Young, *Applied Iterative Methods*. New York: Academinc Press Inc., 1981.

[57] A. Ralston and P. Rabinowitz, *A First Course in Numerical Analysis*. New York: McGraw-Hill Inc., 1978.

[58] E. G. Sauter, *Nonlinear Optics*. New York: John Wiley & Sons Inc., 1996.

[59] H. Nishihara, M. Haruna and T. Suhara, *Optical Integrated Circuits*. New York: McGraw-Hill Book Company, 1989.

[60] A. C. Newell and J. V. Moloney, *Nonlinear Optics*. Redwood City, CA: Addison-Wesley Publishing Company, 1992.

[61] G. P. Agrawal, *Nonlinear Fiber Optics*. San Diego: Academic Press Inc., 1989.

[62] R. A. Sammut and C. Pask, "Gaussian and equivalent-step-index approximation for nonlinear waveguides", *J. Opt. Soc. Am. B*, vol. 8, no. 2, pp. 395–402, 1991.

[63] A. Yariv, *Optical Electronics*, Fourth Edition. Philadelphia: Saunders College Publishing, 1991.

[64] S. L. Chuang, *Physics of Optoelectronic Devices*. New York: John Wiley & Sons Inc., 1995.

[65] W. S. C. Chang, "Periodic structures and their application in integrated optics", *IEEE Trans. Microwave Theory Tech.*, vol. 21, no. 12, pp. 775–785, Dec. 1993.

[66] R. Zengerle and O. Leminger, "Phase-shifted Bragg-grating filters with improved transmission characteristics", *IEEE J. Lightwave Tech.*, vol. 13, no. 12, pp. 2354–2358, Dec. 1995.

[67] V. Van and S. K. Chaudhuri, "Application of a hybrid implicit-explicit FDTD scheme to nonlinear distributed Bragg resonators", in *IPR Proc. Integrated Photon. Res. Meet.*, Victoria, BC, pp. 369–371, 1998.

[68] J. N. Kutz, B. J. Eggleton, J. B. Stark and R. E. Slusher, "Nonlinear pulse propagation in long-period fiber gratings: theory and experiment", *IEEE Journal of Selected Topics in Quantum Electronics*, vol. 3, no. 5, pp. 1232–1245, Oct. 1997.

[69] M. K. Chin, and S. T. Ho, "Design and modeling of waveguide-coupled single-mode microring resonators", *J. Lightwave Technology*, vol. 16, no. 8, pp. 1433–1446, Aug. 1998.

[70] B. E. Little, S. T. Chu, H. A. Haus, J. Foresi, and J.-P. Laine, "Microring resonator channel dropping filters", *J. Lightwave Technology*, vol. 15, no. 6, pp. 998–1005, Jun. 1997.

[71] B. E. Little, J. S. Foresi, G. Steinmeyer, E. R. Thoen, S. T. Chu, H. A. Haus, E. P. Ippen, L. C. Kimerling, and W. Greene, "Ultra-compact Si-SiO$_2$ microring resonator optical channel dropping filters", *IEEE Photonics Technology Letters*, vol. 10, no. 4, pp. 549–551, Apr. 1998.

[72] B. E. Little, J.-P. Laine and S. T. Chu, "Surface-roughness-induced contra-directional coupling in ring and disk resonators", *Optics Letters*, vol. 22, no. 1, pp. 4–6, 1997.

[73] S. C. Hagness. D. Rafizadeh. S. T. Ho. and A. Taflove. "FDTD microcavity simulations: design and experimental realization of waveguide-coupled single-mode ring and whispering-gallery-mode disk resonators". *J. Lightwave Technology*. vol. 15. pp. 2154–2165. 1997.

[74] K. Oda. N. Takato. N. and H. Toba. "A wide-FSR waveguide double-ring resonator for optical FDM transmission systems". *J. Lightwave Technology*. vol. 9. no. 6. pp. 728–736. 1991.

[75] V. Van and B. E. Little. "Design and analysis of nonlinear microring resonators for third-order harmonic generation". in *IPR Proc. Integrated Photon. Res. Meet.*. Santa Barbara. CA. pp. 151–153. 1999.

[76] K. K. Mei and G. Liang. "Electromagnetics of superconductors". *IEEE Trans. Microwave Theory Tech.*. vol. 39. no. 9. pp. 1545–1552. Sep. 1991.

[77] Z. Y. Shen. *High-Temperature Superconducting Microwave Circuits*. Boston: Artech House Inc.. 1994.

[78] T. P. Orlando and K. A. Delin. *Foundations of Applied Superconductivity*. Reading. MA: Addison-Wesley Publishing Company. 1991.

[79] J. D. Doss. *Engineer's Guide to High-Temperature Superconductivity*. New York: John Wiley & Sons. 1989.

[80] S. Sridhar. D.-H. Wu and W. Kennedy. "Temperature dependence of electrodynamic properties of YBa2Cu3Oy crystals". *Physical Review Letters*. vol. 63. no. 17. pp. 1873–1876. Oct. 1989.

[81] M. W. Coffey and J. R. Clem. "Unified theory of effects of vortex pinning and flux creep upon the rf surface impedance of type-II superconductors". *Physical Review Letters*. vol. 67. no. 3. pp. 386–389. Jul. 1991.

[82] M. Golosovsky, D. Davidov, E. Farber, T. Tsach and M. Schieber, "Harmonic generation by field modulation of the microwave complex impedance of high-T_c superconductors", *Physica A*, vol. 168, no. 1, pp. 353–366, Sep. 1990.

[83] D. E. Oates, P. P. Nguyen, G. Dresselhaus, M. S. Dresselhaus, C. W. Lam and A. M. Ali, "Measurements and modeling of linear and nonlinear effects in striplines", *J. Supercond.*, vol. 5, pp. 361–369, 1992.

[84] Y. Kobayashi, T. Imai and H. Kayano, "Microwave measurement of temperature and current dependences of surface impedance for high-T_c superconductors", *IEEE Trans. Microwave Theory Tech.*, vol. 39, no. 9, pp. 1530–1538, Sep. 1991.

[85] D. E. Oates, A. C. Anderson, D. M. Sheen and S. M. Ali, "Stripline resonator measurements of Z_s versus H_{rf} in $YBa_2Cu_3O_{7-x}$ thin films", *IEEE Trans. Microwave Theory Tech.*, vol. 39, no. 9, pp. 1522–1529, Sep. 1991.

[86] C. Wilker, Z. Y. Shen, P. Pang, W. L. Holstein and D. W. Face, "Nonlinear effects in high temperature superconductors: 3rd order intercept from harmonic generation", *IEEE Trans. Appl. Superconduct.*, vol. 5, no. 2, pp. 1665–1670, June 1995.

[87] J. H. Oates, R. T. Shin, D. E. Oates, M. J. Tsuk and P. P. Nguyen, "A nonlinear transmission line model for superconducting stripline resonators", *IEEE Trans. Appl. Superconduct.*, vol. 3, no. 1, pp. 17–22, Mar. 1993.

[88] D. M. Sheen, S. M. Ali, D. E. Oates, R. S. Withers and J. A. Kong, "Current distribution, resistance, and inductance for superconducting strip transmission lines", *IEEE Trans. Appl. Superconduct.*, vol. 1, no. 2, pp. 108–115, June 1991.

[89] D. Antsos, W. Chew, A. L. Riley, B. D. Hunt, M. C. Foote, L. J. Bajuk, D. L. Rascoe and T. W. Cooley, "Modeling of planar quasi-TEM superconducting transmission lines", *IEEE Trans. Microwave Theory Tech.*, vol. 40, no. 6, pp. 1128–1132, June 1992.

[90] J. J. Xia, J. A. Kong and R. T. Shin, "A macroscopic model of nonlinear constitutive relations in superconductors", *IEEE Trans. Microwave Theory Tech.*, vol. 42, no. 10, pp. 1951–1957, Oct. 1994.

[91] A. Maeda, T. Hanaguri, Y. Iino, S. Masuoka, Y. Kokata, J. Shimoyama, K. Kishio, H. Asaoka, Y. Matsushita, M. Hasegawa and H. Takei, "Nonlinear Meissner effect in double layered high-T_c cuprates investigated by measurement of the penetration depth", *Journal of the Physical Society of Japan*, vol. 65, no. 11, pp. 3638–3645, Nov. 1996.

[92] T. Nagashima, S. Harada, M. Hangyo and S. Nakashima, "Inter- and in-plane electromagnetic response of YBCO thin films in the millimeter-wave region and its dependence on weak magnetic field", *Physica C*, vol. 293, pp. 283–287, 1997.

[93] C. P. Bidinosti, W. N. Hardy, D. A. Bonn and R. Liang, "Measurements of the magnetic field dependence of λ in $YBa_2Cu_3O_{6.95}$: results as a function of temperature and field orientation", to appear in *Physical Review B – Condensed Matter*.

[94] D. Xu, S. K. Yip and J. A. Sauls, "Nonlinear Meissner effect in unconventional superconductors", *Physical Review B*, vol. 51, no. 22, pp. 16233–16253, June 1995.

[95] W. C. Lam, D. M. Sheen, S. M. Ali and D. E. Oates, D.E., "Modeling the nonlinearity of superconducting strip transmission lines", *IEEE Trans. Appl. Superconduct.*, vol. 2, no. 2, pp. 58–65, June 1992.

[96] M. A. Megahed and S. M. El-Ghazaly, "Finite difference approach for rigorous full-wave analysis of superconducting microwave structures", *IEEE MTT-S Int. Microwave Symp. Dig.*, pp. 963–966, 1993.

[97] M. A. Megahed and S. M. El-Ghazaly, "Analysis of anisotropic high temperature superconductor planar structures on sapphire anisotropic substrates", *IEEE Trans. Microwave Theory Tech.*, vol. 43, no. 8, pp. 1989–1992, Aug. 1995.

[98] M. A. Megahed and S. M. El-Ghazaly, "Nonlinear analysis of microwave superconductor devices using full-wave electromagnetic model", *IEEE Trans. Microwave Theory Tech.*, vol. 43, no. 11, pp. 2590–2599, Nov. 1995.

[99] V. Van and S. K. Chaudhuri, "Finite-difference time-domain simulation of nonlinear HTS millimeter-wave devices", in *Proc. Third Canadian Applied Superconductivity Workshop*, Vancouver, BC, pp.16–17, 1998.

[100] V. Van and S. K. Chaudhuri, "Finite-difference analysis of nonlinear HTS microwave structures using the London equations", *IEEE MTT-S Int. Microwave Symp. Dig.*, 1999.

[101] G. M. Coutts, R. R. Mansour and S. K. Chaudhuri, "A novel approach to modeling the nonlinear propagation characteristics of HTS planar transmission lines", *IEEE MTT-S Int. Microwave Symp. Dig.*, pp. 1015–1018, 1998.

[102] M. J. Lancaster, *Passive Microwave Device Applications of High-Temperature Superconductors*. Cambridge, UK: Cambridge University Press, 1997.

[103] J. C. Swihart, "Field solution for a thin-film superconducting strip transmission line", *J. Applied Physics*, vol. 32, no. 3, pp. 461–469, Mar. 1961.

[104] J.-G. Ma, "Wave propagation properties in high-temperature superconducting parallel-plate waveguides", *IEEE Microwave and Guided Wave Letters*, vol. 9, no. 5, pp. 183–185, May 1999.

[105] C.-J. Wu, "Propagation characteristics of a thin-film superconducting parallel-plate transmission line in the mixed state", *J. Applied Physics*, vol. 84, no. 6, pp. 3263 – 3266, Sep. 1998.

[106] C.-J. Wu, M.-H. Tsai, H. D. Yang and Y.-S. Tsai, "The effect of superconducting ground plane on microwave characteristics of unpatterned superconducting films in the mixed state", *IEEE Trans. Appl. Superconduct.*, vol. 8, no. 4, pp. 192–202, Dec. 1998.

[107] D. Zhang, H. R. Fetterman and Y. Rahmat-Samii, "High T_c superconducting frequency selective surfaces and their theoretical computer modeling", *IEEE/AP-S Int. Symp. Dig.*, pp. 208–211, 1991.

[108] W. G. Lyons, R. S. Withers, J. M. Hamm, A. C. Anderson, P. M. Mankiewich, M. L. O'Malley and R. E. Howard, "High-T_c superconductive delay line structures and signal conditioning networks", *IEEE Trans. Magnetics*, vol. 27, no. 2, pp. 2932–2935, Mar. 1991.

[109] M. J. W. Rodwell, S. T. Allen, R. Y. Yu, M. G. Case, U. Bhattacharya, M. Reddy, E. Carman, M. Kamegawa, Y. Konishi, J. Pusl and R. Pullela, "Active and nonlinear wave propagation devices in ultrafast electronics and optoelectronics", *Proceedings of the IEEE*, vol. 82, no. 7, pp. 1037–1059, Jul. 1994.

[110] W. C. Whitely, W. E. Kuntz and W. J. Anklam, "50GHz sampler hybrid using a small shockline and an internal SRD", *Proc. 1991 IEEE MTT-S Int. Microwave Symp.*, pp. 895–898, 1991.

[111] G. J. Chen and M. R. Beasley, "Shock-wave generation and pulse sharpening on a series array Josephson junction transmission line", *IEEE Trans. Appl. Superconduct.*, vol. 1, no. 3, pp. 140–144, Sep. 1991.

[112] B. Wedding and D. Jäger, "Phase-matched second harmonic generation and parametric mixing on nonlinear transmission lines", *Eletron. Lett.*, vol. 17, no. 2, pp. 76–77, Jan. 1981.

[113] E. Carman, K. Giboney, M. Case, M. Kamegawa, R. Yu, K. Abe, M. J. W. Rodwell and J. Franklin, "28-39GHz distributed harmonic generation on a soliton nonlinear transmission line", *IEEE Microwave and Guided Wave Lett.*, vol. 1, no. 2, pp. 28–31, Feb. 1991.

[114] R. A. Marsland, M. S. Shakouri and D. M. Bloom, "Millimeter-wave second harmonic generation on a nonlinear transmission line", *Electron. Lett.*, vol. 26, no. 16, pp. 1235–1237, Aug. 1990.

[115] M. S. Shakouri, A. Black, B. A. Auld and D. M. Bloom, "500GHz GaAs MMIC sampling wafer probe", *Electron. Lett.*, vol. 29, no. 6, pp. 557–558, Mar. 1993.

[116] K. S. Champlin and D. R. Singh, "Small-signal second-harmonic generation by a nonlinear transmission line", *IEEE Trans. Microwave Theory Tech.*, vol. 34, no. 3, pp. 351–353, Mar. 1986.

[117] C.-Y. E. Tong, L. Chen and R. Blundell, "Theory of distributed mixing and amplification in a superconducting quasi-particle nonlinear transmission line", *IEEE Trans. Microwave Theory Tech.*, vol. 45, no. 7, pp. 1086–1092, Jul. 1997.

[118] A. C. Scott, F. Y. F. Chu and D. W. McLaughlin, "The soliton: A new concept in applied science", *Proceedings of the IEEE*, vol. 61, no. 10, pp. 1443–1483, Oct. 1973.

[119] S. A. Maas, *Nonlinear Microwave Circuits*. Norwood, MA: Artech House, 1988.

Appendix A

Stability Analysis of the Nonlinear Wave Equation

We present here an analysis of the stability of the fully-explicit FDTD scheme for the nonlinear wave equation,

$$\frac{1}{c^2}\frac{\partial}{\partial t^2}(\varepsilon_r E)=\frac{\partial^2 E}{\partial z^2}+\frac{\partial^2 E}{\partial x^2}. \tag{A.1}$$

Using the index notation $E^n_{i,j} = E(i\Delta z, j\Delta x, n\Delta t)$, the fully-explicit discretized form of the above hyperbolic equation is

$$\begin{aligned}&\frac{(\varepsilon_r E)^{n+1}_{i,j} - 2(\varepsilon_r E)^n_{i,j} + (\varepsilon_r E)^{n-1}_{i,j}}{(c\Delta t)^2} + O\left((\Delta t)^2\right)\\ &= \frac{E^n_{i-1,j} - 2E^n_{i,j} + E^n_{i+1,j}}{(\Delta z)^2} + \frac{E^n_{i,j-1} - 2E^n_{i,j} + E^n_{i,j+1}}{(\Delta x)^2} + O\left((\Delta z)^2, (\Delta x)^2\right)\end{aligned} \tag{A.2}$$

Letting $\theta_z = \frac{c\Delta t}{\Delta z}$, $\theta_x = \frac{c\Delta t}{\Delta x}$, and $g^n_{i,j} = (\varepsilon_r E)^n_{i,j}$, we can rewrite Eq.(A.2) as

$$\begin{aligned}g^{n+1}_{i,j} + g^{n-1}_{i,j} &= 2g^n_{i,j} + \theta_z^2\left(E^n_{i-1,j} - 2E^n_{i,j} + E^n_{i+1,j}\right) + \theta_x^2\left(E^n_{i,j-1} - 2E^n_{i,j} + E^n_{i,j+1}\right)\\ &\quad + O\left((\Delta t)^2, (\Delta z)^2, (\Delta x)^2\right)\\ &= F\left(E^n_{i,j}, E^n_{i-1,j}, E^n_{i+1,j}, E^n_{i,j-1}, E^n_{i,j+1}\right)\end{aligned} \tag{A.3}$$

We shall now show that if the function F is monotonically increasing, then the discretization scheme (A.2) is stable.

From Eq.(A.3) we see that the sum $g^{n+1}_{i,j} + g^{n-1}_{i,j}$ is bounded by the extreme values of F, i.e.,

$$F_{\min} \le g_{i,j}^{n+1} + g_{i,j}^{n-1} \le F_{\max} . \tag{A.4}$$

Define $E_{\min}^{n} = \min\left\{E_{i,j}^{n}\right\}$ and $E_{\max}^{n} = \max\left\{E_{i,j}^{n}\right\}$ for all nodes (i, j). Observing that the quantity $g = \varepsilon_r E$ is also maximum at $E_{\max}$ and minimum at $E_{\min}$, if F is a monotonically increasing function, then we have from Eq.(A.3) that

$$F_{\min} = F\left(E_{\min}^{n}, E_{\min}^{n}, E_{\min}^{n}, E_{\min}^{n}, E_{\min}^{n}\right) = 2g_{\min}^{n} , \tag{A.5}$$

and
$$F_{\max} = F\left(E_{\max}^{n}, E_{\max}^{n}, E_{\max}^{n}, E_{\max}^{n}, E_{\max}^{n}\right) = 2g_{\max}^{n} . \tag{A.6}$$

Relation (A.4) thus becomes

$$2g_{\min}^{n} \le g_{i,j}^{n+1} + g_{i,j}^{n-1} \le 2g_{\max}^{n} . \tag{A.7}$$

Focusing our attention first on the second inequality in (A.7), we have since $g_{i,j}^{n-1} \le g_{\max}^{n-1}$ that

$$g_{i,j}^{n+1} + g_{i,j}^{n-1} \le g_{i,j}^{n+1} + g_{\max}^{n-1} \le 2g_{\max}^{n} . \tag{A.8}$$

Proving by induction, we first assume $g_{\max}^{n} \le g_{\max}^{n-1}$, or

$$- g_{\max}^{n-1} \le -g_{\max}^{n} , \tag{A.9}$$

and add both sides of the second inequality in (A.8) to (A.9) to obtain

$$g_{i,j}^{n+1} \le g_{\max}^{n} . \tag{A.10}$$

In a similar manner, if we assume $g_{\min}^{n} \ge g_{\min}^{n-1}$, then it can be shown that

$$g_{\min}^{n} \le g_{i,j}^{n+1} . \tag{A.11}$$

Together, relations (A.10) and (A.11) give a statement on the boundedness of the quantity g at time step $n+1$:

$$g_{\min}^{n} \le g_{i,j}^{n+1} \le g_{\max}^{n} \qquad \text{for all } i, j. \tag{A.12}$$

The above condition shows that g at any time step is always bounded by the extreme values at the previous time step, implying by the principle of Local Extremum Diminishing that the numerical scheme in Eq.(A.2) is stable.

The stability of the nonlinear scheme deduced above results from our assumption that the function F is monotonically increasing. We now seek to find the conditions for the monotonicity of F, which will also give the stability conditions of the fully-explicit scheme. In order for F to be monotonically increasing, all its first-order partial derivatives must be positive, i.e.,

$$\frac{\partial F}{\partial E_{i,j}^{n}} = 2\frac{\partial g_{i,j}^{n}}{E_{i,j}^{n}} - 2\theta_z^2 - 2\theta_x^2 \geq 0, \tag{A.13}$$

$$\frac{\partial F}{\partial E_{i-1,j}^{n}} = \frac{\partial F}{\partial E_{i+1,j}^{n}} = \theta_z^2 \geq 0, \tag{A.14}$$

and

$$\frac{\partial F}{\partial E_{i,j-1}^{n}} = \frac{\partial F}{\partial E_{i,j+1}^{n}} = \theta_x^2 \geq 0. \tag{A.15}$$

Conditions (A.14) and (A.15) are automatically satisfied. For condition (A.13) to be true, we must have

$$\theta_z^2 + \theta_x^2 \leq \frac{\partial g_{i,j}^{n}}{\partial E_{i,j}^{n}} \tag{A.16}$$

or

$$(c\Delta t)^2 \left(\frac{\partial g_{i,j}^{n}}{\partial E_{i,j}^{n}} \right)^{-1} \left[\frac{1}{(\Delta z)^2} + \frac{1}{(\Delta x)^2} \right] \leq 1. \tag{A.17}$$

Condition (A.17) gives a constraint on the time step Δt and grid sizes Δz and Δx required for the nonlinear fully-explicit FDTD scheme to be stable.

Appendix B

Dispersion Analysis of the Linear Wave Equation

B.1 Fully-Explicit Scheme

In the linear medium region, the explicit discrete equation (A.2) for a node (h, k) becomes

$$\frac{E_{h,k}^{n+1} - 2E_{h,k}^{n} + E_{h,k}^{n-1}}{(v\Delta t)^2} = \frac{E_{h-1,k}^{n} - 2E_{h,k}^{n} + E_{h+1,k}^{n}}{(\Delta z)^2} + \frac{E_{h,k-1}^{n} - 2E_{h,k}^{n} + E_{h,k+1}^{n}}{(\Delta x)^2}. \tag{B.1}$$

where $v = c/\sqrt{\varepsilon_r}$ is the velocity of light in the medium. Letting $\theta_z = \frac{v\Delta t}{\Delta z}$ and $\theta_x = \frac{v\Delta t}{\Delta x}$, we can rewrite the above equation as

$$E_{h,k}^{n+1} - 2\left(1 - \theta_z^2 - \theta_x^2\right)E_{h,k}^{n} - \theta_z^2\left(E_{h-1,k}^{n} + E_{h+1,k}^{n}\right) - \theta_x^2\left(E_{h,k-1}^{n} + E_{h,k+1}^{n}\right) + E_{h,k}^{n-1} = 0. \tag{B.2}$$

Define the Fourier mode

$$E_{h,k}^{n} = \lambda^n e^{j\beta_z h\Delta z} e^{j\beta_x k\Delta x}, \tag{B.3}$$

where $j = \sqrt{-1}$, $\lambda = |\lambda| e^{j\phi}$ is in general a complex number, and β_z and β_x are the propagation constants in the z- and x-direction, respectively. Applying the above test solution to Eq.(B.2) and after factoring out the common factor $\lambda^{n-1} e^{j\beta_z h\Delta z} e^{j\beta_x k\Delta x}$, we get

$$\lambda^2 - 2\left(1 - \theta_z^2 - \theta_x^2\right)\lambda - 2\theta_z^2\lambda\cos(\beta_z\Delta z) - 2\theta_x^2\lambda\cos(\beta_x\Delta x) + 1 = 0. \tag{B.4}$$

Letting $\psi_z = \beta_z \Delta z/2$ and $\psi_x = \beta_x \Delta x/2$, Eq.(B.4) can be simplified to

$$\lambda^2 - 2\left(1 - 2\theta_z^2 \sin^2 \psi_z - 2\theta_x^2 \sin^2 \psi_x\right)\lambda + 1 = 0 . \tag{B.5}$$

Further defining $\xi^2 = \theta_z^2 \sin^2 \psi_z + \theta_x^2 \sin^2 \psi_x$, we obtain the solution to Eq.(B.5) as

$$\lambda = \left(1 - \xi^2\right) \pm j2\xi\sqrt{1 - \xi^2} \tag{B.6}$$

Assuming $\xi \le 1$, which is the stability condition of the fully-explicit scheme, the amplitude of λ is

$$|\lambda| = \left[\left(1 - \xi^2\right)^2 + 4\xi^2\left(1 - \xi^2\right)\right]^{1/2} = 1, \tag{B.7}$$

and the phase is given by

$$\tan\phi = \pm\frac{2\xi}{\sqrt{1 - \xi^2}} . \tag{B.8}$$

Expanding the right-hand side of Eq.(B.8) in a Taylor series, we get

$$\tan\phi = \pm\left(2\xi + 3\xi^3 + \tfrac{23}{4}\xi^5 - \tfrac{9}{2}\xi^7 + \ldots\right), \tag{B.9}$$

from which the phase ϕ can be estimated as

$$\phi = \pm\tan^{-1}\left(2\xi + 3\xi^3 + \tfrac{23}{4}\xi^5 - \tfrac{9}{2}\xi^7 + \ldots\right) \approx \pm\left(2\xi + \tfrac{1}{3}\xi^3 + \ldots\right). \tag{B.10}$$

To express ϕ in terms of Δt, Δz, and Δx, we approximate ξ using Taylor series expansion:

$$\begin{aligned}
\xi &= \left(\theta_z^2 \sin^2 \psi_z + \theta_x^2 \sin^2 \psi_x\right)^{1/2} \\
&= \left[\theta_z^2\left(\psi_z - \tfrac{1}{3!}\psi_z^3 + \tfrac{1}{5!}\psi_z^5 - \ldots\right)^2 + \theta_x^2\left(\psi_x - \tfrac{1}{3!}\psi_x^3 + \tfrac{1}{5!}\psi_x^5 - \ldots\right)^2\right]^{1/2} \\
&= \left[\left(\theta_z^2\psi_z^2 + \theta_x^2\psi_x^2\right) - \tfrac{1}{3}\left(\theta_z^2\psi_z^4 + \theta_x^2\psi_x^4\right) + \ldots\right]^{1/2} \\
&= \left\{\left(\frac{v\Delta t}{2}\right)^2\left(\beta_z^2 + \beta_x^2\right) - \frac{1}{12}\left(\frac{v\Delta t}{2}\right)^2\left[\left(\beta_z^2\Delta z\right)^2 + \left(\beta_x^2\Delta x\right)^2\right]\right\}^{1/2} .
\end{aligned}$$

Using the relation $k^2 = \beta_z^2 + \beta_x^2$, we get

$$\xi = \frac{kv\Delta t}{2}\left\{1 - \frac{1}{24}\left[\left(\frac{\beta_z^2 \Delta z}{k}\right)^2 + \left(\frac{\beta_x^2 \Delta x}{k}\right)^2\right]\right\}. \tag{B.11}$$

Substituting the above result into Eq.(B.10) gives the final form for the phase

$$\phi \approx \pm kv\Delta t\left\{1 - \frac{1}{24}\left[\left(\frac{\beta_z^2 \Delta z}{k}\right)^2 + \left(\frac{\beta_x^2 \Delta x}{k}\right)^2\right] + \frac{1}{24}(kv\Delta t)^2\right\}. \tag{B.12}$$

B.2 Weighted-Average Scheme

The discrete equation for the weighted-average scheme is

$$\begin{aligned}\frac{E_{h,k}^{n+1} - 2E_{h,k}^{n} + E_{h,k}^{n-1}}{(v\Delta t)^2} = {} & \frac{1}{4}\left[\frac{E_{h-1,k}^{n+1} - 2E_{h,k}^{n+1} + E_{h+1,k}^{n+1}}{(\Delta z)^2} + \frac{E_{h,k-1}^{n+1} - 2E_{h,k}^{n+1} + E_{h,k+1}^{n+1}}{(\Delta x)^2}\right] \\ & + \frac{1}{2}\left[\frac{E_{h-1,k}^{n} - 2E_{h,k}^{n} + E_{h+1,k}^{n}}{(\Delta z)^2} + \frac{E_{h,k-1}^{n} - 2E_{h,k}^{n} + E_{h,k+1}^{n}}{(\Delta x)^2}\right] \\ & + \frac{1}{4}\left[\frac{E_{h-1,k}^{n-1} - 2E_{h,k}^{n-1} + E_{h+1,k}^{n-1}}{(\Delta z)^2} + \frac{E_{h,k-1}^{n-1} - 2E_{h,k}^{n-1} + E_{h,k+1}^{n-1}}{(\Delta x)^2}\right]\end{aligned} \tag{B.13}$$

which can be rewritten as

$$\begin{aligned}&\left(1 + \frac{\theta_z^2}{2} + \frac{\theta_x^2}{2}\right)E_{h,k}^{n+1} - \frac{\theta_z^2}{4}\left(E_{h-1,k}^{n+1} + E_{h+1,k}^{n+1}\right) - \frac{\theta_x^2}{4}\left(E_{h,k-1}^{n+1} + E_{h,k+1}^{n+1}\right) \\ &-\left(2 - \theta_z^2 - \theta_x^2\right)E_{h,k}^{n} - \frac{\theta_z^2}{2}\left(E_{h-1,k}^{n} + E_{h+1,k}^{n}\right) - \frac{\theta_x^2}{2}\left(E_{h,k-1}^{n} + E_{h,k+1}^{n}\right) \\ &+\left(1 + \frac{\theta_z^2}{2} + \frac{\theta_x^2}{2}\right)E_{h,k}^{n-1} - \frac{\theta_z^2}{4}\left(E_{h-1,k}^{n-1} + E_{h+1,k}^{n-1}\right) - \frac{\theta_x^2}{4}\left(E_{h,k-1}^{n-1} + E_{h,k+1}^{n-1}\right) = 0.\end{aligned} \tag{B.14}$$

Applying the Fourier mode given in Eq.(B.3) and after simplification, we get

$$\left(1+\theta_z^2\sin^2\psi_z+\theta_x^2\sin^2\psi_x\right)\lambda^2-2\left(1-\theta_z^2\sin^2\psi_z-\theta_x^2\sin^2\psi_x\right)\lambda \\ +\left(1+\theta_z^2\sin^2\psi_z+\theta_x^2\sin^2\psi_x\right)=0, \tag{B.15}$$

or in terms of ξ,

$$\left(1+\xi^2\right)\lambda^2-2\left(1-\xi^2\right)\lambda+\left(1+\xi^2\right)=0. \tag{B.16}$$

The solution to Eq.(B.16) is

$$\lambda=\frac{\left(1-\xi^2\right)\pm j2\xi}{1+\xi^2}, \tag{B.17}$$

from which we see that the amplitude is

$$|\lambda|=\frac{\sqrt{\left(1-\xi^2\right)^2+4\xi^2}}{1+\xi^2}=1, \tag{B.18}$$

and the phase is given by

$$\tan\phi=\pm\frac{2\xi}{1-\xi^2}=\pm2\left(\xi+\xi^3+\xi^5+\ldots\right),$$

or $$\phi\approx\pm\left(2\xi-\tfrac{2}{3}\xi^3+\ldots\right) \tag{B.19}$$

Using Eq.(B.11) for ξ, we get the final result

$$\phi\approx\pm kv\Delta t\left\{1-\frac{1}{24}\left[\left(\frac{\beta_z^2\Delta z}{k}\right)^2+\left(\frac{\beta_x^2\Delta x}{k}\right)^2\right]-\frac{1}{12}(kv\Delta t)^2\right\}. \tag{B.20}$$

B.3 Fully-Implicit Scheme

The fully-implicit discretization of the wave equation is

$$\frac{E_{h,k}^{n+1} - 2E_{h,k}^{n} + E_{h,k}^{n-1}}{(v\Delta t)^2} = \frac{E_{h-1,k}^{n+1} - 2E_{h,k}^{n+1} + E_{h+1,k}^{n+1}}{(\Delta z)^2} + \frac{E_{h,k-1}^{n+1} - 2E_{h,k}^{n+1} + E_{h,k+1}^{n+1}}{(\Delta x)^2} \tag{B.21}$$

which can be written in terms of θ_z and θ_x as

$$\left(1 + 2\theta_z^2 + 2\theta_x^2\right)E_{h,k}^{n+1} - \theta_z^2\left(E_{h-1,k}^{n+1} + E_{h+1,k}^{n+1}\right) - \theta_x^2\left(E_{h,k-1}^{n+1} + E_{h,k+1}^{n+1}\right) - 2E_{h,k}^{n} + E_{h,k}^{n-1} = 0. \tag{B.22}$$

Applying the Fourier mode in Eq.(B.3) to the above equation and after some simplification, we get

$$\left(1 + 4\theta_z^2 \sin^2 \psi_z + 4\theta_x^2 \sin^2 \psi_x\right)\lambda^2 - 2\lambda + 1 = 0\,, \tag{B.23}$$

or in terms of ξ,

$$\left(1 + 4\xi^2\right)\lambda^2 - 2\lambda + 1 = 0\,. \tag{B.24}$$

The solution to the above equation is

$$\lambda = \frac{1 \pm j2\xi}{1 + 4\xi^2} \tag{B.25}$$

from which we see that the amplitude is given by

$$|\lambda| = \frac{1}{\sqrt{1 + 4\xi^2}} \le 1\,. \tag{B.26}$$

Thus the fully-implicit scheme suffers from amplitude attenuation. The attenuation factor can be shown to depend predominantly on the time step as

$$|\lambda| \approx 1 - \tfrac{1}{2}(kv\Delta t)^2\,. \tag{B.27}$$